Title

Electronic Structures and Numerical Simulations for Twisted Bilayer Graphene

Author

Zhu, Qinyi

Publication Date

2023

Peer reviewed|Thesis/dissertation

Electronic Structures and Numerical Simulations for Twisted Bilayer Graphene

by

Qinyi Zhu

A dissertation submitted in partial satisfaction of the

requirements for the degree of

Doctor of Philosophy

in

Mathematics

in the

Graduate Division

of the

University of California, Berkeley

Committee in charge:

Professor Lin Lin, Chair
Professor Per-Olof Persson
Professor Sung-Jin Oh

Fall 2023

Electronic Structures and Numerical Simulations for Twisted Bilayer Graphene

Abstract

Electronic Structures and Numerical Simulations for Twisted Bilayer Graphene

by

Qinyi Zhu

Doctor of Philosophy in Mathematics

University of California, Berkeley

Professor Lin Lin, Chair

The correlated insulating and superconducting phases of magic angle twisted bilayer graphene (TBG) have received intense research attention in the past few years. Since each moiré unit cell of magic angle TBG contains around ten thousand carbon atoms, to take into account electron correlations among different moiré unit cells, a faithful atomistic model of TBG would involve hundreds of thousands of carbon atoms. This is extremely challenging for numerical studies of TBG even at the level of tight-binding models. As a result, the Bistritzer-MacDonald (BM) model, a continuum tight-binding model, has become a widely adopted starting point for further numerical studies. The BM model reveals that the flat bands of interest are energetically separated from the other bands and protected by $C_{2z}\mathcal{T}$ symmetry. Therefore, a reasonable starting point involves projecting the interacting models onto the flat bands and studying the approximate symmetries. This gives rise to the "interacting Bistritzer-MacDonald" (IBM) model, which takes the form of an extended Hubbard model with pairwise long-range interactions. Although the IBM model is not uniquely defined, and a unified physical description of the correlated phases has yet to emerge, such a downfolding procedure has been used by a number of recent works for studying phase diagrams of TBG beyond the tight-binding approximation.

This dissertation aims to present a comprehensive review and detailed proof of the magic angle twisted bilayer graphene, its Hamiltonian, and corresponding symmetries. The unique symmetries of TBG enable the use of various numerical approximations, including the Hartree-Fock method. The geometric and electronic symmetries of TBG restrict the ground state space. Consequently, Hartree-Fock provides a remarkably accurate approximation in the chiral limit where a $U(4) \times U(4)$ symmetry

exists. This accuracy is attributed to the existence of a specific $U(4) \times U(4)$ symmetric ground state within the space of Slater determinant states. Understanding the symmetries of the BM Hamiltonian is crucial for selecting numerical states to approximate the ground states of TBG. A detailed proof of these symmetries enhances our comprehension of the electronic properties of twisted bilayer graphene, validates the accuracy of the HF method, and facilitates the computation of correlated states via exact diagonalization. Furthermore, the discussion about symmetries justifies the accuracy of quantum chemistry approaches beyond the HF method and exact diagonalization. Following the theoretical discussions, this dissertation delves into post-Hartree-Fock calculations. These calculations may become significant when long-range Coulomb interactions are introduced to the IBM model, and the interaction energy scale exceeds the energy dispersion. The techniques to handle such long-range interactions are well studied in the ab initio quantum chemistry community. Employing mature quantum chemistry software packages, this dissertation conducts both HF and post-HF calculations equally for the ground state and excited state properties of the IBM model at the correlated electron level. This approach offers two significant advantages: 1) In cases involving large systems where exact diagonalization proves impractical, HF and post-HF methods provide a viable alternative on a similar level. 2) For both integer and non-integer fillings, the electronic structures of tBLG are investigated using coupled-cluster-based methods such as CCSD and CCSD(T), along with the quantum chemistry density matrix renormalization group (QC-DMRG) method.

To my husband Jiefu, and our cats, Nilla, Giovanna, Mewtwo, Panghu.

Contents

Acknowledgments

Chapter 1

Introduction

The correlated insulating and superconducting phases of magic angle twisted bilayer graphene (TBG) have received intense research attention in the past few years. Numerous studies [13, 14, 66, 112, 12, 20, 86, 109, 105, 25, 9, 63, 82, 41, 80] have contributed to understanding these phases. To solve the interacting Bistritzer-MacDonald (IBM) model numerically, the simplest approximation is Hartree-Fock (HF) theory, which proves particularly effective in the chiral model due to the existence of $U(4) \times U(4)$ symmetry.[12] Both theoretical ([110, 49, 72, 111, 33, 99, 113, 105, 57, 104, 39, 59, 8, 63, 116, 62, 106, 96, 26, 32, 114, 44, 12, 84, 34, 46, 79, 107, 42, 37, 43, 87, 78, 48, 22, 56, 109, 60, 16, 117, 63, 24, 23]) and experimental ([12, 20, 86, 109, 105, 25, 9, 63, 82, 41, 80]) studies have explored the symmetries and numerical solutions of the IBM model. This dissertation aims to provide a comprehensive review of the $U(4) \times U(4)$ symmetry with detailed proofs and varying perspectives. Beginning with background information and essential notations about bilayer graphene and the BM model[10] in the initial sections, we will explore the approximate symmetries[12, 9, 58, 7] of the IBM model in Chapter 2 and delve into the exact symmetric/anti-symmetric ground states[58, 7, 108] in Chapter 3.

However, in certain parameter regimes, the Coulomb energy scale (around $10 \sim 20$ meV) of the IBM model exceeds the dispersion of the flat bands (approximately ~ 5 meV). Consequently, electron correlation effects may become significant, necessitating post-Hartree-Fock calculations to validate and/or refine the physical insights provided by HF theory. Recent studies on exact diagonalization (ED) [80, 108] and the density matrix renormalization group (DMRG) [43, 86, 74, 100] suggest that HF theory provides a good approximation to the description of ground state properties of TBG, at least at integer filling ($\nu = 0$) (the filling parameter ν refers to the number of electrons per $\mathbf{k}$-point relative to the charge neutrality point). Using mature quantum chemistry software packages, this dissertation will study a wide range of

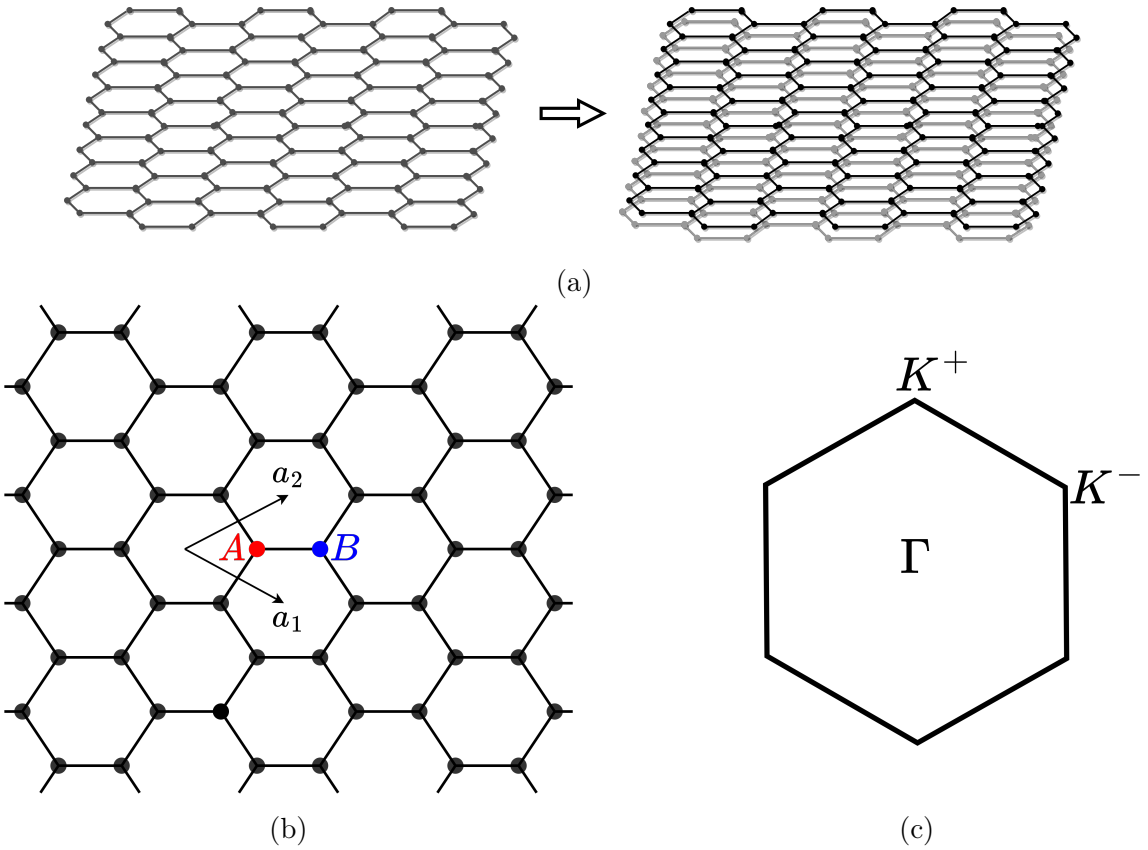

Figure 1.1: (a) Atomic structure of single-layer graphene (left) and bilayer graphene (right). (b) Choice of the rectangular unit cell and corresponding unit vectors $\mathbf{a}_1, \mathbf{a}_2$ in real space, containing two sublattice A and B. The Dirac points of the monolayers K^+ and K^- are included as reference points. (c) Brillouin zone (BZ) of monlayer graphene, aligned by their Γ-point and Dirac points K^+ and K^-.

ground state and excited state properties of the IBM model at the correlated electron level in Chapter 4. Furthermore, this dissertation will discuss some scenarios away from integer filling or the chiral limit for post-Hartree-Fock calculations.[93, 85]

1.1 Graphene

Graphene is a 2D material composed of carbon atoms arranged in a honeycomb structure, as illustrated in Fig. 1.1a. Both single-layer and multi-layer graphene exhibit unique properties due to their distinctive band structure arising from the bonding configuration and structural symmetry. In Fig. 1.1b, we can see that the structural symmetries of graphene include C_2, C_3 rotation symmetry and mirror symmetry around the center of the unit cell, resulting in degenerate energy levels. Moving to Fig. 1.1c, the Brillouin zone (BZ) in reciprocal space has two Dirac points $\Gamma^{\pm}$ where two doubly degenerate energy bands meet.

In this section, we introduce the atomic structure of graphene and derive the corresponding electric structure using the provided notations. It's important to note that the Planck constant is consistently set to $\hbar = 1$. Letting d be the nearest-neighbor distance, the primitive vectors in the unit cell are given by

$$\mathbf{a}_1 = (\frac{3}{2},\ -\frac{\sqrt{3}}{2})d, \quad \mathbf{a}_2 = (\frac{3}{2},\ \frac{\sqrt{3}}{2})d. \tag{1.1}$$

The lattice vector is then expressed as

$$\mathbf{R} = n_1\mathbf{a}_1 + n_2\mathbf{a}_2, \tag{1.2}$$

where n_1 and n_2 are integers. The reciprocal primitive lattice vectors are given by

$$\mathbf{b}_1 = (\frac{1}{3},\ -\frac{1}{\sqrt{3}})\frac{2\pi}{d}, \quad \mathbf{b}_2 = (\frac{1}{3},\ \frac{1}{\sqrt{3}})\frac{2\pi}{d}. \tag{1.3}$$

In the tight-binding model, we only need to consider interactions between nearest neighboring atomic sites. As illustrated in Fig. 1.1b, we denote these two types of atomic sites as sublattice A and sublattice B, with atomic positions $\mathbf{r}_A$ and $\mathbf{r}_B$ respectively. Using σ to represent the sublattice, and given the lattice vectors $\mathbf{R}$, the set of sublattice $\sigma = A/B$, is defined as

$$\mathbf{R}_A = \mathbf{R} + \mathbf{r}_A, \quad \mathbf{R}_B = \mathbf{R} + \mathbf{r}_B. \tag{1.4}$$

Using Bloch's theorem, we express the atomic orbitals for sublattices A and B as Bloch sums:

$$\begin{aligned} \psi^A_{\mathbf{k}}(\mathbf{r}) &= \frac{1}{\sqrt{N}}\sum_{\mathbf{R}} e^{i\mathbf{k}\cdot(\mathbf{R}+\mathbf{r}_A)}\psi(\mathbf{r}-\mathbf{R}-\mathbf{r}_A), \\ \psi^B_{\mathbf{k}}(\mathbf{r}) &= \frac{1}{\sqrt{N}}\sum_{\mathbf{R}} e^{i\mathbf{k}\cdot(\mathbf{R}+\mathbf{r}_B)}\psi(\mathbf{r}-\mathbf{R}-\mathbf{r}_B), \end{aligned} \tag{1.5}$$

where $\mathbf{R} = n_1\mathbf{a}_1 + n_2\mathbf{a}_2$ denotes the lattice position, $\mathbf{k}$ denotes the momentum, and $\psi(\mathbf{r})$ represents the sets of p_z atomic orbitals centered at sublattice A with atomic position $\mathbf{R} + \mathbf{r}_A$ and sublattice B with atomic position $\mathbf{R} + \mathbf{r}_B$. It is assumed that $\langle\psi_{\mathbf{k}}^{\sigma}(\mathbf{r})|\psi_{\mathbf{k}}^{\sigma'}(\mathbf{r})\rangle = \delta_{\sigma\sigma'}$. The single-electron wavefunctions can then be expressed as a linear combination of the two sublattice orbitals, $\psi_{\mathbf{k}}^{A}(\mathbf{r})$ and $\psi_{\mathbf{k}}^{B}(\mathbf{r})$:

$$\Psi_{\mathbf{k}}(\mathbf{r}) = C_A\psi_{\mathbf{k}}^{A}(\mathbf{r}) + C_B\psi_{\mathbf{k}}^{B}(\mathbf{r}), \tag{1.6}$$

where C_A and C_B are complex numbers satisfying $|C_A|^2 + |C_B|^2 = 1$. Using the tight-binding model, we construct the tight-binding Hamiltonian:

$$\begin{pmatrix} \hat{h}_{\mathbf{k}}^{AA} & \hat{h}_{\mathbf{k}}^{AB} \\ \hat{h}_{\mathbf{k}}^{BA} & \hat{h}_{\mathbf{k}}^{BB} \end{pmatrix} \begin{pmatrix} C_A \\ C_B \end{pmatrix} = E_{\mathbf{k}} \begin{pmatrix} C_A \\ C_B \end{pmatrix}. \tag{1.7}$$

The projected Hamiltonian is given by $\hat{h}_{\mathbf{k}}^{\sigma\sigma'} = \langle\psi_{\mathbf{k}}^{\sigma}(\mathbf{r})|\hat{H}|\psi_{\mathbf{k}}^{\sigma'}(\mathbf{r})\rangle$ where $\hat{H}$ is the atomic Hamiltonian and $\hat{H}^*(\mathbf{r}) = \hat{H}$:

$$\begin{aligned} \hat{h}_{\mathbf{k}}^{AA} = \hat{h}_{\mathbf{k}}^{BB} &= \langle\psi_{\mathbf{k}}^{A}(\mathbf{r})|\hat{H}|\psi_{\mathbf{k}}^{A}(\mathbf{r})\rangle\,, \\ \hat{h}_{\mathbf{k}}^{AB} &= \langle\psi_{\mathbf{k}}^{A}(\mathbf{r})|\hat{H}|\psi_{\mathbf{k}}^{B}(\mathbf{r})\rangle\,, \\ &= (e^{i\mathbf{k}\cdot\mathbf{l}_1} + e^{i\mathbf{k}\cdot\mathbf{l}_2} + e^{i\mathbf{k}\cdot\mathbf{l}_3})\,\langle\psi(\mathbf{r}-\mathbf{r}_A)|\hat{H}|\psi(\mathbf{r}-\mathbf{r}_B)\rangle\,, \\ \hat{h}_{\mathbf{k}}^{BA} &= \langle\psi_{\mathbf{k}}^{B}(\mathbf{r})|\hat{H}|\psi_{\mathbf{k}}^{A}(\mathbf{r})\rangle\,, \\ &= (e^{i\mathbf{k}\cdot(-\mathbf{l}_1)} + e^{i\mathbf{k}\cdot(-\mathbf{l}_2)} + e^{i\mathbf{k}\cdot(-\mathbf{l}_3)})\,\langle\psi(\mathbf{r}-\mathbf{r}_B)|\hat{H}|\psi(\mathbf{r}-\mathbf{r}_A)\rangle\,, \end{aligned} \tag{1.8}$$

where $\mathbf{l}_1 = \mathbf{r}_B - \mathbf{r}_A$, $\mathbf{l}_2 = \mathbf{r}_B - \mathbf{a}_1 - \mathbf{r}_A$, $\mathbf{l}_3 = \mathbf{r}_B - \mathbf{a}_2 - \mathbf{r}_A$ represent the distance from one sublattice A site to the nearest three B sublattice sites. Also, $\langle\psi_{\mathbf{k}}^{A}(\mathbf{r})|\hat{H}|\psi_{\mathbf{k}}^{A}(\mathbf{r})\rangle$ and $\langle\psi(\mathbf{r}-\mathbf{r}_A)|\hat{H}|\psi(\mathbf{r}-\mathbf{r}_B)\rangle$ are two constant numbers independent of momentum $\mathbf{k}$. As a result, we can set

$$\begin{aligned} \langle\psi_{\mathbf{k}}^{A}(\mathbf{r})|\hat{H}|\psi_{\mathbf{k}}^{A}(\mathbf{r})\rangle &= \gamma_A, \\ \langle\psi(\mathbf{r}-\mathbf{r}_A)|\hat{H}|\psi(\mathbf{r}-\mathbf{r}_B)\rangle &= \gamma_{AB}, \end{aligned} \tag{1.9}$$

then the tight-binding Hamiltonian can be simplified into

$$\begin{aligned} &\begin{pmatrix} \hat{h}_{\mathbf{k}}^{AA} & \hat{h}_{\mathbf{k}}^{AB} \\ \hat{h}_{\mathbf{k}}^{BA} & \hat{h}_{\mathbf{k}}^{BB} \end{pmatrix}, \\ &= \begin{pmatrix} \gamma_A & (e^{i\mathbf{k}\cdot\mathbf{l}_1} + e^{i\mathbf{k}\cdot\mathbf{l}_2} + e^{i\mathbf{k}\cdot\mathbf{l}_3})\gamma_{AB} \\ (e^{-i\mathbf{k}\cdot\mathbf{l}_1} + e^{-i\mathbf{k}\cdot\mathbf{l}_2} + e^{-i\mathbf{k}\cdot\mathbf{l}_3})\gamma_{AB}^* & \gamma_A \end{pmatrix}, \\ &= \begin{pmatrix} 0 & (e^{i\mathbf{k}\cdot\mathbf{l}_1} + e^{i\mathbf{k}\cdot\mathbf{l}_2} + e^{i\mathbf{k}\cdot\mathbf{l}_3})\gamma_{AB} \\ [(e^{i\mathbf{k}\cdot\mathbf{l}_1} + e^{i\mathbf{k}\cdot\mathbf{l}_2} + e^{i\mathbf{k}\cdot\mathbf{l}_3})\gamma_{AB}]^* & 0 \end{pmatrix} + \gamma_A I, \\ &= \begin{pmatrix} 0 & \Gamma_{\mathbf{k}} \\ \Gamma_{\mathbf{k}}^* & 0 \end{pmatrix} + \gamma_A I, \end{aligned} \tag{1.10}$$

where

$$\begin{aligned}\Gamma_{\mathbf{k}} &= \gamma_{AB}(e^{i\mathbf{k}\cdot\mathbf{l}_1} + e^{i\mathbf{k}\cdot\mathbf{l}_2} + e^{i\mathbf{k}\cdot\mathbf{l}_3}),\\ &= \gamma_{AB}(e^{i\mathbf{k}\cdot(\mathbf{r}_B-\mathbf{r}_A)} + e^{i\mathbf{k}\cdot(\mathbf{r}_B-\mathbf{r}_A-\mathbf{a}_1)} + e^{i\mathbf{k}\cdot(\mathbf{r}_B-\mathbf{r}_A-\mathbf{a}_2)}),\\ &= \gamma_{AB}(e^{i\mathbf{k}\cdot\frac{\mathbf{a}_1+\mathbf{a}_2}{3}} + e^{i\mathbf{k}\cdot\frac{-2\mathbf{a}_1+\mathbf{a}_2}{3}} + e^{i\mathbf{k}\cdot\frac{\mathbf{a}_1-2\mathbf{a}_2}{3}}),\\ |\Gamma_{\mathbf{k}}| &= |\gamma_{AB}|\sqrt{1+4\cos(\frac{3d}{2}k_x)\cos(\frac{\sqrt{3}d}{2}k_y)+4\cos^2(\frac{\sqrt{3}d}{2}k_y)}.\end{aligned} \tag{1.11}$$

Then, two eigenvalues are

$$\epsilon^{\pm}_{\mathbf{k}} = \pm|\Gamma_{\mathbf{k}}|, \tag{1.12}$$

which denotes the upper energy bands ($\epsilon^{+}_{\mathbf{k}}$) and lower energy bands ($\epsilon^{-}_{\mathbf{k}}$) for single-layer graphene, as shown in Fig. 1.2. The two doubly degenerate energy bands meet at the Dirac points:

$$\begin{aligned}\mathbf{K} &= (\frac{1}{3},\ \frac{1}{3\sqrt{3}})\frac{2\pi}{d} = \frac{\mathbf{b}_1+2\mathbf{b}_2}{3},\\ \mathbf{K}' &= -\mathbf{K} = (-\frac{1}{3},\ -\frac{1}{3\sqrt{3}})\frac{2\pi}{d} = \frac{-\mathbf{b}_1-2\mathbf{b}_2}{3},\end{aligned} \tag{1.13}$$

such that $|\Gamma_{\mathbf{K}}| = |\Gamma_{\mathbf{K}'}| = 0$.

The energy bands linearly disperse from the two Dirac points. At the Dirac point $\mathbf{K}$, the tight-binding Hamiltonian can be written as the identity matrix since:

$$\begin{aligned}\Gamma_{\mathbf{K}} &= \gamma_{AB}(e^{i\mathbf{K}\cdot\frac{\mathbf{a}_1+\mathbf{a}_2}{3}} + e^{i\mathbf{K}\cdot\frac{-2\mathbf{a}_1+\mathbf{a}_2}{3}} + e^{i\mathbf{K}\cdot\frac{\mathbf{a}_1-2\mathbf{a}_2}{3}}),\\ &= \gamma_{AB}(e^{i\frac{2\pi}{3}} + e^{0} + e^{-i\frac{2\pi}{3}}) = 0.\end{aligned} \tag{1.14}$$

Besides that, away from the Dirac point with a small momentum $|\mathbf{k}| \ll |\mathbf{K}|$, we have

$$\begin{aligned}\Gamma_{\mathbf{k}+\mathbf{K}} &\approx \frac{\partial\Gamma_{\mathbf{k}}}{\partial\mathbf{k}}(\mathbf{K})\cdot\mathbf{k},\\ &= \gamma_{AB}(\frac{\mathbf{a}_1+\mathbf{a}_2}{3}\cdot e^{i\mathbf{K}\cdot\frac{\mathbf{a}_1+\mathbf{a}_2}{3}} + \frac{-2\mathbf{a}_1+\mathbf{a}_2}{3}\cdot e^{i\mathbf{K}\cdot\frac{-2\mathbf{a}_1+\mathbf{a}_2}{3}} + \frac{\mathbf{a}_1-2\mathbf{a}_2}{3}\cdot e^{i\mathbf{K}\cdot\frac{\mathbf{a}_1-2\mathbf{a}_2}{3}})\cdot\mathbf{k},\\ &= \frac{3d\gamma_{AB}}{2}(k_x - ik_y).\end{aligned} \tag{1.15}$$

Then, the corresponding Hamiltonian is

$$\begin{pmatrix}\hat{h}^{AA}_{\mathbf{K}+\mathbf{k}} & \hat{h}^{AB}_{\mathbf{K}+\mathbf{k}}\\ \hat{h}^{BA}_{\mathbf{K}+\mathbf{k}} & \hat{h}^{BB}_{\mathbf{K}+\mathbf{k}}\end{pmatrix} = \hbar v_F\begin{pmatrix}0 & k_x-ik_y\\ k_x+ik_y & 0\end{pmatrix}, \tag{1.16}$$

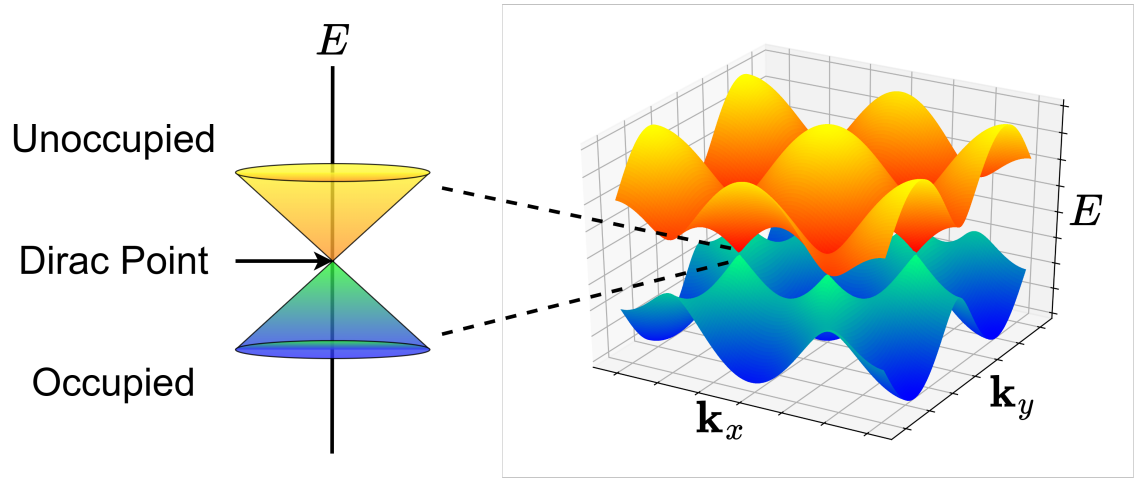

Figure 1.2: The upper energy bands (orange) and lower energy bands (blue) for the single-layer graphene. In half-filling system, the upper energy bands are fully unoccupied, while the lower energy bands are fully occupied. The two doubly degenerate energy bands meet at the Dirac points.

where $v_F = \frac{3d\gamma_{AB}}{2\hbar}$ denotes the Fermi velocity near the Dirac point $\mathbf{K}$. Similarly, near the Dirac point $\mathbf{K}'$, we have

$$\begin{pmatrix} \hat{h}^{AA}_{\mathbf{K}-\mathbf{k}} & \hat{h}^{AB}_{\mathbf{K}-\mathbf{k}} \\ \hat{h}^{BA}_{\mathbf{K}-\mathbf{k}} & \hat{h}^{BB}_{\mathbf{K}-\mathbf{k}} \end{pmatrix} = \hbar v_F \begin{pmatrix} 0 & -k_x - ik_y \\ -k_x + ik_y & 0 \end{pmatrix}. \tag{1.17}$$

Therefore, both the graphene $\mathbf{K}$- and $\mathbf{K}'$-valley Hamiltonian are linearied models.

1.2 Bilayer Graphene

In the section, we will introduce the notations for the non-interacting twisted bilayer graphene. The structural and electronic symmetries of graphene layers enable us to rewrite the Hamiltonian using operators. But before that, let's first review bilayer graphene and its band structures. Firstly, there are two graphene layers perfectly stacked together at two sublattice A sites (AA stacking points), as shown in Fig. 1.3a. Then we twist the top and bottom layers around one AA stacking point by the counterclockwise angles $\frac{\theta}{2}$ and $-\frac{\theta}{2}$ respectively. Note that this twisted angle θ is very small, such that the lattice forms a Moiré pattern with very large unit cells and primitive vectors. As a result, the Moiré reciprocal primitive vectors are very small,

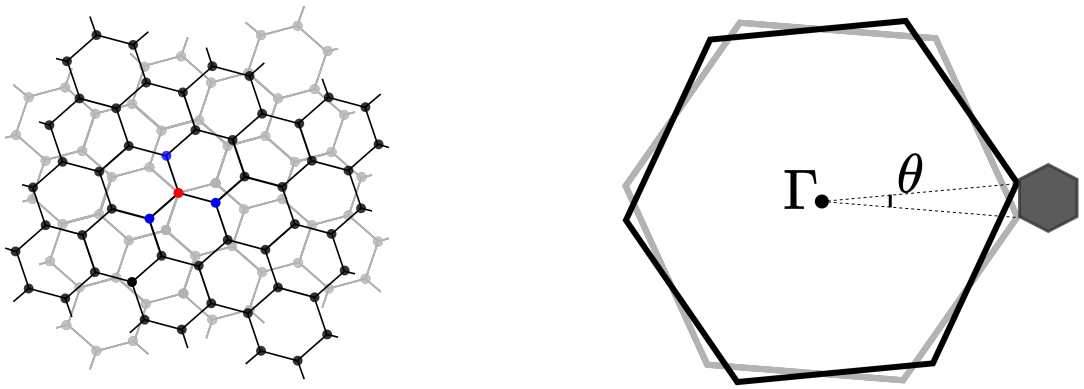

(a) (b)

Figure 1.3: (a) Illustration of twisted bilayer graphene in real space. Red (Blue) sites is for the sublattice A (B). Black (gray) is for the top (bottom) layer. The origin is chosen at an AA region center (perfect AA stacking point). (b) Two monolayer graphene Brillouin zones (BZ) depicted by a dashed red line and solid blue line, respectively, aligned by their Γ-point and twisted by an angle θ, with the corresponding Dirac points K^+ and K^-. The Moiré Brillouin zone (MBZ) is indicated by the grey shaded region centered at Γ_{MBZ}.

and the Moiré Brillouin zone (MBZ) is also very small compared to the monolayer graphene Brillouin zone, as depicted in Fig. 1.3b.

The two graphene layers in twisted bilayer graphene are rotated by a small angle θ. Therefore, to express the structural properties of tBLG more conveniently, we define a rotation matrix $R(\theta)$, which rotates by θ radians counterclockwise about one given AA-stacking point:

$$R(\theta) = \begin{pmatrix} \cos\theta & -\sin\theta \\ \sin\theta & \cos\theta \end{pmatrix} \tag{1.18}$$

Since graphene forms a hexagonal lattice, rotations by 120° are particularly important, and we define $C_3 := R(2\pi/3)$. When we twist the top layer (labeled by $l = 1 = t$) and bottom layer (labeled by $l = -1 = b$) around that given AA-stacking point by the counterclockwise angles $\theta/2$ and $-\theta/2$, respectively, we also rotate the

Dirac point $\mathbf{K}$ to

$$\mathbf{K}_l = R(l\frac{\theta}{2})\mathbf{K}, \quad l \in \{t = 1, b = -1\}.$$

When θ is very small, the lattice forms a Moiré pattern with translation vectors of length $\sim \theta^{-1}$. Correspondingly, the Moiré Brillouin zone (or "mini" Brillouin zone, MBZ) is very small compared to the monolayer graphene Brillouin zone (BZ).

Let

$$k_D = |\mathbf{K}| = \frac{4\pi}{3}, \quad k_\theta = 2\sin(\frac{\theta}{2})k_D. \tag{1.19}$$

Define

$$\mathbf{q}_1 = \mathbf{K}_b - \mathbf{K}_t = (R(-\frac{\theta}{2}) - R(\frac{\theta}{2}))\mathbf{K} = 2k_D\sin(\frac{\theta}{2})(0,\ -1)^\top = k_\theta(0,\ -1)^\top,$$

and

$$\mathbf{q}_2 = C_3\mathbf{q}_1 = k_\theta(\frac{\sqrt{3}}{2}\ , \frac{1}{2})^\top, \quad \mathbf{q}_3 = C_3^2\mathbf{q}_1 = k_\theta(-\frac{\sqrt{3}}{2},\ \frac{1}{2})^\top.$$

In this convention, $\mathbf{q}_j = -\sqrt{3}k_\theta\boldsymbol{\delta}_j = -\frac{8\pi}{\sqrt{3}}\sin(\frac{\theta}{2})\boldsymbol{\delta}_j$.

We also define the two reciprocal lattice vectors for the MBZ as

$$\begin{aligned}
\widetilde{\mathbf{b}}_1 =&(R(-\frac{\theta}{2}) - R(\frac{\theta}{2}))\mathbf{b}_1 = -(\mathbf{q}_2 - \mathbf{q}_1) = \sqrt{3}k_\theta\left(-\frac{1}{2},\ -\frac{\sqrt{3}}{2}\right)^\top, \\
\widetilde{\mathbf{b}}_2 =&(R(-\frac{\theta}{2}) - R(\frac{\theta}{2}))\mathbf{b}_2 = -(\mathbf{q}_3 - \mathbf{q}_1) = \sqrt{3}k_\theta\left(\frac{1}{2},\ -\frac{\sqrt{3}}{2}\right)^\top.
\end{aligned} \tag{1.20}$$

Note that $|\mathbf{q}_j| = k_\theta$ and $\left|\widetilde{\mathbf{b}}_i\right| = \sqrt{3}k_\theta$. The lattice vectors dual to $\widetilde{\mathbf{b}}_1, \widetilde{\mathbf{b}}_2$ define the moiré unit cell in real space

$$\widetilde{\mathbf{a}}_1 = L_M\left(-\frac{\sqrt{3}}{2},\ -\frac{1}{2}\right)^\top, \quad \widetilde{\mathbf{a}}_2 = L_M\left(\frac{\sqrt{3}}{2},\ -\frac{1}{2}\right)^\top,$$

where $L_M = |\widetilde{\mathbf{a}}_i| = \frac{k_D}{k_\theta} = \frac{1}{2\sin\frac{\theta}{2}}$ is the moiré length scale in real space. In the discussion below,

$$\mathbb{L} = \{\mathbf{R} = m_1\widetilde{\mathbf{a}}_1 + m_2\widetilde{\mathbf{a}}_2 | m_j \in \mathbb{Z}\}$$

denotes the moiré lattice in real space,

$$\mathbb{L}^* = \{\mathbf{G} = m_1\widetilde{\mathbf{b}}_1 + m_2\widetilde{\mathbf{b}}_2 | m_j \in \mathbb{Z}\}$$

denotes the moiré lattice in reciprocal space. We also denote Ω, Ω^* as the moiré unit cell and the first moiré Brillouin zone, respectively.

1.3 Bistritzer-MacDonald Model

In this section, we will briefly review the BM model.[10] For convenience, we ignore the spin index s and abbreviate the creation operator as $\hat{c}^\dagger_{\mathbf{k},l,\tau,\sigma}$. When the twisted angle between two layers θ is very small, the unit cell of TBG is very large, and the MBZ is very small. In this case, coupling between the two valleys can be neglected. The single-valley Hamiltonian in valley $\tau = \mathbf{K} = +1$ can be written as

$$\begin{aligned}\hat{H}^{\tau=\mathbf{K}}_{BM} = &\sum_{\mathbf{k}\in\mathrm{MBZ}}\sum_{l}\sum_{\sigma\sigma'}\hat{c}^\dagger_{\mathbf{k},l,\tau,\sigma}[\hat{h}_l(\mathbf{k})]_{\sigma\sigma'}\hat{c}_{\mathbf{k},l,\tau,\sigma'} \\ &+(\sum_{\mathbf{k}\in\mathrm{MBZ}}\sum_{\sigma\sigma'}\sum_{j=1}^{3}\hat{c}^\dagger_{\mathbf{k}+\mathbf{q}_j,t,\tau,\sigma}\hat{T}_j\hat{c}_{\mathbf{k},b,\tau,\sigma'}+h.c.),\end{aligned} \tag{1.21}$$

where $\mathbf{k}$ denotes the momentum in the MBZ, $l = \pm 1 = t/b$ denotes the layer and $\sigma = \pm 1 = A/B$ denotes the sublattice; $\hat{h}_l(\mathbf{k})$ is the single-particle Hamiltonian in the first-quantized momentum space for layer l, and $\hat{T}_j$ represents the interlayer interaction with $\mathbf{q}_1 = \mathbf{K}_b - \mathbf{K}_t$, $\mathbf{q}_2 = C_{3z}\mathbf{q}_1$, $\mathbf{q}_3 = C_{3z}\mathbf{q}_2$. $C_{3z} = R(2\pi/3)$ is the counterclockwise 120° rotation around the valley $\mathbf{K}_t$ in the top layer. Note that $\{\mathbf{q}_j\}_{j=1,2,3}$ relates the momentum $\mathbf{k}+\mathbf{q}_j$ in the top layer and $\mathbf{k}$ in the bottom layer, representing the interlayer interactions.

The monolayer graphene has a linearized Hamiltonian near both the $\mathbf{K}_l$ and $\mathbf{K}'_l$ valley, as in Eqs. (1.15) and (1.17). Using the σ operator, we are able to rewrite this Hamiltonian in the second quantization:

$$\hat{h}(\mathbf{k}) = v_F(k_x\sigma_x + k_y\sigma_y). \tag{1.22}$$

As a result, the single-particle Hamiltonian $\hat{h}_l(\mathbf{k})$ is the linearized monolayer graphene in valley $\mathbf{K}_l$ with a twist angle $\pm\frac{\theta}{2}$:

$$\begin{aligned}\hat{h}_t(\mathbf{k}) &= v_F(k_x\sigma_x + k_y\sigma_y)e^{i\frac{\theta}{2}\sigma_z}, \\ \hat{h}_b(\mathbf{k}) &= v_F(k_x\sigma_x + k_y\sigma_y)e^{-i\frac{\theta}{2}\sigma_z}.\end{aligned} \tag{1.23}$$

Similarly, in valley $\mathbf{K}'$, we have

$$\begin{aligned}\hat{h}'_t(\mathbf{k}) &= v_F(-k_x\sigma_x + k_y\sigma_y)e^{i\frac{\theta}{2}\sigma_z}, \\ \hat{h}'_b(\mathbf{k}) &= v_F(-k_x\sigma_x + k_y\sigma_y)e^{-i\frac{\theta}{2}\sigma_z}.\end{aligned} \tag{1.24}$$

Also the interlayer interaction are given by

$$\begin{aligned}\hat{T}_j &= w_0\sigma_0 + w_1\sigma_x e^{i\frac{2\pi(j-1)}{3}\sigma_z}, \\ &= w_0\sigma_0 + w_1[\sigma_x\cos\frac{2\pi(j-1)}{3} + \sigma_y\sin\frac{2\pi(j-1)}{3}],\end{aligned} \tag{1.25}$$

where w_0/w_1 denote the hopping magnitudes from an A site to an A/B site respectively, and $R(\frac{2\pi}{3}) = e^{i\frac{2\pi}{3}\sigma_z}$ denotes the C_{3z} rotation symmetry. Both w_0, w_1 are positive numbers, representing the overlap of the minus and positive "blobs" of the p_z orbitals from the top and bottom layers.

Under the assumption of neglecting intervalley interactions, the BM Hamiltonian without intervalley interaction is given by

$$\hat{H}_0 = \sum_{\tau=\mathbf{K},\mathbf{K}'} \hat{H}^{\tau}_{BM}. \tag{1.26}$$

With Eq Eq. (2.5) and the BM model in Eq Eq. (1.21), using the commutation/anti-commutation relations between Pauli matrices, it can be proved that

$$\begin{aligned} &[C_{2x}, \hat{H}_0] = [C_{2z}, \hat{H}_0] = [\mathcal{T}, \hat{H}_0] = [C_{2z}\mathcal{T}, \hat{H}_0] = 0, \\ &\{\mathcal{P}, \hat{H}_0\} = \{C_{2z}\mathcal{P}, \hat{H}_0\} = \{\mathcal{P}\mathcal{T}, \hat{H}_0\} = 0. \end{aligned} \tag{1.27}$$

Note that the single-valley Hamiltonian does not have the C_{2z} rotation symmetry and the time-reversal symmetry $\mathcal{T}$ since these two symmetries map one valley to the other. The Bistrizer-Macdonald model for twisted bilayer graphene is defined by interlayer and intralayer hoppings between the two layers in momentum space. The proof for $C_{2z}\mathcal{T}$ symmetry is as follows. Additionally, we can prove the commutation/anti-commutation relations for all symmetries using similar techniques.

The action of particle-hole symmetry on the single-valley Hamiltonian can be written as

$$\begin{aligned} \mathcal{P}\hat{H}_0\mathcal{P}^{-1} = &\sum_k \sum_l \sum_{\sigma\sigma'} \mathcal{P}\hat{c}^{\dagger}_{\mathbf{k},l,\tau,\sigma}[\hat{h}_l(\mathbf{k})]_{\sigma\sigma'}\hat{c}_{\mathbf{k},l,\tau,\sigma'}\mathcal{P}^{-1} \\ &+ \sum_{\mathbf{k}} \sum_{\sigma\sigma'} \sum_{j=1}^{3} \mathcal{P}(\hat{c}^{\dagger}_{\mathbf{k}+\mathbf{q}_j,t,\tau,\sigma}\hat{T}_j\hat{c}_{\mathbf{k},b,\tau,\sigma'} + h.c.)\mathcal{P}^{-1}. \end{aligned}$$

For the first term, we have

$$\begin{aligned} &\mathcal{P}\hat{c}^{\dagger}_{\mathbf{k},l,+1,\sigma}[\hat{h}_l(\mathbf{k})]_{\sigma\sigma'}\hat{c}_{\mathbf{k},l,+1,\sigma'}\mathcal{P}^{-1}, \\ &= \mathcal{P}\hat{c}^{\dagger}_{\mathbf{k},l,+1,\sigma}\mathcal{P}^{-1}\mathcal{P}[\hat{h}_l(\mathbf{k})]_{\sigma\sigma'}\mathcal{P}^{-1}\mathcal{P}\hat{c}_{\mathbf{k},l,+1,\sigma'}\mathcal{P}^{-1}, \\ &= \hat{c}^{\dagger}_{-\mathbf{k},-l,+1,-\sigma}\mathcal{P}[\hat{h}_l(\mathbf{k})]_{\sigma\sigma'}\mathcal{P}^{-1}\hat{c}_{-\mathbf{k},-l,+1,-\sigma'}, \\ &= -\hat{c}^{\dagger}_{-\mathbf{k},-l,+,-\sigma}[\hat{h}'_l(\mathbf{k})]_{\sigma\sigma'}\hat{c}_{-\mathbf{k},-l,+,-\sigma'}, \end{aligned}$$

where

$$\begin{aligned}\mathcal{P}\hat{h}(\mathbf{k})\mathcal{P}^{-1} &= (i\sigma_x l_y\mathcal{K})\hat{h}(\mathbf{k})(i\sigma_x l_y\mathcal{K}),\\ &= v_F(il_y\sigma_x\mathcal{K})(k_x\sigma_x + k_y\sigma_y)(-il_y\sigma_x\mathcal{K}),\\ &= v_F(k_x\sigma_x - k_y\sigma_y) = -\hat{h}'(\mathbf{k})\end{aligned}$$

holds for small twist angle θ.

For the second term, we have

$$\begin{aligned}&\mathcal{P}\sum_j \hat{c}^\dagger_{\mathbf{k}+\mathbf{q}_j,+1,\tau,\sigma}\hat{T}_j\hat{c}_{\mathbf{k},-1,\tau,\sigma}\mathcal{P}^{-1},\\ &= \sum_j \mathcal{P}\hat{c}^\dagger_{\mathbf{k}+\mathbf{q}_j,+1,\tau,\sigma}\mathcal{P}^{-1}\mathcal{P}\hat{T}_j\mathcal{P}^{-1}\mathcal{P}\hat{c}_{\mathbf{k},-1,\tau,\sigma}\mathcal{P}^{-1},\\ &= -\sum_j \hat{c}^\dagger_{-\mathbf{k}-\mathbf{q}_j,-1,\tau,-\sigma}\mathcal{P}\hat{T}_j\mathcal{P}^{-1}\hat{c}_{-\mathbf{k},+1,\tau,-\sigma},\\ &= -\sum_j \hat{c}^\dagger_{-\mathbf{k}-\mathbf{q}_j,-1,\tau,-\sigma}\hat{T}_j\hat{c}_{-\mathbf{k},+1,\tau,-\sigma},\end{aligned}$$

where we use $\hat{T}_j = w_0\sigma_0 + w_1\sigma_x\cos\frac{2\pi(j-1)}{3} + \sigma_y\sin\frac{2\pi(j-1)}{3}$ and

$$\begin{aligned}\mathcal{P}\hat{T}_j\mathcal{P}^{-1} &= -w_0\sigma_0 + w_1\mathcal{P}[\sigma_x\cos\frac{2\pi(j-1)}{3} + \sigma_y\sin\frac{2\pi(j-1)}{3}]\mathcal{P}^{-1},\\ &= -w_0\sigma_0 + w_1(i\sigma_x l_y\mathcal{K})[\sigma_x\cos\frac{2\pi(j-1)}{3} + \sigma_y\sin\frac{2\pi(j-1)}{3}](-i\sigma_x l_y\mathcal{K}),\\ &= -w_0\sigma_0 + w_1[\sigma_x\cos\frac{2\pi(j-1)}{3} - \sigma_y\sin\frac{2\pi(j-1)}{3}].\end{aligned}$$

$$\Rightarrow$$

$$\mathcal{P}\hat{T}_1\mathcal{P}^{-1} = \hat{T}_1, \quad \mathcal{P}\hat{T}_2\mathcal{P}^{-1} = \hat{T}_3, \quad \mathcal{P}\hat{T}_3\mathcal{P}^{-1} = \hat{T}_2.$$

Adding these two terms together, we can verify that particle-hole symmetry anti-commutes with the BM Hamiltonian:

$$\{\mathcal{P}, \hat{H}_0\} = 0.$$

1.4 Organization

In the first chapter, this dissertation introduces the fundamental knowledge of graphene. Starting with the tight-binding model of monolayer graphene, we then delve into

the Bistritzer-MacDonald (BM) model of twisted bilayer graphene (TBG). The BM Hamiltonian serves as the fundamental starting point for all subsequent theoretical proofs and numerical solutions. Following the foundational introduction, the second chapter explores the geometric and electronic symmetries of TBG. Detailed proofs are provided through representation analysis, confirming that the Hartree-Fock method offers a remarkably accurate approximation to the BM model at the chiral limit, due to the existence of $U(4) \times U(4)$ symmetry[12, 9]. Additionally, perturbation theory is employed to investigate the ground energy scales and the accuracy of various mean-field methods away from the chiral limit.[12] From a different perspective, the third chapter of this dissertation derives both the exact and approximate ground states of TBG.[58, 7, 108] In the final chapter, we revisit and summarize our previous discussions, presenting our work on the quantum chemistry approach for twisted bilayer graphene.[30] This work provides a description of the IBM model compatible with quantum chemistry language and implementations, along with an initial study of the performance of various quantum chemistry methods for the ground state properties of the IBM model.

Chapter 2

Representation Analysis and Approximate Symmetry

In this section, we present a detailed proof of the symmetry groups associated with the non-interacting Bistritzer-MacDonald model, as investigated by Bultinck et al [12] and Bernevig et al [9, 58, 7], using Lie algebras. There are also other references [45, 44, 84, 34] that discussed similar symmetries using different methods. To begin, we provide a brief review of the representation theory of Lie groups, utilizing Pauli matrices as an illustrative example.[38, 52, 27] Following this, we summarize the symmetries of the BM/IBM Hamiltonian in both general case and special scenarios, such as the chiral limit.[94, 88, 8] At the chiral limit, an additional chiral symmetry merges, leading to the existence of a $U(4) \times U(4)$ symmetry. [12, 9, 58] Finally, we employ perturbation theory to discuss the approximate energy contributions away from the chiral limit.[94, 12]

2.1 Pauli Matrices

The Pauli matrices, denoted as σ_x, σ_y, and σ_z, form a set of three 2×2 complex matrices. Each Pauli matrix is a Hermitian, involutory and unitary matrix. They are defined as follows:

$$\sigma_x = \begin{pmatrix} 0 & 1 \\ 1 & 0 \end{pmatrix}, \quad \sigma_y = \begin{pmatrix} 0 & -i \\ i & 0 \end{pmatrix}, \quad \sigma_z = \begin{pmatrix} 1 & 0 \\ 0 & -1 \end{pmatrix}.$$

These matrices play a fundamental role in the representation theory of Lie groups and serve as a useful illustrative example in our exploration of symmetry groups associated with the non-interacting Bistritzer-MacDonald model.

All three Pauli matrices collectively span the $\mathfrak{su}(2)$ Lie algebra. This is due to their satisfaction of the commutation relations given by[52, 27]

$$[\sigma_i, \sigma_j] = 2i\epsilon_{ijk}\sigma_k, \tag{2.1}$$

where ϵ_{ijk} is the Levi-Civita symbol. The associated Lie group, $SU(2)$, comprises unitary 2-by-2 matrices with a unit determinant. Consequently, a set of Pauli matrices, scaled by $\frac{i}{2}$, denoted as $\frac{i}{2}\sigma_{a_{a=x,y,z}}$, can be regarded as the generators of $SU(2)$ group. Observables in the $SU(2)$ group can be expressed as exponentials of linear combinations of these three generators:

$$\mathfrak{su}(2) = \{\frac{i}{2}\sigma_x, \frac{i}{2}\sigma_y, \frac{i}{2}\sigma_z\}. \tag{2.2}$$

Lie groups are commonly employed as symmetry groups in the context of quantum systems, where their Lie algebras serve as representations of infinitesimal symmetry motions. Consequently, Lie algebras and their representations play a pivotal role in physics. In the upcoming section, we will leverage Lie algebra and representation analysis to explore the symmetry groups within twisted bilayer graphene, both in the chiral and non-chiral limits.

2.2 Structural Symmetries

In this section, we will delve into the structural symmetries of tBLG using second-quantized operators. The structural symmetries of the BM Hamiltonian encompass the rotational symmetries C_{3z}, C_{2z} and the mirror symmetry M_y.[118, 61, 95, 11] Additionally, the band structures give rise to the time-reversal symmetry $\mathcal{T}$. By combining the rotational symmetry C_{2z} with the time-reversal symmetry $\mathcal{T}$, we establish a $C_{2z\mathcal{T}}$ symmetry within each valley. At the chiral limit $w_0 = 0$, the BM Hamiltonian exhibits an extra chiral symmetry $\mathcal{S}$:

$$\{\mathcal{S}, \mathcal{H}_{BM}\} = 0.$$

To express the symmetry operators, we introduce the creation/annilation operators for the single-particle Hamiltonian [9]:

$$\begin{aligned}
\hat{c}^\dagger_{\mathbf{k},l,\tau=+1,\sigma,s} &= \begin{cases} \hat{c}^\dagger_{\mathbf{K}_t+\mathbf{k}-\mathbf{Q},l=+1,\tau=+1,\sigma,s}, \\ \hat{c}^\dagger_{\mathbf{K}_b+\mathbf{k}-\mathbf{Q},l=-1,\tau=+1,\sigma,s} \end{cases}, \\
\hat{c}^\dagger_{\mathbf{k},l,\tau=-1,\sigma,s} &= \begin{cases} \hat{c}^\dagger_{\mathbf{K}'_t+\mathbf{k}-\mathbf{Q},l=+1,\tau=-1,\sigma,s} \\ \hat{c}^\dagger_{\mathbf{K}'_b+\mathbf{k}-\mathbf{Q},l=-1,\tau=-1,\sigma,s} \end{cases}.
\end{aligned} \tag{2.3}$$

Here, $\mathbf{k}$ represents the momentum in MBZ; $l = \pm 1 = t/b$, $\tau = \pm 1 = \mathbf{K}/\mathbf{K}'$, $\sigma = \pm 1 = A/B$, and $s = \pm 1 = \uparrow / \downarrow$ denote the layer, valley, sublattice, and spin, respectively. The symbols $\mathbf{K}/\mathbf{K}'$ represent the Dirac points in the top/bottom layer graphene BZ, and $\mathbf{Q} = n_1\widetilde{\mathbf{b}}_1 + n_2\widetilde{\mathbf{b}}_2$ represents the Moiré reciprocal lattice sites generated by the Moiré reciprocal vectors $\widetilde{\mathbf{b}}_1$ and $\widetilde{\mathbf{b}}_2$.

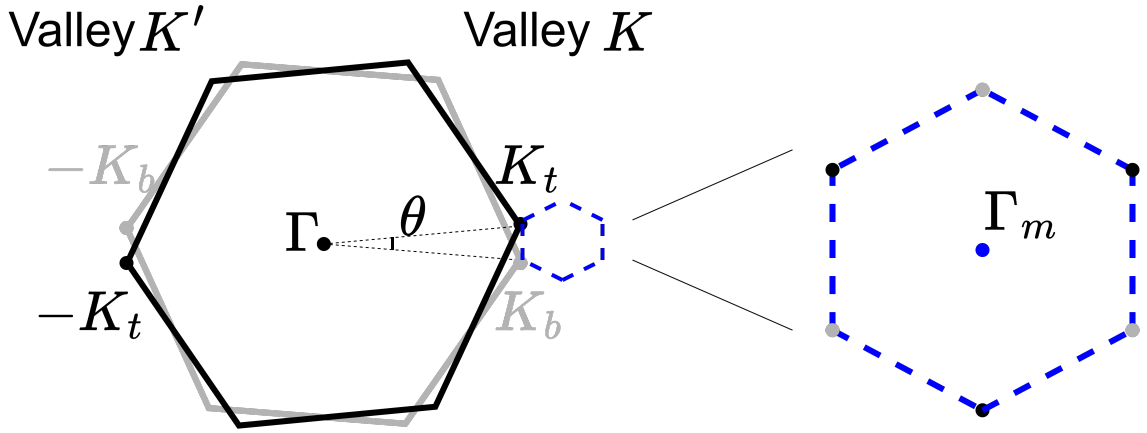

Figure 2.1: Illustration of the relation between the graphene BZs of of two layers and the moire BZ (MBZ).

Intuition of Symmetries

In this subsection, we aim to elucidate the action of symmetries in both real and momentum space, providing an intuitive understanding of symmetry operators. As depicted in Fig. 1.3a, the geometric structure reveals that tBLG exhibits C_{2z} and C_{3z} symmetries around the AA-stacking point. Next, let's delve into the action of these rotation symmetries on the momentum space. Assuming a three-dimensional lattice and labelling each lattice vector with the subscript $n = (n_1, n_2, n_3)$ as 3-tuple of integers,

$$\mathbf{r}_n = n_1\mathbf{a}_1 + n_2\mathbf{a}_2 + n_3\mathbf{a}_3,$$

then the reciprocal lattice can be expressed as

$$\mathbf{q}_m = m_1\mathbf{b}_1 + m_2\mathbf{b}_2 + m_3\mathbf{b}_3,$$

where

$$\mathbf{b}_i = \frac{2\pi}{V}\mathbf{a}_j \times \mathbf{a}_k,$$

and $V = \mathbf{a}_1 \cdot (\mathbf{a}_2 \times \mathbf{a}_3) = \mathbf{a}_2 \cdot (\mathbf{a}_3 \times \mathbf{a}_1) = \mathbf{a}_3 \cdot (\mathbf{a}_1 \times \mathbf{a}_2)$ is the scalar triple product. Then for a rotation matrix $R(\theta)$ with an angle θ as defined in Eq. (1.18), the action of the rotation on lattice vectors satisfies

$$(R(\theta)\mathbf{a}_j) \times (R(\theta)\mathbf{a}_k) = R(\theta)(\mathbf{a}_j \times \mathbf{a}_k).$$

Consequently, we simultaneously rotate both real space and momentum space. When rotating the Graphene BZ around the AA stacking point (Γ point) using C_{2z} symmetry, as illustrated in Fig. 1.3b, the valleys $\mathbf{K}$ and $\mathbf{K}'$ interchange, implying that C_{2z} symmetry maps one valley to the other. Additionally, C_{2z} symmetry maps $\mathbf{k}$ to $-\mathbf{k}$ in the MBZ, while the sublattice and layer numbers remain unchanged.

On the other hand, for C_{2x} symmetry, it swaps both the layers and sublattice numbers, while remaining within the same valley.

In addition to rotational symmetries, tBLG possesses a time-reversal symmetry $\mathcal{T}$, which establishes a relationship between the two Dirac points $\mathbf{K}$ and $\mathbf{K}'$ in each layer. The time-reversal transformation is characterized by taking the complex conjugation of the wave function in real space. Consider the wave function of graphene in the microscopic theory, this transformation complex conjugates the amplitudes, flips the sign of $\mathbf{k}$, interchanges the valley numbers, and leaves the sublattice numbers unchanged.

Since all observables are in the complex 2-dimensional Hilbert space, the layer operator l, valley operator τ, sublattice operator σ can be conveniently expressed using Pauli matrices:

$$l_x/\tau_x/\sigma_x = \begin{pmatrix} 0 & 1 \\ 1 & 0 \end{pmatrix}_{l/\tau/\sigma},\ l_y/\tau_y/\sigma_y = \begin{pmatrix} 0 & -i \\ i & 0 \end{pmatrix}_{l/\tau/\sigma},\ l_z/\tau_z/\sigma_z = \begin{pmatrix} 1 & 0 \\ 0 & -1 \end{pmatrix}_{l/\tau/\sigma}.$$

Let's examine the actions of the symmetry operators on the layer, valley, and sublattice, denoted by l_x, τ_x, and σ_x respectively. These operators swap the layer, valley, and sublattice, while l_z, τ_z, and σ_z yield the layer number, valley number, and sublattice number, respectively.

Additionally, we define a complex conjugation operator $\mathcal{K}$ and the identity operator $I = l_0 = \sigma_0 = \tau_0$. With these definitions, the symmetries can be expressed as:

$$\begin{aligned} C_{2x} &= l_x\sigma_x = l_x \otimes \tau_0 \otimes \sigma_x, \quad C_{2x}\mathbf{k} = \mathbf{k}, \\ C_{2z} &= \tau_x\sigma_x = l_0 \otimes \tau_x \otimes \sigma_x, \quad C_{2z}\mathbf{k} = -\mathbf{k} \\ \mathcal{T} &= \tau_x = l_0 \otimes \tau_x \otimes \sigma_0, \quad \mathcal{T}\mathbf{k} = -\mathbf{k}, \\ \mathcal{P} &= il_y\sigma_x = il_y \otimes \tau_0 \otimes \sigma_x, \quad \mathcal{P}\mathbf{k} = -\mathbf{k} \end{aligned} \tag{2.4}$$

where $\mathcal{P}$ is an anti-unitary particle-hole symmetry defined here for convenience. It's worth noting that both time-reversal and particle-hole symmetry are anti-unitary, satisfying $\mathcal{T}^2 = \mathcal{P}^2 = -1$, and include a complex conjugation operator. For simplicity, spin is ignored as it's independent of these symmetries.

Considering the small twisted angle θ, we also have an approximate valley-$U(1)$ symmetry, and a Moiré translation symmetry. Neglecting interactions between valleys, we can focus on one valley.

Representation Matrix

For convenience, we express the action of a spinless symmetry operator $\hat{O}$ on the fermion basis $\hat{c}^\dagger_{\mathbf{k},l,\tau,\sigma,s}$ using representation matrices. Similar to Ref [9], the representation matrices can be written as

$$\hat{O}\hat{c}^\dagger_{\mathbf{k},l,\tau,\sigma,s}\hat{O}^{-1} = \sum_{l',\tau',\sigma'} [D(\hat{O})]_{l,\tau,\sigma,l',\tau',\sigma'}\hat{c}^\dagger_{\hat{O}\mathbf{k},l',\tau',\sigma',s}.$$

Here, $D(\hat{O})$ is the representation matrix of the symmetry operation $\hat{O}$ in the index space $\{l,\ \tau,\ \sigma\}$, and $\hat{O}\mathbf{k}$ is the momentum after applying $\hat{O}$ to momentum $\mathbf{k}$. In particular, $C_{2z}\mathbf{k} = \mathcal{T}\mathbf{k} = \mathcal{P}\mathbf{k} = -\mathbf{k}$. Then the sewing matrices of all the symmetries in Eq. (2.4) are as follows:

$$\begin{aligned}
[D(C_{2x})]_{l,\tau,\sigma,l',\tau',\sigma'} &= \delta_{l',-l}\delta_{\tau',\tau}\delta_{\sigma',-\sigma},\\
[D(C_{2z})]_{l,\tau,\sigma,l',\tau',\sigma'} &= \delta_{l',l}\delta_{\tau',-\tau}\delta_{\sigma',-\sigma},\\
[D(\mathcal{T})]_{l,\tau,\sigma,l',\tau',\sigma'} &= \delta_{l',l}\delta_{\tau',-\tau}\delta_{\sigma',\sigma},\\
[D(C_{2z}\mathcal{T})]_{l,\tau,\sigma,l',\tau',\sigma'} &= \delta_{l',l}\delta_{\tau',\tau}\delta_{\sigma',-\sigma},\\
[D(\mathcal{P})]_{l,\tau,\sigma,l',\tau',\sigma'} &= \delta_{l',-l}\delta_{\tau',\tau}\delta_{\sigma',-\sigma}\zeta_l.
\end{aligned} \tag{2.5}$$

where $\zeta_l = \pm 1$ for $l = \pm$.

2.3 $U(2) \times U(2)$ Symmetry

Since the BM Hamiltonian is diagonal in valley and independent of spin, BM Hamiltonian has a $U(2)\times U(2)$ symmetry[9, 58] with eight generators $\tau_0 s_0$, $\tau_0 s_x$, $\tau_0 s_y$, $\tau_0 s_z$, $\tau_z s_0$, $\tau_z s_x$, $\tau_z s_y$, $\tau_z s_z$, where $\tau_0,\ s_0$ are identity matrices and $\tau_{x,y,z},\ s_{x,y,z}$ are Pauli matrices. We will introduce more about these generators next.

By Noether's theorem, charge conservation has corresponding symmetry $U_C(1)$. Together with Pauli matrices (the generators of $SU(2)$), the spin-charge symmetry

span a $U(2)$ symmetry. Similarly, there exists a $U(2)$ valley spin-charge symmetry. In the other words, for charge conservation $U_C(1)$, valley charge conservation $U_V(1)$, and spin symmetry $SU(2)_{K/K'}$ in two valleys (K/K'), BM model for two valleys has the symmetry $U(2)_K \times U(2)_{K'} \simeq U_C(1) \times U_V(1) \times SU(2)_K \times SU(2)_{K'}$. And the 8 generators of this $U(2) \times U(2)$ symmetry are $s^{ab} = \{\sigma_0\tau_a s_b\}$, $a = \{0, z\}$, $b = \{0, x, y, z\}$. These 8 generators satisfy:

$$\begin{aligned}[s^{ab},\ s^{cd}] &= [\sigma_0 \otimes \tau_a \otimes s_b,\ \sigma_0 \otimes \tau_c \otimes s_d] = \sigma_0 \otimes \tau_a\tau_c \otimes [s_b,\ s_d], \\ &= \sigma_0 \otimes (\delta_{ac}\tau_0 + (1-\delta_{ac})\tau_z) \otimes 2i\epsilon_{bde}s_e, \\ &= 2i\epsilon_{bde}(\delta_{ac}\sigma_0\tau_0 s_e + (1-\delta_{ac})\sigma_0\tau_z s_e).\end{aligned} \tag{2.6}$$

In particular, $s^{0b} = \{\tau_0 s_b\}$ gives the global spin-charge $U(2)$ symmetry, while $s^{zb} = \{\tau_0 s_b\}$ gives the valley spin-charge $U(2)$ symmetry.

2.4 $U(4)$ Symmetry

Particle-Hole Symmetry

In the presence of a small twisted angle, the projected BM Hamiltonian exhibits a unitary single-particle particle-hole symmetry denoted as $\mathcal{P}$. Under the flat band assumption, the projected kinetic term $\hat{H}_0$ is zero, and the projected interaction term commutes with particle-hole symmetry $[\hat{H}_I, \mathcal{P}] = 0$.

Due to the existence of C_{2z} symmetry, then we can obtain $[\hat{H}_I, C_{2z}\mathcal{P}] = 0$. Therefore, $C_{2z}\mathcal{P}$ enlarges the original $U(2) \times U(2)$ symmetry into a $U(4)_{\mathcal{P}}$ symmetry.[12, 9, 58, 45, 44, 84, 34] Note that here we consider $C_{2z}\mathcal{P}$ symmetry rather than C_{2z} or $\mathcal{P}$ symmetry, because the momentum $\mathbf{k}$ is invariant under $C_{2z}\mathcal{P}$ symmetry:

$$C_{2z}\mathbf{k} = -\mathbf{k}, \quad \mathcal{P}\mathbf{k} = -\mathbf{k}, \quad C_{2z}\mathcal{P} = \mathbf{k}. \tag{2.7}$$

Assuming the gauge $C_{2z}\mathcal{P} = \sigma_y\tau_y$, the 16 generators of this $U(4)_{\mathcal{P}}$ symmetry can be expressed as

$$s^{ab} = \{\sigma_0\tau_0 s_b,\ \sigma_y\tau_x s_b,\ \sigma_y\tau_y s_b,\ \sigma_0\tau_z s_b\}, \quad a, b = \{0, x, y, z\},$$

satisfying the commutation relations:

$$[\sigma_0\tau_0 s_a,\ \sigma_y\tau_x s_b] = \sigma_y \otimes \tau_x \otimes [s_a,\ s_b] = 2i\epsilon_{abc}\sigma_y\tau_x s_c, \tag{2.8a}$$
$$[\sigma_0\tau_0 s_a,\ \sigma_y\tau_y s_b] = \sigma_y \otimes \tau_y \otimes [s_a,\ s_b] = 2i\epsilon_{abc}\sigma_y\tau_y s_c, \tag{2.8b}$$
$$[\sigma_0\tau_0 s_a,\ \sigma_0\tau_z s_b] = \sigma_0 \otimes \tau_z \otimes [s_a,\ s_b] = 2i\epsilon_{abc}\sigma_0\tau_z s_c, \tag{2.8c}$$
$$\begin{aligned}[\sigma_y\tau_x s_a,\ \sigma_y\tau_y s_b] &= \sigma_0 \otimes [\tau_x \otimes s_a,\ \tau_y \otimes s_b] = \sigma_0 \otimes [\tau_x,\ \tau_y] \otimes [s_a,\ s_b], \\ &= \sigma_0 \otimes 2i\tau_z \otimes 2i\epsilon_{abc}s_c = -4\epsilon_{abc}\sigma_0\tau_z s_c,\end{aligned} \tag{2.8d}$$
$$\begin{aligned}[\sigma_y\tau_x s_a,\ \sigma_0\tau_z s_b] &= \sigma_y \otimes [\tau_x \otimes s_a,\ \tau_z \otimes s_b] = \sigma_y \otimes [\tau_x,\ \tau_z] \otimes [s_a,\ s_b], \\ &= \sigma_y \otimes -2i\tau_y \otimes 2i\epsilon_{abc}s_c = 4\epsilon_{abc}\sigma_y\tau_y s_c,\end{aligned} \tag{2.8e}$$
$$\begin{aligned}[\sigma_y\tau_y s_a,\ \sigma_0\tau_z s_b] &= \sigma_y \otimes [\tau_y \otimes s_a,\ \tau_z \otimes s_b] = \sigma_y \otimes [\tau_y,\ \tau_z] \otimes [s_a,\ s_b], \\ &= \sigma_y \otimes 2i\tau_x \otimes 2i\epsilon_{abc}s_c = -4\epsilon_{abc}\sigma_y\tau_x s_c.\end{aligned} \tag{2.8f}$$

These commutation relations highlight the algebraic structure of the $U(4)_{\mathcal{P}}$ symmetry.

Chiral Symmetry

In the chiral limit, where the ratio $w_0/w_1 = 0$ tends to zero, an additional unitary chiral symmetry denoted as $\mathcal{C}$ merges. This symmetry anti-commutes with the projected BM Hamiltonian, denoted as $\{\mathcal{C},\ \hat{H}_0\} = 0$. When combined with the $C_{2z}\mathcal{P}$ symmetry, which also anti-commutes with $\hat{H}_0$, a new symmetry $C_{2z}\mathcal{P}\mathcal{C}$ is obtained. This new symmetry satisfies a commutation relation:

$$\begin{aligned}\{\mathcal{C},\ \hat{H}_0\} &= \{C_{2z}\mathcal{P},\ \hat{H}_0\} = 0, \\ [C_{2z}\mathcal{P}\mathcal{C},\ \hat{H}_0] &= C_{2z}\mathcal{P}\mathcal{C}\hat{H}_0 - \hat{H}_0 C_{2z}\mathcal{P}\mathcal{C} = C_{2z}\mathcal{P}\mathcal{C}\hat{H}_0 + C_{2z}\mathcal{P}\hat{H}_0\mathcal{C}, \\ &= C_{2z}\mathcal{P}\mathcal{C}\hat{H}_0 - C_{2z}\mathcal{P}\mathcal{C}\hat{H}_0 = 0.\end{aligned} \tag{2.9}$$

Besides the kinetic term, the interaction term also commutes with this new $C_{2z}\mathcal{P}\mathcal{C}$ symmetry: $[C_{2z}\mathcal{P}\mathcal{C}, \hat{H}_I] = 0$. As a result, we have

$$\begin{aligned}[\mathcal{C},\ \hat{H}_I] &= [C_{2z}\mathcal{P},\ \hat{H}_I] = 0, \\ [C_{2z}\mathcal{P}\mathcal{C},\ \hat{H}_I] &= C_{2z}\mathcal{P}\mathcal{C}\hat{H}_I - \hat{H}_I C_{2z}\mathcal{P}\mathcal{C} = C_{2z}\mathcal{P}\mathcal{C}\hat{H}_I - C_{2z}\mathcal{P}\hat{H}_I\mathcal{C}, \\ &= C_{2z}\mathcal{P}\mathcal{C}\hat{H}_I - C_{2z}\mathcal{P}\mathcal{C}\hat{H}_I = 0.\end{aligned} \tag{2.10}$$

Therefore, $C_{2z}\mathcal{P}\mathcal{C}$ is a full commuting symmetry:

$$[C_{2z}\mathcal{P}\mathcal{C}, \hat{H}] = [C_{2z}\mathcal{P}\mathcal{C}, \hat{H}_0 + \hat{H}_I] = [C_{2z}\mathcal{P}\mathcal{C}, \hat{H}_0] + [C_{2z}\mathcal{P}\mathcal{C}, \hat{H}_I] = 0. \tag{2.11}$$

Moreover, this commuting symmetry $C_{2z}\mathcal{PC}$ extends the original $U(2) \times U(2)$ symmetry to a new $U(4)_{\mathcal{C}}$ symmetry.[12, 9, 58] Note that $C_{2z}\mathcal{PC}$ also preserves the electron momentum: $C_{2z}\mathcal{PC}\mathbf{k} = \mathbf{k}$. The 16 generators of this $U(4)_{\mathcal{C}}$ symmetry are given by

$$s^{ab} = \{\sigma_0\tau_a s_b\}, \quad a, b = \{0, x, y, z\}.$$

These generators satisfy the commutation relation:

$$\begin{aligned}
[\sigma_0\tau_a s_b,\ \sigma_0\tau_c s_d] &= \sigma_0 \otimes [\tau_a \otimes s_b,\ \tau_c \otimes s_d], \\
&= \sigma_0 \otimes [\tau_a,\ \tau_c] \otimes [s_b,\ s_d], \\
&= \sigma_0 \otimes 2i\epsilon_{ace}\tau_e \otimes 2i\epsilon_{bdf}s_f, \\
&= -4\sigma_0\tau_e s_f.
\end{aligned} \tag{2.12}$$

From Eq. Eq. (2.12), it's important to note that $U(4)_{\mathcal{C}}$ symmetry is distinct from the previous $U(4)_{\mathcal{P}}$ symmetry as it acts solely on the valley-spin rotation symmetry without transforming the band space.

2.5 $U(4) \times U(4)$ Symmetry

In this subsection, we present a detailed proof of the $U(4) \times U(4)$, as primarily identified by [12, 9, 58]. By combining the previously established $U(4)_{\mathcal{P}}$ and $U(4)_{\mathcal{C}}$ symmetry, we obtain an enlarged $U(4) \times U(4) = U(4)_{\mathcal{P}} \times U(4)_{\mathcal{C}}$ symmetry with a set of combined generators. This set consists of the 16 generators from $U(4)_{\mathcal{P}}$ and the 16 generators from $U(4)_{\mathcal{C}}$, which can be expressed as follows:

$s^{ab} \cup s'^{ab}, \quad a, b = \{0, x, y, z\},$

$s^{ab} = \{\sigma_0\tau_0 s_b,\ \sigma_y\tau_x s_b,\ \sigma_y\tau_y s_b,\ \sigma_0\tau_z s_b,\},\ s'^{ab} = \{\sigma_y\tau_0 s_b,\ \sigma_0\tau_x s_b,\ \sigma_0\tau_y s_b,\ \sigma_y\tau_z s_b\},$

where the elements of s'^{ab} satisfy:

$$[\sigma_y\tau_0 s_a,\ \sigma_0\tau_x s_b] = \sigma_y \otimes \tau_x \otimes [s_a,\ s_b] = 2i\epsilon_{abc}\sigma_y\tau_x s_c, \tag{2.13a}$$

$$[\sigma_y\tau_0 s_a,\ \sigma_0\tau_y s_b] = \sigma_y \otimes \tau_y \otimes [s_a,\ s_b] = 2i\epsilon_{abc}\sigma_y\tau_y s_c, \tag{2.13b}$$

$$[\sigma_y\tau_0 s_a,\ \sigma_y\tau_z s_b] = \sigma_0 \otimes \tau_z \otimes [s_a,\ s_b] = 2i\epsilon_{abc}\sigma_0\tau_z s_c, \tag{2.13c}$$

$$\begin{aligned}
[\sigma_0\tau_x s_a,\ \sigma_0\tau_y s_b] &= \sigma_0 \otimes [\tau_x \otimes s_a,\ \tau_y \otimes s_b] = \sigma_0 \otimes [\tau_x,\ \tau_y] \otimes [s_a,\ s_b], \\
&= \sigma_0 \otimes 2i\tau_z \otimes 2i\epsilon_{abc}s_c = -4\epsilon_{abc}\sigma_0\tau_z s_c,
\end{aligned} \tag{2.13d}$$

$$\begin{aligned}
[\sigma_0\tau_x s_a,\ \sigma_y\tau_z s_b] &= \sigma_y \otimes [\tau_x \otimes s_a,\ \tau_z \otimes s_b] = \sigma_y \otimes [\tau_x,\ \tau_z] \otimes [s_a,\ s_b], \\
&= \sigma_y \otimes -2i\tau_y \otimes 2i\epsilon_{abc}s_c = 4\epsilon_{abc}\sigma_y\tau_y s_c,
\end{aligned} \tag{2.13e}$$

$$\begin{aligned}
[\sigma_0\tau_y s_a,\ \sigma_y\tau_z s_b] &= \sigma_y \otimes [\tau_y \otimes s_a,\ \tau_z \otimes s_b] = \sigma_y \otimes [\tau_y,\ \tau_z] \otimes [s_a,\ s_b], \\
&= \sigma_y \otimes 2i\tau_x \otimes 2i\epsilon_{abc}s_c = -4\epsilon_{abc}\sigma_y\tau_x s_c,
\end{aligned} \tag{2.13f}$$

and for element $\sigma_a\tau_b s_c \in s^{ab}$ and element $\sigma_{a'}\tau_{b'}s_{c'} \in s'^{ab}$, their commutation relations are written as

$$\begin{aligned}
[\sigma_0\tau_a s_b,\ \sigma_0\tau_{a'}s_{b'}] &= \sigma_0 \otimes [\tau_a,\ \tau_{a'}] \otimes [s_b,\ s_{b'}], \\
&= \sigma_0 \otimes f_{aa'}\tau_{a''} \otimes 2i\epsilon_{bb'b''}s_{b''}, \quad a'' \in \{x, y\}, && \text{(2.14a)} \\
[\sigma_0\tau_a s_b,\ \sigma_y\tau_{a'}s_{b'}] &= \sigma_y \otimes [\tau_a,\ \tau_{a'}] \otimes [s_b,\ s_{b'}], \\
&= \sigma_y \otimes f_{aa'}\tau_{a''} \otimes 2i\epsilon_{bb'b''}s_{b''}, \quad a'' \in \{0, z\}, && \text{(2.14b)} \\
[\sigma_y\tau_a s_b,\ \sigma_0\tau_{a'}s_{b'}] &= \sigma_y \otimes [\tau_a,\ \tau_{a'}] \otimes [s_b,\ s_{b'}], \\
&= \sigma_y \otimes f_{aa'}\tau_{a''} \otimes 2i\epsilon_{bb'b''}s_{b''}, \quad a'' \in \{0, z\}, && \text{(2.14c)} \\
[\sigma_y\tau_a s_b,\ \sigma_y\tau_{a'}s_{b'}] &= \sigma_0 \otimes [\tau_a,\ \tau_{a'}] \otimes [s_b,\ s_{b'}], \\
&= \sigma_0 \otimes f_{aa'}\tau_{a''} \otimes 2i\epsilon_{bb'b''}s_{b''}, \quad a'' \in \{x, y\}. && \text{(2.14d)}
\end{aligned}$$

This combined set of generators encapsulates the symmetry transformations arising from both valley-spin and chiral symmetries, providing a comprehensive framework for understanding the symmetrical properties of the system.

Remark 1. *Both $U(4)_{\mathcal{P}}$ and $U(4)_{\mathcal{C}}$ connect flat bands with the identical Chern number, given by $C = \sigma_z\tau_z s_0$.[12]*

When two operators, $\hat{A}$ and $\hat{B}$ commute, every eigenvector ψ of $\hat{A}$ implies that $\hat{B}\psi$ is also an eigenvector of $\hat{A}$ with the same eigenvalue. This property is essential when considering the term $\mathcal{H}_S$ in the Hamiltonian, which exhibits $U(4) \times U(4)$ symmetry. For any unitary operator $\hat{O} \in U(4)$, the commutation relation $[\hat{O},\ \mathcal{H}_S] = 0$ holds. Each Chern number corresponds to four degenerate levels, as illustrated in Fig. 2.2. These levels are conveniently labeled using the index (s, τ, σ).

Remark 2. *Given that both $U(4)_{\mathcal{PT}}$ and $U(4)_R$ commute with the Chern number C, we can categorize the eight levels into two parts, each characterized by a distinct Chern number, namely $C = \pm 1$.[12]*

The presence of the $U(4) \times U(4)$ symmetry, as explored in previous works[12, 9, 58], results in eight degenerate flat bands in the chiral limit, as depicted in Fig. 2.2.Both $U(4)_{\mathcal{P}}$ and $U(4)_{\mathcal{C}}$ connect these flat bands, sharing the same Chern number $C = \sigma_z\tau_z s_0$. Consequently, the $U(4) \times U(4)$ symmetry can further classify the eight degenerate flat bands into four bands with Chern number $+1$ and four bands with Chern number -1. Each $U(4)$ symmetry operates on either the four Chern bands with Chern number $+1$ or the four Chern bands with Chern number -1. Intorucing the terms that do not preserve $U(4)\times U(4)$ will lead to the splitting of these degenerate levels. To delve into the energy level splitting, we will reformulate

the interaction/kinetic terms using generators and examine the properties of their components.

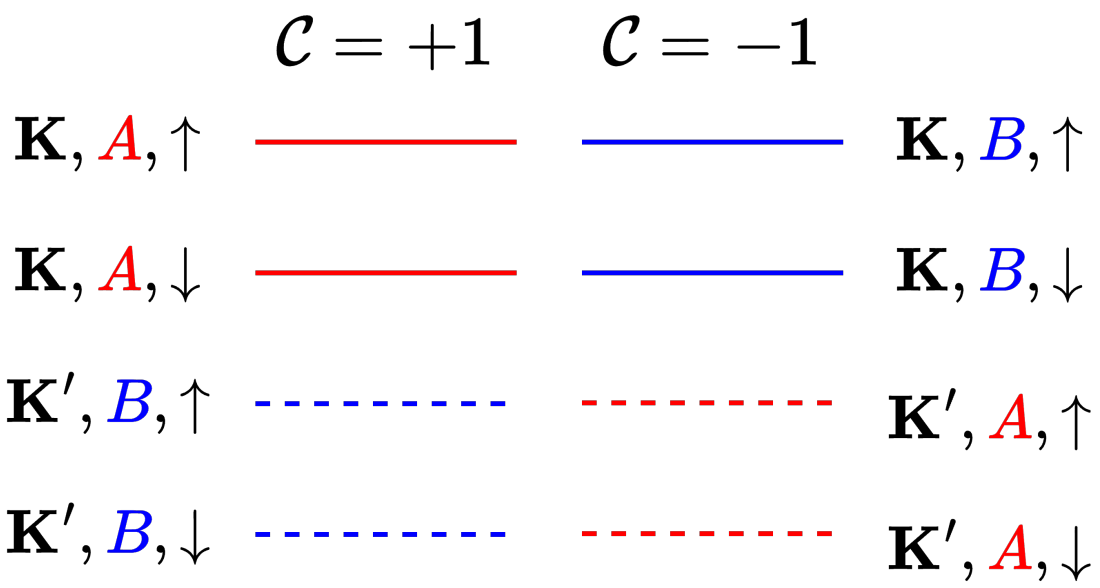

Figure 2.2: Degenerate levels of the $U(4) \times U(4)$ symmetry. This figure is firstly drawn by Ref [12].

2.6 Properties of Components

In the chiral limit, our investigation confirms the presence of a $U(4) \times U(4)$ symmetry in the projected BM Hamiltonian. As initially proposed by Bultinck et al [12], this $U(4) \times U(4)$ symmetry manifests as eight degenerate energy levels. Utilizing the Chern number, these eight degenerate levels can be further categorized into four Chen $+1$ bands and four Chen -1 bands. Within each set of ± 1 Chern bands, an arbitrary unitary transformation in the spin space and a $\tau_x \sigma_x$ symmetry exist, connecting two pairs of bands oriented in the opposite directions in the sublattice-valley space.

The existence of the $U(4) \times U(4)$ symmetry engenders various intriguing properties. Notably, any states that completely occupy or do not occupy any v Chern bands

constitute the ground states under this symmetry. However, at the non-chiral limit, the additional chiral symmetry $\mathcal{C} = \sigma_z$ is absent. Consequently, the $U(4) \times U(4)$ symmetry is not present, and only a residual $U(4)$ symmetry remains. To leverage the $U(4) \times U(4)$ symmetry, we can partition $\hat{H}_I$ and $\hat{H}_0$ into components that either commute or anti-commute with the chiral symmetry, as demonstrated in the supplemental material of Ref [12]:

$$\hat{H}_I = \hat{H}_I^S + \hat{H}_I^A, \quad \hat{H}_0 = \hat{H}_0^S + \hat{H}_0^A, \tag{2.15}$$

$$\hat{H}_I^S = \frac{1}{2A} \sum_{\mathbf{q}} V_{\mathbf{q}} \delta\rho_{\mathbf{q}}^S \delta\rho_{-\mathbf{q}}^S, \tag{2.16}$$

$$\hat{H}_I^A = \frac{1}{2A} \sum_{\mathbf{q}} V_{\mathbf{q}} (\delta\rho_{\mathbf{q}}^A \delta\rho_{-\mathbf{q}}^S + \delta\rho_{\mathbf{q}}^S \delta\rho_{-\mathbf{q}}^A + \delta\rho_{\mathbf{q}}^A \delta\rho_{-\mathbf{q}}^A), \tag{2.17}$$

$$\hat{H}_0^S = \sum_{\mathbf{k}\in\Omega^*} \sum_{n=\pm1} \sum_{\tau\in\{\mathbf{K},\mathbf{K}'\}} \epsilon_{n,\tau}^S(\mathbf{k}) \hat{f}_{n\mathbf{k}\tau}^\dagger \hat{f}_{n\mathbf{k}\tau}, \tag{2.18}$$

$$\hat{H}_0^A = \sum_{\mathbf{k}\in\Omega^*} \sum_{n=\pm1} \sum_{\tau\in\{\mathbf{K},\mathbf{K}'\}} \epsilon_{n,\tau}^A(\mathbf{k}) \hat{f}_{n\mathbf{k}\tau}^\dagger \hat{f}_{n\mathbf{k}\tau}, \tag{2.19}$$

with

$$\begin{aligned}
\delta\rho_{\mathbf{q}}^{S/A} &= \rho_{\mathbf{q}}^{S/A} - \bar{\rho}_{\mathbf{q}}^{S/A}, \\
\rho_{\mathbf{q}}^{S/A} &= \sum_{\mathbf{k}\in MBZ} \sum_{s} \sum_{\tau\sigma,\tau'\sigma'} \hat{c}_{\mathbf{k},\tau,\sigma,s}^\dagger [\Delta_{\mathbf{q}}(\mathbf{k})^{S/A}]_{\tau\sigma,\tau'\sigma'} \hat{c}_{\mathbf{k}+\mathbf{q},\tau',\sigma',s}, \\
\Delta_{\mathbf{q}}(\mathbf{k}) &= \Delta_{\mathbf{q}}^S(\mathbf{k}) + \Delta_{\mathbf{q}}^A(\mathbf{k}).
\end{aligned}$$

and

$$\begin{aligned}
[\mathcal{C}, \hat{H}_I^S] = \{\mathcal{C}, \hat{H}_I^A\} = 0 \implies & [\mathcal{C}, \Delta_{\mathbf{q}}^S(\mathbf{k})] = \{\mathcal{C}, \Delta_{\mathbf{q}}^A(\mathbf{k})\} = 0, \\
[\mathcal{C}, \hat{H}_0^S] = \{\mathcal{C}, \hat{H}_0^A\} = 0 \implies & \epsilon_{n,\tau}^S(\mathbf{k}) = \epsilon_{n,\tau}(\mathbf{k}) \delta_{n,+1}, \\
& \epsilon_{n,\tau}^A(\mathbf{k}) = \epsilon_{n,\tau}(\mathbf{k}) \delta_{n,-1}.
\end{aligned}$$

To deduce the kinetic and interaction terms in the sublattice-valley-spin space, we can leverage the previously defined generators $\sigma_{0,x,y,z}$, $\tau_{0,x,y,z}$, and $s_{0,x,y,z}$. To express the interaction terms, a useful reformulation of the form factors $\Delta_q^{S/A}(\mathbf{k})$ is achieved by defining:

$$\begin{aligned}
\Delta_{\mathbf{q}}^S(\mathbf{k}) &= \frac{1}{2}(\Delta_{\mathbf{q}}(\mathbf{k}) + \sigma_z \Delta_{\mathbf{q}}(\mathbf{k}) \sigma_z), \\
\Delta_{\mathbf{q}}^A(\mathbf{k}) &= \frac{1}{2}(\Delta_{\mathbf{q}}(\mathbf{k}) - \sigma_z \Delta_{\mathbf{q}}(\mathbf{k}) \sigma_z).
\end{aligned} \tag{2.20}$$

Consider two unitary operators $\hat{O}_1$ and $\hat{O}_2$ that do not commute with each other. We can decompose $\hat{O}_1$ into two parts

$$\hat{O}_1 = \frac{\hat{O}_1 + \hat{O}_2\hat{O}_1\hat{O}_2^{-1}}{2} + \frac{\hat{O}_1 - \hat{O}_2\hat{O}_1\hat{O}_2^{-1}}{2}.$$

This decomposition satisfies the following properties:

$$[\hat{O}_1,\ \frac{\hat{O}_1 + \hat{O}_2\hat{O}_1\hat{O}_2^{-1}}{2}] = \{\hat{O}_1,\ \frac{\hat{O}_1 - \hat{O}_2\hat{O}_1\hat{O}_2^{-1}}{2}\} = 0.$$

Symmetric Part of Form Factors

We begin by examining the symmetric part of the form factors, denoted as $\Delta_q^S(\mathbf{k})$.[12] In brief, by utilizing the symmetries of form factors, we can impose the following restrictions:

- $[\mathcal{PT},\ \Delta_q^S(\mathbf{k})] = [\sigma_y\tau_y,\ \Delta_q^S(\mathbf{k})] = 0$ implies that $\sigma_{x,z}\tau_{0,y}$ and $\sigma_{0,y}\tau_{x,z}$ operators are not allowed.
- $[\mathcal{C},\ \Delta_q^S(\mathbf{k})] = [\sigma_x\tau_y,\ \Delta_q^S(\mathbf{k})] = 0$ implies that $\sigma_{y,z}\tau_{0,y}$ and $\sigma_{0,x}\tau_{x,z}$ operators are not allowed.

We can now restrict the symmetric part of form factors $\Delta_{\mathbf{q}}^S(\mathbf{k})$ to include only $\sigma_z\tau_x$ and $\sigma_z\tau_z$. It's important to note that $\Delta_{\mathbf{q}}^S(\mathbf{k})$ is diagonal in valley, rendering $\sigma_z\tau_x$ impermissible. Consequently, we can express $\Delta_{\mathbf{q}}^S(\mathbf{k})$ in a simplified form:

$$\Delta_{\mathbf{q}}^S(\mathbf{k}) = F_q^S(\mathbf{k})e^{i\Phi_{\mathbf{q}}^S(\mathbf{k})\sigma_z\tau_z}. \tag{2.21}$$

Next, let's examine the validity of Eq. (2.21) in detail. Starting from the definition of $\Delta_{\mathbf{q}}(\mathbf{k})$:

$$[\Delta_{\mathbf{q}}(\mathbf{k})]_{\tau\sigma,\tau'\sigma'} =< \mathbf{k},\tau,\sigma \mid \mathbf{k}+\mathbf{q},\tau',\sigma' >= \delta_{\tau,\tau'} < \mathbf{k},\tau,\sigma \mid \mathbf{k}+\mathbf{q},\tau',\sigma' >,$$

we observe that $\Delta_{\mathbf{q}}(\mathbf{k})$ is 4×4 matrix and is diagonal in valley. Consequently, $\Delta_{\mathbf{q}}^S(\mathbf{k})$ is also diagonal in the valley, as it is given by:

$$\Delta_{\mathbf{q}}^S(\mathbf{k}) = \frac{1}{2}(\Delta_{\mathbf{q}}(\mathbf{k}) + \sigma_z\Delta_{\mathbf{q}}(\mathbf{k})\sigma_z).$$

Therefore, $\Delta_q^S(\mathbf{k})$ can be expressed as

$$\Delta_q^S(\mathbf{k}) = \begin{pmatrix} a_1 & a_2 & 0 & 0 \\ a_3 & a_4 & 0 & 0 \\ 0 & 0 & a_5 & a_6 \\ 0 & 0 & a_7 & a_8 \end{pmatrix},$$

where $\{a_i\}_{i=1\sim8}$ represent unknown complex constants. Then symmetries $\mathcal{PT}$ and $\mathcal{C}$ can be denoted as

$$-\mathcal{PT} = -\tau_y \otimes \sigma_y = \begin{pmatrix} 0 & 0 & 0 & 1 \\ 0 & 0 & -1 & 0 \\ 0 & -1 & 0 & 0 \\ 1 & 0 & 0 & 0 \end{pmatrix},$$
$$-i\mathcal{C} = -i\tau_y \otimes \sigma_x = \begin{pmatrix} 0 & 0 & 0 & -1 \\ 0 & 0 & -1 & 0 \\ 0 & 1 & 0 & 0 \\ 1 & 0 & 0 & 0 \end{pmatrix}.$$

Using the commutation relations $[\Delta_q^S(\mathbf{k}),\ \mathcal{PT}] = 0$ and $[\Delta_q^S(\mathbf{k}),\ \mathcal{C}] = 0$, we obtain the following relations:

$$(-\mathcal{PT})\Delta_q^S = \begin{pmatrix} 0 & 0 & a_7 & a_8 \\ 0 & 0 & -a_5 & -a_6 \\ -a_3 & -a_4 & 0 & 0 \\ a_1 & a_2 & 0 & 0 \end{pmatrix} = \begin{pmatrix} 0 & 0 & -a_2 & a_1 \\ 0 & 0 & -a_4 & a_3 \\ a_6 & -a_5 & 0 & 0 \\ a_8 & -a_7 & 0 & 0 \end{pmatrix} = \Delta_q^S(-\mathcal{PT}),$$
$$(-i\mathcal{C})\Delta_q^S = \begin{pmatrix} 0 & 0 & -a_7 & -a_8 \\ 0 & 0 & -a_5 & -a_6 \\ a_3 & a_4 & 0 & 0 \\ a_1 & a_2 & 0 & 0 \end{pmatrix} = \begin{pmatrix} 0 & 0 & -a_2 & -a_1 \\ 0 & 0 & -a_4 & -a_3 \\ a_6 & a_5 & 0 & 0 \\ a_8 & a_7 & 0 & 0 \end{pmatrix} = \Delta_q^S(-i\mathcal{C}).$$

This leads to the conclusions:

$$a_3 = a_6 = 0,$$
$$a_7 = a_2 = 0,$$
$$a_5 = a_4,$$
$$a_8 = a_1.$$

Let $a_1 = a$ and $a_4 = b$. Then symmetric part of the form factor becomes

$$\Delta_q^S(\mathbf{k}) = \begin{pmatrix} a_1 & 0 & 0 & 0 \\ 0 & a_4 & 0 & 0 \\ 0 & 0 & a_4 & 0 \\ 0 & 0 & 0 & a_1 \end{pmatrix} = \begin{pmatrix} a & 0 & 0 & 0 \\ 0 & b & 0 & 0 \\ 0 & 0 & b & 0 \\ 0 & 0 & 0 & a \end{pmatrix}.$$

To obtain the final answer, we introduce an additional symmetry, $C_{2z}\mathcal{T} = \sigma_x\mathcal{K}$. Additionally, to help us deal with the conjugation operator $\mathcal{K}$, we define the basis as

$$|\tau, \sigma\rangle = [v_{1,1},\ v_{1,-1},\ v_{-1,1},\ v_{-1,-1}]^T,$$

where the two indexes represent valley and sublattice, respectively. The action of $C_{2z}\mathcal{T}$ is given by

$$C_{2z}\mathcal{T}\begin{pmatrix} v_{1,1} \\ v_{1,-1} \\ v_{-1,1} \\ v_{-1,-1} \end{pmatrix} = \sigma_x \mathcal{K} \begin{pmatrix} v_{1,1} \\ v_{1,-1} \\ v_{-1,1} \\ v_{-1,-1} \end{pmatrix} = \begin{pmatrix} \bar{v}_{1,-1} \\ \bar{v}_{1,1} \\ \bar{v}_{-1,-1} \\ \bar{v}_{-1,1} \end{pmatrix},$$

The action of Δ_q^S is then:

$$\Delta_q^S \begin{pmatrix} v_{1,1} \\ v_{1,-1} \\ v_{-1,1} \\ v_{-1,-1} \end{pmatrix} = \begin{pmatrix} a v_{1,1} \\ b v_{1,-1} \\ b v_{-1,1} \\ a v_{-1,-1} \end{pmatrix}.$$

$$C_{2z}\mathcal{T}\Delta_q^S \begin{pmatrix} v_{1,1} \\ v_{1,-1} \\ v_{-1,1} \\ v_{-1,-1} \end{pmatrix} = C_{2z}\mathcal{T} \begin{pmatrix} a v_{1,1} \\ b v_{1,-1} \\ b v_{-1,1} \\ a v_{-1,-1} \end{pmatrix} = \begin{pmatrix} \bar{b}\bar{v}_{1,-1} \\ \bar{a}\bar{v}_{1,1} \\ \bar{a}\bar{v}_{-1,-1} \\ \bar{b}\bar{v}_{-1,1} \end{pmatrix},$$

$$\Delta_q^S C_{2z}\mathcal{T} \begin{pmatrix} v_{1,1} \\ v_{1,-1} \\ v_{-1,1} \\ v_{-1,-1} \end{pmatrix} = \Delta_q^S \begin{pmatrix} \bar{v}_{1,-1} \\ \bar{v}_{1,1} \\ \bar{v}_{-1,-1} \\ \bar{v}_{-1,1} \end{pmatrix} = \begin{pmatrix} a\bar{v}_{1,-1} \\ b\bar{v}_{1,1} \\ b\bar{v}_{-1,-1} \\ a\bar{v}_{-1,1} \end{pmatrix},$$

$$=> \ a = \bar{b}.$$

Therefore the term multiplying $\sigma_z\tau_z$ is purely imaginary. Considering other cases, $\Delta_{\mathbf{q}}^S(\mathbf{k})$ can be written as

$$\Delta_{\mathbf{q}}^S(\mathbf{k}) = F_{\mathbf{q}}^S(\mathbf{k}) e^{i\Phi_{\mathbf{q}}^S(\mathbf{k})\sigma_z\tau_z},$$

where $F_{\mathbf{q}}^S(\mathbf{k})$ and $\Phi_{\mathbf{q}}^S(\mathbf{k})$ are two real scalars. It's noteworthy that $e^{i\theta\sigma_i} = I \cdot \cos\theta + i\sigma_i \cdot \sin\theta$ holds for $i = x, y, z$.

In Eq. (2.21), we also have

$$F_{-\mathbf{q}}^S(-\mathbf{k}) = F_{\mathbf{q}}^S(\mathbf{k}), \quad \Phi_{-\mathbf{q}}^S(-\mathbf{k}) = \Phi_{\mathbf{q}}^S(\mathbf{k}), \tag{2.22}$$

due to the existence of time-reversal symmetry $\mathcal{T} = \tau_x\mathcal{K},\ \mathcal{T}\mathbf{k} = -\mathbf{k},\ \mathcal{T}\mathbf{q} = -\mathbf{q}$:

$$\begin{aligned}
\mathcal{T}\Delta^S_{\mathbf{q}}(\mathbf{k}) &= \tau_x\mathcal{K}\Delta^S_{-\mathbf{q}}(-\mathbf{k}),\\
&= \tau_x\mathcal{K}F^S_{-\mathbf{q}}(-\mathbf{k})e^{i\Phi^S_{-\mathbf{q}}(-\mathbf{k})\sigma_z\tau_z},\\
&= \tau_x\mathcal{K}F^S_{-\mathbf{q}}(-\mathbf{k})[I\cdot\cos(\Phi^S_{-\mathbf{q}}(-\mathbf{k})) + i\sigma_z\tau_z\cdot\sin(\Phi^S_{-\mathbf{q}}(-\mathbf{k}))],\\
&= \tau_x F^S_{-\mathbf{q}}(-\mathbf{k})[I\cdot\cos(\Phi^S_{-\mathbf{q}}(-\mathbf{k})) - i\sigma_z\tau_z\cdot\sin(\Phi^S_{-\mathbf{q}}(-\mathbf{k}))]\mathcal{K},\\
&= F^S_{-\mathbf{q}}(-\mathbf{k})[I\cdot\cos(\Phi^S_{-\mathbf{q}}(-\mathbf{k})) + i\sigma_z\tau_z\cdot\sin(\Phi^S_{-\mathbf{q}}(-\mathbf{k}))]\tau_x\mathcal{K},\\
&= \Delta^S_{\mathbf{q}}(\mathbf{k})\mathcal{T}.
\end{aligned} \tag{2.23}$$

Anti-Symmetric Part of Form Factors

Next, let's direct our attention to the anti-symmetric part of the form factors, denoted as $\Delta^A_q(\mathbf{k})$.[12] By leveraging the symmetries and anti-symmetries in these form factors, we can impose the following restrictions:

- $[\mathcal{PT},\ \Delta^A_q(\mathbf{k})] = [\sigma_y\tau_y,\ \Delta^A_q(\mathbf{k})] = 0$ implies that $\sigma_{x,z}\tau_{0,y}$ and $\sigma_{0,y}\tau_{x,z}$ operators are not allowed.
- $\{\mathcal{C},\ \Delta^A_q(\mathbf{k})\} = \{\sigma_x\tau_y,\ \Delta^A_q(\mathbf{k})\} = 0$ implies that $\sigma_{0,x}\tau_{0,y}$ and $\sigma_{y,z}\tau_{x,z}$ operators are not allowed.

Subsequently, we can restrict the symmetric component of the form factors, $\Delta^A_{\mathbf{q}}(\mathbf{k})$, to $\sigma_x\tau_z$ and $\sigma_x\tau_x$. Notably, $\Delta^A_{\mathbf{q}}(\mathbf{k})$ is diagonal in valley, thus excluding $\sigma_x\tau_x$. Consequently, we can express $\Delta^A_{\mathbf{q}}(\mathbf{k})$ in a simplified form:

$$\Delta^A_{\mathbf{q}}(\mathbf{k}) = \sigma_x\tau_z F^A_{\mathbf{q}}(\mathbf{k})e^{i\Phi^A_{\mathbf{q}}(\mathbf{k})\sigma_z\tau_z}, \tag{2.24}$$

where $F^A_{\mathbf{q}}(\mathbf{k})$ and $\Phi^A_{\mathbf{q}}(\mathbf{k})$ represent real scalars.

To substantiate the statement in Eq. (2.24), let's delve into the details. Commencing with the definition of $\Delta_{\mathbf{q}}(\mathbf{k})$:

$$[\Delta_{\mathbf{q}}(\mathbf{k})]_{\tau\sigma,\tau'\sigma'} =< \mathbf{k},\tau,\sigma \mid \mathbf{k}+\mathbf{q},\tau',\sigma' >= \delta_{\tau,\tau'} < \mathbf{k},\tau,\sigma \mid \mathbf{k}+\mathbf{q},\tau',\sigma' >,$$

we establish that $\Delta_{\mathbf{q}}(\mathbf{k})$ is a 4×4 matrix, and crucially, is diagonal in the valley index. Extending this characteristic, we find that $\Delta^A_{\mathbf{q}}(\mathbf{k})$ inherits this diagonal valley property, given by:

$$\Delta^A_{\mathbf{q}}(\mathbf{k}) = \frac{1}{2}(\Delta_{\mathbf{q}}(\mathbf{k}) - \sigma_z\Delta_{\mathbf{q}}(\mathbf{k})\sigma_z).$$

Let's proceed with the following insights from the given expressions:

$$\Delta_q^A(\mathbf{k}) = \begin{pmatrix} a_1 & a_2 & 0 & 0 \\ a_3 & a_4 & 0 & 0 \\ 0 & 0 & a_5 & a_6 \\ 0 & 0 & a_7 & a_8 \end{pmatrix},$$

where $\{a_i\}_{i=1\sim 8}$ are unknown complex constants. The symmetries $\mathcal{PT}$ and $\mathcal{C}$ are represented by the matrices:

$$-\mathcal{PT} = -\tau_y \otimes \sigma_y = \begin{pmatrix} 0 & 0 & 0 & 1 \\ 0 & 0 & -1 & 0 \\ 0 & -1 & 0 & 0 \\ 1 & 0 & 0 & 0 \end{pmatrix},$$
$$-i\mathcal{C} = -i\tau_y \otimes \sigma_x = \begin{pmatrix} 0 & 0 & 0 & -1 \\ 0 & 0 & -1 & 0 \\ 0 & 1 & 0 & 0 \\ 1 & 0 & 0 & 0 \end{pmatrix}.$$

Applying the commutation/anti-commutation relations $[\Delta_q^S(\mathbf{k}),\ \mathcal{PT}] = 0$ and $\{\Delta_q^S(\mathbf{k}),\ \mathcal{C}\} = 0$, we get:

$$(-\mathcal{PT})\Delta_q^A = \begin{pmatrix} 0 & 0 & a_7 & a_8 \\ 0 & 0 & -a_5 & -a_6 \\ -a_3 & -a_4 & 0 & 0 \\ a_1 & a_2 & 0 & 0 \end{pmatrix} = \begin{pmatrix} 0 & 0 & -a_2 & a_1 \\ 0 & 0 & -a_4 & a_3 \\ a_6 & -a_5 & 0 & 0 \\ a_8 & -a_7 & 0 & 0 \end{pmatrix} = \Delta_q^A(-\mathcal{PT}),$$
$$(-i\mathcal{C})\Delta_q^A = \begin{pmatrix} 0 & 0 & -a_7 & -a_8 \\ 0 & 0 & -a_5 & -a_6 \\ a_3 & a_4 & 0 & 0 \\ a_1 & a_2 & 0 & 0 \end{pmatrix} = \begin{pmatrix} 0 & 0 & a_2 & a_1 \\ 0 & 0 & a_4 & a_3 \\ -a_6 & -a_5 & 0 & 0 \\ -a_8 & -a_7 & 0 & 0 \end{pmatrix} = -\Delta_q^A(-i\mathcal{C}),$$

leading to the following constraints:

$$\begin{aligned} a_3 &= -a_6, \\ a_2 &= -a_7, \\ a_5 &= a_4 = 0, \\ a_8 &= a_1 = 0. \end{aligned}$$

Let $a_2 = a$ and $a_3 = b$, expressing the anti-symmetric part as

$$\Delta_q^A(\mathbf{k}) = \begin{pmatrix} 0 & a_2 & 0 & 0 \\ a_3 & 0 & 0 & 0 \\ 0 & 0 & 0 & -a_3 \\ 0 & 0 & -a_2 & 0 \end{pmatrix} = \begin{pmatrix} 0 & a & 0 & 0 \\ b & 0 & 0 & 0 \\ 0 & 0 & 0 & -b \\ 0 & 0 & -a & 0 \end{pmatrix}.$$

The additional symmetry we are considering is $C_{2z}\mathcal{T} = \sigma_x\mathcal{K}$, where $\mathcal{K}$ denotes the complex conjugation. Defining the basis $|\tau, \sigma\rangle = [v_{1,1},\ v_{1,-1},\ v_{-1,1},\ v_{-1,-1}]^T$, the action of $C_{2z}\mathcal{T}$ is

$$C_{2z}\mathcal{T}\begin{pmatrix} v_{1,1} \\ v_{1,-1} \\ v_{-1,1} \\ v_{-1,-1} \end{pmatrix} = \sigma_x\mathcal{K}\begin{pmatrix} v_{1,1} \\ v_{1,-1} \\ v_{-1,1} \\ v_{-1,-1} \end{pmatrix} = \begin{pmatrix} \bar{v}_{1,-1} \\ \bar{v}_{1,1} \\ \bar{v}_{-1,-1} \\ \bar{v}_{-1,1} \end{pmatrix},$$

and the action of Δ_q^A is

$$\Delta_q^A\begin{pmatrix} v_{1,1} \\ v_{1,-1} \\ v_{-1,1} \\ v_{-1,-1} \end{pmatrix} = \begin{pmatrix} av_{1,-1} \\ bv_{1,1} \\ -bv_{-1,-1} \\ -av_{-1,1} \end{pmatrix}.$$

$$C_{2z}\mathcal{T}\Delta_q^S\begin{pmatrix} v_{1,1} \\ v_{1,-1} \\ v_{-1,1} \\ v_{-1,-1} \end{pmatrix} = \begin{pmatrix} av_{1,-1} \\ bv_{1,1} \\ -bv_{-1,-1} \\ -av_{-1,1} \end{pmatrix} = \begin{pmatrix} \bar{b}\bar{v}_{1,1} \\ \bar{a}\bar{v}_{1,-1} \\ -\bar{a}\bar{v}_{-1,1} \\ -\bar{b}\bar{v}_{-1,-1} \end{pmatrix},$$

$$\Delta_q^S C_{2z}\mathcal{T}\begin{pmatrix} v_{1,1} \\ v_{1,-1} \\ v_{-1,1} \\ v_{-1,-1} \end{pmatrix} = \Delta_q^S\begin{pmatrix} \bar{v}_{1,-1} \\ \bar{v}_{1,1} \\ \bar{v}_{-1,-1} \\ \bar{v}_{-1,1} \end{pmatrix} = \begin{pmatrix} a\bar{v}_{1,1} \\ b\bar{v}_{1,-1} \\ -b\bar{v}_{-1,1} \\ -a\bar{v}_{-1,-1} \end{pmatrix},$$

$$=> \ a = \bar{b}.$$

Therefore the term multiplying $\sigma_x\tau_z$ is purely real. Considering other cases, $\Delta_{\mathbf{q}}^A(\mathbf{k})$ can be written as

$$\Delta_{\mathbf{q}}^A(\mathbf{k}) = \sigma_x\tau_z F_{\mathbf{q}}^A(\mathbf{k}) e^{i\Phi_{\mathbf{q}}^A(\mathbf{k})\sigma_z\tau_z},$$

where $F_{\mathbf{q}}^S(\mathbf{k})$ and $\Phi_{\mathbf{q}}^S(\mathbf{k})$ are two real scalars.

In Eq. (2.21), we have also established

$$F_{-\mathbf{q}}^A(-\mathbf{k}) = -F_{\mathbf{q}}^A(\mathbf{k}), \quad \Phi_{-\mathbf{q}}^A(-\mathbf{k}) = \Phi_{\mathbf{q}}^A(\mathbf{k}), \tag{2.25}$$

due to the existence of time-reversal symmetry $\mathcal{T} = \tau_x\mathcal{K},\ \mathcal{T}\mathbf{k} = -\mathbf{k},\ \mathcal{T}\mathbf{q} = -\mathbf{q}$:

$$\begin{aligned}
\mathcal{T}\Delta^A_{\mathbf{q}}(\mathbf{k}) &= \tau_x\mathcal{K}\cdot\Delta^A_{-\mathbf{q}}(-\mathbf{k}),\\
&= \tau_x\mathcal{K}\cdot\sigma_x\tau_z F^A_{-\mathbf{q}}(-\mathbf{k})e^{i\Phi^A_{-\mathbf{q}}(-\mathbf{k})\sigma_z\tau_z},\\
&= \tau_x\mathcal{K}\cdot\sigma_x\tau_z F^A_{-\mathbf{q}}(-\mathbf{k})[I\cdot\cos(\Phi^A_{-\mathbf{q}}(-\mathbf{k})) + i\sigma_z\tau_z\cdot\sin(\Phi^A_{-\mathbf{q}}(-\mathbf{k}))],\\
&= \tau_x\cdot\sigma_x\tau_z F^A_{-\mathbf{q}}(-\mathbf{k})[I\cdot\cos(\Phi^A_{-\mathbf{q}}(-\mathbf{k})) - i\sigma_z\tau_z\cdot\sin(\Phi^A_{-\mathbf{q}}(-\mathbf{k}))]\mathcal{K},\\
&= -\sigma_x\tau_z\cdot\tau_x F^A_{-\mathbf{q}}(-\mathbf{k})[I\cdot\cos(\Phi^A_{-\mathbf{q}}(-\mathbf{k})) - i\sigma_z\tau_z\cdot\sin(\Phi^A_{-\mathbf{q}}(-\mathbf{k}))]\mathcal{K},\\
&= -\sigma_x\tau_z F^A_{-\mathbf{q}}(-\mathbf{k})[I\cdot\cos(\Phi^A_{-\mathbf{q}}(-\mathbf{k})) + i\sigma_z\tau_z\cdot\sin(\Phi^A_{-\mathbf{q}}(-\mathbf{k}))]\tau_x\mathcal{K},\\
&= \Delta^A_{\mathbf{q}}(\mathbf{k})\mathcal{T}.
\end{aligned} \tag{2.26}$$

Symmetric Part of Kinetic Term

Finally, let's delve into the discussion of the kinetic term $\hat{H}_0$:[12]

$$\hat{H}_0 = \hat{H}^S_0 + \hat{H}^A_0 = \sum_{\mathbf{k}\in\Omega^*}\sum_{n=\pm1}\sum_{\tau\in\{\mathbf{K},\mathbf{K}'\}}\epsilon_{n,\tau}(\mathbf{k})\hat{f}^\dagger_{n\mathbf{k}\tau}\hat{f}_{n\mathbf{k}\tau}.$$

Using the symmetries of kinetic term (BM Hamiltonian), we can impose the following restrictions:

- $\{\mathcal{PT},\ \epsilon^A(\mathbf{k})\} = \{\sigma_y\tau_y,\ \epsilon^A(\mathbf{k})\} = 0$ implies that $\sigma_{x,z}\tau_{x,z}$ and $\sigma_{0,y}\tau_{0,y}$ operators are not allowed.
- $[\mathcal{C},\ \epsilon^A(\mathbf{k})] = [\sigma_z,\ \epsilon^A(\mathbf{k})] = 0$ implies that $\sigma_{x,y}\tau_{0,x,y,z}$ operators are not allowed.
- $U(1)$ symmetry in valley implies that $\sigma_{0,x,y,z}\tau_{x,y}$ operators are not allowed.

Therefore, we can restrict $\epsilon^A(\mathbf{k})$ to $\sigma_0\tau_{x,z}$ and $\sigma_z\tau_{0,y}$ using $\mathcal{PT}$ and $\mathcal{C}$ symmetry. We can also exclude $\sigma_0\tau_x$ and $\sigma_z\tau_{0,y}$ using $U(1)$ symmetry. Thus, $\epsilon^A(\mathbf{k})$ can be simply written as

$$\epsilon^A(\mathbf{k}) = \epsilon_0(\mathbf{k})\tau_z, \tag{2.27}$$

where $\epsilon_0(\mathbf{k})$ is a real scalar. Note that the $C_{2z}\mathcal{T} = \sigma_x\mathcal{K}$ symmetry doesn't enforce further restrictions on $\epsilon^A(\mathbf{k})$.

Anti-Symmetric Part of Kinetic Term

Using the symmetries of kinetic term (BM Hamiltonian), we can impose the following restrictions:

- $\{\mathcal{PT},\ \epsilon^A(\mathbf{k})\} = \{\sigma_y\tau_y,\ \epsilon^A(\mathbf{k})\} = 0$ implies that $\sigma_{x,z}\tau_{x,z}$ and $\sigma_{0,y}\tau_{0,y}$ operators are not allowed.
- $\{\mathcal{C},\ \epsilon^S(\mathbf{k})\} = \{\sigma_z,\ \epsilon^S(\mathbf{k})\} = 0$ implies that $\sigma_{0,z}\tau_{0,x,y,z}$ operators are not allowed.
- $U(1)$ symmetry in valley implies that $\sigma_{0,x,y,z}\tau_{x,y}$ operators are not allowed.

Then we can restrict $\epsilon^S(\mathbf{k})$ to $\sigma_x\tau_{0,y}$ and $\sigma_y\tau_{x,z}$ using $\mathcal{PT}$ and $\mathcal{C}$ symmetry. We can also exclude $\sigma_y\tau_x$ using $U(1)$ symmetry. Thus, $\epsilon^S(\mathbf{k})$ can be simply written as

$$\epsilon^S(\mathbf{k}) = \epsilon_x(\mathbf{k})\sigma_x + \epsilon_y(\mathbf{k})\sigma_y\tau_z, \tag{2.28}$$

where $\epsilon_x(\mathbf{k})$ and $\epsilon_y(\mathbf{k})$ are real scalars. Note that the $C_{2z}\mathcal{T} = \sigma_x\mathcal{K}$ symmetry does enforce further restrictions onto $\epsilon^S(\mathbf{k})$:

$$\sigma_x = \tau_0 \otimes \sigma_x = \begin{pmatrix} 0 & 1 & 0 & 0 \\ 1 & 0 & 0 & 0 \\ 0 & 0 & 0 & 1 \\ 0 & 0 & 1 & 0 \end{pmatrix},$$

$$\sigma_y\tau_z = \tau_z \otimes \sigma_y = \begin{pmatrix} 0 & -i & 0 & 0 \\ i & 0 & 0 & 0 \\ 0 & 0 & 0 & i \\ 0 & 0 & -i & 0 \end{pmatrix},$$

$$\epsilon_x(\mathbf{k})\sigma_x + \epsilon_y(\mathbf{k})\sigma_y\tau_z = \begin{pmatrix} 0 & \epsilon_x(\mathbf{k}) - i\epsilon_y(\mathbf{k}) & 0 & 0 \\ \epsilon_x(\mathbf{k}) + i\epsilon_y(\mathbf{k}) & 0 & 0 & 0 \\ 0 & 0 & 0 & \epsilon_x(\mathbf{k}) + i\epsilon_y(\mathbf{k}) \\ 0 & 0 & \epsilon_x(\mathbf{k}) - i\epsilon_y(\mathbf{k}) & 0 \end{pmatrix}$$

$$C_{2z}\mathcal{T}\begin{pmatrix} v_{1,1} \\ v_{1,-1} \\ v_{-1,1} \\ v_{-1,-1} \end{pmatrix} = \sigma_x\mathcal{K}\begin{pmatrix} v_{1,1} \\ v_{1,-1} \\ v_{-1,1} \\ v_{-1,-1} \end{pmatrix} = \begin{pmatrix} \bar{v}_{1,-1} \\ \bar{v}_{1,1} \\ \bar{v}_{-1,-1} \\ \bar{v}_{-1,1} \end{pmatrix},$$

then we have

$$(\epsilon_x(\mathbf{k})\sigma_x+\epsilon_y(\mathbf{k})\sigma_y\tau_z)\begin{pmatrix}v_{1,1}\\v_{1,-1}\\v_{-1,1}\\v_{-1,-1}\end{pmatrix}=\begin{pmatrix}(\epsilon_x(\mathbf{k})-i\epsilon_y(\mathbf{k}))v_{1,-1}\\(\epsilon_x(\mathbf{k})+i\epsilon_y(\mathbf{k}))v_{1,1}\\(\epsilon_x(\mathbf{k})+i\epsilon_y(\mathbf{k}))v_{-1,-1}\\(\epsilon_x(\mathbf{k})-i\epsilon_y(\mathbf{k}))v_{-1,1}\end{pmatrix},$$

$$\begin{aligned}C_{2z}\mathcal{T}(\epsilon_x(\mathbf{k})\sigma_x+\epsilon_y(\mathbf{k})\sigma_y\tau_z)\begin{pmatrix}v_{1,1}\\v_{1,-1}\\v_{-1,1}\\v_{-1,-1}\end{pmatrix}&=C_{2z}\mathcal{T}\begin{pmatrix}(\epsilon_x(\mathbf{k})-i\epsilon_y(\mathbf{k}))v_{1,-1}\\(\epsilon_x(\mathbf{k})+i\epsilon_y(\mathbf{k}))v_{1,1}\\(\epsilon_x(\mathbf{k})+i\epsilon_y(\mathbf{k}))v_{-1,-1}\\(\epsilon_x(\mathbf{k})-i\epsilon_y(\mathbf{k}))v_{-1,1}\end{pmatrix}\\&=\begin{pmatrix}(\epsilon_x(\mathbf{k})-i\epsilon_y(\mathbf{k}))\bar{v}_{1,1}\\(\epsilon_x(\mathbf{k})+i\epsilon_y(\mathbf{k}))\bar{v}_{1,-1}\\(\epsilon_x(\mathbf{k})+i\epsilon_y(\mathbf{k}))\bar{v}_{-1,1}\\(\epsilon_x(\mathbf{k})-i\epsilon_y(\mathbf{k}))\bar{v}_{-1,-1}\end{pmatrix},\end{aligned}$$

$$\begin{aligned}(\epsilon_x(\mathbf{k})\sigma_x+\epsilon_y(\mathbf{k})\sigma_y\tau_z)C_{2z}\mathcal{T}\begin{pmatrix}v_{1,1}\\v_{1,-1}\\v_{-1,1}\\v_{-1,-1}\end{pmatrix}&=(\epsilon_x(\mathbf{k})\sigma_x+\epsilon_y(\mathbf{k})\sigma_y\tau_z)\begin{pmatrix}\bar{v}_{1,-1}\\\bar{v}_{1,1}\\\bar{v}_{-1,-1}\\\bar{v}_{-1,1}\end{pmatrix},\\&=\begin{pmatrix}(\epsilon_x(\mathbf{k})-i\epsilon_y(\mathbf{k}))\bar{v}_{1,1}\\(\epsilon_x(\mathbf{k})+i\epsilon_y(\mathbf{k}))\bar{v}_{1,-1}\\(\epsilon_x(\mathbf{k})+i\epsilon_y(\mathbf{k}))\bar{v}_{-1,1}\\(\epsilon_x(\mathbf{k})-i\epsilon_y(\mathbf{k}))\bar{v}_{-1,-1}\end{pmatrix}.\end{aligned}$$

Then we have $(\epsilon_x(\mathbf{k})\sigma_x+\epsilon_y(\mathbf{k})\sigma_y\tau_z)C_{2z}\mathcal{T}=C_{2z}\mathcal{T}(\epsilon_x(\mathbf{k})\sigma_x+\epsilon_y(\mathbf{k})\sigma_y\tau_z)$. Therefore, we are able to set

$$\begin{aligned}\epsilon_x(\mathbf{k})&=f(\mathbf{k})\cos(\phi_0(\mathbf{k})),\\\epsilon_y(\mathbf{k})&=f(\mathbf{k})\sin(\phi_0(\mathbf{k})),\end{aligned}\tag{2.29}$$

which gives

$$\begin{aligned}\epsilon^S(\mathbf{k})&=f(\mathbf{k})\cos(\phi_0(\mathbf{k}))\sigma_x+f(\mathbf{k})\sin(\phi_0(\mathbf{k}))\sigma_y\tau_z,\\&=f(\mathbf{k})\sigma_x\cdot[I\cdot\cos(\phi_0(\mathbf{k}))+i\sigma_z\tau_z\cdot\sin(\phi_0(\mathbf{k}))],\\&=f(\mathbf{k})\sigma_x e^{i\phi_0(\mathbf{k})\sigma_z\tau_z},\end{aligned}\tag{2.30}$$

where $f(\mathbf{k})$ and $\phi_0(\mathbf{k})$ are real scalars.

Combining Eq. (2.28) and Eq. (2.27), we can express the kinetic terms as follows:

$$\epsilon_0(\mathbf{k})=\frac{1}{8}\mathrm{Tr}[\epsilon^A(\mathbf{k})\tau_z],\quad \epsilon_x(\mathbf{k})=\frac{1}{8}\mathrm{Tr}[\epsilon^S(\mathbf{k})\sigma_x],\quad \epsilon_y(\mathbf{k})=\frac{1}{8}\mathrm{Tr}[\epsilon^S(\mathbf{k})\sigma_y\tau_z].$$

It's important to note that the detailed proof of these expressions is primarily presented in the supplemental material of Ref. [12].

2.7 Symmetries of Components

The symmetries of each component are summarized in Table 2.1.[12] The symmetric form factor $\Delta^S_{\mathbf{q}}(\mathbf{k})$ preserves both $\mathcal{PT}$ and $\mathcal{C}$ symmetry; therefore, $\Delta^S_{\mathbf{q}}(\mathbf{k})$ has a corresponding $U(4)_{\mathcal{P}} \times U(4)_{\mathcal{C}}$ symmetry. On the other hand, the anti-symmetric form factor $\Delta^A_{\mathbf{q}}(\mathbf{k})$ preserves only $\mathcal{PT}$ symmetry while breaks $\mathcal{C}$ symmetry. Thus, $\Delta^A_{\mathbf{q}}(\mathbf{k})$ has a $U(4)_{\mathcal{P}}$ symmetry. The symmetries of form factors give rise to the symmetries of the interaction term. As a result, $\hat{H}^S$ and $\hat{H}^A$ have $U(4)_{\mathcal{P}} \times U(4)_{\mathcal{C}}$ symmetry and $U(4)_{\mathcal{P}}$ symmetry, respectively. Similarly, for the symmetric kinetic term, $\epsilon^S(\mathbf{k})$ anti-commutes with both $\mathcal{PT}$ and $\mathcal{C}$ symmetry, thus enforcing a $U(4)_{\mathcal{C}}$ symmetry. However, the anti-symmetric kinetic term $\epsilon^A(\mathbf{k})$ anti-commutes with $\mathcal{PT}$ and commutes with $\mathcal{C}$ symmetry, leading to the original $U(2)_{\mathbf{K}} \times U(2)_{\mathbf{K}'}$ symmetry.

2.8 Energy scales

The associated energy scales of $\hat{H}^S_I$, $\epsilon^S(\mathbf{k})$, $\hat{H}^A_I$, and $\epsilon^A(\mathbf{k})$ are denoted as U_S, t_S, U_A, and t_A respectively. Table 2.1 summarizes the symmetries of different terms and their energy scales.[12] The energy scale is calculated using the maximum absolute value.

Term	Energy Scale	Symmetry	Type
U_S	$15 - 25$ meV	$U(4)_{\mathcal{P}} \times U(4)_{\mathcal{C}}$	symmetric
t_S	$4 - 6$ meV	$U(4)_{\mathcal{C}}$	symmetric
U_A	$4 - 6$ meV	$U(4)_{\mathcal{P}}$	anti-symmetric
t_A	$0.5 - 1$ meV	$U(2)_{\mathbf{K}} \times U(2)_{\mathbf{K}'}$	anti-symmetric

Table 2.1: Energy scales of symmetric and anti-symmetric complements. This energy scales are firstly calculated by Ref [12].

For the kinetic terms, we can estimate the energy scales associated with the symmetric and anti-symmetric terms by averaging $|\epsilon_0(\mathbf{k})|$ and $|\epsilon_x(\mathbf{k}) + i\epsilon_y(\mathbf{k})|$:

$$t_S = \frac{1}{N_{\mathbf{k}}} \sum_{\mathbf{k}} |\epsilon_x(\mathbf{k}) + i\epsilon_y(\mathbf{k})|, \tag{2.31}$$

$$t_A = \frac{1}{N_{\mathbf{k}}} \sum_{\mathbf{k}} |\epsilon_0(\mathbf{k})|, \tag{2.32}$$

where $N_{\mathbf{k}}$ is the number of $\mathbf{k}$ points.

For the interaction terms, the $\mathbf{q}$-averaged form factors can be used to define a characteristic scale for $\hat{H}_S$ and $\hat{H}_A$ in Eq. (2.19) by estimating the maximum absolute value of the exchange (Fock energy) as

$$U_S = \frac{1}{2AN_{\mathbf{k}}} \sum_{\mathbf{k},\mathbf{q}} V_{\mathbf{q}} |F^S_{\mathbf{q}}(\mathbf{k})|^2, \tag{2.33}$$

$$U_A = \frac{1}{2AN_{\mathbf{k}}} \sum_{\mathbf{k},\mathbf{q}} V_{\mathbf{q}} (2|F^S_{\mathbf{q}}(\mathbf{k}) F^A_{\mathbf{q}}(\mathbf{k})| + |F^A_{\mathbf{q}}(\mathbf{k})|^2). \tag{2.34}$$

Here, $N_{\mathbf{k}}$ is the number of $\mathbf{k}$ points, and A is the area of the system.

The plots of energy functions of U_S, t_S, U_A and t_A can be found in previous works [12]. Averaging these functions over $\mathbf{k}$ provide the values for the bounds: U_S and U_A are determined to be 18, and 4.5 meV, respectively. [12] Additionally, we find $t_S = 5$ meV and $t_A = 0.5$ meV. [12] With these energy scales, it follows that $U_S \gg U_A, t_S, t_A$. As a result, starting from the exact solutions of $\hat{H}^S_I$, the energy scales enable us to employ the perturbation theory to compute the ground state energies of $\hat{H}^A_I, \hat{H}^S_0$. Furthermore, since we have $U_A, t_S \gg t_A$, we can then apply second-order perturbation theory to determine the energies of $\hat{H}^A_0$.

2.9 Mean-Field Methods

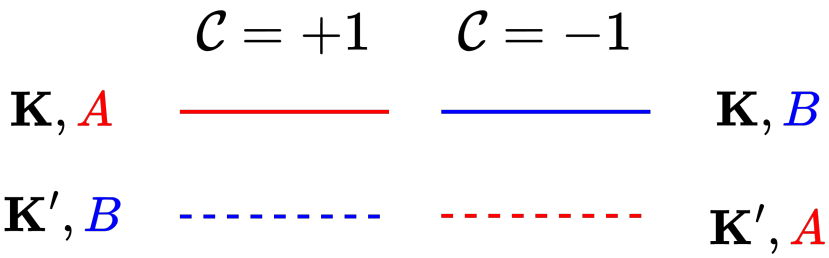

Figure 2.3: Degenerate levels of the $U(2) \times U(2)$ symmetry in the spinless model. This figure is firstly drawn by Ref [12].

Mean-field methods, such as Hartree-Fock method, are commonly employed in the numerical calculations of the IBM Hamiltonian. In Hartree-Fock calculations,

we solve for the set of self-consistent ground-state Slater determinant states characterized by the one-electron density matrices. During numerical simulations, various initial conditions and symmetries are enforced, including C_{2z}, C_3, $\mathcal{T}$, $\mathcal{P}$, $U_V(1)$ and $C_{2z}\mathcal{T}$ symmetry. Depending on the different enforced symmetries, these self-consistent solutions can be grouped into five categories: a) Quantum Hall (QH) insulator state, that preserves C_{2z} and $U_V(1)$ symmetry, while breaks $\mathcal{T}$ symmetry; b) Valley-Hall (VH) state, that preserves $\mathcal{T}$ and $U_V(1)$ symmetry, while breaks C_{2z} symmetry; ; c) Semi-Metallic (SM) state, that preserves C_{2z}, $\mathcal{T}$ and $U_V(1)$ symmetry, while breaks C_3 symmetry; ; d) Valley-Polarized (VP) state, that preserves $C_{2z}\mathcal{T}$ and $U_V(1)$ symmetry, while breaks C_{2z} and $\mathcal{T}$ symmetry; ; e) Kramers Inter-Valley Coherent (K-IVC) state, that preserves a combined symmetry $\mathcal{T}' = \tau_y\mathcal{K}$, while breaks $\mathcal{T}$ and $U_V(1)$ symmetry. More details are in Table 2.2.

states	preserve	break
QH	C_{2z}, $U_V(1)$	$\mathcal{T}$
VH	$\mathcal{T}$, $U_V(1)$	C_{2z}
SM	C_{2z}, $\mathcal{T}$, $U_V(1)$	C_3
VP	$C_{2z}\mathcal{T}$, $U_V(1)$	C_{2z}, $\mathcal{T}$
K-IVC	$\mathcal{T}' = \tau_y\mathcal{K}$	$\mathcal{T}$, $U_V(1)$

Table 2.2: Slater determinant states and their symmetries

After defining the self-consistent states, we can use perturbation theory to compute the approximate ground state energies. The IBM Hamiltonian can be decomposed into four parts using the generators we defined in previous sections:

$$\hat{H}_{IBM} = \hat{H}_0^S + \hat{H}_0^A + \hat{H}_I^S + \hat{H}_I^A + \hat{H}_0^S + \hat{H}_0^A,$$

where the associated energy scales of these four terms are U_S, t_S, U_A and t_A, respectively, as shown in Figure 2.1. It's worth noting that only $\hat{H}_I^S$ preserves $U(4) \times U(4)$, and U_S is significantly larger than the other terms. Therefore, we can initiate the calculations from the exact solutions of $\hat{H}_I^S$ and subsequently introduce other terms to lift the degeneracy of states. Second-order perturbation theory is applied, and the density matrix is expressed as $P = \frac{1}{2}(1 + Q)$.

Exact Solutions of $\hat{H}_I^S$

Remark 3. *Any state Q satisfying $[Q, \sigma_z\tau_z] = 0$ is a ground state of $\hat{H}_I^S$.*

All K-IVC, QH, VH, SM, VP states satisfy $[Q, \sigma_z\tau_z] = 0$, and therefore are all ground states of $\hat{H}_I^S$. The proof of this statement is straightforward. $\hat{H}_I^S = \frac{1}{2A}\sum_{\mathbf{q}} V_{\mathbf{q}}\delta\rho_{\mathbf{q}}^S\delta\rho_{-\mathbf{q}}^S$ is a positive semi-definite operator, which implies that any state satisfying $\delta\rho_q^S|\Psi>=0$ for $q \neq 0$ is a ground state. Using VP states as an example here, the Slater determinant of VP states with completely filled bands can be written as

$$|\Psi_{VP}\rangle = \prod_{\mathbf{k}'} c^\dagger_{\mathbf{k}',+,A} c^\dagger_{\mathbf{k}',+,B}\,|0\rangle$$

For operator ρ_q^S,

$$\rho_q^S = \sum_{\mathbf{k}\in MBZ}\sum_{\tau\sigma,\tau'\sigma'} c^\dagger_{\mathbf{k},\tau,\sigma}[\Delta_q(\mathbf{k})^S]_{\tau\sigma,\tau'\sigma'}c_{\mathbf{k}+q,\tau',\sigma'},$$

note that for $q \neq 0$,

$$c^\dagger_{\mathbf{k},\tau,\sigma}c_{\mathbf{k}+q,\tau',\sigma'}\,|\Psi_{VP}\rangle = 0,$$

the action of operator ρ_q^S on this VP state is

$$\rho_q^S\,|\Psi_{VP}\rangle = 0,$$

for all $q \neq 0$.

Also note that $\delta\rho_q^S = \rho_q^S - \bar{\rho}_q^S$, $\bar{\rho}_q^S = \langle\rho_q\rangle = \langle\Psi_{base}|\rho_q|\Psi_{base}\rangle$. There are several different possible choices for base state Ψ_{base}, such as $|\Psi_{VP}\rangle$ with

$$\langle\Psi_{VP}|\rho_q^S|\Psi_{VP}\rangle = 0, \quad q \neq 0,$$

and

$$\begin{aligned}
\langle\Psi_{VP}|\rho_0^S|\Psi_{VP}\rangle &= \sum_{\mathbf{k}}\sum_{\tau\sigma,\tau'\sigma'}\langle\Psi_{VP}|[\Delta_0^S(\mathbf{k})]_{\tau\sigma,\tau'\sigma'}c^\dagger_{\mathbf{k},\tau,\sigma}c_{\mathbf{k},\tau',\sigma'}|\Psi_{VP}\rangle\,,\\
&= \sum_{\mathbf{k}}\sum_{\tau\sigma,\tau'\sigma'}\langle\Psi_{VP}|[\Delta_0^S(\mathbf{k})]_{\tau\sigma,\tau'\sigma'}\delta_{\tau,+}\delta_{\tau',+}\delta_{\sigma,\sigma'}|\Psi_{VP}\rangle\,,\\
&= \sum_{\mathbf{k}}\sum_{\sigma}\langle\Psi_{VP}|[\Delta_0^S(\mathbf{k})]_{+\sigma,+\sigma}|\Psi_{VP}\rangle\,,\\
&= \sum_{\mathbf{k}}\sum_{\sigma}[\Delta_0^S(\mathbf{k})]_{+\sigma,+\sigma}.
\end{aligned}$$

Note that $[\Delta_0(\mathbf{k})]_{+\sigma,+\sigma} = \langle\mathbf{k},+,\sigma|\mathbf{k},+,\sigma\rangle = 1$, then

$$[\Delta_0^S(\mathbf{k})]_{+\sigma,+\sigma} = [\frac{1}{2}(\Delta_q(\mathbf{k}) + \sigma_z\Delta_0(\mathbf{k})\sigma_z)]_{+\sigma,+\sigma} = 1.$$

Therefore $\langle\Psi_{VP}|\rho_0^S|\Psi_{VP}\rangle = 2N_k$, where N_k is the number of k points.

Similarly, for VH states $|\Psi_{VH}\rangle = \prod_{\mathbf{k}'} c^\dagger_{\mathbf{k}',+,A} c^\dagger_{\mathbf{k}',-,A}|0\rangle$, and QH states $|\Psi_{QH}\rangle = \prod_{\mathbf{k}'} c^\dagger_{\mathbf{k}',+,A} c^\dagger_{\mathbf{k}',-,B}|0\rangle$, they both satisfy:

$$\langle\Psi_{VH}|\rho_0^S|\Psi_{VH}\rangle = \sum_{\mathbf{k}}\sum_{\tau}[\Delta_0^S(\mathbf{k})]_{\tau A,\tau A} = 2N_k,$$
$$\langle\Psi_{QH}|\rho_0^S|\Psi_{QH}\rangle = \sum_{\mathbf{k}}\sum_{\tau\cdot\sigma=1}[\Delta_0^S(\mathbf{k})]_{\tau\sigma,\tau\sigma} = 2N_k.$$

Then for operator $\delta\rho_q^S$, we have

$$\delta\rho_q^S|\Psi_{VP}\rangle = 0$$

for $q \neq 0$, and

$$\langle\Psi_{VP}|\delta\rho_q^S|\Psi_{VP}\rangle = \langle\Psi_{VP}|\rho_q^S - \bar{\rho}_q^S|\Psi_{VP}\rangle = 0,$$

for $q = 0$.

Finally, for Hamiltonian $\mathcal{H}_S$, we have

$$\begin{aligned}\langle\Psi_{VP}|\mathcal{H}_S|\Psi_{VP}\rangle &= \langle\Psi_{VP}|\frac{1}{2A}\sum_q V_q\delta\rho_q^S\delta\rho_{-q}^S|\Psi_{VP}\rangle\,,\\ &= \frac{V_0}{2A}\langle\Psi_{VP}|\delta\rho_0^S\delta\rho_0^S|\Psi_{VP}\rangle\,,\\ &= \frac{V_0}{2A}|\langle\Psi_{VP}|\delta\rho_0^S|\Psi_{VP}\rangle|^2,\\ &= 0.\end{aligned}$$

Since $\mathcal{H}_S$ is a positive semi-definite operator, $|\Psi_{VP}\rangle$ is the ground state of $\hat{H}_I^S$. Besides the VP state, the other K-IVC, QH, VH, SM states are also the ground states of $\hat{H}_I^S$, and Hartree-Fock can find the exact solution of $\hat{H}_I^S$ using these states in principle.

Energy Contributions of $\hat{H}_0^S$

Starting from a VP state, we select an electron-hole pair with momentum $\mathbf{k}$ and valley $\tau = \mathbf{K}$, defining a state where one electron with Chern number $+1$ is annihilated, and one hole with Chern number -1 is filled:

$$|\Psi_{\mathbf{k}}\rangle = c^\dagger_{\mathbf{k},\mathbf{K},-1}c_{\mathbf{k},\mathbf{K},+1}|\Psi_{VP}\rangle\,, \tag{2.35}$$

then the energy of this state is given by

$$\begin{aligned} E_{\mathbf{k},\mathbf{k}'} &= \langle \Psi_{\mathbf{k}} | \hat{H}_I^S | \Psi_{\mathbf{k}'} \rangle \,, \\ &= \langle \Psi_{\mathbf{k}} | \frac{1}{2A} \sum_{\mathbf{q}} V_{\mathbf{q}} \delta\rho_{\mathbf{q}}^S \delta\rho_{-\mathbf{q}}^S | \Psi_{\mathbf{k}'} \rangle \,. \end{aligned} \tag{2.36}$$

Using Eq. Eq. (2.21) and the fact that $\Delta_{\mathbf{q}}(\mathbf{k})^\dagger = \Delta_{-\mathbf{q}}(\mathbf{k}+\mathbf{q})$, we have

$$\begin{aligned} \rho_{\mathbf{q}}^S |\Psi_{\mathbf{k}}\rangle &= \sum_{\mathbf{k}''} \sum_{\tau\sigma,\tau'\sigma'} [\Delta_{\mathbf{q}}^S(\mathbf{k}'')]_{\tau\sigma,\tau'\sigma'} c^\dagger_{\mathbf{k}'',\tau,\sigma} c_{\mathbf{k}''+\mathbf{q},\tau',\sigma'} |\Psi_{\mathbf{k}}\rangle \,, \\ &= \sum_{\mathbf{k}''} \sum_{\tau\sigma,\tau'\sigma'} [F_{\mathbf{q}}^S(\mathbf{k}'') e^{i\Phi_{\mathbf{q}}^S(\mathbf{k}'')\sigma_z\tau_z}]_{\tau\sigma,\tau'\sigma'} c^\dagger_{\mathbf{k}'',\tau,\sigma} c_{\mathbf{k}''+\mathbf{q},\tau',\sigma'} |c^\dagger_{\mathbf{k},\mathbf{K},-1} c_{\mathbf{k},\mathbf{K},+1} \Psi_{VP}\rangle \,, \\ &= \sum_{\mathbf{k}''} \sum_{\tau\sigma,\tau'\sigma'} [F_{\mathbf{q}}^S(\mathbf{k}'') e^{i\Phi_{\mathbf{q}}^S(\mathbf{k}'')\sigma_z\tau_z}]_{\tau\sigma,\tau'\sigma'} c^\dagger_{\mathbf{k}'',\tau,\sigma} c_{\mathbf{k}''+\mathbf{q},\tau',\sigma'} c^\dagger_{\mathbf{k},\mathbf{K},-1} c_{\mathbf{k},\mathbf{K},+1} |\Psi_{VP}\rangle \,, \\ &= \sum_{\mathbf{k}''} \sum_{\sigma,\sigma'} [F_{\mathbf{q}}^S(\mathbf{k}'') e^{i\Phi_{\mathbf{q}}^S(\mathbf{k}'')\sigma_z\tau_z}]_{\tau\sigma,\tau'\sigma'} c^\dagger_{\mathbf{k}'',\mathbf{K},\sigma} c_{\mathbf{k}''+\mathbf{q},\mathbf{K},\sigma'} c^\dagger_{\mathbf{k},\mathbf{K},-1} c_{\mathbf{k},\mathbf{K},+1} |\Psi_{VP}\rangle \,, \\ &= \sum_{\mathbf{k}''} F_{\mathbf{q}}^S(\mathbf{k}'') e^{i\Phi_{\mathbf{q}}^S(\mathbf{k}'')} c^\dagger_{\mathbf{k}'',\mathbf{K},+1} c_{\mathbf{k}''+\mathbf{q},\mathbf{K},+1} c^\dagger_{\mathbf{k},\mathbf{K},-1} c_{\mathbf{k},\mathbf{K},+1} |\Psi_{VP}\rangle \\ &\qquad + F_{\mathbf{q}}^S(\mathbf{k}'') e^{-i\Phi_{\mathbf{q}}^S(\mathbf{k}'')} c^\dagger_{\mathbf{k}'',\mathbf{K},-1} c_{\mathbf{k}''+\mathbf{q},\mathbf{K},-1} c^\dagger_{\mathbf{k},\mathbf{K},-1} c_{\mathbf{k},\mathbf{K},+1} |\Psi_{VP}\rangle \,, \\ &= F_{\mathbf{q}}^S(\mathbf{k}) e^{i\Phi_{\mathbf{q}}^S(\mathbf{k})} c^\dagger_{\mathbf{k},\mathbf{K},+1} c_{\mathbf{k}+\mathbf{q},\mathbf{K},+1} c^\dagger_{\mathbf{k},\mathbf{K},-1} c_{\mathbf{k},\mathbf{K},+1} |\Psi_{VP}\rangle \\ &\qquad + F_{\mathbf{q}}^S(\mathbf{k}-\mathbf{q}) e^{-i\Phi_{\mathbf{q}}^S(\mathbf{k}-\mathbf{q})} c^\dagger_{\mathbf{k}-\mathbf{q},\mathbf{K},-1} c_{\mathbf{k},\mathbf{K},-1} c^\dagger_{\mathbf{k},\mathbf{K},-1} c_{\mathbf{k},\mathbf{K},+1} |\Psi_{VP}\rangle \,; \\ \rho_{-\mathbf{q}}^S |\Psi_{\mathbf{k}'}\rangle &= \sum_{\mathbf{k}''} F_{-\mathbf{q}}^S(\mathbf{k}'') e^{i\Phi_{-\mathbf{q}}^S(\mathbf{k}'')} c^\dagger_{\mathbf{k}'',\mathbf{K},+1} c_{\mathbf{k}''-\mathbf{q},\mathbf{K},+1} c^\dagger_{\mathbf{k}',\mathbf{K},-1} c_{\mathbf{k}',\mathbf{K},+1} |\Psi_{VP}\rangle \\ &\qquad + F_{-\mathbf{q}}^S(\mathbf{k}'') e^{-i\Phi_{-\mathbf{q}}^S(\mathbf{k}'')} c^\dagger_{\mathbf{k}'',\mathbf{K},-1} c_{\mathbf{k}''-\mathbf{q},\mathbf{K},-1} c^\dagger_{\mathbf{k}',\mathbf{K},-1} c_{\mathbf{k}',\mathbf{K},+1} |\Psi_{VP}\rangle \,, \\ &= F_{-\mathbf{q}}^S(\mathbf{k}') e^{i\Phi_{-\mathbf{q}}^S(\mathbf{k}')} c^\dagger_{\mathbf{k}',\mathbf{K},+1} c_{\mathbf{k}'-\mathbf{q},\mathbf{K},+1} c^\dagger_{\mathbf{k}',\mathbf{K},-1} c_{\mathbf{k}',\mathbf{K},+1} |\Psi_{VP}\rangle \\ &\qquad + F_{-\mathbf{q}}^S(\mathbf{k}'+\mathbf{q}) e^{-i\Phi_{-\mathbf{q}}^S(\mathbf{k}'+\mathbf{q})} c^\dagger_{\mathbf{k}'+\mathbf{q},\mathbf{K},-1} c_{\mathbf{k}',\mathbf{K},-1} c^\dagger_{\mathbf{k}',\mathbf{K},-1} c_{\mathbf{k}',\mathbf{K},+1} |\Psi_{VP}\rangle \,, \\ &= [F_{\mathbf{q}}^S(\mathbf{k}'-\mathbf{q})]^\dagger e^{i[\Phi_{\mathbf{q}}^S(\mathbf{k}'-\mathbf{q})]^\dagger} c^\dagger_{\mathbf{k}',\mathbf{K},+1} c_{\mathbf{k}'-\mathbf{q},\mathbf{K},+1} c^\dagger_{\mathbf{k}',\mathbf{K},-1} c_{\mathbf{k}',\mathbf{K},+1} |\Psi_{VP}\rangle \\ &\qquad + [F_{\mathbf{q}}^S(\mathbf{k}')]^\dagger e^{-i[\Phi_{\mathbf{q}}^S(\mathbf{k}')]^\dagger} c^\dagger_{\mathbf{k}'+\mathbf{q},\mathbf{K},-1} c_{\mathbf{k}',\mathbf{K},-1} c^\dagger_{\mathbf{k}',\mathbf{K},-1} c_{\mathbf{k}',\mathbf{K},+1} |\Psi_{VP}\rangle \,. \end{aligned}$$

As a result, the energy of this state is changed into

$$\begin{aligned} E_{\mathbf{k},\mathbf{k}'} &= \frac{1}{2A}\sum_{\mathbf{q}} V_{\mathbf{q}} \left\langle \Psi_{\mathbf{k}} | \delta\rho^S_{\mathbf{q}} \delta\rho^S_{-\mathbf{q}} | \Psi_{\mathbf{k}'} \right\rangle, \\ &= \frac{1}{2A}\sum_{\mathbf{q}} V_{\mathbf{q}} (2\delta_{\mathbf{k},\mathbf{k}'} |F^S_{\mathbf{q}}(\mathbf{k})|^2 - 2\delta_{\mathbf{k}+\mathbf{q},\mathbf{k}'} |F^S_{\mathbf{q}}(\mathbf{k})|^2 e^{2i\Phi^S_{\mathbf{q}}(\mathbf{k})}), \\ &= \frac{1}{A}\sum_{\mathbf{q}} V_{\mathbf{q}} |F^S_{\mathbf{q}}(\mathbf{k})|^2 (\delta_{\mathbf{k},\mathbf{k}'} - \delta_{\mathbf{k}+\mathbf{q},\mathbf{k}'} e^{2i\Phi^S_{\mathbf{q}}(\mathbf{k})}). \end{aligned} \tag{2.37}$$

Then we obtain the second-order energies:

$$\Delta E^{(2)} = -\frac{1}{N_{\mathbf{k}}}\sum_{\mathbf{k},\mathbf{k}'} [\epsilon_x(\mathbf{k}) + i\epsilon_y(\mathbf{k})](E_{\mathbf{k},\mathbf{k}'})^{-1}[\epsilon_x(\mathbf{k}') - i\epsilon_y(\mathbf{k}')] = -J. \tag{2.38}$$

Note that we mentioned earlier that $U(4)_R$ commutes with σ_x. According to second perturbation theory, when Q doesn't commute with σ_x, the energy is lowered by $J \sim t_S/U_S \sim 1 - 2emV$.

Energy Contributions of $\hat{H}^A_I$

Note that we mentioned that $U(4)_{\mathcal{PT}}$ commute with $\sigma_x\tau_z$ before. By second perturbation theory, when Q doesn't commute with $\sigma_x\tau_z$, the energy is increased by $\lambda \sim U_A^2/U_S \sim 1meV$.

Energy Contributions of $\hat{H}^A_0$

To understand the competition between different states, we will start with spinless model and replace $U(4) \to U(2)$. The occupation of different states is shown in Fig. 2.4. For example, VH states preserve time reversal symmetry, so the energy stays the same when we map two valleys into each other, as shown in the second row. QH states preserve C_2 symmetry, so the energy stays the same when we map two valleys into each other and two sublattices into each other simultaneously.

As depicted in Fig. 2.4, $[Q, \sigma_x] = 0$ holds for VP states, so the energy reduction from t_S is blocked; $[Q, \sigma_x\tau_z]$ holds for VP/K-IVC states, so the energy increase from U_A is blocked. In summary, K-IVC states have the lowest energy.

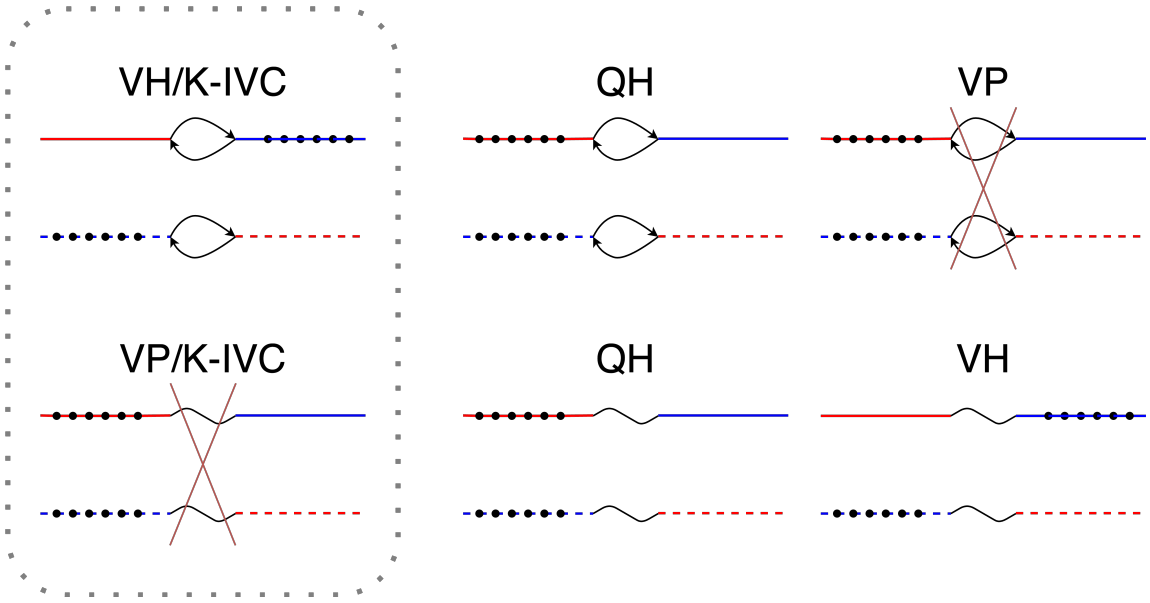

Figure 2.4: Schematic illustration of the symmetry reduction and ground-state selection in the spinless model. The first and second row represent the intersublattice dispersion and interaction respectively. This numerical methods are firstly discussed in Ref [12].

Chapter 3

Exact Ground States and Neutral Excitations

In this chapter, we validate the exact ground states for twisted bilayer graphene using perturbation theory. These exact ground states were initially proposed and discussed in Refs [58, 7, 108]. Our derivation in this chapter follows a similar approach to the one outlined in Chapter 2.[45, 44, 84, 12, 34, 9] There are mainly three difference: a) we derive the exact ground states for multiple integer fillings $-4 \leq \nu \leq 4$ relative to charge neutrality; b) we adopt a new perspective (Chern band basis) instead of the representation analysis; c) we consider the spin dimension here, although it doesn't significantly alter the results. The general existence of $U(2)_{\mathbf{K}} \times U(2)_{\mathbf{K}'}$ symmetry implies that our Hamiltonian is independent of spin.

In practice, we often assume that the flat bands [13, 79, 112, 66, 89, 109, 65] in the BM model have exactly zero eigenvalues, resulting in a zero kinetic term in our projected IBM model, i.e., $\hat{H}_0 = 0$. However, this assumption doesn't hold in most cases and introduces a small energy correction to our ground state calculations. In addition to the flat band assumption, we can decompose our form factors into a chiral-symmetric part $\hat{H}_I^S$ and a nonchiral-symmetric part $\hat{H}_I^A$. The chiral-symmetric part $\hat{H}_I^S$ exhibits a convenient $U(4) \times U(4)$ symmetry[12, 9, 58], allowing for the straightforward determination of exact ground states for all integer fillings. Subsequently, starting from the exact solutions of the chiral-symmetric part, we treat the contribution from the nonchiral-symmetric part as an energy correction with a relatively low energy scale. Consequently, perturbation theory is employed here to discuss the exact ground states and their corresponding neutral excitations.[9]

3.1 Chern band basis and Projected Hamiltonian

In Section 2.2, we introduced the representation matrices of symmetries, where these matrices denote the action of the corresponding symmetries in the space l, μ, σ. However, we are not always working in the original basis. Sometimes, it is more convenient to choose a specific band space and perform a unitary projection on the Hamiltonian, especially for numerical simulations. In this context, the matrix representation of symmetries in the new band space is referred to as sewing matrices. In this section, we provide the definition of the sewing matrices in the Chern band basis.

Electronic Structure

Let's begin by reviewing the electronic structure of the BM Hamiltonian in Eq. (1.21).[9] The eigenstates $u_{n\tau}(\mathbf{k}, l, \sigma)$ of the BM Hamiltonian $\hat{H}_0$ with eigenvalues $\epsilon_{n\tau}(\mathbf{k})$ can be expressed as follows:

$$\hat{H}_0 u_{n\tau}(\mathbf{k}, l, \sigma) = \epsilon_{n\tau}(\mathbf{k}) u_{n\tau}(\mathbf{k}, l, \sigma), \tag{3.1}$$

where n denotes the band number, and $\mathbf{k}$, l, τ, σ represent the momentum, valley, and sublattice, respectively. It's important to note that the energies $\epsilon_{n\tau}(\mathbf{k})$ only depend on the valley and band number. Additionally, the existence of C_{2z} symmetry and particle-hole symmetry $\mathcal{P}$ imposes constraints on the eigenstates:

$$\epsilon_{n\tau}(\mathbf{k}) = \epsilon_{n,-\tau}(-\mathbf{k}), \quad \epsilon_{n\tau}(\mathbf{k}) = -\epsilon_{-n,\tau}(-\mathbf{k}). \tag{3.2}$$

In the given band basis, the creation operators are transformed as follows:

$$\hat{f}^\dagger_{n,\mathbf{k},\tau} = \sum_{l,\sigma} u_{n\tau}(\mathbf{k}, l, \sigma) \hat{c}^\dagger_{\mathbf{k},l,\tau,\sigma}. \tag{3.3}$$

The corresponding projected Hamiltonian can then be written as:

$$\hat{H}_0 = \sum_{\mathbf{k}} \sum_{n\tau} \epsilon_{n\tau}(\mathbf{k}) \hat{f}^\dagger_{n,\mathbf{k},\tau} \hat{f}_{n,\mathbf{k},\tau},$$

which satisfies

$$\hat{H}_0 \hat{f}^\dagger_{n,\mathbf{k},\tau} |\text{vac}\rangle = \epsilon_{n\tau}(\mathbf{k}) \hat{f}^\dagger_{n,\mathbf{k},\tau} |\text{vac}\rangle .$$

Matrix representation

In this subsection, we will delve into the matrix representations of symmetries in the band space, known as sewing matrices. Assuming the action of a unitary operator g is

$g\hat{c}^\dagger_{\mathbf{k},l,\tau,\sigma}g^{-1} = \sum_{l'\tau'\sigma'} \hat{c}^\dagger_{g\mathbf{k},l',\tau',\sigma'}[D(g)]_{l\tau\sigma,l'\tau'\sigma'}$, where $D(g)$ is the representation matrix of operator g. For computational convenience, we will use the abbreviation $\alpha = (l,\sigma)$ and express $u_{n\tau}(\mathbf{k})$ as a vector, and $D(g)$ and $\hat{h}(\mathbf{k})$ as matrices:

$$\begin{aligned}(\hat{h}(\mathbf{k})u_{n\tau}(\mathbf{k}))(\alpha) &= \epsilon_{n\tau}(\mathbf{k})u_{n\tau}(\mathbf{k},\alpha),\\ (D(g)u_{n\tau}(\mathbf{k}))(\alpha) &= \sum_{\alpha'}[D(g)]_{\alpha\alpha'}u_{n\tau}(\mathbf{k},\alpha').\end{aligned}$$

Due to the commutation relation $D(g)\hat{h}(\mathbf{k}) = \hat{h}(g\mathbf{k})D(g)$, $D(g)u_{n\tau}(\mathbf{k})$ is also an eigenfunction of $\hat{h}(g\mathbf{k})$ with the eigenvalue $\epsilon_{n\tau}(g\mathbf{k}) = \epsilon_{n\tau}(\mathbf{k})$. This implies:

$$\begin{aligned}D(g)\hat{h}(\mathbf{k})u_{n\tau}(\mathbf{k}) &= D(g)\epsilon_{n\tau}(\mathbf{k})u_{n\tau}(\mathbf{k}) = \epsilon_{n\tau}(\mathbf{k})D(g)u_{n\tau}(\mathbf{k}),\\ \hat{h}(g\mathbf{k})D(g)u_{n\tau}(\mathbf{k}) &= \epsilon_{n\tau}(g\mathbf{k})D(g)u_{n\tau}(\mathbf{k}).\end{aligned}$$

Therefore, $[D(g)]_{\tau\tau'}u_{n\tau}(\mathbf{k})$ is an eigenfunction of $h(g\mathbf{k})$, expressed as

$$[D(g)]_{\tau\tau'}u_{n\tau}(\mathbf{k}) = \sum_m [B(g)]_{\mathbf{k},m\tau',n\tau}u_{m\tau'}(g\mathbf{k}), \tag{3.4}$$

where $[B(g)]_{\mathbf{k},m\tau',n\tau}$ is a matrix with dimension equal to the number of indices in α, given by:

$$[B(g)]_{\mathbf{k},m\tau',n\tau} = \langle u_{m\tau'}(g\mathbf{k})|[D(g)]_{\tau\tau'}|u_{n\tau}(\mathbf{k})\rangle\,. \tag{3.5}$$

For the action of unitary operator g, we have

$$\begin{aligned}g\hat{f}^\dagger_{n,\mathbf{k},\tau}g^{-1} &= g(u_{n\tau}(\mathbf{k})\hat{c}^\dagger_{\mathbf{k},\tau})g^{-1},\\ &= g\hat{c}^\dagger_{\mathbf{k},\tau}g^{-1}u_{n\tau}(\mathbf{k}),\\ &= \sum_{\tau'}\hat{c}^\dagger_{g\mathbf{k},\tau'}[D(g)]_{\tau,\tau'}u_{n\tau}(\mathbf{k}),\\ &= \sum_{\tau'}\hat{c}^\dagger_{g\mathbf{k},\tau'}[D(g)]_{\tau\tau'}u_{n\tau}(\mathbf{k}),\\ &= \sum_{\tau'}\hat{c}^\dagger_{g\mathbf{k},\tau'}\sum_m[B(g)]_{\mathbf{k},m\tau',n\tau}u_{m\tau'}(g\mathbf{k}),\\ &= \sum_m u_{m\tau'}(g\mathbf{k})\hat{c}^\dagger_{g\mathbf{k},\tau'}[B(g)]_{\mathbf{k},m\tau',n\tau}.\\ &= \sum_m \hat{f}^\dagger_{m,g\mathbf{k},\tau}[B(g)]_{\mathbf{k},m\tau',n\tau}.\end{aligned}$$

Similarly, for an anti-unitary operator g, we get

$$[D(g)]_{\tau\tau'}u^*_{n\tau}(\mathbf{k}) = \sum_m [B(g)]_{\mathbf{k},m\tau',n\tau}u_{m\tau'}(g\mathbf{k}), \tag{3.6}$$

$$[B(g)]_{\mathbf{k},m\tau',n\tau} = \langle u_{m\tau'}(g\mathbf{k})|[D(g)]_{\tau\tau'}|u^*_{n\tau}(\mathbf{k})\rangle\,, \tag{3.7}$$

$$g\hat{f}^\dagger_{n,\mathbf{k},\tau}g^{-1} = \sum_m \hat{f}^\dagger_{m,g\mathbf{k},\tau}[B(g)]_{\mathbf{k},m\tau',n\tau}. \tag{3.8}$$

For 1-RDM $[P(\mathbf{k})]_{n\tau,m\tau'} = \langle \hat{f}^\dagger_{m,\mathbf{k},\tau'}\hat{f}_{n,\mathbf{k},\tau}\rangle$, we will have

$$gP(\mathbf{k})g^{-1} = (B^\dagger(g)P(\mathbf{k})B(g) - P(\mathbf{k}))_{nm}.$$

Gauge Fixing

Due to symmetry operations of C_{2x}, C_{2z}, and C_{3z}, we find that $\epsilon_n(\mathbf{k}) = \epsilon_n(C_{2x}\mathbf{k}) = \epsilon_n(C_{2z}\mathbf{k}) = \epsilon_n(C_{3z}\mathbf{k})$. The phases of $u_{n\tau}(\mathbf{k})$ can be chosen arbitrarily.

Utilizing Eq. (3.4), we can express the sewing matrices for the anti-unitary symmetry $C_{2z}\mathcal{T}$, the Chern number C, and the unitary symmetry C_{2x} and C_{3z} as follows:

$$D[C_{2z}\mathcal{T}]u^*_{n\tau}(\mathbf{k}) = \sum_m [B(C_{2z}\mathcal{T})]_{mn}u_{m\tau}(\mathbf{k}), \quad [B(C_{2z}\mathcal{T})]_{mn} = \delta_{mn}e^{i\psi_n^{C_{2z}\mathcal{T}}(\mathbf{k})}, \tag{3.9}$$

$$D[C_{2x}]u_{n\tau}(\mathbf{k}) = \sum_m [B(C_{2x})]_{mn}u_{m\tau}(C_{2x}\mathbf{k}), \quad [B(C_{2x})]_{mn} = \delta_{mn}e^{i\psi_n^{C_{2x}}(\mathbf{k})}, \tag{3.10}$$

$$D[C_{3z}]u_{n\tau}(\mathbf{k}) = \sum_m [B(C_{3z})]_{mn}u_{m\tau}(C_{3z}\mathbf{k}), \quad [B(C_{3z})]_{mn} = \delta_{mn}e^{i\psi_n^{C_{3z}}(\mathbf{k})}. \tag{3.11}$$

It's important to note that both $\mathcal{P}$ and $\mathcal{T}$ symmetries include a complex conjugation operator.

For the case of the Chern number $C = \sigma_z$ in the valleyless scenario, we define the sewing matrices as

$$D[C]u_{n\tau}(\mathbf{k}) = \sum_m [B(C)]_{mn}u_{m\tau}(\mathbf{k}). \tag{3.12}$$

Assume the selection of two flat bands, the sewing matrices for $C_{2z}\mathcal{T}$ and C (both independent of $\mathbf{k}$) are constrained by the conditions:

$$(C_{2z}\mathcal{T})^2 = C^2 = 1, \quad \{C_{2z}\mathcal{T}, C\} = 0,$$

which implies:

$$[B(C_{2z}\mathcal{T})]^2 = B[C]^2 = I, \quad B(C_{2z}\mathcal{T})B^*(C) + B(C)B(C_{2z}\mathcal{T}) = 0,$$

yielding:

$$B(C_{2z}\mathcal{T}) = \begin{pmatrix} e^{i\psi_0^{C_{2z}\mathcal{T}}(\mathbf{k})} & 0 \\ 0 & e^{i\psi_1^{C_{2z}\mathcal{T}}(\mathbf{k})} \end{pmatrix}, \ B(C) = \pm \begin{pmatrix} 0 & -ie^{i\frac{\psi_0^{C_{2z}\mathcal{T}}(\mathbf{k})-\psi_1^{C_{2z}\mathcal{T}}(\mathbf{k})}{2}} \\ ie^{i\frac{\psi_1^{C_{2z}\mathcal{T}}(\mathbf{k})-\psi_0^{C_{2z}\mathcal{T}}(\mathbf{k})}{2}} & 0 \end{pmatrix}.$$

Fixing the phases of wavefunctions and the gauge of sewing matrices, we can simplify this to:

$$B(C_{2z}\mathcal{T}) = \begin{pmatrix} 1 & 0 \\ 0 & 1 \end{pmatrix}, \ \ B(C) = \begin{pmatrix} 0 & -i \\ i & 0 \end{pmatrix}.$$

We can interpret this gauge fixing as follows:

$$C_{2z}\mathcal{T} = \sigma_x\mathcal{K} \to \mathcal{K}, \ \ C = \sigma_z \to \sigma_y.$$

Additionally, the Chern band basis can be chosen as:

$$v(\pm\mathbf{k}) = \frac{1}{\sqrt{2}}(u_+(\mathbf{k}) \pm iu_-(\mathbf{k})), \ \ B(C)v(\pm\mathbf{k}) = \pm v(\pm\mathbf{k}). \tag{3.13}$$

Continuing the derivation of the sewing matrices from a new perspective, we leverage the relations:

$$[C_{2z}\mathcal{T}, \mathcal{P}\mathcal{T}] = 0, \ \ \{C_{2z}\mathcal{T}, C\} = 0,$$

which is equivalent to:

$$B(C_{2z}\mathcal{T})B^*(C) + B(C)B(C_{2z}\mathcal{T}) = 0, \ \ B(C_{2z}\mathcal{T})B^*(\mathcal{P}\mathcal{T}) = B(\mathcal{P}\mathcal{T})B^*(C_{2z}\mathcal{T}).$$

Note that $C_{2z}\mathcal{T}$, $\mathcal{P}\mathcal{T}$, C don't change $\mathbf{k}$, and $C_{2z}\mathcal{T}$, $\mathcal{P}\mathcal{T}$ are anti-unitary, while C is unitary.

The sewing matrices for $C_{2z}\mathcal{T}$, C and $\mathcal{P}\mathcal{T}$ take the form:

$$B(C_{2z}\mathcal{T}) = \begin{pmatrix} a_1 & b_1 \\ c_1 & d_1 \end{pmatrix},$$
$$B(C) = \begin{pmatrix} a_2 & b_2 \\ c_2 & d_2 \end{pmatrix},$$
$$B(\mathcal{P}\mathcal{T}) = \begin{pmatrix} a_3 & b_3 \\ c_3 & d_3, \end{pmatrix}.$$

$$B(C_{2z}\mathcal{T})B^*(\mathcal{PT}) = B(\mathcal{PT})B^*(C_{2z}\mathcal{T})$$

$$B(C_{2z}\mathcal{T})B^*(\mathcal{PT}) = \begin{pmatrix} a_1 & b_1 \\ c_1 & d_1 \end{pmatrix}\begin{pmatrix} a_3^* & b_3^* \\ c_3^* & d_3^* \end{pmatrix} = \begin{pmatrix} a_1a_3^* + b_1c_3^* & a_1b_3^* + b_1d_3^* \\ c_1a_3^* + d_1c_3^* & c_1b_3^* + d_1d_3^* \end{pmatrix},$$
$$B(\mathcal{PT})B^*(C_{2z}\mathcal{T}) = \begin{pmatrix} a_3 & b_3 \\ c_3 & d_3 \end{pmatrix}\begin{pmatrix} a_1^* & b_1^* \\ c_1^* & d_1^* \end{pmatrix} = \begin{pmatrix} a_1^*a_3 + c_1^*b_3 & b_1^*a_3 + d_1^*b_3 \\ a_1^*c_3 + c_1^*d_3 & b_1^*c_3 + d_1^*d_3 \end{pmatrix},$$
$$a_1a_3^* + b_1c_3^* = a_1^*a_3 + c_1^*b_3,\ a_1b_3^* + b_1d_3^* = b_1^*a_3 + d_1^*b_3,$$
$$c_1a_3^* + d_1c_3^* = a_1^*c_3 + c_1^*d_3,\ c_1b_3^* + d_1d_3^* = b_1^*c_3 + d_1^*d_3.$$

We choose $C_{2z}\mathcal{T}$ and $\mathcal{PT}$ to be anti-diagonal matrices:

$$a_1 = d_1 = a_3 = d_3 = 0,$$

implying

$$b_1c_3^* = c_1^*b_3.$$

To simplify, we set $b_1 = c_1 = 1$, resulting in $b_3 = -i$ and $c_3 = i$.

$$B(C_{2z}\mathcal{T})B^*(C) + B(C)B(C_{2z}\mathcal{T}) = 0$$

$$B(C_{2z}\mathcal{T})B^*(C) = \begin{pmatrix} a_1 & b_1 \\ c_1 & d_1 \end{pmatrix}\begin{pmatrix} a_2^* & b_2^* \\ c_2^* & d_2^* \end{pmatrix} = \begin{pmatrix} a_1a_2^* + b_1c_2^* & a_1b_2^* + b_1d_2^* \\ c_1a_2^* + d_1c_2^* & c_1b_2^* + d_1d_2^* \end{pmatrix},$$
$$B(C)B(C_{2z}\mathcal{T}) = \begin{pmatrix} a_2 & b_2 \\ c_2 & d_2 \end{pmatrix}\begin{pmatrix} a_1 & b_1 \\ c_1 & d_1 \end{pmatrix} = \begin{pmatrix} a_1a_2 + c_1b_2 & b_1a_2 + d_1b_2 \\ a_1c_2 + c_1d_2 & b_1c_2 + d_1d_2 \end{pmatrix},$$
$$a_1a_2^* + b_1c_2^* + a_1a_2 + c_1b_2 = 0,\ a_1b_2^* + b_1d_2^* + b_1a_2 + d_1b_2 = 0,$$
$$c_1a_2^* + d_1c_2^* + a_1c_2 + c_1d_2 = 0,\ c_1b_2^* + d_1d_2^* + b_1c_2 + d_1d_2 = 0.$$

Given $a_1 = d_1 = 0$ and $b_1 = c_1 = 1$, we find

$$a_2^* + d_2 = b_2^* + c_2 = 0.$$

Further setting $b_2 = c_2 = 0$, $a_2 = 1$, and $d_2 = -1$, we obtain the final form for the sewing matrices:

$$B(C_{2z}\mathcal{T}) = \begin{pmatrix} 0 & 1 \\ 1 & 0 \end{pmatrix} \sim \sigma_x,\quad B(\mathcal{PT}) = \begin{pmatrix} 0 & -i \\ i & 0 \end{pmatrix} \sim \sigma_y,\quad B(\mathcal{C}) = \begin{pmatrix} 1 & 0 \\ 0 & -1 \end{pmatrix} \sim \sigma_z.$$

Projected Hamiltonian with Coulomb Interaction

In this subsection, we introduce the Coulomb interaction to the BM model in Eq. (1.21), resulting in an interacting Bistritzer-MacDonald (IBM) model. We use the eigenstates $u_{n\tau}(\mathbf{k}, l, \sigma)$ of the BM model to conduct the projection on the IBM model. For simplicity, the index l, σ can appear either as a subscript or in the parenthesis, i.e., $\varphi_{n\mathbf{k}\tau,\sigma,l}(\mathbf{G}) \equiv \varphi_{n\mathbf{k}\tau}(\mathbf{G}, \sigma, l)$. We do not assume any specific properties for the chiral model in this section, making the discussion applicable to the general 2-band IBM model. The notation $\alpha = (\mathbf{G}, \sigma, l)$ is used to denote the *internal* indices for convenience.

The creation operator associated with a band takes the form

$$\hat{f}^\dagger_{n,\mathbf{k},\tau} = \sum_{\mathbf{G},\sigma} \hat{c}^\dagger_{\mathbf{k}+\mathbf{G},t,\tau,\sigma} u_{n\tau}(\mathbf{k}, \mathbf{G}, \sigma, t) + \sum_{\mathbf{G},\sigma} \hat{c}^\dagger_{\mathbf{k}+\mathbf{G},b,\tau,\sigma} u_{n\tau}(\mathbf{k}, \mathbf{G}, \sigma, b).$$

We also define

$$\varphi_{n\mathbf{k}}(\mathbf{r}, \sigma, l) = \frac{1}{\sqrt{N_\mathbf{k}}} e^{\mathrm{i}\mathbf{k}\cdot\mathbf{r}} u_{n\tau}(\mathbf{k}, \mathbf{r}, \sigma, l),$$

where $u_{n\tau}(\mathbf{k}, \cdot, \sigma, l)$ is periodic with respect to $\mathbb{L}$.

Assume no truncation with respect to the $\mathbf{G}$ index, we have

$$\begin{aligned}
\hat{f}^\dagger_{n,\mathbf{k},\tau} =& \sum_{\mathbf{G},\sigma,l} \hat{c}^\dagger_{\mathbf{k}+\mathbf{G},l,\tau,\sigma} u_{n\tau}(\mathbf{k}, \mathbf{G}, \sigma, l), \\
=& \frac{1}{\sqrt{N_\mathbf{k}\,|\Omega|}} \int_{\Omega_{N_\mathbf{k}}} \sum_{\mathbf{G},\sigma,l} \hat{a}^\dagger_{\mathbf{r},l,\tau,\sigma} e^{\mathrm{i}(\mathbf{k}+\mathbf{G})\cdot\mathbf{r}} u_{n\tau}(\mathbf{k}, \mathbf{G}, \sigma, l)\, \mathrm{d}\mathbf{r} \\
=& \sum_{\sigma,l} \int_{\Omega_{N_\mathbf{k}}} \hat{a}^\dagger_{\mathbf{r},l,\tau,\sigma} \varphi_{n\mathbf{k}\tau}(\mathbf{r}, \sigma, l)\, \mathrm{d}\mathbf{r}.
\end{aligned} \tag{3.14}$$

Here $\Omega_{N_\mathbf{k}}$ is the moiré supercell, whose area is $N_\mathbf{k}\,|\Omega|$, and $\hat{a}^\dagger_{\mathbf{r},l,\tau,\sigma}$ denotes the creation operator in real space. Considering only valley $\tau = \mathbf{K}$ and defining $\hat{f}^\dagger_{n\mathbf{k}} = \hat{f}^\dagger_{n,\mathbf{k},\tau=\mathbf{K}}$, $\varphi_{n\mathbf{k}} = \varphi_{n\mathbf{k}\tau=\mathbf{K}}$, the interacting model is a quartic Hamiltonian (when focusing on the $\mathbf{K}$ valley, $\mathbf{k}$ is centered at $\mathbf{K}_t$):

$$\hat{H} = \frac{1}{2} \sum_{\substack{\mathbf{k},\mathbf{k}',\mathbf{k}''\in\Omega^* \\ \mathbf{k}'''=\mathbf{k}+\mathbf{k}'-\mathbf{k}''}} \sum_{mm'nn'} \langle m\mathbf{k}, m'\mathbf{k}' | n\mathbf{k}'', n'\mathbf{k}''' \rangle\, \hat{f}^\dagger_{m\mathbf{k}} \hat{f}^\dagger_{m'\mathbf{k}'} \hat{f}_{n'\mathbf{k}'''} \hat{f}_{n\mathbf{k}''}, \tag{3.15}$$

where there exist 2 flat bands in valley $\mathbf{K}$, so the band index $m, n, m', n' \in \{\pm 1\}$ loops over the flat bands only.

In practical applications, we often consider the screened Coulomb interaction, referred to as a double-gate screened Coulomb potential, given by:

$$V(\mathbf{r}) = U_d \sum_{n=-\infty}^{\infty} \frac{(-1)^n}{\sqrt{|\mathbf{r}|^2 + (nd)^2}}. \tag{3.16}$$

Here, $U_d = \epsilon^{-1}$ parametrizes the strength of the screened Coulomb interaction, and ϵ is the screening constant. In Fourier space, the Coulomb interaction takes the form:

$$V(\mathbf{q}) = \int V(\mathbf{r}) e^{-\mathrm{i}\mathbf{q}\cdot\mathbf{r}} \,\mathrm{d}\mathbf{r} = 2\pi U_d \frac{\tanh(|\mathbf{q}|\, d/2)}{|\mathbf{q}|}. \tag{3.17}$$

Then electron repulsion integrals (ERI) are denoted by $\langle m\mathbf{k}, m'\mathbf{k}'|n\mathbf{k}'', n'\mathbf{k}'''\rangle$ in valley $\mathbf{K}$, satisfying the crystal momentum conservation $\mathbf{k}+\mathbf{k}'+\mathbf{k}''+\mathbf{k}''' \in \mathbb{L}^*$. The ERI can be expressed as

$$\begin{aligned}
&\langle m\mathbf{k}, m'\mathbf{k}'|n\mathbf{k}'', n'\mathbf{k}'''\rangle \\
&= \sum_{\sigma,l,\sigma',l'} \int_{\Omega_{N_\mathbf{k}}} V(\mathbf{r}-\mathbf{r}') \varphi^*_{m\mathbf{k}}(\mathbf{r},\sigma,l) \varphi^*_{m'\mathbf{k}'}(\mathbf{r}',\sigma',l') \varphi_{n\mathbf{k}''}(\mathbf{r},\sigma,l) \varphi_{n'\mathbf{k}'''}(\mathbf{r}',\sigma',l') \,\mathrm{d}\mathbf{r}\,\mathrm{d}\mathbf{r}' \\
&= \frac{1}{N_\mathbf{k}^2} \int_{\Omega_{N_\mathbf{k}}} V(\mathbf{r}-\mathbf{r}') e^{\mathrm{i}\mathbf{q}\cdot(\mathbf{r}-\mathbf{r}')} \varrho_{m\mathbf{k},n(\mathbf{k}+\mathbf{q})}(\mathbf{r}) \varrho_{m'\mathbf{k}',n'(\mathbf{k}'-\mathbf{q})}(\mathbf{r}') \,\mathrm{d}\mathbf{r}\,\mathrm{d}\mathbf{r}',
\end{aligned} \tag{3.18}$$

where $\mathbf{q} = \mathbf{k}''-\mathbf{k}$, and by crystal momentum conservation, we can choose $\mathbf{k}''' = \mathbf{k}'-\mathbf{q}$.

The pair product of the periodic components of the flat bands in the real space (summed over the sublattice and layer indices) is defined as

$$\begin{aligned}
\varrho_{m\mathbf{k},n\mathbf{k}''}(\mathbf{r}) =& \sum_{\sigma,l} u^*_m(\mathbf{k},\mathbf{r},\sigma,l) u_n(\mathbf{k}'',\mathbf{r},\sigma,l) \\
=& \frac{1}{|\Omega|^2} \sum_{\mathbf{G},\mathbf{G}'} \sum_{\sigma,l} u^*_m(\mathbf{k},\mathbf{G}',\sigma,l) u_n(\mathbf{k}'',\mathbf{G},\sigma,l) e^{\mathrm{i}(\mathbf{G}-\mathbf{G}')\cdot\mathbf{r}} \\
=& \frac{1}{|\Omega|^2} \sum_{\mathbf{G}} \sum_{\mathbf{G}'} \sum_{\sigma,l} u^*_m(\mathbf{k},\mathbf{G}',\sigma,l) u_n(\mathbf{k}'',\mathbf{G}+\mathbf{G}',\sigma,l) e^{\mathrm{i}\mathbf{G}\cdot\mathbf{r}} \\
=& \frac{1}{|\Omega|^2} \sum_{\mathbf{G}} \sum_{\mathbf{G}'} \sum_{\sigma,l} u^*_m(\mathbf{k},\mathbf{G}',\sigma,l) u_n(\mathbf{k}''+\mathbf{G},\mathbf{G}',\sigma,l) e^{\mathrm{i}\mathbf{G}\cdot\mathbf{r}} \\
=& \frac{1}{|\Omega|} \sum_{\mathbf{G}} e^{\mathrm{i}\mathbf{G}\cdot\mathbf{r}} \varrho_{m\mathbf{k},n\mathbf{k}''}(\mathbf{G}).
\end{aligned} \tag{3.19}$$

The Fourier coefficients of the pair product satisfy

$$\varrho_{m\mathbf{k},n(\mathbf{k}+\mathbf{q})}(\mathbf{G}) = \frac{1}{|\Omega|}\sum_{\mathbf{G}'\in\mathbb{L}^*}\sum_{\sigma,l} u_m^*(\mathbf{k},\mathbf{G}',\sigma,l)u_n(\mathbf{k}+\mathbf{q}+\mathbf{G},\mathbf{G}',\sigma,l) = [\Lambda_{\mathbf{k}}(\mathbf{q}+\mathbf{G})]_{mn}, \tag{3.20}$$

where the matrix $\Lambda_{\mathbf{k}}(\mathbf{q}+\mathbf{G})$ is called the *form factor*.

From Eq. (3.20) we can verify that the form factor satisfies the symmetry condition

$$[\Lambda_{\mathbf{k}}(\mathbf{q}+\mathbf{G})]^*_{mn} = [\Lambda_{\mathbf{k}+\mathbf{q}}(-\mathbf{q}-\mathbf{G})]_{nm}, \tag{3.21}$$

and

$$\Lambda_{\mathbf{k}+\mathbf{G}'}(\mathbf{q}+\mathbf{G}) = \Lambda_{\mathbf{k}}(\mathbf{q}+\mathbf{G}), \quad \forall \mathbf{G}' \in \mathbb{L}^*. \tag{3.22}$$

Using the definitions of the Coulomb interaction $V(\mathbf{q})$ in Eq. (3.17) and the form factor in Eq. (3.20), the ERI can be expressed in the Fourier space as:

$$\begin{aligned}\langle m\mathbf{k}, m'\mathbf{k}'|n\mathbf{k}'', n'\mathbf{k}'''\rangle =& \frac{1}{|\Omega|N_{\mathbf{k}}}\sum_{\mathbf{G}\in\mathbb{L}^*} V(\mathbf{q}+\mathbf{G})\varrho_{m\mathbf{k},n(\mathbf{k}+\mathbf{q})}(\mathbf{G})\varrho_{m'\mathbf{k}',n'(\mathbf{k}'-\mathbf{q})}(-\mathbf{G}).\\ =& \frac{1}{|\Omega|N_{\mathbf{k}}}\sum_{\mathbf{G}\in\mathbb{L}^*} V(\mathbf{q}+\mathbf{G})[\Lambda_{\mathbf{k}}(\mathbf{q}+\mathbf{G})]_{mn}[\Lambda_{\mathbf{k}'}(-\mathbf{q}-\mathbf{G})]_{m'n'}.\end{aligned} \tag{3.23}$$

Finally, the single-valley ($\tau = \mathbf{K}$) IBM Hamiltonian can be written as

$$\begin{aligned}\hat{H}_{\mathrm{IBM}} =& \frac{1}{2}\sum_{\mathbf{k},\mathbf{k}',\mathbf{k}''\in\Omega^*}\sum_{mm'nn'} \langle m\mathbf{k}, m'\mathbf{k}'|n\mathbf{k}'', n'\mathbf{k}'''\rangle\, \hat{f}^\dagger_{m\mathbf{k}}\hat{f}^\dagger_{m'\mathbf{k}'}\hat{f}_{n'\mathbf{k}'''}\hat{f}_{n\mathbf{k}''}\\ =& \frac{1}{2|\Omega|N_{\mathbf{k}}}\sum_{\mathbf{k},\mathbf{k}',\mathbf{k}+\mathbf{q}=\mathbf{k}''\in\Omega^*}\sum_{mm'}\sum_{\mathbf{G}\in\mathbb{L}^*} V(\mathbf{q}+\mathbf{G})[\Lambda_{\mathbf{k}}(\mathbf{q}+\mathbf{G})]_{mn}\\ &\times [\Lambda_{\mathbf{k}'}(-\mathbf{q}-\mathbf{G})]_{m'n'}\hat{f}^\dagger_{m\mathbf{k}}\hat{f}^\dagger_{m'\mathbf{k}'}\hat{f}_{n'(\mathbf{k}'-\mathbf{q})}\hat{f}_{n(\mathbf{k}+\mathbf{q})}.\end{aligned} \tag{3.24}$$

Next, we briefly discuss the properties of IBM model at the chiral limit. (ICM model) In the chiral model, since each flat band can be fully polarized (i.e. completely supported on either the A site or B site) along the sublattice direction A, B, the sublattice index is identical to the band index. Therefore

$$\hat{f}^\dagger_{n\mathbf{k}} = \sum_{\mathbf{G},l}\hat{c}^\dagger_{n,l}(\mathbf{k}+\mathbf{G})u_n(\mathbf{k},\mathbf{G},n,l) = \int_{\Omega_{N_{\mathbf{k}}}}\hat{a}^\dagger_{\mathbf{r},n,l}\varphi_{n\mathbf{k}}(\mathbf{r},n,l). \tag{3.25}$$

The pair product takes the form

$$\varrho_{m\mathbf{k},n\mathbf{k}''}(\mathbf{r}) = \sum_{\sigma,l} u_m^*(\mathbf{k},\mathbf{r},\sigma,l)u_n(\mathbf{k}'',\mathbf{r},\sigma,l) = \varrho_{m\mathbf{k},m\mathbf{k}''}(\mathbf{r})\delta_{m,n}. \tag{3.26}$$

Here the Kronecker delta $\delta_{m,n}$ is due to that $u_{n\tau}(\mathbf{k})$ is fully polarized along σ. We can also redefine the summation range of $\mathbf{q}$ to restrict it to the Brillouin zone:

$$\begin{aligned}\hat{H}_{\mathrm{ICM}} =&\frac{1}{2}\sum_{\mathbf{k},\mathbf{k}',\mathbf{k}''\in\Omega^*}\sum_{mm'nn'}\langle m\mathbf{k}, m'\mathbf{k}'|n\mathbf{k}'', n'\mathbf{k}'''\rangle\, \hat{f}^\dagger_{m\mathbf{k}}\hat{f}^\dagger_{m'\mathbf{k}'}\hat{f}_{n'\mathbf{k}'''}\hat{f}_{n\mathbf{k}''}\\ =&\frac{1}{2|\Omega|N_{\mathbf{k}}}\sum_{\mathbf{q}\in\Omega^*}\sum_{\mathbf{G}\in\mathbb{L}^*}\sum_{\mathbf{k},\mathbf{k}'\in\Omega^*}\sum_{mm'}V(\mathbf{q}+\mathbf{G})[\Lambda_{\mathbf{k}}(\mathbf{q}+\mathbf{G})]_{mm}\\ &\times[\Lambda_{\mathbf{k}'}(-\mathbf{q}-\mathbf{G})]_{m'm'}\hat{f}^\dagger_{m\mathbf{k}}\hat{f}^\dagger_{m'\mathbf{k}'}\hat{f}_{m'(\mathbf{k}'-\mathbf{q})}\hat{f}_{m(\mathbf{k}+\mathbf{q})}.\end{aligned} \tag{3.27}$$

The chiral model satisfies the $C_{2z}\mathcal{T}$ symmetry and the C_{2x} symmetry. These have direct implications in the form factor. These are most conveniently expressed first with respect to the pair product in the real space formulation, and then the properties on the form factors by performing a Fourier transform.

The $C_{2z}\mathcal{T}$ symmetry gives

$$\begin{aligned}\varrho_{1\mathbf{k},1\mathbf{k}''}(\mathbf{r}) &= \sum_l u^*_{1,\mathbf{k}}(\mathbf{r},1,l)u_{1\mathbf{k}''}(\mathbf{r},1,l),\\ &= \sum_l u_{-1,\mathbf{k}}(-\mathbf{r},-1,l)u^*_{-1,\mathbf{k}''}(-\mathbf{r},-1,l) = \varrho^*_{-1\mathbf{k},-1\mathbf{k}''}(-\mathbf{r}).\end{aligned} \tag{3.28}$$

Therefore

$$\begin{aligned}[\Lambda_{\mathbf{k}}(\mathbf{q}+\mathbf{G})]_{1,1} &= \int_\Omega e^{-\mathrm{i}\mathbf{G}\cdot\mathbf{r}}\varrho_{1\mathbf{k},1\mathbf{k}''}(\mathbf{r})\,\mathrm{d}\mathbf{r},\\ &= \int_\Omega e^{\mathrm{i}\mathbf{G}\cdot\mathbf{r}}\varrho^*_{-1\mathbf{k},-1\mathbf{k}''}(\mathbf{r})\,\mathrm{d}\mathbf{r} = [\Lambda_{\mathbf{k}}(\mathbf{q}+\mathbf{G})]^*_{-1,-1}.\end{aligned} \tag{3.29}$$

Therefore in the ICM model, the $C_{2z}\mathcal{T}$ symmetry implies that the form factor (as a diagonal matrix) can be written as

$$[\Lambda_{\mathbf{k}}(\mathbf{q}+\mathbf{G})] = \alpha_0(\mathbf{k},\mathbf{q}+\mathbf{G})\sigma_0 + \mathrm{i}\alpha_z(\mathbf{k},\mathbf{q}+\mathbf{G})\sigma_z, \tag{3.30}$$

where α_0, α_z are *real* functions.

The general condition Eq. (3.21) gives

$$\alpha_0(\mathbf{k},\mathbf{q}+\mathbf{G}) = \alpha_0(\mathbf{k}+\mathbf{q},-\mathbf{q}-\mathbf{G}),\quad \alpha_z(\mathbf{k},\mathbf{q}+\mathbf{G}) = -\alpha_z(\mathbf{k}+\mathbf{q},-\mathbf{q}-\mathbf{G}). \tag{3.31}$$

The C_{2x} symmetry gives

$$\begin{aligned}\varrho_{1\mathbf{k},1\mathbf{k}''}(\mathbf{r}) =& \sum_l u^*_{1,\mathbf{k}}(\mathbf{r},1,l)u_{1\mathbf{k}''}(\mathbf{r},1,l)\\ =& \sum_l u_{-1,\mathbf{k}^*}(-\mathbf{r}^*,-1,-l)u^*_{-1,\mathbf{k}''^*}(-\mathbf{r}^*,-1,-l)\\ =& \sum_l u_{-1,\mathbf{k}^*}(-\mathbf{r}^*,-1,l)u^*_{-1,\mathbf{k}''^*}(-\mathbf{r}^*,-1,l)\\ =& \varrho^*_{-1\mathbf{k}^*,-1\mathbf{k}''^*}(-\mathbf{r}^*).\end{aligned} \tag{3.32}$$

Then

$$\begin{aligned}[\Lambda_{\mathbf{k}}(\mathbf{q}+\mathbf{G})]_{1,1} =& \int_\Omega e^{-\mathrm{i}\mathbf{G}\cdot\mathbf{r}}\varrho_{1\mathbf{k},1\mathbf{k}''}(\mathbf{r})\,\mathrm{d}\mathbf{r}\\ =& \int_\Omega e^{-\mathrm{i}\mathbf{G}\cdot\mathbf{r}}\varrho^*_{1\mathbf{k}^*,1\mathbf{k}''^*}(-\mathbf{r}^*)\,\mathrm{d}\mathbf{r}\\ =& \int_\Omega e^{\mathrm{i}\mathbf{G}\cdot\mathbf{r}}\varrho^*_{1\mathbf{k}^*,1\mathbf{k}''^*}(\mathbf{r}^*)\,\mathrm{d}\mathbf{r}\\ =& \int_\Omega e^{\mathrm{i}\mathbf{G}^*\cdot\mathbf{r}}\varrho^*_{1\mathbf{k}^*,1\mathbf{k}''^*}(\mathbf{r})\,\mathrm{d}\mathbf{r}\\ =& [\Lambda_{\mathbf{k}^*}(\mathbf{q}^*+\mathbf{G}^*)]^*_{1,1}.\end{aligned} \tag{3.33}$$

This gives an additional relation

$$\alpha_0(\mathbf{k},\mathbf{q}+\mathbf{G}) = \alpha_0(\mathbf{k}^*,\mathbf{q}^*+\mathbf{G}^*),\quad \alpha_z(\mathbf{k},\mathbf{q}+\mathbf{G}) = -\alpha_z(\mathbf{k}^*,\mathbf{q}^*+\mathbf{G}^*). \tag{3.34}$$

Now for the particle-hole symmetry, we have

$$\begin{aligned}\varrho_{1\mathbf{k},1\mathbf{k}''}(\mathbf{r}) =& \sum_l u^*_{1,\mathbf{k}}(\mathbf{r},1,l)u_{1\mathbf{k}''}(\mathbf{r},1,l)\\ =& \sum_l u^*_{1,-\mathbf{k}}(-\mathbf{r},1,-l)u_{1,-\mathbf{k}''}(-\mathbf{r},1,-l)\\ =& \varrho_{1(-\mathbf{k}),1(-\mathbf{k}'')}(-\mathbf{r}).\end{aligned} \tag{3.35}$$

In the second equation, we have used the fact that the (-1) sign from $\mathrm{i}l_y$ cancels when multiplied together. Then

$$\begin{aligned}[\Lambda_{\mathbf{k}}(\mathbf{q}+\mathbf{G})]_{1,1} =& \int_\Omega e^{-\mathrm{i}\mathbf{G}\cdot\mathbf{r}}\varrho_{1\mathbf{k},1\mathbf{k}''}(\mathbf{r})\,\mathrm{d}\mathbf{r}\\ =& \int_\Omega e^{-\mathrm{i}\mathbf{G}\cdot\mathbf{r}}\varrho_{1(-\mathbf{k}),1(-\mathbf{k}'')}(-\mathbf{r})\,\mathrm{d}\mathbf{r}\\ =& [\Lambda_{(-\mathbf{k})}(-\mathbf{q}-\mathbf{G})]_{1,1}.\end{aligned} \tag{3.36}$$

This gives an additional relation

$$\alpha_0(\mathbf{k},\mathbf{q}+\mathbf{G})=\alpha_0(-\mathbf{k},-\mathbf{q}-\mathbf{G}),\quad \alpha_z(\mathbf{k},\mathbf{q}+\mathbf{G})=\alpha_z(-\mathbf{k},-\mathbf{q}-\mathbf{G}). \tag{3.37}$$

Together with Eq. (3.31), we find that at $\mathbf{q}=\mathbf{0}$,

$$\begin{aligned}\alpha_0(\mathbf{k},\mathbf{G})&=\alpha_0(-\mathbf{k},-\mathbf{G})=\alpha_0(\mathbf{k},-\mathbf{G}),\\ \alpha_z(\mathbf{k},\mathbf{G})&=-\alpha_z(\mathbf{k},-\mathbf{G})=\alpha_z(-\mathbf{k},-\mathbf{G}).\end{aligned} \tag{3.38}$$

In particular, we have

$$\alpha_z(-\mathbf{k},\mathbf{G})=-\alpha_z(\mathbf{k},\mathbf{G}),\quad \forall\mathbf{G}\in\mathbb{L}^*. \tag{3.39}$$

This gives the the sum rule

$$\sum_{\mathbf{k}}\alpha_z(\mathbf{k},\mathbf{G})=0,\quad \forall\mathbf{G}\in\mathbb{L}^*. \tag{3.40}$$

This relation plays a key role in understanding the ground state property later.[9, 58, 7]

3.2 Candidate States

Previous theoretical works have identified a wealth of possible candidate states with close energies, including insulators in the $U(4)\times U(4)$ manifold, the nematic semimetal (nSM) state, the incommensurate Kekul´e spiral (IKS) state, and the intervalley coherent (K-IVC/T-IVC) state.[109, 21, 63, 11, 116, 54] We have discussed various possible states and their preserved symmetries, as in Table. 2.2. Here we will rewrite these states using Chern band basis[12] with a fixed gauge:

$$v_{\pm,\tau,s}(\mathbf{k})=\frac{u_{\tau,\sigma=+1,s}(\mathbf{k})\pm iu_{\tau,\sigma=-1,s}(\mathbf{k})}{\sqrt{2}}. \tag{3.41}$$

Then our creation/annilation operator in the Chern band basis can be written as

$$\hat{d}^\dagger_{\mathbf{k},\pm,\tau,s}=\frac{\hat{c}^\dagger_{\mathbf{k},\tau,\sigma=+1,s}\pm i\hat{c}^\dagger_{\mathbf{k},\tau,\sigma=-1,s}}{\sqrt{2}}, \tag{3.42}$$

where $\hat{c}^\dagger_{\mathbf{k},\tau,\sigma,s}/\hat{c}_{\mathbf{k},\tau,\sigma,s}$ is the creation/annilation operator with momentum $\mathbf{k}$ in mBZ, valley $\tau\in\{\mathbf{K},\mathbf{K}'\}$, sublattice/band $\sigma=\pm1$, and spin $s=\pm1$. Then using the definition of the Chern band basis, we are able to write our candidate states for an integer filling $\nu+4=\nu_+ +\nu_-$ with total Chern number $\nu_C=\nu_+-\nu_-$. Here we let empty state be $|\text{vac}\rangle$.

- The spin-valley polarized Fock state with Chern number $v_C = v_+ - v_-$, where v_+ and v_- denote the occupation for Chern $\pm$ band respectively. And for each pair of Chern $\pm$ band, $\{\tau_{j_1}, s_{j_1}\}$ is unrelated to $\{\tau_{j_2}, s_{j_2}\}$. Therefore, $|\Psi_v^{v_+,v_-}\rangle$ represents a state that fully occupies any v Chern bands.

$$|\Psi_v^{v_+,v_-}\rangle = \prod_{\mathbf{k}} \prod_{j_1=1}^{v_+} \hat{d}^\dagger_{\mathbf{k},+,\tau_{j_1},s_{j_1}} \prod_{j_2=1}^{v_-} \hat{d}^\dagger_{\mathbf{k},-,\tau_{j_2},s_{j_2}} |\text{vac}\rangle \,, \tag{3.43}$$

- The spin-valley polarized Fock state with Chern number $v_C = v_+ - v_-$, which fully occupies or fully emptys valley-spin favors as $\{\tau, s\}$ possible. And for each pair of Chern $\pm$ band, $\{\tau_{j_1}, s_{j_1}\}$ is equal to $\{\tau_{j_2}, s_{j_2}\}$. Therefore, $|\Psi_v^{v_C}\rangle$ represents a state that fully occupies valley-spin avors $\{\tau_j, s_j\}$ for $1 \leq j \leq \min\{v_+, v_-\}$ in both $\pm$ Chern bands.

$$|\Psi_v^{v_C,\text{full}}\rangle = \prod_{\mathbf{k}} \prod_{j=1}^{v_+} \hat{d}^\dagger_{\mathbf{k},+,\tau_j,s_j} \prod_{j=1}^{v_-} \hat{d}^\dagger_{\mathbf{k},-,\tau_j,s_j} |\text{vac}\rangle \,, \tag{3.44}$$

- The spin-valley polarized Fock state with Chern number $v_C = v_+ - v_-$, which half occupies valley-spin favors as $\{\tau, s\}$ possible. And for each pair of Chern $\pm$ band, $\{\tau_{j_1}, s_{j_1}\}$ is different from $\{\tau_{j_2}, s_{j_2}\}$. Therefore, $|\Psi_v^{v_C}\rangle$ represents a state that half occupies valley-spin avors $\{\tau_j, s_j\}$ for $1 \leq j \leq \min\{v_+, v_-\}$ in both $\pm$ Chern bands. Note that where $\{\tau_j, s_j\}$ are the 4 valley-spin favors arbitrarily sorted in j ($1 \leq j \leq 4$).

$$|\Psi_v^{v_C,\text{half}}\rangle = \prod_{\mathbf{k}} \prod_{j=1}^{v_+} \hat{d}^\dagger_{\mathbf{k},+,\tau_j,s_j} \prod_{j=5-v_-}^{4} \hat{d}^\dagger_{\mathbf{k},-,\tau_j,s_j} |\text{vac}\rangle \,, \tag{3.45}$$

- The half-occupied Fock state with Chern number $v_C = 0$. For each pair of Chern $\pm$ bands, it will pick the bands within the same valley. Therefore $|\Psi_v\rangle$ represents a valley-polarized state that fully occupy both two Chern $\pm$ bands within the same valley. This is a special case of $|\Psi_v^{v_C}\rangle$ in half-filling system.

$$|\Psi_v\rangle = \prod_{\mathbf{k}} \prod_{j=1}^{(v+4)/2} \hat{d}^\dagger_{\mathbf{k},+,\tau_j,s} \hat{d}^\dagger_{\mathbf{k},-,\tau_j,s} |\text{vac}\rangle \,. \tag{3.46}$$

- The K-IVC state with Chern number $v_C = 0$, which is fully intervalley coherent.

$$|\Psi_v^{\text{K-IVC}}\rangle = \prod_{\mathbf{k}} \prod_{j=1}^{(v+4)/2} \prod_{n=\pm} \frac{\hat{d}^\dagger_{\mathbf{k},n,\tau_j,s} - n\tau_j \hat{d}^\dagger_{\mathbf{k},n,-\tau_j,s}}{\sqrt{2}} |\text{vac}\rangle \,. \tag{3.47}$$

- The T-IVC state with Chern number $v_C = 0$, which is fully intervalley coherent.

$$|\Psi_v^{\mathrm{T-IVC}}\rangle = \prod_{\mathbf{k}} \prod_{j=1}^{(v+4)/2} \prod_{n=\pm} \frac{\hat{d}^\dagger_{\mathbf{k},n,\tau_j,s} + in\hat{d}^\dagger_{\mathbf{k},n,-\tau_j,s}}{\sqrt{2}} |\mathrm{vac}\rangle \,. \tag{3.48}$$

- The general lowest insulator state with an arbitrary angle γ.

$$\begin{aligned} |\Psi_v^{v_C}\rangle = &\prod_{\mathbf{k}} \prod_{j=1}^{\min(v_+,v_-)} \prod_{n=\pm} \frac{\hat{d}^\dagger_{\mathbf{k},n,\tau_j,s} + e^{i\tau_j\gamma} n\tau_j \hat{d}^\dagger_{\mathbf{k},n,-\tau_j,s}}{\sqrt{2}} \\ &\times \prod_{j=1+\min(v_+,v_-)}^{\max(v_+,v_-)} \hat{d}^\dagger_{\mathbf{k},\mathrm{sgn}(v_C),\tau_j,s_j} |\mathrm{vac}\rangle \,. \end{aligned} \tag{3.49}$$

3.3 Flat Band Assumption and Chiral Symmetry

In this section, we present detailed calculations of the exact ground states, building upon prior work by Lian et al.[58], Bernevig et al.[7], and Xie et al.[108]. We commence our analysis with a flat band assumption. Specifically, we consider the assumption that the flat bands of the BM model are perfectly flat, characterized by zero eigenvalues. Consequently, upon band projection, our resulting Hamiltonian exhibits zero kinetic terms. This allows us to direct our attention solely towards the

interaction terms:

$$
\begin{aligned}
\hat{H}_I =& \frac{1}{2|\Omega|N_{\mathbf{k}}} \sum_{\mathbf{k},\mathbf{k}',\mathbf{k}+\mathbf{q}=\mathbf{k}''\in\Omega^*} \sum_{mnm'n'} \sum_{\mathbf{G}\in\mathbb{L}^*} \sum_{\tau\tau'} \sum_{ss'} V(\mathbf{q}+\mathbf{G}) [\Lambda_{\mathbf{k}}(\mathbf{q}+\mathbf{G})]^{\tau}_{mn} \\
& \times [\Lambda_{\mathbf{k}'}(-\mathbf{q}-\mathbf{G})]^{\tau'}_{m'n'} \hat{c}^{\dagger}_{\mathbf{k},\tau,m,s} \hat{c}^{\dagger}_{\mathbf{k}',\tau',m',s'} \hat{c}_{\mathbf{k}'-\mathbf{q},\tau',n',s'} \hat{c}_{\mathbf{k}+\mathbf{q},\tau,n,s}, \\
=& \frac{1}{2|\Omega|N_{\mathbf{k}}} \sum_{\mathbf{k},\mathbf{k}',\mathbf{k}+\mathbf{q}=\mathbf{k}''\in\Omega^*} \sum_{\mathbf{G}\in\mathbb{L}^*} V(\mathbf{q}+\mathbf{G}) \sum_{mnm'n'} \sum_{\tau\tau'} \sum_{ss'} \\
& \{[\Lambda_{\mathbf{k}}(\mathbf{q}+\mathbf{G})]^{\tau}_{mn} \hat{c}^{\dagger}_{m,\mathbf{k},\tau,s} \hat{c}_{n,\mathbf{k}+\mathbf{q},\tau,s} - N_{\mathbf{k}} A_G \delta_{\mathbf{q},0}\} \\
& \times \{[\Lambda_{\mathbf{k}'}(-\mathbf{q}-\mathbf{G})]^{\tau'}_{m'n'} \hat{c}^{\dagger}_{\mathbf{k}',\tau',m',s'} \hat{c}_{\mathbf{k}'-\mathbf{q},\tau',n',s'} - N_{\mathbf{k}} A_{-G} \delta_{\mathbf{q},0}\}, \\
& + N_{\mathbf{k}} A_G [\Lambda_{\mathbf{k}'}(-\mathbf{G})]^{\tau'}_{m'n'} \hat{c}^{\dagger}_{\mathbf{k}',\tau',m',s'} \hat{c}_{\mathbf{k}',\tau',n',s'} \\
& + N_{\mathbf{k}} A_{-G} [\Lambda_{\mathbf{k}}(\mathbf{G})]^{\tau}_{mn} \hat{c}^{\dagger}_{\mathbf{k},\tau,m,s} \hat{c}_{\mathbf{k},\tau,n,s} - N_{\mathbf{k}}^2 A_G A_{-G} \\
=& \frac{1}{2|\Omega|N_{\mathbf{k}}} \sum_{\mathbf{k},\mathbf{k}',\mathbf{k}+\mathbf{q}=\mathbf{k}''\in\Omega^*} \sum_{\mathbf{G}\in\mathbb{L}^*} V(\mathbf{q}+\mathbf{G}) \sum_{mnm'n'} \sum_{\tau\tau'} \sum_{ss'} \\
& \{[\Lambda_{\mathbf{k}}(\mathbf{q}+\mathbf{G})]^{\tau}_{mn} \hat{c}^{\dagger}_{\mathbf{k},\tau,m,s} \hat{c}_{\mathbf{k}+\mathbf{q},\tau,n,s} - N_{\mathbf{k}} A_G \delta_{\mathbf{q},0}\} \\
& \times \{[\Lambda_{\mathbf{k}'}(-\mathbf{q}-\mathbf{G})]^{\tau'}_{m'n'} \hat{c}^{\dagger}_{\mathbf{k}',\tau',m',s'} \hat{c}_{\mathbf{k}'-\mathbf{q},\tau',n',s'} - N_{\mathbf{k}} A_{-G} \delta_{\mathbf{q},0}\} \\
& + 2N_{\mathbf{k}} A_{-G} [\Lambda_{\mathbf{k}}(\mathbf{G})]^{\tau}_{mn} \hat{c}^{\dagger}_{\mathbf{k},\tau,m,s} \hat{c}_{\mathbf{k},\tau,n,s} - N_{\mathbf{k}}^2 A_G A_{-G},
\end{aligned}
\tag{3.50}
$$

where $N_{\mathbf{k}}$ is the total number of k-grids and A_G can be any G-dependent coefficients. Using the Chern band basis in Eq. (3.42):

$$
\begin{aligned}
\hat{c}^{\dagger}_{\mathbf{k},\tau,\sigma=+1,s} &= \frac{\hat{d}^{\dagger}_{\mathbf{k},+,\tau,s} + \hat{d}^{\dagger}_{\mathbf{k},-,\tau,s}}{\sqrt{2}}, \\
\hat{c}^{\dagger}_{\mathbf{k},\tau,\sigma=-1,s} &= \frac{\hat{d}^{\dagger}_{\mathbf{k},+,\tau,s} - \hat{d}^{\dagger}_{\mathbf{k},-,\tau,s}}{i\sqrt{2}},
\end{aligned}
\tag{3.51}
$$

and the chiral symmetry $\mathcal{C}$: $[H_I, \mathcal{C}] = 0$, the only nonzero terms in Eq. (3.50) are $\hat{d}^{\dagger}_{\mathbf{k},n,\tau,s} \hat{d}_{\mathbf{k}+\mathbf{q},n,\tau,s} \hat{d}^{\dagger}_{\mathbf{k}',n',\tau',s'} \hat{d}_{\mathbf{k}'-\mathbf{q},n',\tau',s'}$. Consequently, the interaction term is transformed into:

$$
\begin{aligned}
\hat{H}_I =& \frac{1}{2|\Omega|N_{\mathbf{k}}} \sum_{\mathbf{k},\mathbf{k}',\mathbf{k}+\mathbf{q}=\mathbf{k}''\in\Omega^*} \sum_{\mathbf{G}\in\mathbb{L}^*} V(\mathbf{q}+\mathbf{G}) \sum_{nn'=\pm} \sum_{\tau\tau'} \sum_{ss'} \\
& \{[\Lambda_{\mathbf{k}}(\mathbf{q}+\mathbf{G})]^{\tau}_{n} \hat{d}^{\dagger}_{\mathbf{k},n,\tau,s} \hat{d}_{\mathbf{k}+\mathbf{q},n,\tau,s} - N_{\mathbf{k}} A_G \delta_{\mathbf{q},0}\} \\
& \times \{[\Lambda_{\mathbf{k}'}(-\mathbf{q}-\mathbf{G})]^{\tau'}_{n'} \hat{d}^{\dagger}_{\mathbf{k}',n',\tau',s'} \hat{d}_{\mathbf{k}'-\mathbf{q},n',\tau',s'} - N_{\mathbf{k}} A_{-G} \delta_{\mathbf{q},0}\} \\
& + 2N_{\mathbf{k}} A_{-G} [\Lambda_{\mathbf{k}}(\mathbf{G})]^{\tau}_{n} \hat{d}^{\dagger}_{\mathbf{k},n,\tau,s} \hat{d}_{\mathbf{k},n,\tau,s} - N_{\mathbf{k}}^2 A_G A_{-G}.
\end{aligned}
\tag{3.52}
$$

The first term in Eq. (3.50) is semi-positive definite, owing to the satisfaction of the symmetry condition by the form factors $\Lambda_{\mathbf{k}}(\mathbf{q}+\mathbf{G})^\dagger = \Lambda_{\mathbf{k}+\mathbf{q}}(-\mathbf{q}-\mathbf{G})$. As $\hat{H}_I$ is a Hermitian operator, the first term is positive semi-definite if and only if it can be expressed as the product of an operator with its conjugate transpose:

$$\begin{aligned}
&\{\sum_{\mathbf{k}} \Lambda_{\mathbf{k}}(\mathbf{q}+\mathbf{G})]_n^\tau \hat{d}^\dagger_{\mathbf{k},n,\tau,s}\hat{d}_{\mathbf{k}+\mathbf{q},n,\tau,s} - N_{\mathbf{k}}A_G\delta_{\mathbf{q},0}\}^\dagger \\
&= \{\sum_{\mathbf{k}'} [\Lambda_{\mathbf{k}'}(-\mathbf{q}-\mathbf{G})]_{n'}^{\tau'} \hat{d}^\dagger_{\mathbf{k}',n',\tau',s'}\hat{d}_{\mathbf{k}'-\mathbf{q},n',\tau',s'} - N_{\mathbf{k}}A_{-G}\delta_{\mathbf{q},0}\}.
\end{aligned}$$

And the last two terms in Eq. (3.50) remain constant under the flat metric condition, which is defined by the equation:

$$\text{Flat Metric Condition:} \qquad [\Lambda_{\mathbf{k}}(\mathbf{G})]^\tau_{\sigma\sigma'} = \xi(\mathbf{G})\delta_{\sigma\sigma'}. \tag{3.53}$$

In the Chern band basis, the matrix elements of $\Lambda_{\mathbf{k}}(\mathbf{G})$ take the form

$$\begin{aligned}
[\Lambda_{\mathbf{k}}(\mathbf{G})]^\tau_{nn'} =& \langle v_{n,\tau,s}(\mathbf{k})|v_{n',\tau,s}(\mathbf{k})\rangle\,, \\
=& \frac{1}{2}\langle u_{\tau,+1,s}(\mathbf{k}) + inu_{\tau,-1,s}(\mathbf{k})|u_{\tau,+1,s}(\mathbf{k}) + in'u_{\tau,-1,s}(\mathbf{k})\rangle\,, \\
=& \frac{1}{2}(\langle u_{\tau,+1,s}(\mathbf{k})|u_{\tau,+1,s}(\mathbf{k})\rangle + nn'\langle u_{\tau,-1,s}(\mathbf{k})|u_{\tau,-1,s}(\mathbf{k})\rangle), \\
=& \frac{1+nn'}{2}\xi(\mathbf{G}) = \delta_{nn'}\xi(\mathbf{G}).
\end{aligned} \tag{3.54}$$

Consequently, we can simplify the form factors as $[\Lambda_{\mathbf{k}}(\mathbf{G})]^\tau_n$ in the Chern band basis. Now, let $v_+, v_- \in [0,4]$ be two integers satisfying $v_+ + v_- = v + 4$, where $\mathbf{k}$ runs over the MBZ. Let $|\text{vac}\rangle$ be the zero-electron state of flat bands, τ_{j_1}, τ_{j_2} be two arbitrarily chosen valleys between $\mathbf{K}$ and $\mathbf{K}'$. We can verify that $|\Psi_v^{v_+,v_-}\rangle$ is a ground state of H_I, utilizing the spin-valley polarized Fock state in Eq. (3.43):

$$\begin{aligned}
&[\Lambda_{\mathbf{k}}(\mathbf{q}+\mathbf{G})]^\tau_n \hat{d}^\dagger_{\mathbf{k},n,\tau,s}\hat{d}_{\mathbf{k}+\mathbf{q},n,\tau,s}\,|\Psi_v^{v_+,v_-}\rangle\,, \\
=&[\Lambda_{\mathbf{k}}(\mathbf{q}+\mathbf{G})]^\tau_n \hat{d}^\dagger_{\mathbf{k},n,\tau,s}\hat{d}_{\mathbf{k}+\mathbf{q},n,\tau,s}\prod_{\mathbf{k}'}\prod_{j_1=1}^{v_+}\hat{d}^\dagger_{\mathbf{k}',+,\tau_{j_1},s_{j_1}}\prod_{j_2=1}^{v_-}\hat{d}^\dagger_{\mathbf{k}',-,\tau_{j_2},s_{j_2}}\,|\text{vac}\rangle\,, \\
=&[\Lambda_{\mathbf{k}}(\mathbf{q}+\mathbf{G})]^\tau_n \hat{d}^\dagger_{\mathbf{k},n,\tau,s}\hat{d}_{\mathbf{k}+\mathbf{q},n,\tau,s}\hat{d}^\dagger_{\mathbf{k},+,\tau_{j_1},s_{j_1}}\hat{d}^\dagger_{\mathbf{k}+\mathbf{q},+,\tau_{j_1},s_{j_1}}\hat{d}^\dagger_{\mathbf{k},-,\tau_{j_2},s_{j_2}}\hat{d}^\dagger_{\mathbf{k}+\mathbf{q},-,\tau_{j_2},s_{j_2}} \\
&\times\prod_{\mathbf{k}'\neq\mathbf{k},\mathbf{k}+\mathbf{q}}\prod_{j_1=1}^{v_+}\hat{d}^\dagger_{\mathbf{k}',+,\tau_{j_1},s_{j_1}}\prod_{j_2=1}^{v_-}\hat{d}^\dagger_{\mathbf{k}',-,\tau_{j_2},s_{j_2}}\,|\text{vac}\rangle\,.
\end{aligned} \tag{3.55}$$

For $\mathbf{q} \neq 0$, we obtain

$$\begin{aligned}
&[\Lambda_{\mathbf{k}}(\mathbf{q}+\mathbf{G})]_n^{\tau}\hat{d}^{\dagger}_{\mathbf{k},n,\tau,s}\hat{d}_{\mathbf{k}+\mathbf{q},n,\tau,s}\left|\Psi_v^{v_+,v_-}\right\rangle,\\
=&[\Lambda_{\mathbf{k}}(\mathbf{q}+\mathbf{G})]_n^{\tau}\hat{d}^{\dagger}_{\mathbf{k},n,\tau,s}\hat{d}^{\dagger}_{\mathbf{k},+,\tau_{j_1},s_{j_1}}\hat{d}^{\dagger}_{\mathbf{k},-,\tau_{j_2},s_{j_2}}\hat{d}_{\mathbf{k}+\mathbf{q},n,\tau,s}\hat{d}^{\dagger}_{\mathbf{k}+\mathbf{q},+,\tau_{j_1},s_{j_1}}\hat{d}^{\dagger}_{\mathbf{k}+\mathbf{q},-,\tau_{j_2},s_{j_2}}\\
&\times\prod_{\mathbf{k}'\neq\mathbf{k},\mathbf{k}+\mathbf{q}}\prod_{j_1=1}^{v_+}\hat{d}^{\dagger}_{\mathbf{k}',+,\tau_{j_1},s_{j_1}}\prod_{j_2=1}^{v_-}\hat{d}^{\dagger}_{\mathbf{k}',-,\tau_{j_2},s_{j_2}}\left|\mathrm{vac}\right\rangle,\\
=&[\Lambda_{\mathbf{k}}(\mathbf{q}+\mathbf{G})]_n^{\tau}\prod_{\mathbf{k}'\neq\mathbf{k},\mathbf{k}+\mathbf{q}}\prod_{j_1=1}^{v_+}\hat{d}^{\dagger}_{\mathbf{k}',+,\tau_{j_1},s_{j_1}}\prod_{j_2=1}^{v_-}\hat{d}^{\dagger}_{\mathbf{k}',-,\tau_{j_2},s_{j_2}}\\
&\times\hat{d}^{\dagger}_{\mathbf{k},n,\tau,s}\hat{d}^{\dagger}_{\mathbf{k},+,\tau_{j_1},s_{j_1}}\hat{d}^{\dagger}_{\mathbf{k},-,\tau_{j_2},s_{j_2}}\hat{d}_{\mathbf{k}+\mathbf{q},n,\tau,s}\hat{d}^{\dagger}_{\mathbf{k}+\mathbf{q},+,\tau_{j_1},s_{j_1}}\hat{d}^{\dagger}_{\mathbf{k}+\mathbf{q},-,\tau_{j_2},s_{j_2}}\left|\mathrm{vac}\right\rangle=0.
\end{aligned}\tag{3.56}$$

There are two possibilities here: a) If $\hat{d}_{\mathbf{k}+\mathbf{q},n,\tau,s}$ commutes with $d^{\dagger}_{\mathbf{k}+\mathbf{q},+,\tau_{j_1},s_{j_1}}$ and $\hat{d}^{\dagger}_{\mathbf{k}+\mathbf{q},-,\tau_{j_2},s_{j_2}}$, then $\hat{d}_{\mathbf{k}+\mathbf{q},n,\tau,s}\left|\mathrm{vac}\right\rangle = 0$; b) If $\hat{d}^{\dagger}_{\mathbf{k},n,\tau,s}$ is the same as $d^{\dagger}_{\mathbf{k},+,\tau_{j_1},s_{j_1}}$ or $\hat{d}^{\dagger}_{\mathbf{k},-,\tau_{j_2},s_{j_2}}$, then we have $\hat{d}^{\dagger}_{\mathbf{k},n,\tau,s}\hat{d}^{\dagger}_{\mathbf{k},+,\tau_{j_1},s_{j_1}}\hat{d}^{\dagger}_{\mathbf{k},-,\tau_{j_2},s_{j_2}}\left|\mathrm{vac}\right\rangle=0$.

For $\mathbf{q}=0$, we obtain

$$\begin{aligned}
&\sum_{\mathbf{k}}\sum_{\tau,n}[\Lambda_{\mathbf{k}}(\mathbf{G})]_n^{\tau}\hat{d}^{\dagger}_{\mathbf{k},n,\tau,s}\hat{d}_{\mathbf{k},n,\tau,s}\left|\Psi_v^{v_+,v_-}\right\rangle,\\
=&\xi(\mathbf{G})\sum_{\mathbf{k}}\sum_{\tau,n}\hat{d}^{\dagger}_{\mathbf{k},n,\tau,s}\hat{d}_{\mathbf{k},n,\tau,s}\left|\Psi_v^{v_+,v_-}\right\rangle=\xi(\mathbf{G})N_{\mathbf{k}}(v+4)\left|\Psi_v^{v_+,v_-}\right\rangle.
\end{aligned}\tag{3.57}$$

Thus, by selecting $A_G = \frac{v+4}{N_{\mathbf{k}}}\xi(\mathbf{G})$, the state $\left|\Psi_v^{v_+,v_-}\right\rangle$ emerges as a ground state of H_I.

3.4 Interaction Term Contribution

When the chiral symmetry is absent in form facotrs, we decompose the nonchiral form factor into its chiral part and nonchiral components, as given by [58, 7, 108]:

$$[\Lambda^c_{\mathbf{k}}(\mathbf{q}+\mathbf{G})]_n^{\tau}=[\Lambda_{\mathbf{k}}(\mathbf{q}+\mathbf{G})]^{\tau}_{n,n},\quad [\Lambda^{nc}_{\mathbf{k}}(\mathbf{q}+\mathbf{G})]_n^{\tau}=[\Lambda_{\mathbf{k}}(\mathbf{q}+\mathbf{G})]^{\tau}_{n,-n}.\tag{3.58}$$

Subsequently, we decompose the nonchiral interaction term $\hat{H}_I$ into its chiral and nonchiral parts:

$$\hat{H}_I=\hat{H}_I^0+(\hat{H}_I^{01}+\hat{H}_I^{10}+\hat{H}_I^{11}),\tag{3.59}$$

with the corresponding creation/annihilation operators:

$$\begin{aligned}
\hat{H}_I^0 &: \hat{d}^\dagger_{\mathbf{k},n,\tau,s}\hat{d}_{\mathbf{k}+\mathbf{q},n,\tau,s}\hat{d}^\dagger_{\mathbf{k}',n',\tau',s'}\hat{d}_{\mathbf{k}'-\mathbf{q},n',\tau',s'} \\
\hat{H}_I^{01} &: \hat{d}^\dagger_{\mathbf{k},n,\tau,s}\hat{d}_{\mathbf{k}+\mathbf{q},n,\tau,s}\hat{d}^\dagger_{\mathbf{k}',-n',\tau',s'}\hat{d}_{\mathbf{k}'-\mathbf{q},n',\tau',s'} \\
\hat{H}_I^{10} &: \hat{d}^\dagger_{\mathbf{k},-n,\tau,s}\hat{d}_{\mathbf{k}+\mathbf{q},n,\tau,s}\hat{d}^\dagger_{\mathbf{k}',n',\tau',s'}\hat{d}_{\mathbf{k}'-\mathbf{q},n',\tau',s'} \\
\hat{H}_I^{11} &: \hat{d}^\dagger_{\mathbf{k},-n,\tau,s}\hat{d}_{\mathbf{k}+\mathbf{q},n,\tau,s}\hat{d}^\dagger_{\mathbf{k}',-n',\tau',s'}\hat{d}_{\mathbf{k}'-\mathbf{q},n',\tau',s'}
\end{aligned} \tag{3.60}$$

An essential relationship between the chiral and nonchiral interaction terms can be expressed as:

$$\begin{aligned}
&(\hat{H}_I^{01} - \hat{H}_I^{10}) \\
&= \frac{1}{2|\Omega|N_{\mathbf{k}}}\sum_{\mathbf{k}\mathbf{k}'\mathbf{q}\mathbf{G}}\sum_{\tau\tau'}\sum_{nn'}\sum_{ss'} V(\mathbf{q}+\mathbf{G})[\Lambda^c_{\mathbf{k}}(\mathbf{q}+\mathbf{G})]^\tau_n[\Lambda^{nc}_{\mathbf{k}'}(-\mathbf{q}-\mathbf{G})]^{\tau'}_{n'} \\
&\times \hat{d}^\dagger_{\mathbf{k},n,\tau,s}\hat{d}_{\mathbf{k}+\mathbf{q},n,\tau,s}\hat{d}^\dagger_{\mathbf{k}',-n',\tau',s'}\hat{d}_{\mathbf{k}'-\mathbf{q},n',\tau',s'} \\
&- \frac{1}{2|\Omega|N_{\mathbf{k}}}\sum_{\mathbf{k}''\mathbf{k}'''\mathbf{q}'\mathbf{G}'}\sum_{\tau''\tau'''}\sum_{n''n'''}\sum_{s''s'''} V(\mathbf{q}'+\mathbf{G}')[\Lambda^{nc}_{\mathbf{k}''}(\mathbf{q}'+\mathbf{G}')]^{\tau''}_{n''}[\Lambda^c_{\mathbf{k}'''}(-\mathbf{q}'-\mathbf{G}')]^{\tau'''}_{n'''} \\
&\times \hat{d}^\dagger_{\mathbf{k}'',-n'',\tau'',s''}\hat{d}_{\mathbf{k}''+\mathbf{q}',n'',\tau'',s''}\hat{d}^\dagger_{\mathbf{k}''',n''',\tau''',s'''}\hat{d}_{\mathbf{k}'''-\mathbf{q}',n''',\tau''',s'''}, \\
&= \frac{1}{2|\Omega|N_{\mathbf{k}}}\sum_{\mathbf{k}\mathbf{k}'\mathbf{q}\mathbf{G}}\sum_{\tau\tau'}\sum_{nn'}\sum_{ss'} V(\mathbf{q}+\mathbf{G}) \\
&\times \{[\Lambda^c_{\mathbf{k}}(\mathbf{q}+\mathbf{G})]^\tau_n[\Lambda^{nc}_{\mathbf{k}'}(-\mathbf{q}-\mathbf{G})]^{\tau'}_{n'} - [\Lambda^{nc}_{\mathbf{k}'}(-\mathbf{q}-\mathbf{G})]^{\tau'}_{n'}[\Lambda^c_{\mathbf{k}}(\mathbf{q}+\mathbf{G})]^\tau_n\} \\
&\times \hat{d}^\dagger_{\mathbf{k},n,\tau,s}\hat{d}_{\mathbf{k}+\mathbf{q},n,\tau,s}\hat{d}^\dagger_{\mathbf{k}',-n',\tau',s'}\hat{d}_{\mathbf{k}'-\mathbf{q},n',\tau',s'}, \\
&= 0,
\end{aligned} \tag{3.61}$$

where the identity

$$
\begin{aligned}
&\frac{1}{2|\Omega|N_{\mathbf{k}}}\sum_{\mathbf{k}''\mathbf{k}'''\mathbf{q}'\mathbf{G}'}\sum_{\tau''\tau'''}\sum_{n''n'''}\sum_{s''s'''}V(\mathbf{q}'+\mathbf{G}')[\Lambda^{nc}_{\mathbf{k}''}(\mathbf{q}'+\mathbf{G}')]^{\tau''}_{n''}[\Lambda^{c}_{\mathbf{k}'''}(-\mathbf{q}'-\mathbf{G}')]^{\tau'''}_{n'''}\\
&\times \hat{d}^{\dagger}_{\mathbf{k}'',-n'',\tau'',s''}\hat{d}_{\mathbf{k}''+\mathbf{q}',n'',\tau'',s''}\hat{d}^{\dagger}_{\mathbf{k}''',n''',\tau''',s'''}\hat{d}_{\mathbf{k}'''-\mathbf{q}',n''',\tau''',s'''},\\
&=\frac{1}{2|\Omega|N_{\mathbf{k}}}\sum_{\mathbf{k}\mathbf{k}'\mathbf{q}\mathbf{G}}\sum_{\tau\tau'}\sum_{nn'}\sum_{ss'}\\
&\sum_{\mathbf{k}''\mathbf{k}'''\mathbf{q}'\mathbf{G}'}\sum_{\tau''\tau'''}\sum_{n''n'''}\sum_{s''s'''}\delta_{\mathbf{k}'',\mathbf{k}'}\delta_{\mathbf{k}''',\mathbf{k}}\delta_{\mathbf{q}',-\mathbf{q}}\delta_{\mathbf{G}',-\mathbf{G}}\delta_{\tau'',\tau'}\delta_{\tau''',\tau}\delta_{n'',n'}\delta_{n''',n}\delta_{s'',s'}\delta_{s''',s}\\
&\times V(\mathbf{q}'+\mathbf{G}')[\Lambda^{nc}_{\mathbf{k}''}(\mathbf{q}'+\mathbf{G}')]^{\tau''}_{n''}[\Lambda^{c}_{\mathbf{k}'''}(-\mathbf{q}'-\mathbf{G}')]^{\tau'''}_{n'''}\\
&\times \hat{d}^{\dagger}_{\mathbf{k}'',-n'',\tau'',s''}\hat{d}_{\mathbf{k}''+\mathbf{q}',n'',\tau'',s''}\hat{d}^{\dagger}_{\mathbf{k}''',n''',\tau''',s'''}\hat{d}_{\mathbf{k}'''-\mathbf{q}',n''',\tau''',s'''}],\\
&=\frac{1}{2|\Omega|N_{\mathbf{k}}}\sum_{\mathbf{k}\mathbf{k}'\mathbf{q}\mathbf{G}}\sum_{\tau\tau'}\sum_{nn'}\sum_{ss'}V(\mathbf{q}+\mathbf{G})[\Lambda^{nc}_{\mathbf{k}'}(-\mathbf{q}-\mathbf{G})]^{\tau'}_{n'}[\Lambda^{c}_{\mathbf{k}}(\mathbf{q}+\mathbf{G})]^{\tau}_{n}\\
&\times \hat{d}^{\dagger}_{\mathbf{k}',-n',\tau',s'}\hat{d}_{\mathbf{k}'-\mathbf{q},n',\tau',s'}\hat{d}^{\dagger}_{\mathbf{k},n,\tau,s}\hat{d}_{\mathbf{k}+\mathbf{q},n,\tau,s},
\end{aligned}
$$

has been utilized.

Note that for interaction terms, we are able to achieve

$$\langle\Psi^{v_+,v_-}_{v}|\hat{d}^{\dagger}_{\mathbf{k},n,\tau,s}\hat{d}_{\mathbf{k}+\mathbf{q},n,\tau,s}\hat{d}^{\dagger}_{\mathbf{k}',-n',\tau',s'}\hat{d}_{\mathbf{k}'-\mathbf{q},n',\tau',s'}|\Psi^{v_+,v_-}_{v}\rangle=0, \tag{3.62}$$

$$\langle\Psi^{v_+,v_-}_{v}|\hat{d}^{\dagger}_{\mathbf{k},-n,\tau,s}\hat{d}_{\mathbf{k}+\mathbf{q},n,\tau,s}\hat{d}^{\dagger}_{\mathbf{k}',n',\tau',s'}\hat{d}_{\mathbf{k}'-\mathbf{q},n',\tau',s'}|\Psi^{v_+,v_-}_{v}\rangle=0, \tag{3.63}$$

$$
\begin{aligned}
&\langle\Psi^{v_+,v_-}_{v}|\hat{d}^{\dagger}_{\mathbf{k},-n,\tau,s}\hat{d}_{\mathbf{k}+\mathbf{q},n,\tau,s}\hat{d}^{\dagger}_{\mathbf{k}',-n',\tau',s'}\hat{d}_{\mathbf{k}'-\mathbf{q},n',\tau',s'}|\Psi^{v_+,v_-}_{v}\rangle\\
&\qquad=\delta_{\mathbf{k},\mathbf{k}'-\mathbf{q}}\delta_{n,-n'}\delta_{s,s'}\delta_{\tau,\tau'}\sum_{(j_1,j_2)}\delta_{\tau_{j_1},-\tau_{j_2}}(\delta_{\tau,\tau_{j_1}}+\delta_{\tau,\tau_{j_2}}),
\end{aligned}
\tag{3.64}
$$

Here, (j_1, j_2) represents the pairs of Chern $\pm$ bands in $|\Psi^{v_+,v_-}_{v}\rangle$.

Next, we provide the proof of the above equations. Starting with the expression for $\hat{d}^{\dagger}_{\mathbf{k}',-n',\tau',s'}\hat{d}_{\mathbf{k}'-\mathbf{q},n',\tau',s'}\,|\Psi^{v_+,v_-}_{v}\rangle$:

$$
\begin{aligned}
&\hat{d}^{\dagger}_{\mathbf{k}',-n',\tau',s'}\hat{d}_{\mathbf{k}'-\mathbf{q},n',\tau',s'}\,|\Psi^{v_+,v_-}_{v}\rangle\,,\\
&=\hat{d}^{\dagger}_{\mathbf{k}',-n',\tau',s'}\hat{d}_{\mathbf{k}'-\mathbf{q},n',\tau',s'}\prod_{\mathbf{k}''}\prod_{j_1=1}^{v_+}\hat{d}^{\dagger}_{\mathbf{k}'',+,\tau_{j_1},s_{j_1}}\prod_{j_2=1}^{v_-}\hat{d}^{\dagger}_{\mathbf{k}'',-,\tau_{j_2},s_{j_2}}\,|\mathrm{vac}\rangle\,,\\
&=(\prod_{\mathbf{k}''\neq\mathbf{k}',\mathbf{k}'-\mathbf{q}}\prod_{j_1=1}^{v_+}\hat{d}^{\dagger}_{\mathbf{k}'',+,\tau_{j_1},s_{j_1}}\prod_{j_2=1}^{v_-}\hat{d}^{\dagger}_{\mathbf{k}'',-,\tau_{j_2},s_{j_2}})\\
&\times\hat{d}^{\dagger}_{\mathbf{k}',-n',\tau',s'}\hat{d}^{\dagger}_{\mathbf{k}',+,\tau_1,s_1}\hat{d}^{\dagger}_{\mathbf{k}',-,\tau_2,s_2}\hat{d}_{\mathbf{k}'-\mathbf{q},n',\tau',s'}\hat{d}_{\mathbf{k}'-\mathbf{q},+,\tau_1,s_1}\hat{d}_{\mathbf{k}'-\mathbf{q},-,\tau_2,s_2}\,|\mathrm{vac}\rangle\,,
\end{aligned}
\tag{3.65}
$$

and for $\langle\Psi_v^{v_+,v_-}|\,\hat{d}^\dagger_{\mathbf{k},n,\tau,s}\hat{d}_{\mathbf{k}+\mathbf{q},n,\tau,s}$:

$$\begin{aligned}
&\langle\Psi_v^{v_+,v_-}|\,\hat{d}^\dagger_{\mathbf{k},n,\tau,s}\hat{d}_{\mathbf{k}+\mathbf{q},n,\tau,s},\\
&=\langle\mathrm{vac}|\prod_{\mathbf{k}''}\prod_{j_1=1}^{v_+}\hat{d}_{\mathbf{k}'',+,\tau_{j_1},s_{j_1}}\prod_{j_2=1}^{v_-}\hat{d}_{\mathbf{k}'',-,\tau_{j_2},s_{j_2}}\hat{d}^\dagger_{\mathbf{k},n,\tau,s}\hat{d}_{\mathbf{k}+\mathbf{q},n,\tau,s},\\
&=\langle\mathrm{vac}|\,\hat{d}^\dagger_{\mathbf{k},n,\tau,s}\hat{d}^\dagger_{\mathbf{k},+,\tau_1,s_1}\hat{d}^\dagger_{\mathbf{k},-,\tau_2,s_2}\hat{d}_{\mathbf{k}+\mathbf{q},n,\tau,s}\hat{d}_{\mathbf{k}+\mathbf{q},+,\tau_1,s_1}\hat{d}_{\mathbf{k}+\mathbf{q},-,\tau_2,s_2}\\
&\times(\prod_{\mathbf{k}''\neq\mathbf{k},\mathbf{k}+\mathbf{q}}\prod_{j_1=1}^{v_+}\hat{d}_{\mathbf{k}'',+,\tau_{j_1},s_{j_1}}\prod_{j_2=1}^{v_-}\hat{d}_{\mathbf{k}'',-,\tau_{j_2},s_{j_2}}).
\end{aligned}\tag{3.66}$$

Therefore, for Eq. (3.62), we obtain

$$\begin{aligned}
&\langle\Psi_v^{v_+,v_-}|\hat{d}^\dagger_{\mathbf{k},n,\tau,s}\hat{d}_{\mathbf{k}+\mathbf{q},n,\tau,s}\hat{d}^\dagger_{\mathbf{k}',-n',\tau',s'}\hat{d}_{\mathbf{k}'-\mathbf{q},n',\tau',s'}|\Psi_v^{v_+,v_-}\rangle\,,\\
&=\langle\mathrm{vac}|\,\hat{d}^\dagger_{\mathbf{k},n,\tau,s}\hat{d}^\dagger_{\mathbf{k},+,\tau_1,s_1}\hat{d}^\dagger_{\mathbf{k},-,\tau_2,s_2}\hat{d}_{\mathbf{k}+\mathbf{q},n,\tau,s}\hat{d}_{\mathbf{k}+\mathbf{q},+,\tau_1,s_1}\hat{d}_{\mathbf{k}+\mathbf{q},-,\tau_2,s_2}\\
&\times(\prod_{\mathbf{k}''\neq\mathbf{k},\mathbf{k}+\mathbf{q}}\prod_{j_1=1}^{v_+}\hat{d}_{\mathbf{k}'',+,\tau_{j_1},s_{j_1}}\prod_{j_2=1}^{v_-}\hat{d}_{\mathbf{k}'',-,\tau_{j_2},s_{j_2}})\\
&\times(\prod_{\mathbf{k}''\neq\mathbf{k}',\mathbf{k}'-\mathbf{q}}\prod_{j_1=1}^{v_+}\hat{d}^\dagger_{\mathbf{k}'',+,\tau'_{j_1},s'_{j_1}}\prod_{j_2=1}^{v_-}\hat{d}^\dagger_{\mathbf{k}'',-,\tau'_{j_2},s'_{j_2}})\\
&\times\hat{d}^\dagger_{\mathbf{k}',-n',\tau',s'}\hat{d}^\dagger_{\mathbf{k}',+,\tau'_1,s'_1}\hat{d}^\dagger_{\mathbf{k}',-,\tau'_2,s'_2}\hat{d}_{\mathbf{k}'-\mathbf{q},n',\tau',s'}\hat{d}_{\mathbf{k}'-\mathbf{q},+,\tau'_1,s'_1}\hat{d}_{\mathbf{k}'-\mathbf{q},-,\tau'_2,s'_2}\,|\mathrm{vac}\rangle\,,\\
&=\delta_{\mathbf{k},\mathbf{k}'-\mathbf{q}}\,\langle\mathrm{vac}|\,\hat{d}^\dagger_{\mathbf{k},n,\tau,s}\hat{d}^\dagger_{\mathbf{k},+,\tau_1,s_1}\hat{d}^\dagger_{\mathbf{k},-,\tau_2,s_2}\hat{d}^\dagger_{\mathbf{k}',-n',\tau',s'}\hat{d}^\dagger_{\mathbf{k}',+,\tau'_1,s'_1}\hat{d}^\dagger_{\mathbf{k}',-,\tau'_2,s'_2}\\
&\times\hat{d}_{\mathbf{k}+\mathbf{q},n,\tau,s}\hat{d}_{\mathbf{k}+\mathbf{q},+,\tau_1,s_1}\hat{d}_{\mathbf{k}+\mathbf{q},-,\tau_2,s_2}\hat{d}_{\mathbf{k}'-\mathbf{q},n',\tau',s'}\hat{d}_{\mathbf{k}'-\mathbf{q},+,\tau'_1,s'_1}\hat{d}_{\mathbf{k}'-\mathbf{q},-,\tau'_2,s'_2}\,|\mathrm{vac}\rangle\,,\\
&=\delta_{\mathbf{k},\mathbf{k}'-\mathbf{q}}\delta_{n,-n'}\delta_{n,n'}\cdots=0.
\end{aligned}\tag{3.67}$$

Similarly, for Eq. (3.63), we obtain

$$\begin{aligned}
&\langle\Psi_v^{v_+,v_-}|\hat{d}^\dagger_{\mathbf{k},-n,\tau,s}\hat{d}_{\mathbf{k}+\mathbf{q},n,\tau,s}\hat{d}^\dagger_{\mathbf{k}',n',\tau',s'}\hat{d}_{\mathbf{k}'-\mathbf{q},n',\tau',s'}|\Psi_v^{v_+,v_-}\rangle\\
&=\delta_{\mathbf{k},\mathbf{k}'-\mathbf{q}}\,\langle\mathrm{vac}|\,\hat{d}^\dagger_{\mathbf{k},-n,\tau,s}\hat{d}^\dagger_{\mathbf{k},+,\tau_1,s_1}\hat{d}^\dagger_{\mathbf{k},-,\tau_2,s_2}\hat{d}^\dagger_{\mathbf{k}',n',\tau',s'}\hat{d}^\dagger_{\mathbf{k}',+,\tau'_1,s'_1}\hat{d}^\dagger_{\mathbf{k}',-,\tau'_2,s'_2}\\
&\times\hat{d}_{\mathbf{k}+\mathbf{q},n,\tau,s}\hat{d}_{\mathbf{k}+\mathbf{q},+,\tau_1,s_1}\hat{d}_{\mathbf{k}+\mathbf{q},-,\tau_2,s_2}\hat{d}_{\mathbf{k}'-\mathbf{q},n',\tau',s'}\hat{d}_{\mathbf{k}'-\mathbf{q},+,\tau'_1,s'_1}\hat{d}_{\mathbf{k}'-\mathbf{q},-,\tau'_2,s'_2}\,|\mathrm{vac}\rangle\,,\\
&=\delta_{\mathbf{k},\mathbf{k}'-\mathbf{q}}\delta_{n,n'}\delta_{n,-n'}\cdots=0.
\end{aligned}\tag{3.68}$$

Finally, for Eq. (3.64), we obtain

$$\begin{aligned}
&\langle\Psi_v^{v_+,v_-}|\hat{d}^\dagger_{\mathbf{k},-n,\tau,s}\hat{d}_{\mathbf{k}+\mathbf{q},n,\tau,s}\hat{d}^\dagger_{\mathbf{k}',-n',\tau',s'}\hat{d}_{\mathbf{k}'-\mathbf{q},n',\tau',s'}|\Psi_v^{v_+,v_-}\rangle \\
&= \delta_{\mathbf{k},\mathbf{k}'-\mathbf{q}}\langle\mathrm{vac}|\,\hat{d}^\dagger_{\mathbf{k},-n,\tau,s}\hat{d}^\dagger_{\mathbf{k},+,\tau_1,s_1}\hat{d}^\dagger_{\mathbf{k},-,\tau_2,s_2}\hat{d}^\dagger_{\mathbf{k}',-n',\tau',s'}\hat{d}^\dagger_{\mathbf{k}',+,\tau_1',s_1'}\hat{d}^\dagger_{\mathbf{k}',-,\tau_2',s_2'} \\
&\times \hat{d}_{\mathbf{k}+\mathbf{q},n,\tau,s}\hat{d}_{\mathbf{k}+\mathbf{q},+,\tau_1,s_1}\hat{d}_{\mathbf{k}+\mathbf{q},-,\tau_2,s_2}\hat{d}_{\mathbf{k}'-\mathbf{q},n',\tau',s'}\hat{d}_{\mathbf{k}'-\mathbf{q},+,\tau_1',s_1'}\hat{d}_{\mathbf{k}'-\mathbf{q},-,\tau_2',s_2'}\,|\mathrm{vac}\rangle\,, \\
&= \delta_{\mathbf{k},\mathbf{k}'-\mathbf{q}}\delta_{n,-n'}\delta_{s,s'}\delta_{\tau,\tau'}\sum_{(j_1,j_2)}\delta_{\tau_{j_1},-\tau_{j_2}}(\delta_{\tau,\tau_{j_1}}+\delta_{\tau,\tau_{j_2}}),
\end{aligned} \tag{3.69}$$

where the sum over j only includes the spin-valley favors $\{\tau_j, s_j\}$ that only either the $n = +$ or $n = -$ Chern band basis are occupied, namely, half occupied.

Then the first-order energy contribution of the non-chiral part is expressed as

$$\begin{aligned}
E^{(1)}_{v,v_C} &= \langle\Psi_v^{v_+,v_-}|\hat{H}_I^{01}+\hat{H}_I^{10}+\hat{H}_I^{11}|\Psi_v^{v_+,v_-}\rangle\,, \\
&= \langle\Psi_v^{v_+,v_-}|\hat{H}_I^{11}|\Psi_v^{v_+,v_-}\rangle\,, \\
&= \frac{1}{2|\Omega|N_{\mathbf{k}}}\sum_{\mathbf{k}\mathbf{k}'\mathbf{q}}\sum_{\mathbf{G}}V(\mathbf{q}+\mathbf{G})\sum_{nn'}\sum_{\tau\tau'}[\Lambda^{nc}_{\mathbf{k}}(\mathbf{q}+\mathbf{G})]^\tau_n[\Lambda^{nc}_{\mathbf{k}'}(-\mathbf{q}-\mathbf{G})]^{\tau'}_{n'} \\
&\times \delta_{\mathbf{k},\mathbf{k}'-\mathbf{q}}\delta_{n,-n'}\delta_{\tau,\tau'}\sum_{(j_1,j_2)}\delta_{\tau_{j_1},-\tau_{j_2}}(\delta_{\tau,\tau_{j_1}}+\delta_{\tau,\tau_{j_2}}), \\
&= \frac{1}{2|\Omega|N_{\mathbf{k}}}\sum_{\mathbf{k}\mathbf{q}\mathbf{G}}V(\mathbf{q}+\mathbf{G})\sum_{\tau n}[\Lambda^{nc}_{\mathbf{k}}(\mathbf{q}+\mathbf{G})]^\tau_n[\Lambda^{nc}_{\mathbf{k}+\mathbf{q}}(-\mathbf{q}-\mathbf{G})]^\tau_{-n} \\
&\times \sum_{(j_1,j_2)}\delta_{\tau_{j_1},-\tau_{j_2}}(\delta_{\tau,\tau_{j_1}}+\delta_{\tau,\tau_{j_2}}), \\
&= \frac{1}{2|\Omega|N_{\mathbf{k}}}\sum_{\mathbf{k}\mathbf{q}\mathbf{G}}V(\mathbf{q}+\mathbf{G})\sum_{\tau n}|[\Lambda^{nc}_{\mathbf{k}}(\mathbf{q}+\mathbf{G})]^\tau_n|^2\sum_{(j_1,j_2)}\delta_{\tau_{j_1},-\tau_{j_2}}(\delta_{\tau,\tau_{j_1}}+\delta_{\tau,\tau_{j_2}}), \\
\Longrightarrow\ & E^{(1)}_{v,v_c}\geq 0,
\end{aligned} \tag{3.70}$$

where $E^{(1)}_{v,v_C} = 0$ only if either the $n = +$ or $n = -$ Chern band basis is occupied, namely half occupied. If both Chern basis bands of valley τ are occupied or empty,

$E^{(1)}_{v,v_C}$ will be zero. In this case, we have:

$$\begin{aligned} E^{(1)}_{v,v_C} &= \frac{1}{2|\Omega|N_{\mathbf{k}}} \sum_{\mathbf{kqG}} V(\mathbf{q}+\mathbf{G}) \sum_{\tau n} |[\Lambda^{nc}_{\mathbf{k}}(\mathbf{q}+\mathbf{G})]^{\tau}_{n}|^2 \sum_{(j_1,j_2)} \delta_{\tau_{j_1},-\tau_{j_2}} (\delta_{\tau,\tau_{j_1}} + \delta_{\tau,\tau_{j_2}}), \\ &= \frac{1}{2|\Omega|N_{\mathbf{k}}} \sum_{\mathbf{kqG}} V(\mathbf{q}+\mathbf{G}) \sum_{\tau n} |[\Lambda^{nc}_{\mathbf{k}}(\mathbf{q}+\mathbf{G})]^{\tau}_{n}|^2 N_{\mathbf{k}}, \\ &= \frac{1}{2|\Omega|} \sum_{\mathbf{kqG}} V(\mathbf{q}+\mathbf{G}) \sum_{\tau n} |[\Lambda^{nc}_{\mathbf{k}}(\mathbf{q}+\mathbf{G})]^{\tau}_{n}|^2. \end{aligned} \tag{3.71}$$

This expression indicates that $E^{(1)}_{v,v_C}$ is greater than or equal to zero.

In a half-filling system, the state of the system at half occupancy is represented by the half-occupied Fock state $|\Psi_v\rangle$, given by the expression:

$$|\Psi_v\rangle = \prod_{\mathbf{k}} \prod_{j=1}^{(v+4)/2} \hat{d}^{\dagger}_{\mathbf{k},+,\tau_j,s_j} \hat{d}^{\dagger}_{\mathbf{k},-,\tau_j,s_j} |\mathrm{vac}\rangle \,.$$

This expression represents the exact ground state up to the second perturbation theory, as discussed in detail by Lian et al.[58], Bernevig et al.[7], and Xie et al.[108].

We denote $E^{0}_{v,v_C=0} = \langle\Psi_v|\hat{H}^{0}_{I} + \hat{H}^{11}_{I}|\Psi_v\rangle$ as the energy of state $|\Psi_v\rangle$. The second-order contribution of the terms $\hat{H}^{01}_{I} + \hat{H}^{10}_{I}$ is then given by

$$E^{(2)}_{v,v_C=0} = \langle\Psi_v|(\hat{H}^{01}_{I} + \hat{H}^{10}_{I})(E^{0}_{v,v_C=0} - \hat{H}^{0}_{I})^{-1}(\hat{H}^{01}_{I} + \hat{H}^{10}_{I})|\Psi_v\rangle \,. \tag{3.72}$$

Using the relations in Eq. (3.56) and Eq. (3.57), we can obtain

$$\begin{aligned}
\hat{H}_I^{10}\left|\Psi_v\right\rangle &= \frac{1}{2|\Omega|N_{\mathbf{k}}}\sum_{\mathbf{k}\mathbf{k}'\mathbf{q}\mathbf{G}}\sum_{\tau\tau'}\sum_{nn'}\sum_{ss'}V(\mathbf{q}+\mathbf{G})[\Lambda^{nc}_{\mathbf{k}}(\mathbf{q}+\mathbf{G})]^{\tau}_{n}[\Lambda^{c}_{\mathbf{k}'}(-\mathbf{q}-\mathbf{G})]^{\tau'}_{n'} \\
&\times \hat{d}^{\dagger}_{\mathbf{k},-n,\tau,s}\hat{d}_{\mathbf{k}+\mathbf{q},n,\tau,s}\hat{d}^{\dagger}_{\mathbf{k}',n',\tau',s'}\hat{d}_{\mathbf{k}'-\mathbf{q},n',\tau',s'}\left|\Psi_v\right\rangle, \\
&= \frac{1}{2|\Omega|N_{\mathbf{k}}}\sum_{\mathbf{k}\mathbf{k}'\mathbf{q}\mathbf{G}}\sum_{\tau\tau'}\sum_{nn'}\sum_{ss'}V(\mathbf{q}+\mathbf{G})[\Lambda^{nc}_{\mathbf{k}}(\mathbf{q}+\mathbf{G})]^{\tau}_{n}[\Lambda^{c}_{\mathbf{k}'}(-\mathbf{q}-\mathbf{G})]^{\tau'}_{n'} \\
&\times \hat{d}^{\dagger}_{\mathbf{k},-n,\tau,s}\hat{d}_{\mathbf{k}+\mathbf{q},n,\tau,s}\hat{d}^{\dagger}_{\mathbf{k}',n',\tau',s'}\hat{d}_{\mathbf{k}'-\mathbf{q},n',\tau',s'}\prod_{\mathbf{k}''}\prod_{j=1}^{(v+4)/2}\hat{d}^{\dagger}_{\mathbf{k}'',+,\tau_j,s_j}\hat{d}^{\dagger}_{\mathbf{k}'',-,\tau_j,s_j}\left|\mathrm{vac}\right\rangle, \\
&= \frac{1}{2|\Omega|N_{\mathbf{k}}}\sum_{\mathbf{k}\mathbf{k}'\mathbf{q}\mathbf{G}}\sum_{\tau\tau'}\sum_{nn'}\sum_{ss'}V(\mathbf{q}+\mathbf{G})[\Lambda^{nc}_{\mathbf{k}}(\mathbf{q}+\mathbf{G})]^{\tau}_{n}[\Lambda^{c}_{\mathbf{k}'}(-\mathbf{q}-\mathbf{G})]^{\tau'}_{n'} \\
&\times \hat{d}^{\dagger}_{\mathbf{k},-n,\tau,s}\hat{d}_{\mathbf{k}+\mathbf{q},n,\tau,s}\delta_{\mathbf{q},0}\prod_{\mathbf{k}''}\delta_{\mathbf{k}'',\mathbf{k}'}\prod_{j=1}^{(v+4)/2}\delta_{\tau',\tau_j}\delta_{s',s_j}\hat{d}^{\dagger}_{\mathbf{k}'',+,\tau_j,s_j}\hat{d}^{\dagger}_{\mathbf{k}'',-,\tau_j,s_j}\left|\mathrm{vac}\right\rangle, \\
&= \frac{1}{2|\Omega|N_{\mathbf{k}}}\sum_{\mathbf{G}}V(\mathbf{G})\sum_{\mathbf{k}\tau n}[\Lambda^{nc}_{\mathbf{k}}(\mathbf{G})]^{\tau}_{n} \\
&\times \hat{d}^{\dagger}_{\mathbf{k},-n,\tau,s}\hat{d}_{\mathbf{k},n,\tau,s}(\xi(\mathbf{G})\cdot N_{\mathbf{k}}\cdot\frac{v+4}{2}\cdot 2)\left|\Psi_v\right\rangle, \\
&= \frac{v+4}{2|\Omega|}\sum_{\mathbf{G}}V(\mathbf{G})\xi(\mathbf{G})\sum_{\mathbf{k}\tau n}[\Lambda^{nc}_{\mathbf{k}}(\mathbf{G})]^{\tau}_{n}\hat{d}^{\dagger}_{\mathbf{k},-n,\tau,s}\hat{d}_{\mathbf{k},n,\tau,s}\left|\Psi_v\right\rangle.
\end{aligned} \tag{3.73}$$

Utilizing the flat band assumption, we find that the nonchiral part of the form factor at $\mathbf{q}=0$ is zero for the state $|\Psi_v\rangle$:

$$[\Lambda^{nc}_{\mathbf{k}}(\mathbf{G})]^{\tau}_{n} = [\Lambda_{\mathbf{k}}(\mathbf{G})]^{\tau}_{n,-n} = 0. \tag{3.74}$$

Consequently, the action of the operator $\hat{H}_I^{10}$ becomes trivial:

$$\hat{H}_I^{10}\left|\Psi_v\right\rangle = 0,\ \hat{H}_I^{01}\left|\Psi_v\right\rangle = 0 \implies E^{(2)}_{v,v_C=0} = 0. \tag{3.75}$$

and similarly, using Eq. (3.61), the action of $\hat{H}_I^{01}$ is also trivial:

$$\hat{H}_I^{01}\left|\Psi_v\right\rangle = \hat{H}_I^{10}\left|\Psi_v\right\rangle = 0. \tag{3.76}$$

This implies that the second-order contribution to the energy, $E^{(2)}_{v,v_C=0}$, is zero for the state $|\Psi_v\rangle$:

$$E^{(2)}_{v,v_C=0} = \langle\Psi_v|(\hat{H}_I^{01}+\hat{H}_I^{10})(E^{0}_{v,v_C=0}-\hat{H}_I^{0})^{-1}(\hat{H}_I^{01}+\hat{H}_I^{10})|\Psi_v\rangle = 0. \tag{3.77}$$

With the flat band assumption, the eigenstate function $|\Psi_v\rangle$ serves as the exact ground state, accurate up to second-order perturbation theory, within the half-filling system. Now, we transition to exploring the general spin-valley polarized Fock state, which encompasses nonzero Chern numbers $|\Psi_v^{v_+,v_-}\rangle$:

$$
\begin{aligned}
&\hat{H}_I^{10}\,|\Psi_v^{v_+,v_-}\rangle\,,\\
&=\frac{1}{2|\Omega|N_{\mathbf{k}}}\sum_{\mathbf{k}\mathbf{k}'\mathbf{q}\mathbf{G}}\sum_{\tau\tau'}\sum_{nn'}V(\mathbf{q}+\mathbf{G})[\Lambda_{\mathbf{k}}^{nc}(\mathbf{q}+\mathbf{G})]_n^{\tau}[\Lambda_{\mathbf{k}'}^{c}(-\mathbf{q}-\mathbf{G})]_{n'}^{\tau'}\\
&\times\hat{d}^{\dagger}_{\mathbf{k},-n,\tau,s}\hat{d}_{\mathbf{k}+\mathbf{q},n,\tau,s}\hat{d}^{\dagger}_{\mathbf{k}',n',\tau',s'}\hat{d}_{\mathbf{k}'-\mathbf{q},n',\tau',s'}\,|\Psi_v^{v_+,v_-}\rangle\,,\\
&=\frac{1}{2|\Omega|N_{\mathbf{k}}}\sum_{\mathbf{k}\mathbf{k}'\mathbf{q}\mathbf{G}}\sum_{\tau\tau'}\sum_{nn'}\sum_{ss'}V(\mathbf{q}+\mathbf{G})[\Lambda_{\mathbf{k}}^{nc}(\mathbf{q}+\mathbf{G})]_n^{\tau}[\Lambda_{\mathbf{k}'}^{c}(-\mathbf{q}-\mathbf{G})]_{n'}^{\tau'}\\
&\times\hat{d}^{\dagger}_{\mathbf{k},-n,\tau,s}\hat{d}_{\mathbf{k}+\mathbf{q},n,\tau,s}\hat{d}^{\dagger}_{\mathbf{k}',n',\tau',s'}\hat{d}_{\mathbf{k}'-\mathbf{q},n',\tau',s'}\prod_{\mathbf{k}''}\prod_{j_1=1}^{v_+}\hat{d}^{\dagger}_{\mathbf{k}'',+,\tau_{j_1},s_{j_1}}\prod_{j_2=1}^{v_-}\hat{d}^{\dagger}_{\mathbf{k}'',-,\tau_{j_2},s_{j_2}}\,|\mathrm{vac}\rangle\,,\\
&=\frac{1}{2|\Omega|N_{\mathbf{k}}}\sum_{\mathbf{k}\mathbf{k}'\mathbf{q}\mathbf{G}}\sum_{\tau\tau'}\sum_{nn'}\sum_{ss'}V(\mathbf{q}+\mathbf{G})[\Lambda_{\mathbf{k}}^{nc}(\mathbf{q}+\mathbf{G})]_n^{\tau}[\Lambda_{\mathbf{k}'}^{c}(-\mathbf{q}-\mathbf{G})]_{n'}^{\tau'}\\
&\times\hat{d}^{\dagger}_{\mathbf{k},-n,\tau,s}\hat{d}_{\mathbf{k}+\mathbf{q},n,\tau,s}\delta_{\mathbf{q},0}\prod_{\mathbf{k}''}\delta_{\mathbf{k}'',\mathbf{k}'}\prod_{j_1=1}^{v_+}\hat{d}^{\dagger}_{\mathbf{k}'',+,\tau_{j_1},s_{j_1}}\prod_{j_2=1}^{v_-}\hat{d}^{\dagger}_{\mathbf{k}'',-,\tau_{j_2},s_{j_2}}\,|\mathrm{vac}\rangle\,,\\
&=\frac{1}{2|\Omega|N_{\mathbf{k}}}\sum_{\mathbf{G}}V(\mathbf{G})\sum_{\mathbf{k}\tau n}[\Lambda_{\mathbf{k}}^{nc}(\mathbf{G})]_n^{\tau}\\
&\times\hat{d}^{\dagger}_{\mathbf{k},-n,\tau,s}\hat{d}_{\mathbf{k},n,\tau,s}(\xi(\mathbf{G})\cdot N_{\mathbf{k}}\cdot\frac{v+4}{2}\cdot 2)\,|\Psi_v^{v_+,v_-}\rangle\,,\\
&=\frac{v+4}{2|\Omega|}\sum_{\mathbf{G}}V(\mathbf{G})\xi(\mathbf{G})\sum_{\mathbf{k}\tau n}[\Lambda_{\mathbf{k}}^{nc}(\mathbf{G})]_n^{\tau}\hat{d}^{\dagger}_{\mathbf{k},-n,\tau,s}\hat{d}_{\mathbf{k},n,\tau,s}\,|\Psi_v^{v_+,v_-}\rangle\,,\\
&=\frac{1}{2|\Omega|N_{\mathbf{k}}}\sum_{\mathbf{G}}V(\mathbf{G})\xi(\mathbf{G})N_{\mathbf{k}}(v+4)\sum_{\mathbf{k}\tau n}[\Lambda_{\mathbf{k}}^{nc}(\mathbf{G})]_n^{\tau}\\
&\times\hat{d}^{\dagger}_{\mathbf{k},-n,\tau,s}\hat{d}_{\mathbf{k},n,\tau,s}\,|\Psi_v^{v_+,v_-}\rangle\,,\\
&=\frac{v+4}{2|\Omega|}\sum_{\mathbf{G}}V(\mathbf{G})\xi(\mathbf{G})\sum_{\mathbf{k}\tau n}[\Lambda_{\mathbf{k}}^{nc}(\mathbf{G})]_n^{\tau}\hat{d}^{\dagger}_{\mathbf{k},-n,\tau,s}\hat{d}_{\mathbf{k},n,\tau,s}\,|\Psi_v^{v_+,v_-}\rangle\,,
\end{aligned}
\tag{3.78}
$$

which is nonzero. Therefore, for any excited eigenstates from the ground eigenstate

$|\Psi_v^{v_+,v_-}\rangle$ at energies $\langle\Psi_{v,\mathrm{mid}}^{v_+,v_-}|\hat{H}_I^0|\Psi_{v,\mathrm{mid}}^{v_+,v_-}\rangle \geq \langle\Psi_v|\hat{H}_I^0|\Psi_v^{v_+,v_-}\rangle$, we have

$$\begin{aligned}
&\langle\Psi_{\mathrm{mid}}^{v_+,v_-}|\hat{H}_I^{10}|\Psi_v^{v_+,v_-}\rangle\,,\\
&=\frac{v+4}{2|\Omega|}\sum_{\mathbf{G}}V(\mathbf{G})\xi(\mathbf{G})\sum_{\mathbf{k}\tau n}[\Lambda_{\mathbf{k}}^{nc}(\mathbf{G})]_n^\tau\,\langle\Psi_{\mathrm{mid}}^{v_+,v_-}|\hat{d}^\dagger_{\mathbf{k},-n,\tau,s}\hat{d}_{\mathbf{k},n,\tau,s}|\Psi_v^{v_+,v_-}\rangle\,,\\
&=\frac{v+4}{2|\Omega|}\sum_{\mathbf{G}}V(\mathbf{G})\xi(\mathbf{G})\sum_{\mathbf{k}\tau}([\Lambda_{\mathbf{k}}^{nc}(\mathbf{G})]_+^\tau\prod_{j_1}\delta_{\tau,\tau_{j_1}}\delta_{\tau,-\tau_{j_2}}+[\Lambda_{\mathbf{k}}^{nc}(\mathbf{G})]_-^\tau\prod_{j_2}\delta_{\tau,\tau_{j_2}}\delta_{\tau,-\tau_{j_1}}),\\
&=\frac{v+4}{2|\Omega|}\sum_{\mathbf{G}}V(\mathbf{G})\xi(\mathbf{G})\sum_{\mathbf{k}\tau}([\Lambda_{\mathbf{k}}^{nc}(\mathbf{G})]_+^\tau+[\Lambda_{\mathbf{k}}^{nc}(\mathbf{G})]_-^\tau)\prod_{j_1}\delta_{\tau,\tau_{j_1}}\delta_{\tau,-\tau_{j_2}},\\
&\sim(v+4)\text{ or }0,
\end{aligned}\tag{3.79}$$

which is nonzero only if the excited state is a half-occupied state since our ground state is also a half-occupied state due to the first-order perturbation energy. Then for the denominator, we have

$$\begin{aligned}
&E_{v,v_C=v_+-v_-}^0-\langle\Psi_{v,\mathrm{mid}}^{v_+,v_-}|\hat{H}_I^0|\Psi_{v,\mathrm{mid}}^{v_+,v_-}\rangle\,,\\
&=\langle\Psi_v|\hat{H}_I^0+\hat{H}_I^{11}|\Psi_v\rangle-\langle\Psi_{v,\mathrm{mid}}^{v_+,v_-}|\hat{H}_I^0|\Psi_{v,\mathrm{mid}}^{v_+,v_-}\rangle\,,\\
&=E_{v,v_C}^{(1)}-(\langle\Psi_{v,\mathrm{mid}}^{v_+,v_-}|\hat{H}_I^0|\Psi_{v,\mathrm{mid}}^{v_+,v_-}\rangle-\langle\Psi_v|\hat{H}_I^0|\Psi_v\rangle),\\
&=E_{v,v_C}^{(1)}-E_{\mathrm{gap}}<0,
\end{aligned}\tag{3.80}$$

which is the sum of the first-order perturbation energy and the energy gap between the excited and ground state. As a result, this term is smaller than zero.

Then we can define the second-order perturbation energy as

$$\begin{aligned}
E_{v,v_C=v_+-v_-}^{(2)}&=\langle\Psi_v|(\hat{H}_I^{01}+\hat{H}_I^{10})(E_{v,v_C}^0-\hat{H}_I^0)^{-1}(\hat{H}_I^{01}+\hat{H}_I^{10})|\Psi_v\rangle\,,\\
&=-\sum_{\mathrm{mid}}\frac{|\,\langle\Psi_{v,\mathrm{mid}}^{v_+,v_-}|\hat{H}_I^{01}+\hat{H}_I^{10}|\Psi_v^{v_+,v_-}\rangle\,|^2}{E_{\mathrm{gap}}-E_{v,v_C}^{(1)}},\\
&=-\frac{(v+4)^2}{4|\Omega|^2}\sum_{\mathrm{mid}}\frac{1}{E_{\mathrm{gap}}-E_{v,v_C}^{(1)}}(\sum_{\mathbf{G}}V(\mathbf{G})\xi(\mathbf{G})\sum_{\mathbf{k}\tau n}[\Lambda_{\mathbf{k}}^{nc}(\mathbf{G})]_n^\tau)^2,\\
&\sim-(v+4)^2<0.
\end{aligned}\tag{3.81}$$

Consequently, the total perturbation energy is given by:

$$E_{v,v_C}=E_{v,v_C}^{(1)}+E_{v,v_C}^{(2)}\geq 0,\tag{3.82}$$

where the terms $E^{(1)}_{v,v_C}$ and $E^{(2)}_{v,v_C}$ are only nonzero for half-occupied states. Numerical calculation demonstrate that $E_{v,v_C} \geq 0$ for any $0 \leq w_0/w_1 \leq 1$ and $-3 \leq v \leq 3$.

As a result of the perturbation theory, Chern insulator states with $|v| \leq 3$ tend to fully occupied or fully empty to maximize the number of spin-valley flavors. Therefore, the fully-occupied Fock state $|\Psi_v\rangle$ is the exact ground state in the half-filling system, even without the flat band assumption. In general, in other case, exact ground states can written as [58, 7, 108]:

$$|\Psi_v^{v_C,\text{full}}\rangle = \prod_{\mathbf{k}} \prod_{j=1}^{v_+} \hat{d}^\dagger_{\mathbf{k},+,\tau_j,s_j} \prod_{j=1}^{v_-} \hat{d}^\dagger_{\mathbf{k},-,\tau_j,s_j} |\text{vac}\rangle \,.$$

3.5 Kinetic Term Contribution

In this section, we turn off the chiral symmetry again and discuss the corresponding perturbation energies in the kinetic terms ([58, 7, 108]):

$$\hat{H}_0 = \sum_{\mathbf{k}\sigma\tau s} \epsilon_{\sigma\tau}(\mathbf{k}) \hat{c}^\dagger_{\mathbf{k},\tau,\sigma,s} \hat{c}_{\mathbf{k},\tau,\sigma,s}, \tag{3.83}$$

where $\hat{c}^\dagger_{\mathbf{k},\tau,\sigma,s}/\hat{c}_{\mathbf{k},\tau,\sigma,s}$ are the creation/annihilation operators in the BM band basis, respectively, and $\epsilon_{n\tau}(\mathbf{k})$ denotes the single-particle energy from the BM band structure. Due to the symmetries of the BM model, including the commutation relations with C_{2z} symmetry, time-reversal symmetry $\mathcal{T}$, and the anti-commutation relations with the particle-hole symmetry $\mathcal{P}$:

$$[\hat{H}_0, C_{2z}] = \{\hat{H}_0,\ \mathcal{P}\} = 0, \tag{3.84}$$

then the BM energy bands satisfy

$$\epsilon_{\sigma,\tau}(\mathbf{k}) = \epsilon_{\sigma,-\tau}(-\mathbf{k}) = -\epsilon_{-\sigma,\tau}(-\mathbf{k}) = -\epsilon_{-\sigma,-\tau}(\mathbf{k}) = \epsilon_{\sigma,-\tau}(\mathbf{k}). \tag{3.85}$$

As a result, we can rewrite the kinetic term as

$$\begin{aligned}
\hat{H}_0 &= \sum_{\mathbf{k}\sigma\tau s} \epsilon_{\sigma\tau}(\mathbf{k}) \hat{c}^\dagger_{\mathbf{k},\tau,\sigma,s} \hat{c}_{\mathbf{k},\tau,\sigma,s}, \\
&= \sum_{\mathbf{k}\sigma\tau s} \epsilon_{\sigma,+1}(\mathbf{k}) \hat{c}^\dagger_{\mathbf{k},\tau,\sigma,s} \hat{c}_{\mathbf{k},\tau,\sigma,s}, \\
&= \sum_{\mathbf{k}\tau s} \epsilon_{+1,+1}(\mathbf{k}) \hat{c}^\dagger_{\mathbf{k},\tau,+1,s} \hat{c}_{\mathbf{k},\tau,+1,s} + \epsilon_{-1,+1}(\mathbf{k}) \hat{c}^\dagger_{\mathbf{k},\tau,-1,s} \hat{c}_{\mathbf{k},\tau,-1,s}, \\
&= \sum_{\mathbf{k}\sigma\tau s} (\sigma \frac{\epsilon_{+1,+1}(\mathbf{k}) - \epsilon_{-1,+1}(\mathbf{k})}{2} + \frac{\epsilon_{+1,+1}(\mathbf{k}) + \epsilon_{-1,+1}(\mathbf{k})}{2}) \hat{c}^\dagger_{\mathbf{k},\tau,\sigma,s} \hat{c}_{\mathbf{k},\tau,\sigma,s}.
\end{aligned} \tag{3.86}$$

Additionally, in the chiral limit, the BM model has an anti-commutation with chiral symmetry $\mathcal{C} = \sigma_z$:

$$\{\hat{H}_0,\ \mathcal{C}\} = 0, \tag{3.87}$$

then the BM energy bands also satisfy

$$\epsilon_{\sigma,\tau}(\mathbf{k}) = -\epsilon_{-\sigma,\tau}(\mathbf{k}), \tag{3.88}$$

which leads to the the second term in $\hat{H}_0$ is zero in the chiral limit. Away from the chiral limit, the kinetic term is nonzero and we are able to split the kinetic term using the chiral symmetry:

$$\begin{aligned}\hat{H}_0 &= \hat{H}_0^S + \hat{H}_0^A, \\ &= \sum_{\mathbf{k}\sigma\tau s} \epsilon^S_{\sigma\tau}(\mathbf{k})\hat{c}^\dagger_{\mathbf{k},\tau,\sigma,s}\hat{c}_{\mathbf{k},\tau,\sigma,s} + \sum_{\mathbf{k}n\tau s} \epsilon^A_{\sigma\tau}(\mathbf{k})\hat{c}^\dagger_{\mathbf{k},\tau,\sigma,s}\hat{c}_{\mathbf{k},\tau,\sigma,s},\end{aligned} \tag{3.89}$$

which satisfies

$$\begin{aligned}\epsilon^S_{\sigma\tau}(\mathbf{k}) &= \sigma\frac{\epsilon_{+1,+1}(\mathbf{k}) - \epsilon_{-1,+1}(\mathbf{k})}{2}, \\ \epsilon^A_{\sigma\tau}(\mathbf{k}) &= \tau\frac{\epsilon_{+1,+1}(\mathbf{k}) + \epsilon_{-1,+1}(\mathbf{k})}{2}.\end{aligned} \tag{3.90}$$

In the chiral limit, we have $\epsilon^A_{\sigma\tau}(\mathbf{k}) = 0$ due to the anti-commutation relations between the kinetic Hamiltonian and chiral symmetry. As a result, the kinetic energy is nothing but a constant proportional to the number of electrons. Therefore one is able to achieve a full $U(4)$ symmetry and rotate the valley-spin favors (τ, s) with any angles.

Chiral Limit

In this subsection, we utilize the perturbation theory to determine the exact ground states up to the second order in the chiral limit first. The Fock state $|\Psi_v^{v_+,v_-}\rangle$ will serve as the unperturbed ground states. In the chiral limit, the anti-symmetric kinetic term is zero: $\hat{H}_0^A = 0$. Therefore, we only need to consider the perturbation $\hat{H}^S$. Similar to the kinetic terms, we will first initially transform the BM band basis

into the Chern band basis:

$$\begin{aligned}
\hat{H}_0 &= \hat{H}_0^S, \\
&= \sum_{\mathbf{k}\sigma\tau s} \epsilon^S_{\sigma,\tau}(\mathbf{k}) \hat{c}^\dagger_{\mathbf{k},\tau,\sigma,s} \hat{c}_{\mathbf{k},\tau,\sigma,s}, \\
&= \sum_{\mathbf{k}\sigma\tau s} \epsilon^S_{\sigma\tau}(\mathbf{k}) \frac{\hat{d}^\dagger_{\mathbf{k},+,\tau,s} + \sigma \hat{d}^\dagger_{\mathbf{k},-,\tau,s}}{\sqrt{2}} \cdot \frac{\hat{d}_{\mathbf{k},+,\tau,s} + \sigma \hat{d}_{\mathbf{k},-,\tau,s}}{\sqrt{2}}, \\
&= \frac{1}{2} \sum_{\mathbf{k}\sigma\tau s} \epsilon^S_{\sigma\tau}(\mathbf{k}) (\hat{d}^\dagger_{\mathbf{k},+,\tau,s} \hat{d}_{\mathbf{k},+,\tau,s} + \sigma \hat{d}^\dagger_{\mathbf{k},-,\tau,s} \hat{d}_{\mathbf{k},+,\tau,s} \\
&\qquad + \sigma \hat{d}^\dagger_{\mathbf{k},+,\tau,s} \hat{d}_{\mathbf{k},-,\tau,s} + \hat{d}^\dagger_{\mathbf{k},-,\tau,s} \hat{d}_{\mathbf{k},-,\tau,s}), \\
&= \frac{1}{2} \sum_{\mathbf{k}\tau s} (\epsilon_{+1,+1}(\mathbf{k}) - \epsilon_{-1,+1}(\mathbf{k})) \cdot (\hat{d}^\dagger_{\mathbf{k},-,\tau,s} \hat{d}_{\mathbf{k},+,\tau,s} + \hat{d}^\dagger_{\mathbf{k},+,\tau,s} \hat{d}_{\mathbf{k},-,\tau,s}), \\
&= \frac{1}{2} \sum_{\mathbf{k}\tau s} (\epsilon_{+1,+1}(\mathbf{k}) - \epsilon_{-1,+1}(\mathbf{k})) \cdot (\hat{d}^\dagger_{\mathbf{k},-,\tau,s} \hat{d}_{\mathbf{k},+,\tau,s} + \hat{d}^\dagger_{\mathbf{k},+,\tau,s} \hat{d}_{\mathbf{k},-,\tau,s}), \\
&= \sum_{\mathbf{k}\tau s} \epsilon^S(\mathbf{k}) (\hat{d}^\dagger_{\mathbf{k},-,\tau,s} \hat{d}_{\mathbf{k},+,\tau,s} + \hat{d}^\dagger_{\mathbf{k},+,\tau,s} \hat{d}_{\mathbf{k},-,\tau,s}),
\end{aligned} \tag{3.91}$$

where $d^\dagger_{\mathbf{k},n,\tau,s}/d_{\mathbf{k},n,\tau,s}$ represent the creation/annihilation operators in the Chern band $\pm$ basis, $\epsilon^S_{+1,\tau}(\mathbf{k}) = -\epsilon^S_{-1,\tau}(\mathbf{k})$ is used and we define $\epsilon^S_{1,\tau}(\mathbf{k}) = \frac{\epsilon_{+1,+1}(\mathbf{k}) - \epsilon_{-1,+1}(\mathbf{k})}{2}$. Therefore $\hat{H}_0$ switches the Chern band number $\pm$ of an electron within the same valley and spin. We can switch the Chern band only if the valley-spin flavors $\{\tau, s\}$ are half-occupied, which means that only one of two Chern $\pm$ bands is occupied in each valley-spin flavor.

Then the first-order energy contribution of the non-chiral part is written as

$$\begin{aligned}
E^{(1)}_{v,v_C=v_+-v_-} &= \langle \Psi^{v_+,v_-}_v | \hat{H}^S_0 | \Psi^{v_+,v_-}_v \rangle, \\
&= \sum_{\mathbf{k}\tau s} \epsilon^S(\mathbf{k}) \langle \Psi^{v_+,v_-}_v | (\hat{d}^\dagger_{\mathbf{k},-,\tau,s} \hat{d}_{\mathbf{k},+,\tau,s} + \hat{d}^\dagger_{\mathbf{k},+,\tau,s} \hat{d}_{\mathbf{k},-,\tau,s}) | \Psi^{v_+,v_-}_v \rangle, \\
&= 0,
\end{aligned} \tag{3.92}$$

which is zero since the $|\Psi^{v_+,v_-}_v\rangle$ fully occupies the Chern bands for all momentum $\mathbf{k}$. Next, we will move forward to the second-order perturbation energy:

$$\begin{aligned}
E^{(2)}_{v,v_C=v_+-v_-} &= \langle \Psi^{v_+,v_-}_v | \hat{H}^S_0 (E^0_{v,v_C} - \hat{H}^S_0)^{-1} \hat{H}^S_0 | \Psi^{v_+,v_-}_v \rangle, \\
&= -\sum_{\text{mid}} \frac{|\langle \Psi^{v_+,v_-}_{v,\text{mid}} | \hat{H}^S_0 | \Psi^{v_+,v_-}_v \rangle|^2}{E_{\text{mid}} - E^0_{v,v_C}},
\end{aligned} \tag{3.93}$$

where $E^0_{v,v_C} = \langle \Psi^{v_+,v_-}_v | \hat{H}^0_I + \hat{H}^S_0 | \Psi^{v_+,v_-}_v \rangle$ as the energies of the unperturbed ground state $|\Psi^{v_+,v_-}_v\rangle$ and $\Psi^{v_+,v_-}_{v,\text{mid}}$ is the excited eigenstates from the ground eigenstate $|\Psi^{v_+,v_-}_v\rangle$ at energies $E_{\text{mid}} = \langle \Psi^{v_+,v_-}_{v,\text{mid}} | \hat{H}^0_I | \Psi^{v_+,v_-}_{v,\text{mid}} \rangle > \langle \Psi^{v_+,v_-}_v | \hat{H}^0_I | \Psi^{v_+,v_-}_v \rangle = E^0_{v,v_C}$ such that

$$E_{\text{mid}} - E^0_{v,v_C} = \langle \Psi^{v_+,v_-}_{v,\text{mid}} | \hat{H}^0_I | \Psi^{v_+,v_-}_{v,\text{mid}} \rangle - E^0_{v,v_C} > 0, \tag{3.94}$$

which is the energy gap between the excited and ground state. As a result, this term is greater than zero. Next, we compute the action of $\hat{H}^S_0$ on the state $|\Psi^{v_+,v_-}_v\rangle$:

$$\begin{aligned}
\hat{H}^S_0 \left|\Psi^{v_+,v_-}_v\right\rangle &= \sum_{\mathbf{k}\tau s} \epsilon^S(\mathbf{k}) (\hat{d}^\dagger_{\mathbf{k},-,\tau,s} \hat{d}_{\mathbf{k},+,\tau,s} + \hat{d}^\dagger_{\mathbf{k},+,\tau,s} \hat{d}_{\mathbf{k},-,\tau,s}) \left|\Psi^{v_+,v_-}_v\right\rangle, \\
&= \sum_{\mathbf{k}\tau s} \epsilon^S(\mathbf{k}) (\hat{d}^\dagger_{\mathbf{k},-,\tau,s} \hat{d}_{\mathbf{k},+,\tau,s} + \hat{d}^\dagger_{\mathbf{k},+,\tau,s} \hat{d}_{\mathbf{k},-,\tau,s}) \\
&\qquad \times \prod_{\mathbf{k}'} \prod_{j_1=1}^{v_+} \hat{d}^\dagger_{\mathbf{k}',+,\tau_{j_1},s_{j_1}} \prod_{j_2=1}^{v_-} \hat{d}^\dagger_{\mathbf{k}',-,\tau_{j_2},s_{j_2}} |\text{vac}\rangle, \\
&= \sum_{\mathbf{k}\tau s} \epsilon^S(\mathbf{k}) (\hat{d}^\dagger_{\mathbf{k},-,\tau,s} \hat{d}_{\mathbf{k},+,\tau,s} + \hat{d}^\dagger_{\mathbf{k},+,\tau,s} \hat{d}_{\mathbf{k},-,\tau,s}) \\
&\qquad \times \prod_{\mathbf{k}'} \delta_{\mathbf{k}',\mathbf{k}} \prod_{j_1=1}^{v_+} \hat{d}^\dagger_{\mathbf{k}',+,\tau_{j_1},s_{j_1}} \prod_{j_2=1}^{v_-} \hat{d}^\dagger_{\mathbf{k}',-,\tau_{j_2},s_{j_2}} |\text{vac}\rangle, \\
&= \sum_{\mathbf{k}\tau s} \epsilon^S(\mathbf{k}) (\hat{d}^\dagger_{\mathbf{k},-,\tau,s} \hat{d}_{\mathbf{k},+,\tau,s} \prod_{j_1=1}^{v_+} \hat{d}^\dagger_{\mathbf{k},+,\tau_{j_1},s_{j_1}} \prod_{j_2=1}^{v_-} \hat{d}^\dagger_{\mathbf{k},-,\tau_{j_2},s_{j_2}} |\text{vac}\rangle \\
&\qquad + \hat{d}^\dagger_{\mathbf{k},+,\tau,s} \hat{d}_{\mathbf{k},-,\tau,s} \prod_{j_1=1}^{v_+} \hat{d}^\dagger_{\mathbf{k},+,\tau_{j_1},s_{j_1}} \prod_{j_2=1}^{v_-} \hat{d}^\dagger_{\mathbf{k},-,\tau_{j_2},s_{j_2}} |\text{vac}\rangle) \\
&= \sum_{\mathbf{k}\tau s} \epsilon^S(\mathbf{k}) (\hat{d}^\dagger_{\mathbf{k},-,\tau,s} \hat{d}_{\mathbf{k},+,\tau,s} \prod_{j_1=1}^{v_+} \delta_{\tau,\tau_{j_1}} \hat{d}^\dagger_{\mathbf{k},+,\tau_{j_1},s_{j_1}} \prod_{j_2=1}^{v_-} \delta_{\tau,-\tau_{j_2}} \hat{d}^\dagger_{\mathbf{k},-,\tau_{j_2},s_{j_2}} |\text{vac}\rangle \\
&\qquad + \hat{d}^\dagger_{\mathbf{k},+,\tau,s} \hat{d}_{\mathbf{k},-,\tau,s} \prod_{j_1=1}^{v_+} \delta_{\tau,-\tau_{j_1}} \hat{d}^\dagger_{\mathbf{k},+,\tau_{j_1},s_{j_1}} \prod_{j_2=1}^{v_-} \delta_{\tau,\tau_{j_2}} \hat{d}^\dagger_{\mathbf{k},-,\tau_{j_2},s_{j_2}} |\text{vac}\rangle) \\
&= \sum_{\mathbf{k}\tau s} \epsilon^S(\mathbf{k}) (\hat{d}^\dagger_{\mathbf{k},-,\tau,s} \hat{d}_{\mathbf{k},+,\tau,s} \prod_{j_1=1}^{v_+} \delta_{\tau,\tau_{j_1}} \delta_{s,s_{j_1}} \prod_{j_2=1}^{v_-} \delta_{\tau,-\tau_{j_2}} \delta_{s,-s_{j_2}} \\
&\qquad + \hat{d}^\dagger_{\mathbf{k},+,\tau,s} \hat{d}_{\mathbf{k},-,\tau,s} \prod_{j_1=1}^{v_+} \delta_{\tau,-\tau_{j_1}} \delta_{s,-s_{j_1}} \prod_{j_2=1}^{v_-} \delta_{\tau,\tau_{j_2}} \delta_{s,s_{j_2}} |\Psi^{v_+,v_-}_v\rangle),
\end{aligned} \tag{3.95}$$

where the first term is nonzero only when the spin-valley favors $\{\tau, s\}$ are occupied for Chern band + basis, while the spin-valley favors $\{\tau, s\}$ are unoccupied for Chern band − basis. On the other hand, the second term is nonzero only when the spin-valley favors $\{\tau, s\}$ are occupied for Chern band − basis, while the spin-valley favors $\{\tau, s\}$ are unoccupied for Chern band + basis. Therefore, for any excited eigenstates $|\Psi^{v_+,v_-}_{v,\mathrm{mid}}\rangle$ from the ground eigenstate $|\Psi^{v_+,v_-}_{v}\rangle$ at energies $\langle\Psi^{v_+,v_-}_{v,\mathrm{mid}}|\hat{H}^0_I|\Psi^{v_+,v_-}_{v,\mathrm{mid}}\rangle \geq \langle\Psi_v|\hat{H}^0_I|\Psi^{v_+,v_-}_{v}\rangle$, we have

$$\begin{aligned}
&\langle\Psi^{v_+,v_-}_{v,\mathrm{mid}}|\hat{H}^S_0|\Psi^{v_+,v_-}_{v}\rangle\,,\\
&=\sum_{\mathbf{k}\tau s}\epsilon^S(\mathbf{k})\,\langle\Psi^{v_+,v_-}_{v,\mathrm{mid}}|\,(\hat{d}^\dagger_{\mathbf{k},-,\tau,s}\hat{d}_{\mathbf{k},+,\tau,s}\prod_{j_1=1}^{v_+}\delta_{\tau,\tau_{j_1}}\delta_{s,s_{j_1}}\prod_{j_2=1}^{v_-}\delta_{\tau,-\tau_{j_2}}\delta_{s,-s_{j_2}}\\
&\qquad\qquad+\hat{d}^\dagger_{\mathbf{k},+,\tau,s}\hat{d}_{\mathbf{k},-,\tau,s}\prod_{j_1=1}^{v_+}\delta_{\tau,-\tau_{j_1}}\delta_{s,-s_{j_1}}\prod_{j_2=1}^{v_-}\delta_{\tau,\tau_{j_2}}\delta_{s,s_{j_2}}\,|\Psi^{v_+,v_-}_{v}\rangle\,,
\end{aligned}\tag{3.96}$$

which is nonzero only for the excited states:

$$|\Psi^{v_+,v_-}_{v,\mathrm{mid}}\rangle = |\Psi^{v_+,v_-}_{v,\mathrm{mid}},\mathbf{k},n,\tau,s\rangle = \hat{d}^\dagger_{\mathbf{k},n,\tau,s}\hat{d}_{\mathbf{k},-n,\tau,s}\,|\Psi^{v_+,v_-}_{v}\rangle\,,\tag{3.97}$$

which means that valley-spin favors $\{\tau, s\}$ are fully occupied in Chern band $n = \pm$ basis and valley-spin favors $\{\tau, s\}$ are fully empty in Chern band $-n = \mp$ basis for the excited state $|\Psi^{v_+,v_-}_{v,\mathrm{mid}}\rangle$. Then, taking the sum of all nonzero terms, we have

$$\langle\Psi^{v_+,v_-}_{v,\mathrm{mid}}|\hat{H}^S_0|\Psi^{v_+,v_-}_{v}\rangle = \sum_{\mathbf{k}}\epsilon^S(\mathbf{k}) = N^S_{\mathrm{mid}},\tag{3.98}$$

which is a constant number and independent of Chern band number, valley, spin. We use N^S_{mid} to denote this number.

Then the second-order perturbation energy can be written as

$$\begin{aligned}
E^{(2)}_{v,v_C} &= -\sum_{\mathrm{mid}}\frac{|\,\langle\Psi^{v_+,v_-}_{v,\mathrm{mid}}|\hat{H}^S_0|\Psi^{v_+,v_-}_{v}\rangle\,|^2}{E_{\mathrm{mid}}-E^0_{v,v_C}},\\
&= -\sum_{\mathbf{k},n,\tau,s}\frac{|\,\langle\Psi^{v_+,v_-}_{v,\mathrm{mid}},\mathbf{k},n,\tau,s|\hat{H}^S_0|\Psi^{v_+,v_-}_{v}\rangle\,|^2}{E_{\mathrm{mid}}-E^0_{v,v_C}},\\
&= -\sum_{\mathrm{mid}}\frac{|N^S_{\mathrm{mid}}|^2}{E_{\mathrm{mid}}-E^0_{v,v_C}} < 0,
\end{aligned}\tag{3.99}$$

where the summation is over all half-occupied valley-spin flavors $\{\tau, s\}$. Therefore, the second-order perturbation reaches its minimum when the state $|\Psi^{v_+,v_-}_{v}\rangle$ has as

many half-occupied valley-spin flavors $\{\tau, s\}$ as possible. In this case, the number of possible half-occupied excited states $|\Psi^{v_+,v_-}_{v,\text{mid}}, \mathbf{k}, n, \tau, s\rangle$ will decrease. As a result, the spin-valley polarized Fock state with Chern number $v_C = v_+ - v_-$ in Eq. (3.45), which half occupies valley-spin favors as $\{\tau, s\}$ possible, is the exact ground states up to the second order ([58, 7, 108]):

$$|\Psi^{v_C,\text{half}}_v\rangle = \prod_{\mathbf{k}} \prod_{j=1}^{v_+} \hat{d}^\dagger_{\mathbf{k},+,\tau_j,s_j} \prod_{j=5-v_-}^{4} \hat{d}^\dagger_{\mathbf{k},-,\tau_j,s_j} |\text{vac}\rangle ,$$

where $\{\tau_j, s_j\}$ are the 4 valley-spin favors arbitrarily sorted in j ($1 \le j \le 4$). This state has $4-|v|$ half-occupied valley-spin flavors, and has a second-order perturbation energy ([58, 7, 108]

$$) : E^{(2)}_{v,v_C} \sim -(4 - |v|). \tag{3.100}$$

Non-Chiral Limit

Next, in this subsection, we employ the perturbation theory to determine the exact ground states up to the second order in the non-chiral limit. Once again, the Fock state $|\Psi^{v_+,v_-}_v\rangle$ will serve as the unperturbed ground states. Away from the chiral limit, both the symmetric and anti-symmetric kinetic terms are nonzero. Therefore, we need to consider the perturbation $\hat{H}^S + \hat{H}^A$. Similar to the kinetic terms, we initially change the BM band basis into the Chern band basis. For the anti-symmetric part, we have

$$\begin{aligned}
\hat{H}^A_0 &= \sum_{\mathbf{k}\sigma\tau s} \epsilon^A_{\sigma,\tau}(\mathbf{k}) \hat{c}^\dagger_{\mathbf{k},\tau,\sigma,s} \hat{c}_{\mathbf{k},\tau,\sigma,s}, \\
&= \sum_{\mathbf{k}\sigma\tau s} \epsilon^A_{\sigma\tau}(\mathbf{k}) \frac{\hat{d}^\dagger_{\mathbf{k},+,\tau,s} + \sigma \hat{d}^\dagger_{\mathbf{k},-,\tau,s}}{\sqrt{2}} \cdot \frac{\hat{d}_{\mathbf{k},+,\tau,s} + \sigma \hat{d}_{\mathbf{k},-,\tau,s}}{\sqrt{2}}, \\
&= \frac{1}{2} \sum_{\mathbf{k}\sigma\tau s} \epsilon^A_{\sigma\tau}(\mathbf{k}) (\hat{d}^\dagger_{\mathbf{k},+,\tau,s} \hat{d}_{\mathbf{k},+,\tau,s} + \sigma \hat{d}^\dagger_{\mathbf{k},-,\tau,s} \hat{d}_{\mathbf{k},+,\tau,s} \\
&\qquad + \sigma \hat{d}^\dagger_{\mathbf{k},+,\tau,s} \hat{d}_{\mathbf{k},-,\tau,s} + \hat{d}^\dagger_{\mathbf{k},-,\tau,s} \hat{d}_{\mathbf{k},-,\tau,s}), \\
&= \frac{1}{2} \sum_{\mathbf{k}\tau s} \tau(\epsilon_{+1,+1}(\mathbf{k}) + \epsilon_{-1,+1}(\mathbf{k})) \cdot (\hat{d}^\dagger_{\mathbf{k},+,\tau,s} \hat{d}_{\mathbf{k},+,\tau,s} + \hat{d}^\dagger_{\mathbf{k},-,\tau,s} \hat{d}_{\mathbf{k},-,\tau,s}), \\
&= \frac{1}{2} \sum_{\mathbf{k}ns} (\epsilon_{+1,+1}(\mathbf{k}) + \epsilon_{-1,+1}(\mathbf{k})) \cdot (\hat{d}^\dagger_{\mathbf{k},n,+1,s} \hat{d}_{\mathbf{k},n,+1,s} - \hat{d}^\dagger_{\mathbf{k},n,-1,s} \hat{d}_{\mathbf{k},n,-1,s}), \\
&= \sum_{\mathbf{k}ns} \epsilon^A(\mathbf{k}) (\hat{d}^\dagger_{\mathbf{k},n,+1,s} \hat{d}_{\mathbf{k},n,+1,s} - \hat{d}^\dagger_{\mathbf{k},n,-1,s} \hat{d}_{\mathbf{k},n,-1,s}),
\end{aligned} \tag{3.101}$$

and then for the symmetric part:

$$\hat{H}_0^S = \sum_{\mathbf{k}\tau s} \epsilon^S(\mathbf{k})(\hat{d}^\dagger_{\mathbf{k},-,\tau,s}\hat{d}_{\mathbf{k},+,\tau,s} + \hat{d}^\dagger_{\mathbf{k},+,\tau,s}\hat{d}_{\mathbf{k},-,\tau,s}),$$

where $d^\dagger_{\mathbf{k},n,\tau,s}/d_{\mathbf{k},n,\tau,s}$ is the creation/annihilation operators in the Chern band $\pm$ basis, $\epsilon^A_{\sigma,+1}(\mathbf{k}) = -\epsilon^A_{\sigma,-1}(\mathbf{k})/\epsilon^S_{+1,\tau}(\mathbf{k}) = -\epsilon^S_{-1,\tau}(\mathbf{k})$ is used and we define $\epsilon^S_{1,\tau}(\mathbf{k}) = \frac{\epsilon_{+1,+1}(\mathbf{k})-\epsilon_{-1,+1}(\mathbf{k})}{2}$. Besides that, we also have $\epsilon^A_{\sigma,+1}(\mathbf{k}) = -\epsilon^A_{\sigma,+1}(-\mathbf{k})$ and $\epsilon^S_{\sigma,+1}(\mathbf{k}) = \epsilon^S_{\sigma,+1}(-\mathbf{k})$. Then the total kinetic is

$$\hat{H}_0 = \hat{H}_0^S + \hat{H}_0^A.$$

Then the first-order energy contribution of the non-chiral part is written as

$$\begin{aligned}
E^{(1)}_{v,v_C=v_+-v_-} &= \langle \Psi_v^{v_+,v_-}|\hat{H}_0^S + \hat{H}_0^A|\Psi_v^{v_+,v_-}\rangle\,, \\
&= \sum_{\mathbf{k}\tau s} \epsilon^S(\mathbf{k})\,\langle \Psi_v^{v_+,v_-}|(\hat{d}^\dagger_{\mathbf{k},-,\tau,s}\hat{d}_{\mathbf{k},+,\tau,s} + \hat{d}^\dagger_{\mathbf{k},+,\tau,s}\hat{d}_{\mathbf{k},-,\tau,s})|\Psi_v^{v_+,v_-}\rangle \\
&+ \sum_{\mathbf{k}ns} \epsilon^A(\mathbf{k})\,\langle \Psi_v^{v_+,v_-}|(\hat{d}^\dagger_{\mathbf{k},n,+1,s}\hat{d}_{\mathbf{k},n,+1,s} - \hat{d}^\dagger_{\mathbf{k},n,-1,s}\hat{d}_{\mathbf{k},n,-1,s})|\Psi_v^{v_+,v_-}\rangle\,, \\
&= \sum_{\mathbf{k}ns} \epsilon^A(\mathbf{k})\,\langle \Psi_v^{v_+,v_-}|(\hat{d}^\dagger_{\mathbf{k},n,+1,s}\hat{d}_{\mathbf{k},n,+1,s} - \hat{d}^\dagger_{\mathbf{k},n,-1,s}\hat{d}_{\mathbf{k},n,-1,s})|\Psi_v^{v_+,v_-}\rangle\,, \\
&\geq 0,
\end{aligned} \tag{3.102}$$

which is zero when $|\Psi_v^{v_+,v_-}\rangle$ fully occupies two spin-valley favors $\{+1,s\}$ and $\{-1,s\}$ for Chern band $n=\pm$; and nonzero when only one of spin-valley favors $\{+1,s\}$ and $\{-1,s\}$ is occupied for Chern band $n=\pm$. Therefore, the fully-occupied $|\Psi_v^{v_C,\text{full}}\rangle$ state in Eq. (3.44) achieves the lowest zero energy:

$$E^{(1),\text{full}}_{v,v_C} = \langle \Psi_v^{v_C,\text{full}}|\hat{H}_0^S + \hat{H}_0^A|\Psi_v^{v_C,\text{full}}\rangle = 0,$$

while the half-occupied $|\Psi_v^{v_C,\text{half}}\rangle$ state in Eq. (3.45) achieves the highest energy:

$$E^{(1),\text{half}}_{v,v_C} = \langle \Psi_v^{v_C,\text{half}}|\hat{H}_0^S + \hat{H}_0^A|\Psi_v^{v_C,\text{half}}\rangle = \sum_{\mathbf{k}} \epsilon^A(\mathbf{k})(v_+ - v_-) = v_C N^A_{\text{mid}},$$

where N^A_{mid} is used to denote the sum of all anti-symmetric single-particle-energies.

Next, we will move forward to the second-order perturbation energy:

$$\begin{aligned}
E^{(2)}_{v,v_C=v_+-v_-} &= \langle \Psi_v^{v_+,v_-}|(\hat{H}_0^S + \hat{H}_0^A)(E^0_{v,v_C} - (\hat{H}_0^S + \hat{H}_0^A))^{-1}(\hat{H}_0^S + \hat{H}_0^A)|\Psi_v^{v_+,v_-}\rangle\,, \\
&= -\sum_{\text{mid}} \frac{|\,\langle \Psi_{v,\text{mid}}^{v_+,v_-}|(\hat{H}_0^S + \hat{H}_0^A)|\Psi_v^{v_+,v_-}\rangle\,|^2}{E_{\text{mid}} - E^0_{v,v_C}},
\end{aligned} \tag{3.103}$$

where $E^0_{v,v_C} = \langle \Psi^{v_+,v_-}_v | \hat{H}^0_I + (\hat{H}^S_0 + \hat{H}^A_0) | \Psi^{v_+,v_-}_v \rangle$ as the energies of the unperturbed ground state $|\Psi^{v_+,v_-}_v\rangle$ and $\Psi^{v_+,v_-}_{v,\text{mid}}$ is the excited eigenstates from the ground eigenstate $|\Psi^{v_+,v_-}_v\rangle$ at energies $E_{\text{mid}} = \langle \Psi^{v_+,v_-}_{v,\text{mid}} | \hat{H}^0_I | \Psi^{v_+,v_-}_{v,\text{mid}} \rangle > \langle \Psi^{v_+,v_-}_v | \hat{H}^0_I | \Psi^{v_+,v_-}_v \rangle = E^0_{v,v_C}$ such that

$$E_{\text{mid}} - E^0_{v,v_C} = E^{(1)}_{v,v_C} + \langle \Psi^{v_+,v_-}_{v,\text{mid}} | \hat{H}^0_I | \Psi^{v_+,v_-}_{v,\text{mid}} \rangle - E^0_{v,v_C} > 0, \tag{3.104}$$

which is sum of the first-order perturbation energy and the energy gap between the excited and ground state. As a result, this term is greater than zero. Next, we compute the action of $\hat{H}^S_0$ and $\hat{H}^A_0$ on the state $|\Psi^{v_+,v_-}_v\rangle$:

$$\begin{aligned}
\hat{H}^S_0 \, |\Psi^{v_+,v_-}_v\rangle = \sum_{\mathbf{k}\tau s} \epsilon^S(\mathbf{k}) (\hat{d}^\dagger_{\mathbf{k},-,\tau,s} \hat{d}_{\mathbf{k},+,\tau,s} \prod_{j_1=1}^{v_+} \delta_{\tau,\tau_{j_1}} \delta_{s,s_{j_1}} \prod_{j_2=1}^{v_-} \delta_{\tau,-\tau_{j_2}} \delta_{s,-s_{j_2}} \\
+ \hat{d}^\dagger_{\mathbf{k},+,\tau,s} \hat{d}_{\mathbf{k},-,\tau,s} \prod_{j_1=1}^{v_+} \delta_{\tau,-\tau_{j_1}} \delta_{s,-s_{j_1}} \prod_{j_2=1}^{v_-} \delta_{\tau,\tau_{j_2}} \delta_{s,s_{j_2}} \, |\Psi^{v_+,v_-}_v\rangle),
\end{aligned} \tag{3.105}$$

and

$$\begin{aligned}
\hat{H}^A_0 \, |\Psi^{v_+,v_-}_v\rangle &= \sum_{\mathbf{k}ns} \epsilon^A(\mathbf{k}) (\hat{d}^\dagger_{\mathbf{k},n,+1,s} \hat{d}_{\mathbf{k},n,+1,s} - \hat{d}^\dagger_{\mathbf{k},n,-1,s} \hat{d}_{\mathbf{k},n,-1,s}) \, |\Psi^{v_+,v_-}_v\rangle \,, \\
&= \sum_{\mathbf{k}\tau s} \epsilon^A(\mathbf{k}) (\hat{d}^\dagger_{\mathbf{k},n,+1,s} \hat{d}_{\mathbf{k},n,+1,s} - \hat{d}^\dagger_{\mathbf{k},n,-1,s} \hat{d}_{\mathbf{k},n,-1,s}) \\
&\qquad \times \prod_{\mathbf{k}'} \prod_{j_1=1}^{v_+} \hat{d}^\dagger_{\mathbf{k}',+,\tau_{j_1},s_{j_1}} \prod_{j_2=1}^{v_-} \hat{d}^\dagger_{\mathbf{k}',-,\tau_{j_2},s_{j_2}} \, |\text{vac}\rangle \,, \\
&= \sum_{\mathbf{k}ns} \epsilon^A(\mathbf{k}) (\hat{d}^\dagger_{\mathbf{k},n,+1,s} \hat{d}_{\mathbf{k},n,+1,s} - \hat{d}^\dagger_{\mathbf{k},n,-1,s} \hat{d}_{\mathbf{k},n,-1,s}) \\
&\qquad \times \prod_{\mathbf{k}'} \delta_{\mathbf{k}',\mathbf{k}} \prod_{j_1=1}^{v_+} \hat{d}^\dagger_{\mathbf{k}',+,\tau_{j_1},s_{j_1}} \prod_{j_2=1}^{v_-} \hat{d}^\dagger_{\mathbf{k}',-,\tau_{j_2},s_{j_2}} \, |\text{vac}\rangle \,, \\
&= \sum_{\mathbf{k}ns} \epsilon^A(\mathbf{k}) (\hat{d}^\dagger_{\mathbf{k},n,+1,s} \hat{d}_{\mathbf{k},n,+1,s} \prod_{j_1=1}^{v_+} \hat{d}^\dagger_{\mathbf{k},+,\tau_{j_1},s_{j_1}} \prod_{j_2=1}^{v_-} \hat{d}^\dagger_{\mathbf{k},-,\tau_{j_2},s_{j_2}} \, |\text{vac}\rangle \\
&\qquad - \hat{d}^\dagger_{\mathbf{k},n,-1,s} \hat{d}_{\mathbf{k},n,-1,s} \prod_{j_1=1}^{v_+} \hat{d}^\dagger_{\mathbf{k},+,\tau_{j_1},s_{j_1}} \prod_{j_2=1}^{v_-} \hat{d}^\dagger_{\mathbf{k},-,\tau_{j_2},s_{j_2}} \, |\text{vac}\rangle) \\
&= \sum_{\mathbf{k}ns} \epsilon^A(\mathbf{k}) (\hat{d}^\dagger_{\mathbf{k},n,+1,s} \hat{d}_{\mathbf{k},n,+1,s} \sum_{j_1 j_2} (\delta_{n,+} \delta_{+1,\tau_{j_1}} \delta_{s,s_{j_1}} + \delta_{n,-} \delta_{+1,\tau_{j_2}} \delta_{s,s_{j_2}}) \\
&\qquad - \hat{d}^\dagger_{\mathbf{k},n,-1,s} \hat{d}_{\mathbf{k},n,-1,s} \sum_{j_1 j_2} (\delta_{n,+} \delta_{-1,\tau_{j_1}} \delta_{s,s_{j_1}} + \delta_{n,-} \delta_{-1,\tau_{j_2}} \delta_{s,s_{j_2}}) \, |\Psi^{v_+,v_-}_v\rangle \,.
\end{aligned} \tag{3.106}$$

For the symmetric part, the first term is nonzero only when the spin-valley favors $\{\tau, s\}$ are occupied for Chern band + basis, while the spin-valley favors $\{\tau, s\}$ are unoccupied for Chern band − basis. On the other hand, the second term is nonzero only when the spin-valley favors $\{\tau, s\}$ are occupied for Chern band − basis, while the spin-valley favors $\{\tau, s\}$ are unoccupied for Chern band + basis. As a result, the only nonzero excited states are

$$|\Psi^{v_+,v_-}_{v,\text{mid}}\rangle = |\Psi^{v_+,v_-}_{v,\text{mid}}, \mathbf{k}, n, \tau, s\rangle = \hat{d}^\dagger_{\mathbf{k},n,\tau,s}\hat{d}_{\mathbf{k},-n,\tau,s}\,|\Psi^{v_+,v_-}_{v}\rangle\,, \tag{3.107}$$

with

$$\langle\Psi^{v_+,v_-}_{v,\text{mid}}|\hat{H}^S_0|\Psi^{v_+,v_-}_{v}\rangle = \sum_{\mathbf{k}}\epsilon^S(\mathbf{k}) = N^S_{\text{mid}}. \tag{3.108}$$

For the anti-symmetric part, the first term is nonzero only when the spin-valley favors $\{+1, s\}$ are occupied for Chern band $n = \pm$ basis. Also, the second term is nonzero only when the spin-valley favors $\{-1, s\}$ are occupied for Chern band $n = \pm$ basis. Therefore, for any excited eigenstates $|\Psi^{v_+,v_-}_{v,\text{mid}}\rangle$ from the ground eigenstate $|\Psi^{v_+,v_-}_{v}\rangle$ at energies $\langle\Psi^{v_+,v_-}_{v,\text{mid}}|\hat{H}^0_I|\Psi^{v_+,v_-}_{v,\text{mid}}\rangle \geq \langle\Psi_v|\hat{H}^0_I|\Psi^{v_+,v_-}_{v}\rangle$, we have

$$\begin{aligned}
&\langle\Psi^{v_+,v_-}_{v,\text{mid}}|\hat{H}^A_0|\Psi^{v_+,v_-}_{v}\rangle\,,\\
&= \sum_{\mathbf{k}ns}\epsilon^A(\mathbf{k})\,\langle\Psi^{v_+,v_-}_{v,\text{mid}}|\,(\hat{d}^\dagger_{\mathbf{k},n,+1,s}\hat{d}_{\mathbf{k},n,+1,s}\sum_{j_1j_2}(\delta_{n,+}\delta_{+1,\tau_{j_1}}\delta_{s,s_{j_1}} + \delta_{n,-}\delta_{+1,\tau_{j_2}}\delta_{s,s_{j_2}})\\
&\qquad\qquad - \hat{d}^\dagger_{\mathbf{k},n,-1,s}\hat{d}_{\mathbf{k},n,-1,s}\sum_{j_1j_2}(\delta_{n,+}\delta_{-1,\tau_{j_1}}\delta_{s,s_{j_1}} + \delta_{n,-}\delta_{-1,\tau_{j_2}}\delta_{s,s_{j_2}})\,|\Psi^{v_+,v_-}_{v}\rangle\,,\\
&= 0,
\end{aligned} \tag{3.109}$$

which is always zero for any excited states:

$$|\Psi^{v_+,v_-}_{v,\text{mid}}\rangle = \hat{d}^\dagger_{\mathbf{k},n,\tau,s}\hat{d}_{\mathbf{k}',n',\tau',s'}\,|\Psi^{v_+,v_-}_{v}\rangle\,, \tag{3.110}$$

which means that one electron is excited to fill one hole. Then, taking the sum of all nonzero terms in the symmetric and anti-symmetric parts, we have

$$\langle\Psi^{v_+,v_-}_{v,\text{mid}}|\hat{H}^S_0 + \hat{H}^A_0|\Psi^{v_+,v_-}_{v}\rangle = \sum_{\mathbf{k}}\epsilon^S(\mathbf{k}) = N^S_{\text{mid}}, \tag{3.111}$$

which is a constant number and independent of Chern band number, valley, spin. N^S_{mid} is used here to denote this number.

Then the second-order perturbation energy stays the same as in the chiral limit:

$$E^{(2)}_{v,v_C} = -\sum_{\text{mid}} \frac{|N^S_{\text{mid}}|^2}{E_{\text{mid}} - E^0_{v,v_C}} < 0, \tag{3.112}$$

where the summation is over all half-occupied valley-spin flavors $\{\tau, s\}$. Therefore, the second-order perturbation reaches its minimum when the state $|\Psi^{v_+,v_-}_v\rangle$ has as many half-occupied valley-spin flavors $\{\tau, s\}$ as possible. In this case, the number of possible half-occupied excited states $|\Psi^{v_+,v_-}_{v,\text{mid}}, \mathbf{k}, n, \tau, s\rangle$ will decrease. As a result, the spin-valley polarized Fock state with Chern number $v_C = v_+ - v_-$ in Eq. (3.45), which half occupies valley-spin favors as $\{\tau, s\}$ possible, is the exact ground states up to the second order:

$$|\Psi^{v_C,\text{half}}_v\rangle = \prod_{\mathbf{k}} \prod_{j=1}^{v_+} \hat{d}^\dagger_{\mathbf{k},+,\tau_j,s_j} \prod_{j=5-v_-}^{4} \hat{d}^\dagger_{\mathbf{k},-,\tau_j,s_j} |\text{vac}\rangle ,$$

where $\{\tau_j, s_j\}$ are the 4 valley-spin favors arbitrarily sorted in j $(1 \le j \le 4)$. This state has $4-|v|$ half-occupied valley-spin flavors, and has a second-order perturbation energy:

$$E^{(2)}_{v,v_C} \sim -(4 - |v|). \tag{3.113}$$

As a result, the lowest total perturbation energy is achieved for the half-occupied $|\Psi^{v_C,\text{half}}_v\rangle$ state in Eq. (3.45):

$$E^{\text{half}}_{v,v_C} = E^{(1),\text{half}}_{v,v_C} + E^{(2),\text{half}}_{v,v_C} = v_C N^A_{\text{mid}} - \sum_{\text{mid}} \frac{|N^S_{\text{mid}}|^2}{E_{\text{mid}} - E^0_{v,v_C}} < 0, \tag{3.114}$$

and the highest total perturbation energy is achieved for the fully-occupied $|\Psi^{v_C,\text{full}}_v\rangle$ state in Eq. (3.44):

$$E^{\text{full}}_{v,v_C} = E^{(1),\text{full}}_{v,v_C} + E^{(2),\text{full}}_{v,v_C} = 0. \tag{3.115}$$

Therefore the numerical results show that the second-order perturbation energy is

$$E_{v,v_C} = E^{(1)}_{v,v_C} + E^{(2)}_{v,v_C} \le 0,$$

and the half-occupied state $|\Psi^{v_C,\text{half}}_v\rangle$ is the exact ground state.

3.6 Neural Excitations

In this section, we summarize the energy contributions from the interaction term and kinetic term.[58, 7, 108] For the interaction term in the non-chiral limit, we have a

positive energy contribution, and we use λ to denote the second-order perturbation energy:

$$\lambda = E_{I,v,v_C} \geq 0 \tag{3.116}$$

where the fully-occupied Fock state $|\Psi_v^{v_C,\text{full}}\rangle$ is the corresponding exact ground state. However, when we add the symmetric/anti-symmetric kinetic terms to the perturbation, a negative energy contribution is achieved, and $-J$ is used to denote the energy up to the second-order:

$$-J = E_{0,v,v_C} \leq 0 \tag{3.117}$$

where the half-occupied Fock state $|\Psi_v^{v_C,\text{half}}\rangle$ is the corresponding exact ground state. As a result, the total perturbation energy can be expressed as

$$E_{v,v_C} = \lambda - J. \tag{3.118}$$

Thus, in the presence of both the interaction and kinetic terms, the K-IVC state benefits from both perturbations and has the lowest energy in the half-filling system [58, 7, 108]:

$$|\Psi_v^{\text{K-IVC}}\rangle = \prod_{\mathbf{k}} \prod_{j=1}^{(v+4)/2} \prod_{n=\pm} \frac{\hat{d}^\dagger_{\mathbf{k},n,\tau_j,s} - n\tau_j \hat{d}^\dagger_{\mathbf{k},n,-\tau_j,s}}{\sqrt{2}} |\text{vac}\rangle \,.$$

Chapter 4

Quantum Chemistry Approach

Overview of Implementation

The BM Hamiltonian is defined by taking two copies of graphene, rotating them relative to each other by an angle θ, and adding inter-layer coupling terms. The relative strength of this inter-layer coupling is controlled by two parameters w_0 and w_1, which control the strength of AA hopping and AB hopping, respectively. Following Ref. [86], we fix $\theta = 1.05$ and $w_1 = 109$ meV and vary the ratio w_0/w_1 between 0 and 0.95. The value used in Ref. [86] is $w_0 = 80$ meV, $w_1 = 109$ meV, which corresponds to a ratio $w_0/w_1 \approx 0.73$. However, in-plane lattice relaxation, which expands AB regions and contracts AA regions [15], as well as out-of-plane relaxation, which increases the interlayer separation in AA regions relative to AB regions [71], could change the value of w_0/w_1. The limit $w_0/w_1 = 0$ is referred to as the chiral limit [95]. The (non-interacting) BM model at the chiral limit exhibits additional symmetries, which have been used extensively in the theoretical studies of the BM model (e.g., the existence of flat bands at certain magic angles) [101, 5, 53, 97, 3, 4, 6, 95].

In this work, we follow Ref. [86] and assume that the IBM model contains only valley K and spin $\uparrow$; in other words, the model is spinless and valleyless. In this case, the charge neutrality point refers to the setting of 1 electron per $\mathbf{k}$ point. This model neglects certain electron-electron interactions (even at the mean-field level) and limits the exploration of certain phases, such as the Kramers intervalley-coherent (K-IVC) state [12] in the full model. On the other hand, ED calculations for the full model suggest that the TBG system is often spin and valley polarized [80]. Post-Hartree-Fock calculations of the phase diagram for the IBM model with valley and spin degrees of freedom will be studied in the future. Our implementation is based on the Python-based Simulations of Chemistry Framework (PySCF) [91, 92]. After constructing the quantum many-body Hamiltonian by means of the form factors from the BM

model [12, 86], HF and post-HF calculations, as well as calculations with integer and non-integer fillings, can be carried out on the same footing. Our post-HF calculations are performed using the coupled cluster singles and doubles (CCSD) method, the perturbative non-iterative energy correction to CCSD (called CCSD(T)) [81], and the density matrix renormalization group (DMRG) [102] method, in particular its quantum chemical formulation (with specific algorithmic choices designed for quartic Hamiltonians, sometimes called QC-DMRG [103, 17, 19]) as implemented in Block2 [115].

Symmetry Breaking Order Parameters

In order to study the phase diagram of TBG, we need to define order parameters to quantify the spontaneous symmetry breaking in the density matrix. The order parameters are often basis dependent, and hence basis changes (sometimes called gauge fixing) tailored for each symmetry may be needed. For instance, one of the most important symmetries of TBG is the $C_{2z}\mathcal{T}$ symmetry, which characterizes the quantum anomalous Hall (QAH) state. The $C_{2z}\mathcal{T}$ order parameter is defined in the Chern band basis [12, 86, 9, 43], which needs to be carefully constructed due to the topological obstruction in constructing the Wannier states. We present a new set of gauge-invariant order parameters defined using the sewing matrices [29, 9], which can be applied to both unitary and antiunitary symmetries without the need for basis change. These gauge-invariant order parameters can therefore be computed conveniently in the band basis of the BM model, and can be used to quantify the symmetry breaking in the density matrix. Our numerical results verify that the phase diagrams obtained from the gauge-invariant and gauge-dependent order parameters previously reported in the literature are consistent.

Subtraction Schemes

The construction of the BM model already implicitly takes electron interactions into consideration via the single-electron dispersion. Hence, adding an additional Coulomb interaction term to the BM model leads to double-counting errors. In the literature, there are a number of different proposals for removing the double-counting effects. These different choices lead to model discrepancies which can be an important source of uncertainty in TBG modeling. We compare the average scheme (AVG) [43, 9], and the decoupled scheme (DEC) [12, 86, 109] for removing such double-counting effects. The former defines a model that is particle-hole symmetric, and the latter uses a more physical reference density matrix. While the results obtained from the two IBM models qualitatively agree, important differences remain even when all

other simulation parameters are reasonably converged. For instance, we find that the $C_{2z}\mathcal{T}$ order parameter in the average scheme is very close to an integer 1 near the chiral limit, indicating that the system is fully polarized in the Chern basis, and the order parameter undergoes a sharp transition to 0 around $w_0/w_1 \approx 0.8$. In the decoupled scheme, the $C_{2z}\mathcal{T}$ order parameter is around 0.8 at the chiral limit, and the order parameter changes non-monotonically as the ratio increases, the transition region becomes much wider for the same system size. In the average scheme, the interaction Hamiltonian at the chiral limit is positive semidefinite [9] and exhibits an enlarged $U(4) \times U(4)$ symmetry [12, 9]. The ground state energy at integer filling is zero, which can be exactly achieved using a single Slater determinant given by the HF solution. With the decoupled scheme, the correlation energy is nonzero even at the chiral limit and $\nu = 0$, and we find that the correlation energy is generally larger than that in the average scheme. The differences due to model discrepancies can be even larger than post-HF electron correlation effects. As a result, in the absence of an interacting model for the TBG system that is fully based on first principles, we may need to investigate an ensemble of interacting models to cross-validate the results.

Integer Versus Non-Integer Fillings

At integer filling ($\nu = 0$), i.e., the charge neutral point, we find that total energies from HF, CCSD, CCSD(T), and DMRG largely agree with each other, and correlation energies (defined as the difference between the HF energy and the post-HF energy) are generally less than 0.5 meV per moiré site. Using the gauge-invariant order parameters, our results confirm that at integer filling, the system is either in a $C_{2z}\mathcal{T}$ symmetry breaking and insulating state, or in a $C_{2z}\mathcal{T}$ trivial and metallic state [86]. We also perform the first systematic study of the IBM model near integer filling (for $|\nu| < 0.2$). In this regime, we find states that are $C_{2z}\mathcal{T}$ symmetry breaking and metallic. Furthermore, the IBM model can host many states that are energetically close to the ground state, and it can be difficult to converge to the "true" global minima for all levels of theories. To highlight this difficulty, we explored two different initialization schemes: (1) Fixed initialization, which uses the one-particle reduced density matrix that follows that in Ref. [86]. (2) Random initialization, which uses a random one-particle reduced density matrix satisfying the electron number constraint.

We observe that the energy corrections provided by post-HF methods can be larger than that in the integer filling case. Although this trend agrees with the exact diagonalization calculations of the full IBM model in [80], the quantitative magnitude of the corrections in our simulations can depend on the local minima

attained at the HF level. The various local minima are not simply an artifact of the HF approximation. For example, we find also that the results of the DMRG calculations can also strongly depend on the HF orbitals, and all DMRG calculations yield solutions with relatively low Fermi-Dirac entropy, which suggests that these minima are all close to single Slater determinants, i.e. solutions that can be described relatively well by the HF approximation.

4.1 Preliminaries

The tight-binding models for monolayer graphene, bilayer graphene, and the BM model for twisted bilayer graphene have been extensively studied in the literatrues and also in Chapter 1. We therefore only provide a minimal introduction to the BM model and the wavefunctions involved; we refer the reader to e.g. Refs. [12, 9] and the references therein for a more detailed discussion. Throughout this section, we adopt atomic units, except for energies which are reported in millielectron volts.

Recall that the BM model depends on two parameters w_0 and w_1, which control the strength of AA hopping and AB hopping respectively. Through this section we fix $\theta = 1.05$, $w_1 = 109$ meV and vary the ratio w_0/w_1 between 0 and 0.95. Subsequently, we denote the moiré unit cell by Ω, its area by $|\Omega|$, and the moiré Bravais lattice by $\mathbb{L}$. Correspondingly, we denote the moiré Brillouin zone (mBZ) by Ω^* and the moiré reciprocal lattice $\mathbb{L}^*$. The mBZ is discretized using a Monkhorst-Pack (MP) grid [69] of size $N_{\mathbf{k}} = n_{k_x} \cdot n_{k_y}$. When the MP grid includes the Γ-point of the mBZ, the computation can be identified with a moiré supercell consisting of $N_{\mathbf{k}}$ unit cells with a sample area $N_{\mathbf{k}} |\Omega|$. A given BM wavefunction, i.e., a BM band, can be labeled by a tuple $(n, \mathbf{k}, \tau, s)$, where n is the band index, $\mathbf{k} \in$ mBZ is the $\mathbf{k}$-point index, $s \in \{\uparrow, \downarrow\}$ is the spin index, and $\tau \in \{\mathbf{K}, \mathbf{K}'\}$ is the valley index. Since the spin and valley indices often do not appear explicitly in the Hamiltonian, they are also referred to as *flavor indices*. For simplicity, we follow the assumption in Ref. [86], and drop the flavor indices s, τ, i.e., the system is spinless and valleyless.

Let $\mathbf{r}$ be the real space index in the moiré supercell, by Bloch's theorem, we can express a BM orbital in real space as

$$\psi_{n\mathbf{k}}(\mathbf{r}, \sigma, l) = \frac{1}{\sqrt{N_{\mathbf{k}}}} e^{\mathrm{i}\mathbf{k}\cdot\mathbf{r}} u_n(\mathbf{k}, \mathbf{r}, \sigma, l) = \frac{1}{\sqrt{N_{\mathbf{k}}\,|\Omega|}} \sum_{\mathbf{G}} e^{\mathrm{i}(\mathbf{k}+\mathbf{G})\cdot\mathbf{r}} u_n(\mathbf{k}, \mathbf{G}, \sigma, l). \tag{4.1}$$

Here $\mathbf{G} \in \mathbb{L}^*$ is the plane-wave index, $\sigma \in \{A = 1, B = -1\}$ is the sublattice index, $l \in \{1, -1\}$ is the layer index. We also refer to $(\mathbf{G}, \sigma, l)$ or $(\mathbf{r}, \sigma, l)$ as *internal indices*. Note that $u_{n\mathbf{k}}(\mathbf{r}, \sigma, l)$ is periodic with respect to $\mathbb{L}$, i.e., $u_n(\mathbf{k}, \mathbf{r}, \sigma, l) = u_n(\mathbf{k}, \mathbf{r} + \mathbf{R}, \sigma, l), \forall \mathbf{R} \in \mathbb{L}$. The normalization condition is chosen such that u_n is

normalized within the moiré unit cell. Moreover, the factor $\frac{1}{\sqrt{N_{\mathbf{k}}}}$ ensures that $\psi_{n\mathbf{k}}$ is normalized within the moiré supercell. With some abuse of notation, we use $u_n(\mathbf{k}, \mathbf{r}, \sigma, l)$ and $u_n(\mathbf{k}, \mathbf{G}, \sigma, l)$ to denote the coefficients of a BM wavefunction in real space and reciprocal space, respectively. In practical calculations, the number of plane-wave indices $\mathbf{G}$ needs to be truncated to a finite size. Throughout this section, we omit the range of summation unless otherwise specified. Subsequently, we refer to the set of all plane waves indexed by $\mathbf{G}$ with sublattice index σ and layer index l as the primitive basis of the BM model and denote the corresponding Fock space by $\mathcal{F}$. Let $\hat{c}^\dagger_{\mathbf{k},\mathbf{G},l,\sigma}, \hat{c}_{\mathbf{k},\mathbf{G},l,\sigma}$ be the creation and annihilation operators acting on $\mathcal{F}$, respectively. Then the creation and annihilation operators corresponding to the band $n\mathbf{k}$ are

$$\begin{aligned} \hat{f}^\dagger_{n\mathbf{k}} &= \sum_{\mathbf{G},\sigma,l} \hat{c}^\dagger_{\mathbf{k},\mathbf{G},l,\sigma} u_n(\mathbf{k}, \mathbf{G}, \sigma, l), \\ \hat{f}_{n\mathbf{k}} &= \sum_{\mathbf{G},\sigma,l} \hat{c}_{\mathbf{k},\mathbf{G},l,\sigma} u^*_n(\mathbf{k}, \mathbf{G}, \sigma, l). \end{aligned} \tag{4.2}$$

Here u^*_n denotes the complex conjugation of u_n. The band creation and annihilation operators satisfy the canonical anticommutation relation, i.e., $\{\hat{f}^\dagger_{n\mathbf{k}}, \hat{f}_{n'\mathbf{k}'}\} = \delta_{nn'}\delta_{\mathbf{k}\mathbf{k}'}$, and define the band basis of the BM model. Note that the definition of the band creation and annihilation operators can be periodically extended outside the mBZ according to

$$\hat{f}^\dagger_{n(\mathbf{k}+\mathbf{G})} = \hat{f}^\dagger_{n\mathbf{k}}, \quad \hat{f}_{n(\mathbf{k}+\mathbf{G})} = \hat{f}_{n\mathbf{k}}, \quad \mathbf{G} \in \mathbb{L}^*. \tag{4.3}$$

4.2 Interacting Bistritzer-MacDonald Model

For values of the ratio $w_0/w_1 \in [0, 0.95]$, the spinless, valleyless BM Hamiltonian has a direct gap between two bands with roughly zero energy and the remainder of the spectrum (see e.g., Fig. 4.1c for $w_0/w_1 = 0.7$). We refer to these two bands as the flat bands of the BM model and label them by the index $n \in \{-1, 1\}$. The Hamiltonian of the IBM model restricted to these flat bands takes the form

$$\begin{aligned} \hat{H}_{\mathrm{IBM}} =& \hat{H}_0 + \hat{H}_I \\ =& \sum_{\mathbf{k}\in\Omega^*} \sum_{mn} \hat{f}^\dagger_{m\mathbf{k}} [h(\mathbf{k})]_{mn} \hat{f}_{n\mathbf{k}} \\ &+ \frac{1}{2} \sum_{\substack{\mathbf{k},\mathbf{k}',\mathbf{k}''\in\Omega^* \\ \mathbf{k}'''=\mathbf{k}+\mathbf{k}'-\mathbf{k}''}} \sum_{mm'nn'} \langle m\mathbf{k}, m'\mathbf{k}' | n\mathbf{k}'', n'\mathbf{k}''' \rangle \, \hat{f}^\dagger_{m\mathbf{k}} \hat{f}^\dagger_{m'\mathbf{k}'} \hat{f}_{n'\mathbf{k}'''} \hat{f}_{n\mathbf{k}''}, \end{aligned} \tag{4.4}$$

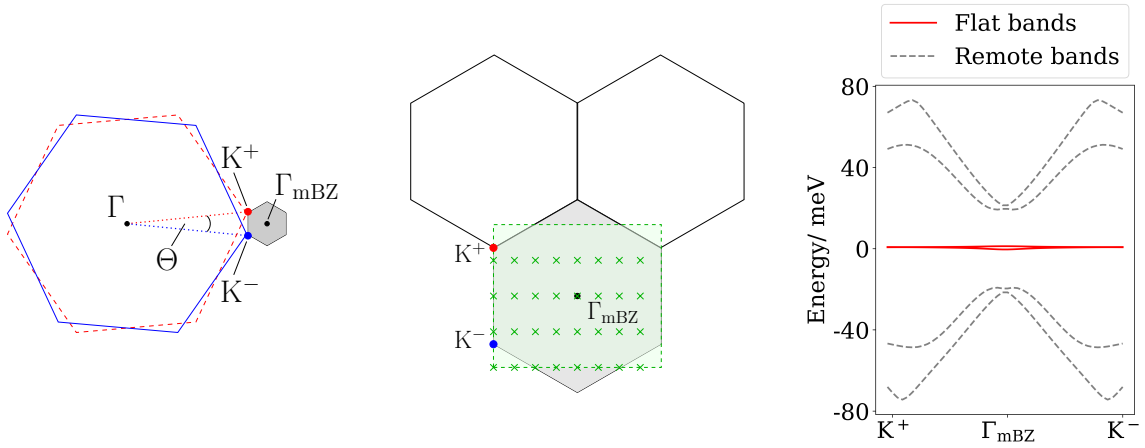

(a) (b) (c)

Figure 4.1: (a) Two monolayer graphene Brillouin zones (BZ) depicted by a dashed red line and solid blue line, respectively, aligned by their Γ-point and twisted by an angle Θ, with the corresponding Dirac points K^+ and K^-. The moiré Brillouin zone (mBZ) is indicated by the grey shaded region centered at $\Gamma_{\mathrm{m}BZ}$. (b) Choice of the rectangular unit cell in reciprocal space (green shaded area encircled by green dashed line, see Ref. [86]) relative to the mBZ. The green crosses show a mBZ discretization grid of 8×4 **k**-points. The Dirac points of the monolayers K^+ and K^- are included as reference points. (c) Band structure of the BM Hamiltonian over the mBZ, with the corresponding flat bands (solid red lines) and remote bands (dashed grey lines). The interacting BM Hamiltonian is then projected onto the subspace spanned by the two flat bands; the system's parameters are $\theta = 1.05°$, $w_1 = 109$ meV and $w_0/w_1 = 0.7$.

where $\hat{H}_0$ and $\hat{H}_I$ are the quadratic term and the quartic term, respectively. The ground state of the IBM model is then defined as the solution to the minimization problem

$$E_0 = \min_{\substack{|\Psi\rangle\in\mathcal{F},\ \langle\Psi|\Psi\rangle=1 \\ \langle\Psi|\hat{N}|\Psi\rangle=N_e}} \langle\Psi|\hat{H}|\Psi\rangle\,, \tag{4.5}$$

where $N_e = (\nu+1)N_{\mathbf{k}}$ is the total number of electrons, and $\hat{N} = \sum_{\mathbf{k}}\sum_n \hat{f}^\dagger_{n\mathbf{k}}\hat{f}_{n\mathbf{k}}$ is the total number operator. The number of electrons per $\mathbf{k}$-point is given by $\nu+1$ and we subsequently refer to ν as the *filling factor*. Note that in this convention, the particle filling is reported with respect to the charge neutral point. Since there are only two bands per $\mathbf{k}$-point, the only non-trivial integer value for the filling factor is $\nu = 0$, which is also called the integer filling case (or the particle-hole symmetric case) of the IBM model in the spinless, valleyless regime.

The main object of interest in this work is the one-particle reduced density matrix (1-RDM) corresponding to the ground state $|\Psi\rangle$ defined as

$$[P(\mathbf{k})]_{nm} = \langle\Psi|\hat{f}^\dagger_{m\mathbf{k}}\hat{f}_{n\mathbf{k}}|\Psi\rangle\,. \tag{4.6}$$

We emphasize that the 1-RDM is well-defined in the entire moiré reciprocal space due to the periodic extension in Eq. (4.3). Using the 1-RDM, we find that for any $\mathbf{k}$, $\mathbf{k}'$ in the moiré reciprocal space,

$$\langle\Psi|\hat{f}^\dagger_{m\mathbf{k}}\hat{f}_{n\mathbf{k}'}|\Psi\rangle = P(\mathbf{k})_{nm}\sum_{\mathbf{G}\in\mathbb{L}^*}\delta_{\mathbf{k},\mathbf{k}'+\mathbf{G}}. \tag{4.7}$$

The quartic term $\hat{H}_I$ describes the (screened) Coulomb interaction via the two-electron repulsion integrals (ERI) denoted by $\langle m\mathbf{k}, m'\mathbf{k}'|n\mathbf{k}'', n'\mathbf{k}'''\rangle$. The coefficients of the quadratic term can be written as

$$h(\mathbf{k}) = h_{\mathrm{BM}}(\mathbf{k}) - h_{\mathrm{sub}}(\mathbf{k}), \tag{4.8}$$

where $[h_{\mathrm{BM}}(\mathbf{k})]_{mn} = \varepsilon^{\mathrm{BM}}_n(\mathbf{k})\delta_{mn}$ is given by the BM band energy. The second term $h_{\mathrm{sub}}(\mathbf{k})$ is called the subtraction Hamiltonian, which removes the double-counting of the Coulomb interaction within the flat bands, and is defined in terms of the Hartree-Fock potential (see Section 4.3). The derivation of the Coulomb interaction term is presented in **??**.

4.3 Computational methods and implementation

Hartree-Fock Theory

The Hartree-Fock approximation is the starting point for various correlated electronic-structure methods [35]. The underlying assumption is that the many-body wavefunction takes the form of a Slater determinant, i.e.,

$$|\Psi_S\rangle = \prod_{\mathbf{k}} \prod_{i\in \mathrm{occ}} \hat{b}^\dagger_{i\mathbf{k}} |\mathrm{vac}\rangle \,, \tag{4.9}$$

where $|\mathrm{vac}\rangle$ is the vacuum state, and

$$\hat{b}^\dagger_{i\mathbf{k}} = \sum_n \hat{f}^\dagger_{n\mathbf{k}} \Xi_{ni}(\mathbf{k}) \tag{4.10}$$

defines the creation operator for the Hartree-Fock orbitals for each $\mathbf{k} \in \Omega^*$.

For integer filling, the number of occupied orbitals per $\mathbf{k}$-point is $\nu + 1$ (indexed by occ). The 1-RDM associated with a given Slater determinant $|\Psi_S\rangle$ is then

$$[P(\mathbf{k})]_{nm} = \langle \Psi_S | \hat{f}^\dagger_{m\mathbf{k}} \hat{f}_{n\mathbf{k}} | \Psi_S \rangle = \sum_{i\in \mathrm{occ}} \Xi_{ni}(\mathbf{k}) \Xi^*_{mi}(\mathbf{k}). \tag{4.11}$$

Following the standard derivation of Hartree-Fock theory (see e.g., [93, 67]), we begin with the characterization of the Hartree-Fock energy, i.e.,

$$E_{\mathrm{HF}} = \min_{P\in\mathcal{M}} \mathrm{Tr}[PH] = \min_{P\in\mathcal{M}} \mathcal{E}^{(HF)}(P), \tag{4.12}$$

where $\mathcal{M}$ is the set of 1-RDMs associated with the possible single Slater determinants of the system. A common way to seek the solution to Eq. (4.12) is by finding a stationary point of $\mathcal{E}^{(HF)}$, which is equivalent to diagonalizing the Fock operator [93] $\hat{F}[P] = \hat{H}_0 + \hat{V}_{HF}[P]$, where $\hat{V}_{HF}[P]$ is the Hartree-Fock potential.

The Hartree-Fock potential can be written in terms of the so-called *form factor* matrix, $\Lambda_{\mathbf{k}}(\mathbf{q}+\mathbf{G})$. Simply speaking, the form factor is given by the Fourier coefficients of the pair product of the periodic Bloch functions of the BM model $\{u_{n\mathbf{k}}\}$.

This matrix is calculated via the following formula (see **??**):

$$[\Lambda_{\mathbf{k}}(\mathbf{q}+\mathbf{G})]_{mn} = \frac{1}{|\Omega|} \sum_{\mathbf{G}'\in\mathbb{L}^*} \sum_{\sigma,l} u^*_m(\mathbf{k},\mathbf{G}',\sigma,l) u_n(\mathbf{k}+\mathbf{q}+\mathbf{G},\mathbf{G}',\sigma,l). \tag{4.13}$$

With this definition, the Hartree-Fock potential takes the compact form

$$\hat{V}_{\mathrm{HF}}[P] = \hat{J}[P] - \hat{K}[P] = \sum_{\mathbf{k}\in\Omega^*} \hat{f}^\dagger_{m\mathbf{k}} [v_{\mathrm{hf}}[P](\mathbf{k})]_{mn} \hat{f}_{n\mathbf{k}}, \tag{4.14}$$

where the matrix elements are given by

$$\begin{aligned}[v_{\mathrm{hf}}[P](\mathbf{k})]_{mn} =& \frac{1}{|\Omega|} \sum_{\mathbf{G}\in\mathbb{L}^*} V(\mathbf{G}) \left(\frac{1}{N_{\mathbf{k}}} \sum_{\mathbf{k}'\in\Omega^*} \mathrm{Tr}[\Lambda_{\mathbf{k}'}(-\mathbf{G}) P(\mathbf{k}')] \right) [\Lambda_{\mathbf{k}}(\mathbf{G})]_{mn} \\ & - \frac{1}{|\Omega| N_{\mathbf{k}}} \sum_{\mathbf{q}'} \sum_{m'n'} V(\mathbf{q}') [\Lambda_{\mathbf{k}}(\mathbf{q}')]_{mn'} [P(\mathbf{k}+\mathbf{q}')]_{n'm'} [\Lambda_{\mathbf{k}+\mathbf{q}'}(-\mathbf{q}')]_{m'n}.\end{aligned} \tag{4.15}$$

We here employ the quantum chemistry notation where H_0 is the core Hamiltonian, $\hat{J}[\cdot]$ and $\hat{K}[\cdot]$ are the Coulomb and exchange operators, respectively. For completeness, the derivation of the expressions of $\hat{J}[\cdot]$ and $\hat{K}[\cdot]$ are given in **??**. This non-linear eigenvalue problem is then determined by self-consistently evaluating the 1-RDM [55].

In quantum chemistry discussions of Hartree-Fock theory, it is also common to require that $\hat{f}^\dagger_{nk}$ commutes with the electronic spin operator $\hat{S}_z$. When no such restriction is used, the theory is termed *generalized* Hartree-Fock theory (GHF). In the current treatment, the electronic spin is fully polarized. However, there is a pseudospin variable, namely the sublattice index σ. We will have no restriction that $\hat{f}^\dagger_{nk}$ commutes with the sublattice pseudospin operator. Thus we will refer later to carrying out GHF calculations, in the sense of no restriction on the pseudospin.

Subtraction Hamiltonian

Since the BM band energies already take the electron-electron interaction between the two layers of graphene into account, the screened Coulomb potential in the IBM model would double count such interactions. As a remedy, one can introduce a subtraction Hamiltonian, see Eq. (4.8). At the level of Hartree-Fock theory [12], this subtraction Hamiltonian can be evaluated by means of the Hartree-Fock potential Eq. (4.15) with respect to an *a* priori chosen reference density P^0, i.e., $h_{\mathrm{sub}}(\mathbf{k}) = v_{\mathrm{hf}}[P^0](\mathbf{k})$. Then, since the mapping $P \mapsto v_{\mathrm{hf}}[P]$ is linear, the Fock operator including the subtraction part, denoted $\hat{F}_{sub}$, can be written as

$$\hat{F}_{sub}[P(\mathbf{k})] = \hat{F}[P(\mathbf{k})] - \hat{V}_{HF}[P^0(\mathbf{k})] = \sum_{\mathbf{k}\in\mathrm{mBZ}} \sum_{mn} \hat{f}^\dagger_{m\mathbf{k}} [h_{\mathrm{BM}}(\mathbf{k})]_{mn} \hat{f}_{n\mathbf{k}} + \hat{V}_{\mathrm{HF}}[\delta P(\mathbf{k})], \tag{4.16}$$

where $\delta P(\mathbf{k}) = P(\mathbf{k}) - P^0(\mathbf{k})$.

Following Eq. (4.6), $P^0(\mathbf{k})$ should be interpreted as the coefficients of the reference density matrix in the BM band basis. The choice of a reference density matrix $P^0(\mathbf{k})$ is not unique and should also be viewed as part of the IBM model. For instance, in Ref. [9, 98], the choice is

$$P^0(\mathbf{k}) = \frac{1}{2} I, \tag{4.17}$$

which is called the *average scheme*, and can be justified when the particle-hole symmetry is conserved or weakly broken. In Ref. [109, 12, 80], $P^0(\mathbf{k})$ is obtained by projecting the zero temperature limit of the density matrix corresponding to two decoupled graphene layers to the BM band basis of the TBG system; this is referred to as the *decoupled scheme*. In the computational simulations presented here, we follow the procedure used in Ref. [86], where terms from the frozen negative energy sea of the BM model are not included in the decoupled subtraction Hamiltonian (cf. [80, Eq. 2]). For additional details on the different decoupled schemes used in the literature, see **??**.

The zero temperature limit ensures that P^0 is uniquely defined even if some of the band energies of the two decoupled graphene layers may become degenerate. Furthermore, the choice of P^0 is only used to define the quadratic part of the IBM Hamiltonian and is assumed to be independent of the filling factor ν. Unless otherwise specified, we adopt the decoupled scheme in all calculations.

Coupled Cluster Theory

Coupled cluster theory is one of the most widely used post-Hartree-Fock correlated wavefunction methods in quantum chemistry [2, 35].

In this ansatz, the ground-state wavefunction takes the form

$$|\Psi\rangle = e^{T(\mathbf{t})} |\Phi_0\rangle, \tag{4.18}$$

where

$$T(\mathbf{t}) = \sum_{\mu} t_\mu X_\mu \tag{4.19}$$

is the cluster operator determined by the cluster amplitudes $\mathbf{t}$, and $|\Phi_0\rangle$ is a chosen reference Slater determinant (most commonly the Hartree-Fock solution). The operators X_μ are the excitation operators with respect to the chosen reference $|\Phi_0\rangle$, i.e.,

$$X_\mu = X^{a_1,\ldots,a_k}_{i_1,\ldots,i_k} = \hat{a}^\dagger_{a_1} \ldots \hat{a}^\dagger_{a_k} \hat{a}_{i_k} \ldots \hat{a}_{i_1}, \tag{4.20}$$

where, for the sake of compactness, we have combined the occupied orbital indices $\{i_l\}$ and virtual orbital indices $\{a_l\}$ in the multi-index μ. The ground-state energy can then be computed as

$$\mathcal{E}(\mathbf{t}) = \langle \Phi_0 | e^{-T(\mathbf{t})} H e^{T(\mathbf{t})} | \Phi_0 \rangle. \tag{4.21}$$

The cluster amplitudes $\mathbf{t}$ are determined by the coupled cluster equations, i.e., a set of polynomial equations of at most degree four (given at most quartic terms in the Hamiltonian) with respect to $\mathbf{t}$:

$$0 = F_\mu(\mathbf{t}) = \langle \Phi_0 | X_\mu^\dagger e^{-T(\mathbf{t})} H e^{T(\mathbf{t})} | \Phi_0 \rangle, \qquad \forall \mu. \tag{4.22}$$

More compactly, Eqs. (4.21) and (4.22) can be combined in the coupled cluster Lagrangian

$$\mathcal{L}(\mathbf{t}, \boldsymbol{\lambda}) = \mathcal{E}(\mathbf{t}) + \langle \boldsymbol{\lambda}, \mathbf{F}(\mathbf{t}) \rangle = \langle \Phi_0 | (I + \Lambda(\boldsymbol{\lambda})) e^{-T(\mathbf{t})} H e^{T(\mathbf{t})} | \Phi_0 \rangle, \tag{4.23}$$

where

$$\Lambda(\boldsymbol{\lambda}) = \sum_\mu \lambda_\mu X_\mu^\dagger. \tag{4.24}$$

The states $|e^{T(\mathbf{t})}\Phi_0\rangle$ and $\langle \Phi_0(I + \Lambda(\lambda))e^{-T(\mathbf{t})}|$ are commonly referred to as the right and left coupled cluster solutions, respectively. The N-RDM in coupled cluster theory is given by

$$\varrho_{CC}(\mathbf{t}, \boldsymbol{\lambda}) = |e^{T(\mathbf{t})}\Phi_0\rangle\langle\Phi_0(I + \Lambda(\boldsymbol{\lambda}))e^{-T(\mathbf{t})}| \tag{4.25}$$

ensuring that $\mathrm{Tr}[H\varrho_{CC}(\mathbf{t}, \boldsymbol{\lambda})] = \mathcal{E}(\mathbf{t})$. The corresponding 1-RDM is then given by

$$[P_{CC}(\mathbf{t}, \boldsymbol{\lambda})]_{p,q} = \langle \Phi_0(I + \Lambda(\boldsymbol{\lambda}))e^{-T(\mathbf{t})} | a_p^\dagger a_q | e^{T(\mathbf{t})}\Phi_0 \rangle, \tag{4.26}$$

see [35] for more details. We emphasize that this ansatz, in its untruncated form, is equivalent to the full configuration interaction method (i.e., the exact diagonalization method) [70, 83, 51], and is thus computationally infeasible for large systems. In the past decades, different levels of approximation have been suggested to reduce computational complexity (see e.g., [2, 18, 76, 68]). The variant used in the subsequent simulations (and arguably one of the most widely used approximate versions of coupled cluster theory) is the truncation of the cluster operator in Eq. (4.19) to only contain one-body and two-body excitations, also known as the coupled cluster singles and doubles (CCSD) method. Note that due to the exponentiation of the cluster operator, the corresponding wavefunction expansion in Eq. (4.18) will still contain contributions from higher excited determinants. One of the central benefits of the exponential ansatz is that it ensures that the energy is size consistent and size

extensive, in particular, for (rank complete) truncations of T such as in CCSD [35]. As in the Hartree-Fock discussion above, we place no restrictions on the (pseudo)spin properties of the excitation operators. Thus we work with the generalized CC ansatz in this work.

Aside from steering the accuracy of the CC approach directly through truncations of the cluster operator in Eq. (4.19), great effort has been put into developing methods that improve the CCSD energy by means of simple, state selective, non-iterative energy corrections that, when added to the CCSD energy, improve the energy of the electronic states of interest [81, 77, 64, 75, 40, 50, 28]. This includes the CCSD(T) [81] method, which yields a perturbative non-iterative energy correction that accounts for the effect of triexcited clusters (i.e., triples) using arguments based on the many-body perturbation theory.

Implementation in PySCF

We use the Python-based Simulations of Chemistry Framework (PySCF) [91, 92] to perform calculations for the IBM model in Eq. (4.4), which can be defined as a "customized Hamiltonian" accessed through the one- and two-electron integrals referred to as `h1e` and `eri`. These integrals are complex-valued, therefore, minor adjustments to PySCF need to be made to enable calculations using these customized Hamiltonians. We also use the "molecular" formulation in PySCF, i.e., the `h1e` and `eri` are stored without taking advantage of the **k**-point symmetry [68]. This can increase the storage cost by a factor of $N_{\mathbf{k}}$, and the computational cost by a polynomial of $N_{\mathbf{k}}$. Interfacing the **k**-point symmetry (periodic boundary condition or "pbc") modules of PySCF is possible and is left here for future work.

Once `h1e` and `eri` are constructed, the PySCF software package allows us to perform GHF and GCCSD calculations on the same footing with a simple code structure. Here is an example:

```
from PySCF import gto, scf, cc

def get_veff(mol, dm, *args):
    vj, vk= scf.hf.dot_eri_dm(eri, dm)
    return vj- vk

mol= gto.M()
mol.incore_anyway= True
mol.nelectron= nelec

ghf_mf= scf.GHF(mol)
ghf_mf.get_hcore= lambda *args: h1e
ghf_mf.get_ovlp= lambda *args: ovlp
```

```
ghf_mf._eri= eri
ghf_mf.get_veff= get_veff

# Running GHF
ghf_mf.kernel()

# Running GCCSD
gcc = cc.GCCSD(ghf_mf)
gcc.kernel()
```

Listing 4.1: Example code running GHF and GCCSD in PySCF from precomputed integrals.

After the calculations, PySCF also provides compact instructions to evaluate the 1-RDMs so that we can evaluate the observables to detect the symmetry breaking in Section 4.4.

Similarly, the `h1e` and `eri` objects may be saved and used to define the Hamiltonian for the Block2 program for a QC-DMRG calculation (DMRG calculations can be performed directly through a PySCF interface). Thus DMRG calculations can be used to assess the same ground state as targeted by the HF and CC calculations, and we will use such results for benchmarking in this work. Further details of the DMRG calculations are provided in Appendix **??**.

4.4 Symmetries

Both the BM and IBM models satisfy a number of symmetries which have been used extensively to analyze the properties of both models, particularly in the chiral limit [12, 9]. For TBG, the symmetries of interest are point-group symmetries, time-reversal symmetry, and their compositions. Point-group symmetries are unitary and time-reversal symmetry is antiunitary. Some relevant symmetries in the valley and spin-polarized BM and IBM models are summarized in Table 4.1.

In this section, we propose a set of gauge-invariant order parameters which can be used to detect spontaneous symmetry breaking in the 1-RDM $P(\mathbf{k})$. Our final results are summarized in Table 4.2. We defer proofs of the claims given in this section to **????**.

Detecting Symmetry Breaking: Unitary Case

We begin by considering the simpler case of unitary symmetries. For a point-group symmetry g, due to the properties of the Bloch transform, there exists a unitary

Symmetry	Real space	Momentum space	Type
C_{2z}	swap sublattice	swaps valleys; $\mathbf{k} \to -\mathbf{k}$	Unitary
C_{3z}	rotate by 120°	$\mathbf{k} \to C_{3z}\mathbf{k}$	Unitary
$\mathcal{T}$		swaps valleys; $\mathbf{k} \to -\mathbf{k}$	Antiunitary
$C_{2z}\mathcal{T}$	swap sublattice	$\mathbf{k} \to \mathbf{k}$	Antiunitary

Table 4.1: Some relevant symmetry operations for the spinless, valleyless IBM model.

$D(g)$, called the *representation matrix*, so that the creation operators, $c^\dagger_{\mathbf{k}}$, transform via the rule

$$\begin{aligned}(g\hat{c}^\dagger_{\mathbf{k}}g^{-1})(\alpha) &= \sum_{\alpha'} \hat{c}^\dagger_{g\mathbf{k}}(\alpha')[D(g)]_{\alpha',\alpha},\\ (g\hat{c}_{\mathbf{k}}g^{-1})(\alpha) &= \sum_{\alpha'} \hat{c}_{g\mathbf{k}}(\alpha')[D(g)]^*_{\alpha',\alpha}.\end{aligned} \tag{4.27}$$

For instance, C_{3z} is a unitary symmetry, and it maps $\mathbf{k}$ to $C_{3z}\mathbf{k}$. Its representation matrix in the primitive basis can be written as

$$[D(C_{3z})]_{\mathbf{G}'\sigma'l',\mathbf{G}\sigma l} = \delta_{\mathbf{G}',C_{3z}\mathbf{G}}(e^{\mathrm{i}\frac{2\pi}{3}\sigma_z})_{\sigma',\sigma}\delta_{l',l}. \tag{4.28}$$

Since the IBM model is defined in terms of the band creation operators, $\{f^\dagger_{n\mathbf{k}}\}$, we need to determine how the symmetry g acts on the band creation operators. The object which encodes this symmetry action is known as the *sewing matrix* [29, 9]. Given a set of bands $\{u_{n\mathbf{k}}\}$ and a unitary symmetry operation g, the sewing matrix $[B(g)]_{\mathbf{k}}$ is defined as:

$$[B(g)]_{\mathbf{k},mn} := \langle u_m(g\mathbf{k})|D(g)|u_n(\mathbf{k})\rangle\,. \tag{4.29}$$

Assuming $[B(g)]_{\mathbf{k}}$ is unitary, the band creation operators transform under g by the rule (see **??**):

$$\begin{aligned}g\hat{f}^\dagger_{n\mathbf{k}}g^{-1} &= \sum_m \hat{f}^\dagger_{m,g\mathbf{k}}[B(g)]_{\mathbf{k},mn},\\ g\hat{f}_{n\mathbf{k}}g^{-1} &= \sum_m \hat{f}_{m,g\mathbf{k}}[B(g)^\dagger]_{\mathbf{k},mn}.\end{aligned} \tag{4.30}$$

The unitarity of $[B(g)]_{\mathbf{k}}$ is satisfied when the energy bands $\{u_{n\mathbf{k}}\}$ are isolated, i.e., there is an energy gap between the chosen bands and the rest of the energy bands (**??**).

Using this transformation rule and recalling that the 1-RDM for a state $|\Psi\rangle$ is defined by $[P(\mathbf{k})]_{mn} = \langle\Psi|\hat{f}^\dagger_{n\mathbf{k}}\hat{f}_{m\mathbf{k}}|\Psi\rangle$, we can conclude that if the following commutator-like quantity

$$\begin{aligned}\mathcal{C}_{\mathbf{k}}(g) &= \left\| [B(g)]^\dagger_{\mathbf{k}} P(g\mathbf{k}) [B(g)]_{\mathbf{k}} - P(\mathbf{k}) \right\| \\ &= \| P(g\mathbf{k})[B(g)]_{\mathbf{k}} - [B(g)]_{\mathbf{k}} P(\mathbf{k}) \|\end{aligned} \tag{4.31}$$

does not vanish, then the 1-RDM breaks the symmetry g. Here $\|\cdot\|$ can be any unitarily invariant norm. Additionally, it can be shown that $\mathcal{C}_{\mathbf{k}}(g)$ is invariant under gauge transformations of the band creation operators (see **??**).

Detecting Symmetry Breaking: Antiunitary Case

We now turn to consider the case of antiunitary symmetries. Any antiunitary symmetry $\widetilde{g}$ can be written as $\widetilde{g} = g\mathcal{K}$. Here g is a unitary symmetry and $\mathcal{K}$ is complex conjugation satisfying $\mathcal{K}(a\,|\mathbf{G},\sigma,l\rangle) = a^*\,|\mathbf{G},\sigma,l\rangle$ for any $a \in \mathbb{C}$. For an antiunitary symmetry $g\mathcal{K}$, we define the representation matrix as $D(g\mathcal{K}) := D(g)$. For instance, $C_{2z}\mathcal{T}$ is an antiunitary symmetry. It satisfies $(C_{2z}\mathcal{T})\mathbf{k} = \mathbf{k}$, and its representation matrix in the primitive basis can be written as

$$[D(C_{2z}\mathcal{T})]_{\mathbf{G}'\sigma'l',\mathbf{G}\sigma l} = \delta_{\mathbf{G}',\mathbf{G}}(\sigma_x)_{\sigma',\sigma}\delta_{l',l}. \tag{4.32}$$

Given a set of bands $\{u_n(\mathbf{k})\}$ and an antiunitary symmetry operation $g\mathcal{K}$, the corresponding sewing matrix $[B(g\mathcal{K})]_{\mathbf{k}}$ is defined by the formula:

$$[B(g\mathcal{K})]_{\mathbf{k},mn} := \langle u_m(g\mathbf{k})|D(g)|u^*_n(\mathbf{k})\rangle\,. \tag{4.33}$$

As before, when these bands are isolated, $[B(g\mathcal{K})]_{\mathbf{k}}$ is unitary (**??**) and the band creation operators transform under $g\mathcal{K}$ by the same rule as in Eq. (4.30).

Similar to calculations to the unitary case, if the following commutator-like quantity

$$\begin{aligned}\mathcal{C}_{\mathbf{k}}(g\mathcal{K}) &= \left\| [B(g\mathcal{K})]^\top_{\mathbf{k}} P(g\mathbf{k})^* [B(g\mathcal{K})]^*_{\mathbf{k}} - P(\mathbf{k}) \right\| \\ &= \| P(g\mathbf{k})[B(g\mathcal{K})]_{\mathbf{k}} - [B(g\mathcal{K})]_{\mathbf{k}} P(\mathbf{k})^* \|\end{aligned} \tag{4.34}$$

does not vanish, then the 1-RDM breaks the antiunitary symmetry $g\mathcal{K}$. Furthermore, $\mathcal{C}_{\mathbf{k}}(g\mathcal{K})$ is invariant under gauge transformations of the band creation operators (see **??**).

	Sewing matrix	Order parameter
Unitary (g)	$\langle u_m(g\mathbf{k})\|D(g)\|u_n(\mathbf{k})\rangle$	$\|P(g\mathbf{k})[B(g)]_{\mathbf{k}} - [B(g)]_{\mathbf{k}}P(\mathbf{k})\|$
Antiunitary ($g\mathcal{K}$)	$\langle u_m(g\mathbf{k})\|D(g)\|u_n^*(\mathbf{k})\rangle$	$\|P(g\mathbf{k})[B(g\mathcal{K})]_{\mathbf{k}} - [B(g\mathcal{K})]_{\mathbf{k}}P(\mathbf{k})^*\|$

Table 4.2: The definitions of the sewing matrix and symmetry order parameter for a unitary symmetry g and an antiunitary symmetry $g\mathcal{K}$.

Connection with the $C_{2z}\mathcal{T}$ order parameter in the Chern band basis

Let us also show the connection between $\mathcal{C}_{\mathbf{k}}(\mathcal{C}_{2z}\mathcal{T})$ and the order parameter used in [86] using a particular gauge fixing called the Chern band basis. According to the gauge choice of the Chern band basis, the sewing matrix takes the form

$$[B(C_{2z}\mathcal{T})]_{\mathbf{k}} = \sigma_x e^{\mathrm{i}\theta(\mathbf{k})}.$$

The sewing matrix in this basis resembles the representation matrix in the primitive basis in Eq. (4.32), except that $\theta(\mathbf{k})$ is a $\mathbf{k}$-dependent phase factor. In this basis, the $C_{2z}\mathcal{T}$ symmetry breaking can be detected by computing

$$\gamma_z(\mathbf{k}) = \mathrm{Tr}[P(\mathbf{k})\sigma_z] = P_{11}(\mathbf{k}) - P_{22}(\mathbf{k}). \tag{4.35}$$

Note that the commutator for the $C_{2z}\mathcal{T}$ symmetry satisfies

$$P(\mathbf{k})[B(C_{2z}\mathcal{T})]_{\mathbf{k}} - [B(C_{2z}\mathcal{T})]_{\mathbf{k}}P(\mathbf{k})^* = e^{\mathrm{i}\theta(\mathbf{k})}\begin{pmatrix} P_{21}(\mathbf{k}) - P_{12}(\mathbf{k})^* & P_{22}(\mathbf{k}) - P_{11}(\mathbf{k}) \\ P_{11}(\mathbf{k}) - P_{22}(\mathbf{k}) & P_{12}(\mathbf{k}) - P_{21}(\mathbf{k})^* \end{pmatrix},$$

where we have used the fact that $P_{11}(\mathbf{k})$ and $P_{22}(\mathbf{k})$ are real. Therefore $\gamma_z(\mathbf{k})$ can be interpreted as checking the magnitude of the off-diagonal element of the commutator in the Chern band basis. However, the order parameter $\gamma_z(\mathbf{k})$ is designed specifically for the Chern band basis and $C_{2z}\mathcal{T}$ symmetry, and does not generalize to other band bases and other symmetries. On the other hand, the commutator can be used with any symmetry of interest and works for any band basis.

4.5 Numerical results

Throughout our tests, we will use $\mathbf{k}$-mesh of size (n_{k_x}, n_{k_y}), and we always fix $n_{k_x} = 2n_{k_y}$. The number of $\mathbf{G}$ vectors is controlled by the number of *shells* n_{shell}, which

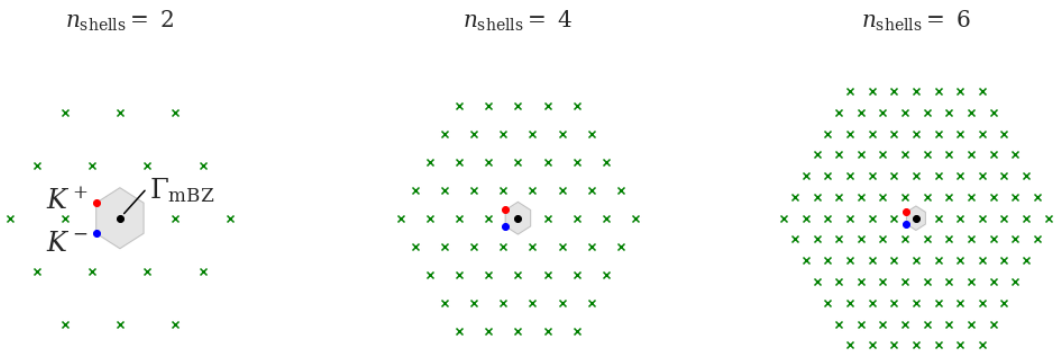

Figure 4.2: A plot of the moiré reciprocal lattice points included for $n_{shells} = 2, 4, 6$ with the two valleys (K^+, K^-) and the Gamma point $(\Gamma_{\text{m}BZ})$ marked. Note that the points are closed under C_{3x} rotation and can be given by the formula $\{\mathbf{G}_{\text{m}oiré}[m, n]^\top : |m + n| \leq n_{shells}, (m, n) \in \mathbb{Z}^2\}$ where $\mathbf{G}_{\text{m}oiré}$ is the generating matrix for the moiré lattice.

specifies a number moiré reciprocal lattice vectors used in the interlayer coupling term in the BM model (see Fig. 4.2). The number of included moiré reciprocal lattice vectors is bounded by $3(n_{\text{shell}} + 1)^2$. The inverse temperature used in the decoupled subtraction scheme (**??**) is $\beta = 1000$ eV^{-1}. We express $\mathcal{C}_{\mathbf{k}}(C_{2z}\mathcal{T})$ in Eq. (4.34) in the spectral norm, and report the order parameter averaged over the number of **k**-points. We begin by studying the convergence of the IBM model with respect to discretization parameters in Section 4.5. Then we report the results of HF and post-HF calculations in the integer filling regime in Section 4.5 and compare the effects of different subtraction schemes in Section 4.5. Finally, we report the effects that initialization has on HF and post-HF calculations in the non-integer filling regime in Section 4.5.

Convergence of parameters at the Hartree-Fock level

As mentioned in Section 4.3, we do not exploit **k**-point symmetry in our current implementation using PySCF. As such, for larger **k**-meshes we incur significantly higher memory costs as compared to code which does exploit this symmetry. For our convergence tests, we test system sizes $n_{k_x} = 4, 8, 12$ exclusively using PySCF, and system sizes $n_{k_x} = 16, 20$ are tested using a separate code used in Ref. [86].

In Fig. 4.3a, we show the results of testing the convergence of Hartree-Fock energy

with respect to the number of shells $n_{\text{shell}} = 2, 4, 6, 10$ at ratios $w_0/w_1 = 0, 0.3, 0.6, 0.9$ with the **k**-mesh fixed to $n_{k_x} = 12$. In Fig. 4.3b, we show the results of the convergence test of Hartree-Fock energy per electron with respect to the number of **k**-points $n_{k_x} = 4, 8, 12, 16, 20$ at ratios $w_0/w_1 = 0.0, 0.3, 0.6, 0.9$ with the number of shells fixed to $n_{\text{shell}} = 6$. The energy differences reported in Figs. 4.3a and 4.3b are the differences between consecutive energies of n_{shell} and n_{k_x}, respectively. From these experiments, we find that the choice $n_{k_x} = 8$ and $n_{\text{shell}} = 8$ provides a good compromise between accuracy and required computation time.

Aside from the Hartree-Fock energy, we investigate the convergence of the HOMO-LUMO gap with respect to the number of **k**-points $n_{k_x} = 4, 8, 12, 16, 20$, see Fig. 4.4a. The computations suggest that when $w_0/w_1 = 0.9$, the band gap is significantly smaller than its value when $w_0/w_1 < 0.7$ (~ 30 meV), and that the gap decreases as the Brillouin zone sampling refines. By extrapolating to the thermodynamic limit, we find that the limiting value of the band gap when $w_0/w_1 = 0.9$ is 3meV, see Fig. 4.4a (b). On the other hand, when $w_0/w_1 = 0.9$, the fact that the two band, single valley model has a nonzero Wilson loop winding number [89] combined with the numerical observation that the density matrix preserves the $C_{2z}\mathcal{T}$ symmetry, implies that the Hartree-Fock gap must close *somewhere* in the Brillouin zone [1]. To verify this statement, we perform an additional *non-self-consistent* Hartree-Fock calculation with a fine Brillouin zone sampling scheme (see **??**). This confirms that the Hartree-Fock gap should indeed vanish, and the residual value of the 3 meV band gap should be attributed to the extrapolation error from finite-size self-consistent Hartree-Fock calculations.

Integer filling

We here present HF, CCSD, CCSD(T), and DMRG calculations for twisted bilayer graphene at integer filling, i.e., $\nu = 0$ which amounts to one electron per moiré site. The subsequently presented results are obtained for a discretization of TBG using $n_{k_x} = 2n_{k_y} = 8$, $n_{\text{shell}} = 8$, and using the decoupled subtraction scheme. The computations are performed for different ratios of the interlayer moiré potential parameters, i.e., $w_0/w_1 \in [0, 0.95]$. The correlation energy per moiré site is defined to be the difference between the total energies from the correlated wavefunction method, i.e., CCSD, CCSD(T), or DMRG, and the HF energy. All energies are reported per moiré site.

Fig. 4.5a shows that the total energy is not monotone with respect to ratio w_0/w_1, and attains a maximum at around $w_0/w_1 = 0.5$. However, the correlation energy monotonically decreases with respect to the ratio until $w_0/w_1 = 0.8$, see Fig. 4.5b. The magnitude of the correlation energy per site is small, which qualitatively agrees

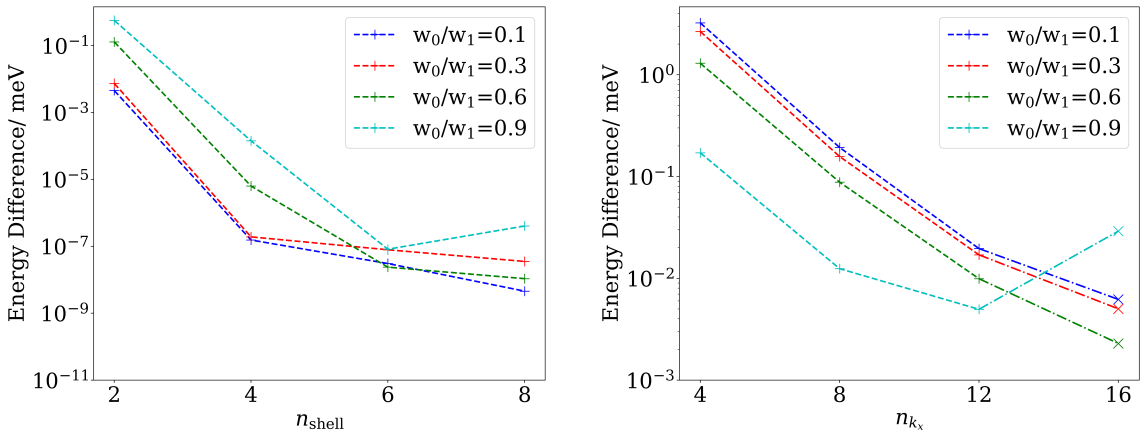

Figure 4.3: (a) The convergence test of Hartree-Fock with respect to the number of shells n_{shell} at ratio $w_0/w_1 = 0.0, 0.3, 0.6, 0.9$. $n_{k_x} = 2n_{k_y} = 8$ is fixed. (b) The convergence test of Hartree-Fock with respect to the number of **k**-points $n_{k_x} = 2n_{k_y}$ at ratio $w_0/w_1 = 0.0, 0.3, 0.6, 0.9$. $n_{\text{shell}} = 6$ is fixed. Calculations with $n_{k_x} = 4, 8, 12$ are computed using the molecular structure module provided by PySCF, while $n_{k_x} = 16, 20$ are computed using a separate code exploiting **k**-point symmetry.

with the theoretical prediction that the correlation energy vanishes (i.e., Hartree-Fock theory gives the exact ground state energy) at the chiral limit [12]. However, the reason why the correlation energy does not exactly vanish at the chiral limit is due to the choice of the subtraction Hamiltonian, which we elaborate on in more detail in Section 4.5. Compared to the energy evaluated at the CCSD level, the additional correlation energy obtained by CCSD(T) is negligible, see Fig. 4.5b. Further comparison of the CCSD and CCSD(T) energies with DMRG energies extrapolated to the infinite bond-dimension limit shows that CCSD and CCSD(T) recover 95.4–100% and 98.5–100% of the correlation energy, respectively. Note that due to the high computational cost, we only compute extrapolated DMRG results for every other point in Figs. 4.5a and 4.5b; this suffices since there are no significant details in the intermediate range.

We also report the Fermi-Dirac entropy per moiré site:

$$S_{\text{FD}} = -\frac{1}{n_{k_x} n_{k_y}} \sum_i \left(p_i \ln p_i + (1 - p_i) \ln(1 - p_i) \right), \tag{4.36}$$

where $\{p_i\}$ are the eigenvalues of the 1-RDM. By construction, $S_{\text{FD}} = 0$ in the

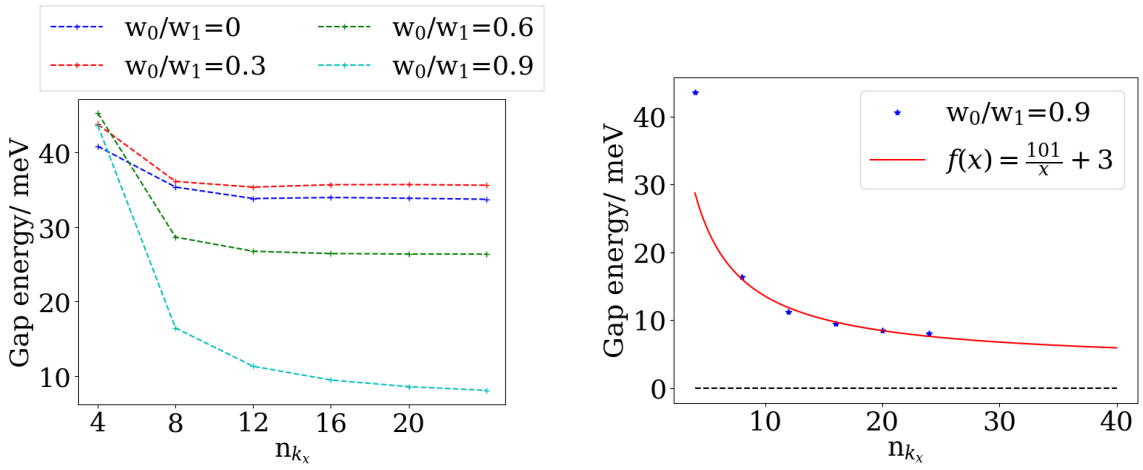

Figure 4.4: (a) Convergence test of the HOMO-LUMO gap with respect to the number of **k**-points $n_{k_x} = 2n_{k_y}$ at ratio $w_0/w_1 = 0.0, 0.3, 0.6, 0.9$. $n_{\text{shell}} = 6$ is fixed. Calculations with $n_{k_x} = 4, 8, 12$ are computed using the molecular structure module provided by PySCF. (b) Extrapolation of the HOMO-LUMO gap as a function of n_{k_x} at $w_0/w_1 = 0.9$. The fitted function is $f(x) = \frac{a}{x} + c$ where $a = 101$, and $c = 3$. The residual value of the 3 meV band gap at the thermodynamic limit should be attributed to the extrapolation error from finite-size self-consistent Hartree-Fock calculations.

Hartree-Fock theory. We find that the Fermi-Dirac entropy is between 0.009 and 0.032 from the DMRG calculations. This reveals that the solutions for all parameter ratios are close to being single Slater determinants.

Investigating the HOMO-LUMO gap, we observe a gap closing as we transition from the chiral limit to $w_0/w_1 = 1$, see Fig. 4.6. The HOMO-LUMO gap closes around $w_0/w_1 = 0.85$, indicating a transition from an insulating to a metallic phase. This is in agreement with the finding in Fig. 4.4a.

Next, we investigate the effect of electronic correlations on the order parameter $\mathcal{C}_{\mathbf{k}}(C_{2z}\mathcal{T})$ in Eq. (4.34). Fig. 4.7 reports the $C_{2z}\mathcal{T}$ order parameter as a function of the ratio w_0/w_1, which shows a transition from the $C_{2z}\mathcal{T}$ broken phase to a $C_{2z}\mathcal{T}$ symmetric phase, and the phase transition occurs around $w_0/w_1 = 0.8$. This agrees with the result in [86], where the order parameter uses the expression Eq. (4.35) in the Chern band basis. Fig. 4.7b shows that compared to CCSD, HF slightly overestimates the symmetry breaking, and the difference between HF and CCSD

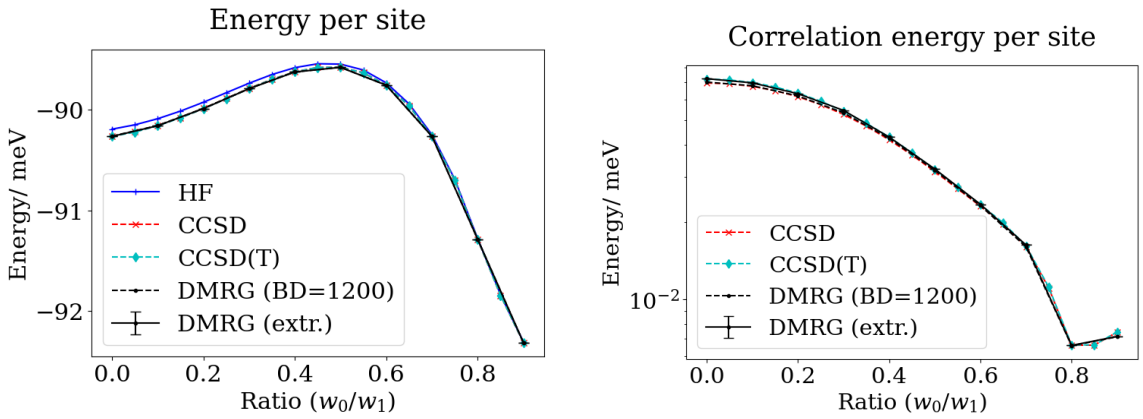

Figure 4.5: (a) The HF, CCSD, CCSD(T), and DMRG (bond-dimension is $BD = 1200$ and extrapolated to the infinite bond dimension limit [DMRG (extr.)]) energies per moiré site in meV as a function of the ratio w_0/w_1. (b) The absolute value of CCSD, CCSD(T), and DMRG (bond-dimension $BD = 1200$ and extrapolated to the infinite bond dimension limit [DMRG (extr.)]) correlation energies in meV per moiré site as a function of the ratio w_0/w_1.

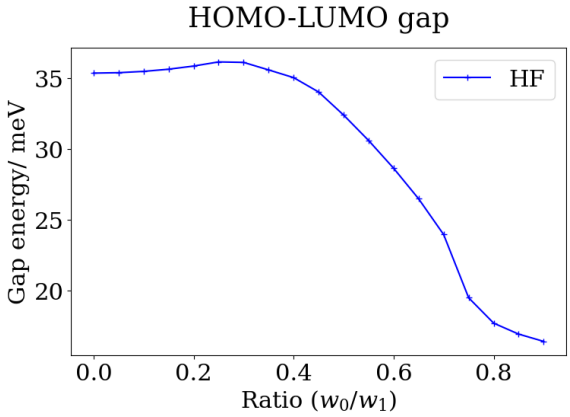

Figure 4.6: The HOMO-LUMO gap as a function of the ratio w_0/w_1.

decreases as the ratio w_0/w_1 increases.

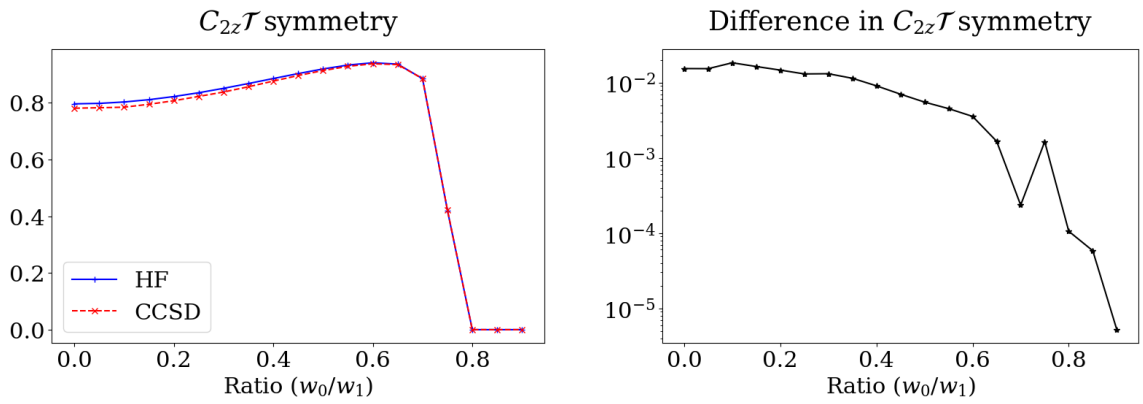

(a) (b)

Figure 4.7: (a) The HF and CCSD $C_{2z}\mathcal{T}$ symmetry predictions as a function of the ratio w_0/w_1. (b) The absolute value of the difference of the $C_{2z}\mathcal{T}$ symmetry characteristic of CCSD and the HF as a function of the ratio w_0/w_1.

Model discrepancies due to the subtraction Hamiltonian

To assess the effect of the subtraction Hamiltonian obtained from the decoupled scheme, we report the results using another subtraction Hamiltonian obtained from the average scheme (see Section 4.3). We demonstrate the differences of the total energy and the $C_{2z}\mathcal{T}$ order parameter. Additionally, we compute and compare the effect of the subtraction Hamiltonians on the band structure, see **??**.

Comparing energies at the HF and CCSD level of theory we first note that using the decoupled scheme yields a more pronounced maximum in the energy, i.e., the curvature around the maximum is greater when employing the decoupled scheme, see Fig. 4.8a. Moreover, we observe that employing the average scheme subtraction Hamiltonian yields an overall lower correlation energy, see Fig. 4.8b. Interestingly, both subtraction Hamiltonians yield a similar amount of electronic correlation near $w_0/w_1 \geq 0.8$. Aside from the magnitude of the correlation, we find that the electronic correlation increases as a function of w_0/w_1 when using the average scheme subtraction Hamiltonian whereas the electronic correlation decreases as a function of w_0/w_1 when using the decoupled scheme subtraction Hamiltonian.

The different subtraction Hamiltonians also affect the order parameter, see Fig. 4.9. We observe a very clean first-order phase transition when employing the average scheme subtraction Hamiltonian whereas the decoupled scheme subtraction Hamiltonian yields a more continuous transition. This agrees with earlier numerical results

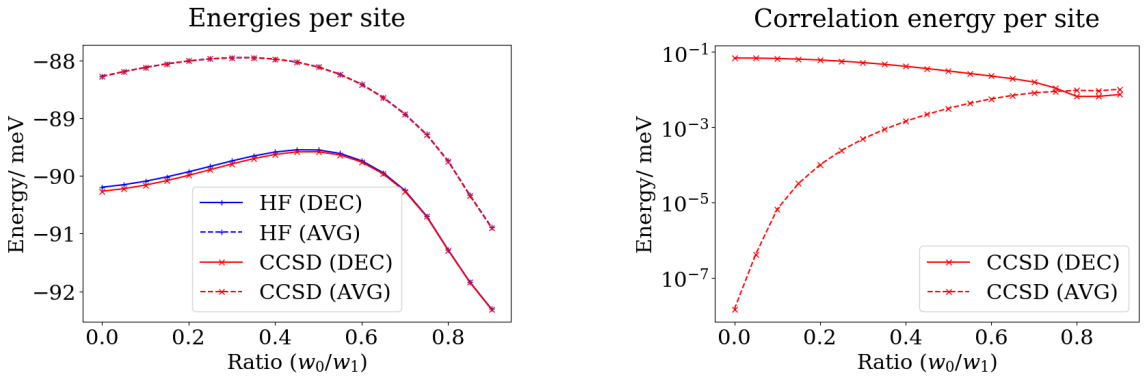

(a) (b)

Figure 4.8: (a) The HF and CCSD energies per moiré site in meV as a function of the ratio w_0/w_1 for decoupled and average scheme subtraction Hamiltonians. (b) The absolute value of CCSD correlation energies in meV per moiré site as a function of the ratio w_0/w_1 for decoupled and average scheme subtraction Hamiltonians.

in [43, Fig. 6]. Correlation effects on the order parameter appear to be larger in the decoupled scheme near the chiral limit, see Fig. 4.9b.

In the non-integer filling regime, we observe that the decoupled and average scheme subtraction Hamiltonian yield qualitatively similar results, see Fig. 4.10a. We here initialize the HF computations with a one-particle reduced density matrix following [86]. We find that for the decoupled scheme subtraction Hamiltonian, the total energy changes more rapidly with respect to ν (i.e., a larger curvature in ν), and the energy correction through post-HF methods is smaller than the energy corrections using the average scheme, i.e., using the decoupled scheme subtraction Hamiltonian yields stronger electronic correlation effects.

Non-integer filling

We now proceed to HF, CCSD, CCSD(T), and DMRG calculations at non-integer fillings. The subsequently presented results are again obtained for a discretization of TBG using $n_{k_x} = 2n_{k_y} = 8$, $n_{\text{shell}} = 8$. The TBG is here modeled with $n_{elec} \in \{26, 28, 30, 32, 34, 36, 38\}$, i.e., with a filling factor of $\nu = n_{elec}/32 - 1$, and $|\nu| < 0.2$. We moreover fix the initialization of the HF calculations following [86] while adjusting the particle number correspondingly. We will investigate the effect of correlated methods first by varying the filling factor ν at the chiral limit, and then

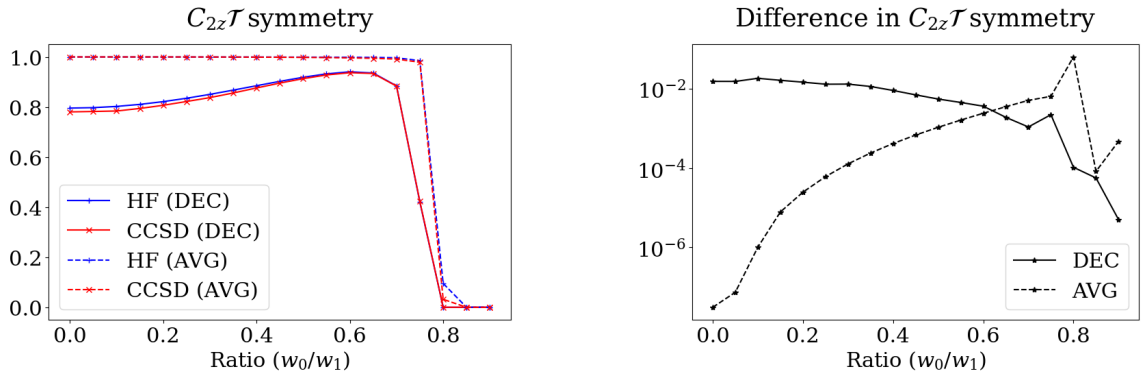

(a) (b)

Figure 4.9: (a) The HF and CCSD $C_{2z}\mathcal{T}$ symmetry predictions as a function of the ratio w_0/w_1 for decoupled and average scheme subtraction Hamiltonian. (b) The absolute value of the difference of the $C_{2z}\mathcal{T}$ symmetry characteristic of CCSD and the HF as a function of the ratio w_0/w_1 for decoupled and average scheme subtraction Hamiltonian.

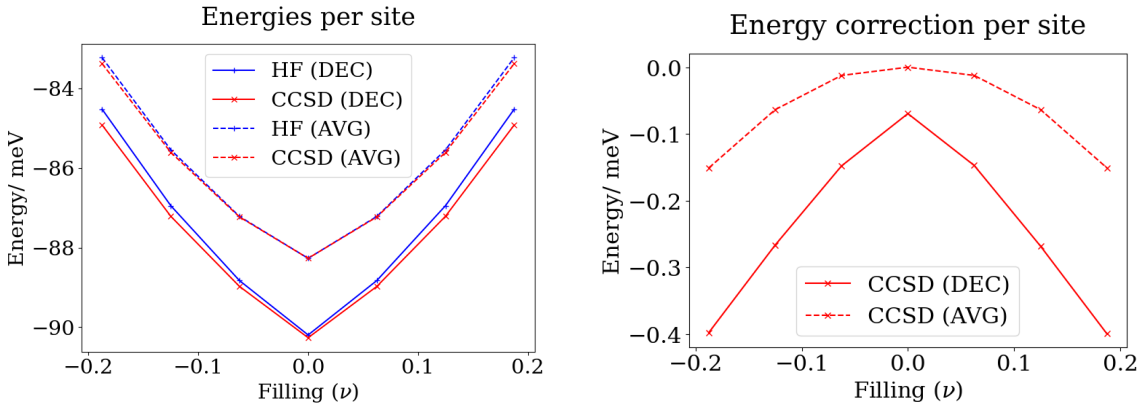

(a) (b)

Figure 4.10: (a) The HF and CCSD energies per moiré site in meV in the chiral limit as a function of the filling for decoupled and average scheme subtraction Hamiltonian. (b) The CCSD energy correction per moiré site in meV in the chiral limit as a function of the filling for decoupled and average scheme subtraction Hamiltonian

by varying both the filling factor ν and the interlayer coupling ratio w_0/w_1. In the next subsection, we will see that the "true" HF global minimum can be sensitive to the initial guess and difficult to reach. Hence, we will refer to the difference between post-HF energies and the HF energy only as an "energy correction" rather than the "correlation energy".

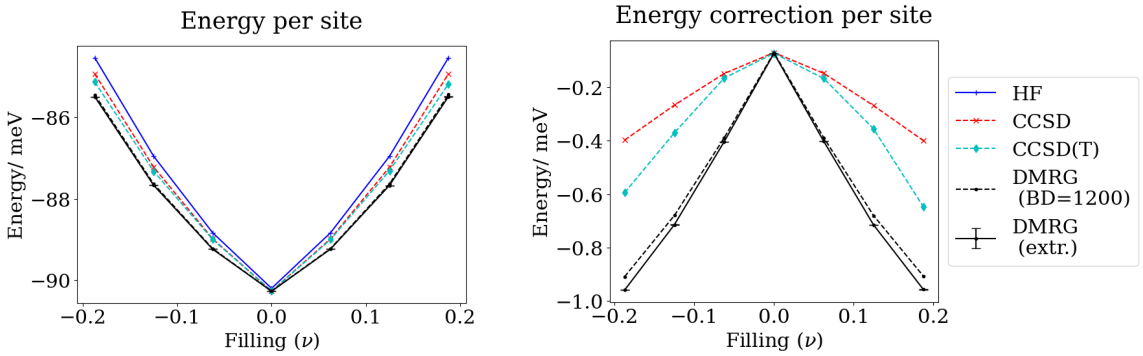

(a) $w_0/w_1 = 0$ (b) $w_0/w_1 = 0$

Figure 4.11: (a) The HF and CCSD, CCSD(T), and DMRG energies per moiré site in meV in the chiral limit ($w_0/w_1 = 0$) as a function of the filling. (b) The CCSD, CCSD(T), and DMRG correlation energies per moiré site in meV in the chiral limit as a function of the filling.

At the chiral limit, Fig. 4.11a and 4.11b show that the energy correction by means of post-HF methods increases as ν deviates from 0. However, DMRG benchmark computations reveal that the Fermi-Dirac entropy in Eq. (4.36) is very small for all filling factors under consideration (see Table 4.3). This indicates that the solution is relatively well described by a single Slater determinant, and thus by the HF theory.

Filling (ν)	-0.188	-0.125	-0.062	0	0.062	0.125	0.188
S_{FD}	0.067	0.051	0.107	0.033	0.107	0.052	0.069

Table 4.3: Fermi-Dirac entropy of the DMRG computations with bond dimension 1100 in the chiral limit for different fillings ν.

We find that at this point, DMRG calculations are too expensive to be applied to evaluate the entire 2D phase diagram. Hence we investigate the landscape of the energy correction provided by CCSD with respect to the filling and the ratio w_0/w_1,

we observe that the magnitude of the energy correction increases with respect to $|\nu|$ (see Fig. 4.12a). Note that Fig. 4.12a is on a logarithmic scale, that is, we here depict the absolute values of the obtained energy corrections. The computed energy corrections are consistently negative. We also investigate the HOMO-LUMO gap landscape with respect to the filling and the ratio w_0/w_1 in Fig. 4.12b. We observe that the HOMO-LUMO gap reaches its maximum at the chiral limit at $\nu = 0$. When transitioning into the fractional filling regime (i.e., at $|\nu| > 0.0625$), the HOMO-LUMO gap decreases by one order of magnitude, indicating a metallic phase.

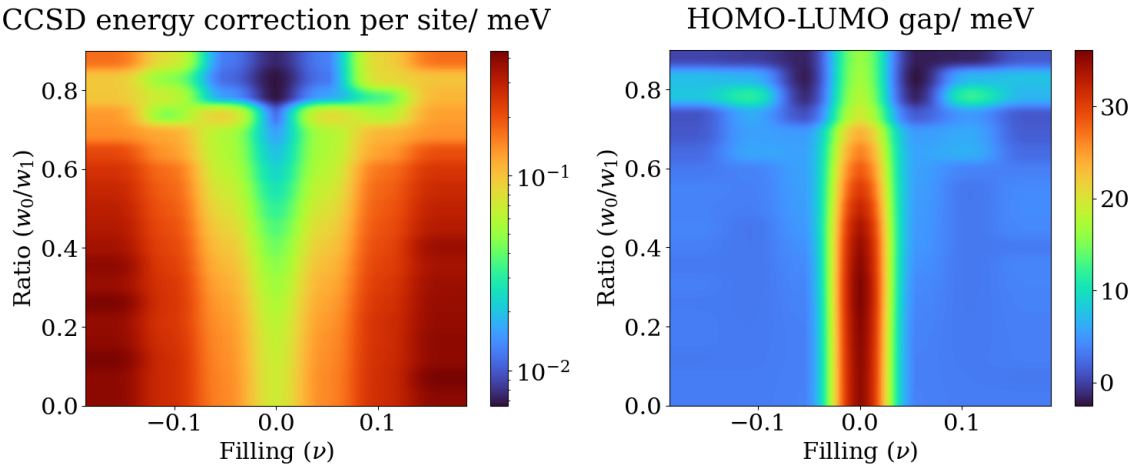

(a) (b)

(b) Phase diagram of the HOMO-LUMO gap in meV with respect to the filling and the ratio w_0/w_1.

(b) Phase diagram of the HOMO-LUMO gap in meV with respect to the filling and the ratio w_0/w_1.

Figure 4.12: (a) Energy surface of the CCSD energy correction per moiré site in meV with respect to the filling and the ratio w_0/w_1.
(b) Phase diagram of the HOMO-LUMO gap in meV with respect to the filling and the ratio w_0/w_1.

In Fig. 4.13a we report the phase diagram of the order parameter for the $C_{2z}\mathcal{T}$ symmetry with respect to the filling ν and the ratio w_0/w_1. We find that the difference between the order parameters obtained by HF and CCSD also increases as $|\nu|$ deviates from 0, but the phase diagrams qualitatively agree with each other, see Fig. 4.13b. The phase diagram indicates that the location of the phase transition from a $C_{2z}\mathcal{T}$ broken phase to a $C_{2z}\mathcal{T}$ symmetric phase is a function of the filling

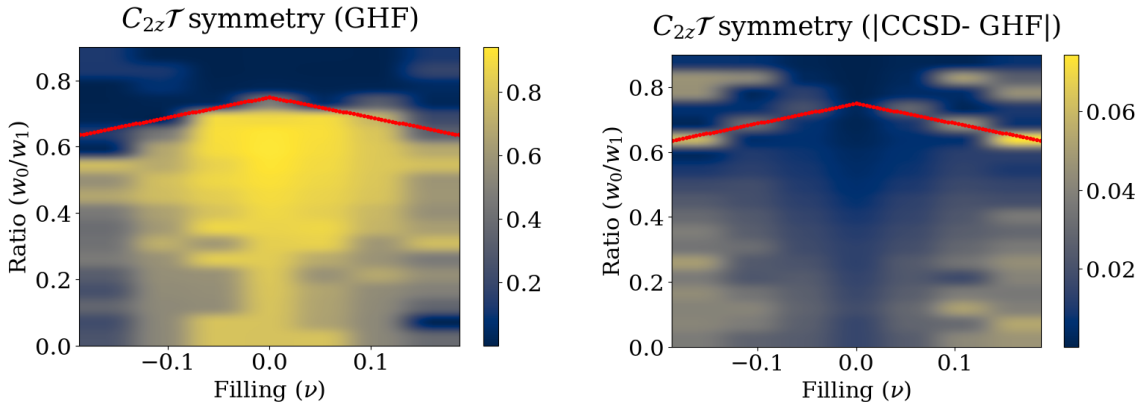

(a) (b)

Phase diagram of $C_{2z}\mathcal{T}$ symmetry predictions at the HF level of theory. The dotted red line indicates the phase transition as a function of the filling ν. (b) Phase diagram of the difference of $C_{2z}\mathcal{T}$ symmetry predictions comparing CCSD and HF. The dotted red line indicates the phase transition as a function of the filling ν.

Phase diagram of $C_{2z}\mathcal{T}$ symmetry predictions at the HF level of theory. The dotted red line indicates the phase transition as a function of the filling ν. (b) Phase diagram of the difference of $C_{2z}\mathcal{T}$ symmetry predictions comparing CCSD and HF. The dotted red line indicates the phase transition as a function of the filling ν.

Figure 4.13: (a)
Phase diagram of $C_{2z}\mathcal{T}$ symmetry predictions at the HF level of theory. The dotted red line indicates the phase transition as a function of the filling ν. (b) Phase diagram of the difference of $C_{2z}\mathcal{T}$ symmetry predictions comparing CCSD and HF. The dotted red line indicates the phase transition as a function of the filling ν.

ν. We highlight this dependence with a dotted red line in Fig. 4.13b. Recall that at integer filling, the system is either in a $C_{2z}\mathcal{T}$ symmetry breaking and insulating state, or in a $C_{2z}\mathcal{T}$ trivial and metallic state [86]. However, in the non-integer filling case, we find that the system can be in a $C_{2z}\mathcal{T}$ symmetry breaking and metallic state. We also find that the difference between CCSD and HF is negative except for a few points on the phase diagram, indicating that HF tends to slightly over-polarize the $C_{2z}\mathcal{T}$ order parameters.

Impact of the Initial One-Particle Reduced Density Matrix

In the previous section, we employed a particular initial 1-RDM for the HF calculations. We now investigate the effect of the initial guess, by drawing initial 1-RDMs from three different schemes:

Scheme 1 Generate 1-RDM from a random distribution.

Scheme 2 Construct 1-RDM from a random distribution and enforce translation symmetry.

Scheme 3 Build 1-RDM from the band structure at the charge neutrality point and enforce translation symmetry.

Specifically, Ref. [7] finds that with the average subtraction scheme and at the chiral limit $w_0/w_1 = 0$, the charge ± 1 excitations from the charge neutrality point can be derived analytically. The charge $+1$ state can be identified with the Hartree-Fock state by adding an orbital at the conduction band minimum (CBM), and the charge -1 state with the Hartree-Fock state by removing an orbital at the valence band maximum (VBM), respectively. We generalize this observation to larger dopings by adding / removing $|\nu| N_{\mathbf{k}}$ orbitals in the conduction / valence bands to obtain an initial guess in Scheme 3. We then introduce a small amount of numerical noise by adding Gaussian random matrices, and impose physical constraints (pure state and translation symmetry conditions).

We perform computations at the HF and CCSD level of theory for different fillings in the chiral limit. At half-filling, HF and CCSD can robustly converge to the global minimum for all three schemes. On the other hand, the outcome obtained away from the charge neutrality point can vary significantly depending on the method used to generate the initial guess. When we draw the initial 1-RDM from Scheme 1, even after employing various techniques in quantum chemistry calculations (e.g., level-shifting, second-order optimizers, and temperature annealing), the HF result can still depend on the initial random guess, indicating the existence of multiple local minima. The energy differences of these local minima are small, but the magnitude of these differences can be comparable to that of the CCSD energy correction (see Figs. 4.14a and 4.15a).

Figs. 4.14 and 4.15 illustrate that that the magnitudes of the energy fluctuation in Scheme 1 (random initial guess without translation symmetry) and Scheme 2 (random initial guess with translation symmetry) are comparable. Remarkably, the physically motivated initial guess (Scheme 3) significantly reduces the energy fluctuation across all independent runs and provides consistent Hartree-Fock and CCSD energies.

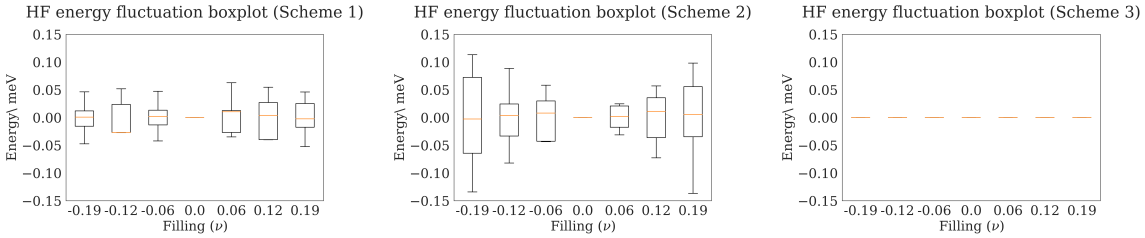

(a) (b) (c)

Figure 4.14: Boxplot showing the initial 1-RDM dependence of energy calculations at the HF level of theory for 20 random initializations from (a) Scheme 1, (b) Scheme 2, and (c) Scheme 3.

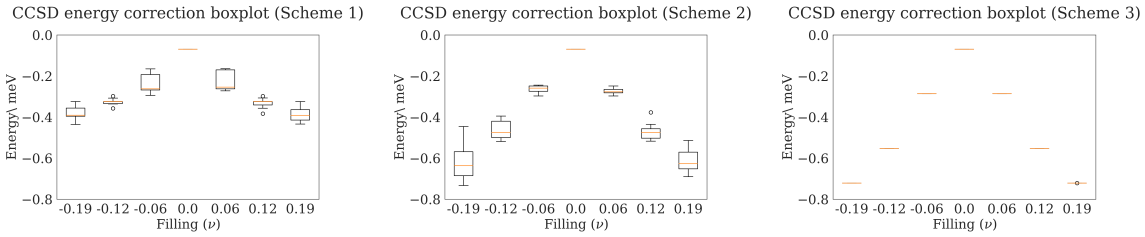

(a) (b) (c)

Figure 4.15: Boxplot showing the initial 1-RDM dependence of energy calculations at the CCSD level of theory for 20 random initializations from (a) Scheme 1, (b) Scheme 2, and (c) Scheme 3.

While there are many local minima that are energetically close to the ground state, the amount of variation in the gauge-invariant $C_{2z}\mathcal{T}$ order parameter can be significantly larger for many initial guesses. This is the case both for HF and CCSD calculations. As depicted in Figs. 4.16 and 4.17, enforcing the translation symmetry (Scheme 2) reduces the magnitude of the fluctuation in the $C_{2z}\mathcal{T}$ order parameter, and consistent order parameters can be obtained using the physically motivated initialization strategy as in Scheme 3.

Fig. 4.18 shows the 2D HF phase diagram obtained by performing 15 independent calculations and evaluating the $C_{2z}\mathcal{T}$ order parameter from the lowest energy state. The resulting phase diagrams qualitatively agree with that of Fig. 4.13a. Despite the existence of multiple local minima causing numerical fluctuations in the $C_{2z}\mathcal{T}$ order parameters at different points in the phase diagram, the qualitative features of the

diagram remain unchanged.

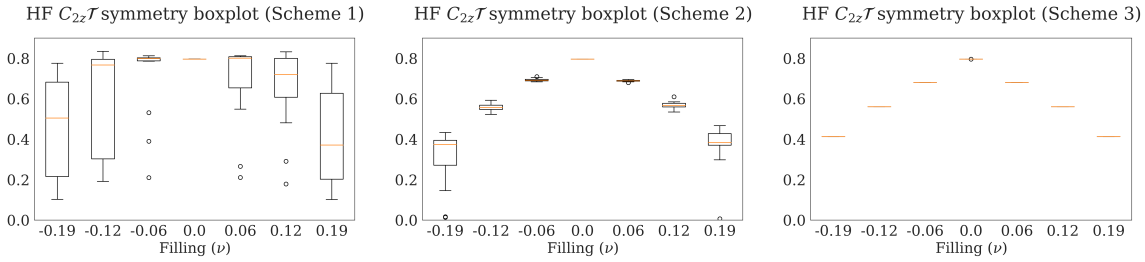

(a) (b) (c)

Figure 4.16: Boxplot showing the initial 1-RDM dependence of $C_{2z}\mathcal{T}$ calculations at the HF level of theory for 20 random initializations from (a) Scheme 1, (b) Scheme 2, and (c) Scheme 3.

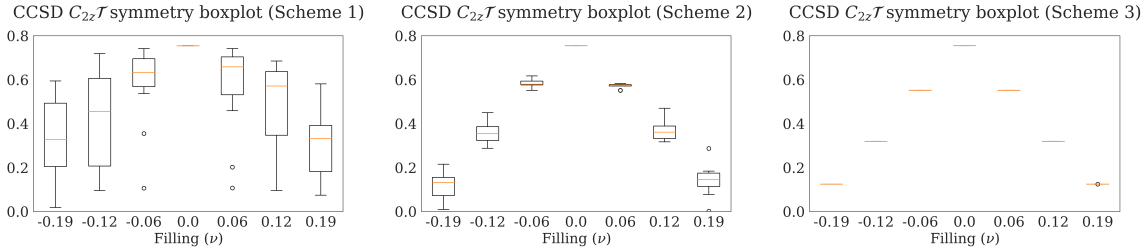

(a) (b) (c)

Figure 4.17: Boxplot showing the initial 1-RDM dependence of $C_{2z}\mathcal{T}$ calculations at the CCSD level of theory for 20 random initializations from (a) Scheme 1, (b) Scheme 2, and (c) Scheme 3.

To further study the behavior of the local minima and robustness of the numerical methods, we extract two 1-RDM initializations from the above performed experiment at filling $\nu = -0.125$ that yield different $C_{2z}\mathcal{T}$ order parameters, and we perform DMRG calculations with bond dimension 1800 using Scheme 1. We find that the result from DMRG is close to that of HF and CCSD in this regime, in terms of the energy and the value of the $C_{2z}\mathcal{T}$ order parameter. In particular, the DMRG results are also sensitive to the choice of the initial guess, see Table 4.4. Both CCSD and DMRG calculations show that the Fermi-Dirac entropy of these local minima is consistently low, suggesting that the solution is again close to being a single Slater determinant.

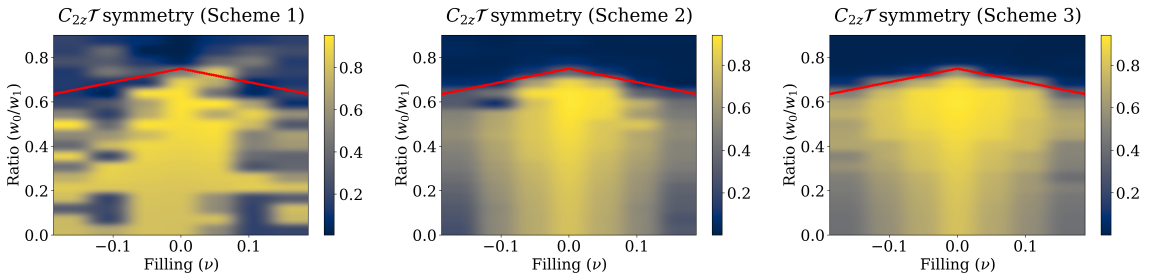

(a) (b) (c)

Figure 4.18: Phase diagram of $C_{2z}\mathcal{T}$ symmetry predictions at the HF level of theory from (a) Scheme 1, (b) Scheme 2, and (c) Scheme 3. The dotted red line indicates the phase transition as a function of the filling ν.

Initialization	Method	E	$C_{2z}\mathcal{T}$	S_{FD}	e_{corr}
Sample 1	HF	-87.522	0.81	0.00	
	CCSD	-87.865	0.64	0.14	-0.343
	DMRG	-87.823	0.78	0.10	-0.301
Sample 2	HF	-87.426	0.33	0.00	
	CCSD	-87.832	0.22	0.14	-0.404
	DMRG	-87.747	0.31	0.09	-0.321

Table 4.4: Energy, $C_{2z}\mathcal{T}$ order parameter, and Fermi-Dirac entropy using two instances of initialization from Scheme 1 and different methods at filling $\nu = -0.125$.

Chapter 5

Conclusion

In this dissertation, we demonstrate the fruitful application of correlated quantum chemistry techniques to study interacting models of the magic angle TBG system. We compare Hartree-Fock, coupled cluster, and DMRG calculations for ground state properties at both integer and non-integer fillings within a spinless, valleyless IBM model. The exploration of full-flavored IBM models, excited state properties, and other quantum chemistry methods is also within our scope and will be pursued in future research.

We identify model discrepancies as a significant source of uncertainty. To address this, an ensemble of interacting models may be required to cross-validate the results. To some extent, the IBM model design inherently incorporates this model discrepancy: starting from a non-interacting continuum BM model, we introduce electron-electron interaction as an afterthought. A more reductionist approach would involve commencing with an interacting electron model at the continuum level, tuning parameters at a simplified level of theory (such as Hartree-Fock), and studying electron-correlation effects by projecting the model onto a smaller number of degrees of freedom. Such an approach ensures at least self-consistency, with all errors and discrepancies eventually attributable to errors in the continuum model. The gauge-invariant order parameters, which are applicable to both unitary and antiunitary symmetries, could also be convenient in this setting since their implementation does not depend on the choice of the basis. Methods based on quantum embedding theories [31, 47, 90] may also become useful in mitigating the modeling errors and in studying electron correlation effects in this process.

Our current implementation treats all degrees of freedom equally, including the BM band index (or the sublattice index in the Chern band basis) and the $\mathbf{k}$-point index. It can also include other flavor indices, such as spin and valley degrees of freedom. While this supercell treatment of the IBM model significantly reduces

implementation efforts, proper consideration of crystal momentum conservation can further reduce the scaling of both computational and storage costs with respect to $N_{\mathbf{k}}$ (see e.g., [36, 68]), and will be explored in the future. Quantum chemistry packages are often designed to treat one particular flavor (spin). Therefore some further modifications may be needed if we would like to perform flavor-restricted/unrestricted calculations (which generalizes the spin restricted/unrestricted calculations in standard quantum chemistry methods).

Our numerical results indicate that even in the near integer filling regime ($|\nu| < 0.2$), it can be very challenging to converge to the global minima starting from random initial guesses. This challenge extends to both mean-field theories such as HF and DMRG calculations, which are typically considered more robust and less sensitive to initial guesses. However, careful initialization strategies and enforcing symmetries (such as translation symmetry) significantly improve the robustness of the procedure. We find that in the near integer filling regime, the system can be in a $C_{2z}\mathcal{T}$ symmetry breaking and metallic phase. Nonetheless, the entropy of these states is observed to be small, and can thus be relatively well described by a single Slater determinant. It seems reasonable to expect that the nature of the states can become qualitatively different as $|\nu|$ increases, supported by recent findings that at $\nu = -2/3$ (or 1/3 filling), the state of the system can be related to a fractional quantum Hall state (FQHE) which is distinct from a Slater determinant [73].

Bibliography

[1] Junyeong Ahn, Sungjoon Park, and Bohm-Jung Yang. "Failure of Nielsen-Ninomiya Theorem and Fragile Topology in Two-Dimensional Systems with Space-Time Inversion Symmetry: Application to Twisted Bilayer Graphene at Magic Angle". In: *Physical Review X* 9.2 (Apr. 22, 2019), p. 021013. ISSN: 2160-3308. DOI: 10.1103/PhysRevX.9.021013.

[2] Rodney J Bartlett and Monika Musiał. "Coupled-cluster theory in quantum chemistry". In: *Rev. Mod. Phys.* 79.1 (2007), p. 291.

[3] Simon Becker, Tristan Humbert, and Maciej Zworski. "Fine structure of flat bands in a chiral model of magic angles". In: *arXiv preprint arXiv:2208.01628* (2022).

[4] Simon Becker, Tristan Humbert, and Maciej Zworski. "Integrability in the chiral model of magic angles". In: *arXiv preprint arXiv:2208.01620* (2022).

[5] Simon Becker et al. "Mathematics of magic angles in a model of twisted bilayer graphene". In: *Probability and Mathematical Physics* 3.1 (2022), pp. 69–103.

[6] Simon Becker et al. "Spectral characterization of magic angles in twisted bilayer graphene". In: *Phys. Rev. B* 103.16 (2021), p. 165113.

[7] B Andrei Bernevig et al. "Twisted bilayer graphene. V. Exact analytic many-body excitations in Coulomb Hamiltonians: Charge gap, Goldstone modes, and absence of Cooper pairing". In: *Physical Review B* 103.20 (2021), p. 205415.

[8] B. Andrei Bernevig et al. "Twisted bilayer graphene. I. Matrix elements, approximations, perturbation theory, and a $\mathbf{k} \cdot \mathbf{p}$ two-band model". In: *Physical Review B* 103.20 (May 2021). ISSN: 2469-9969. DOI: 10.1103/physrevb.103.205411. URL: http://dx.doi.org/10.1103/PhysRevB.103.205411.

[9] B. Andrei Bernevig et al. "Twisted bilayer graphene. III. Interacting Hamiltonian and exact symmetries". In: *Phys. Rev. B* 103.20 (2021), p. 205413.

[10] R. Bistritzer and A. H. MacDonald. "Moiré bands in twisted double-layer graphene". In: *Proc. Natl. Acad. Sci.* 108.30 (2011), pp. 12233–12237.

[11] Nick Bultinck, Shubhayu Chatterjee, and Michael P. Zaletel. "Mechanism for Anomalous Hall Ferromagnetism in Twisted Bilayer Graphene". In: *Physical Review Letters* 124.16 (Apr. 2020). ISSN: 1079-7114. DOI: 10.1103/physrevlett.124.166601. URL: http://dx.doi.org/10.1103/PhysRevLett.124.166601.

[12] Nick Bultinck et al. "Ground State and Hidden Symmetry of Magic-Angle Graphene at Even Integer Filling". In: *Phys. Rev. X* 10.3 (2020), p. 031034.

[13] Yuan Cao et al. "Correlated insulator behaviour at half-filling in magic-angle graphene superlattices". In: *Nature* 556.7699 (Mar. 2018), pp. 80–84.

[14] Yuan Cao et al. "Unconventional superconductivity in magic-angle graphene superlattices". In: *Nature* 556.7699 (Mar. 2018), pp. 43–50.

[15] Stephen Carr et al. "Exact continuum model for low-energy electronic states of twisted bilayer graphene". In: *Phys. Rev. Res.* 1.1 (2019), p. 013001.

[16] Tommaso Cea and Francisco Guinea. "Band structure and insulating states driven by Coulomb interaction in twisted bilayer graphene". In: *Phys. Rev. B* 102 (4 July 2020), p. 045107. DOI: 10.1103/PhysRevB.102.045107. URL: https://link.aps.org/doi/10.1103/PhysRevB.102.045107.

[17] Garnet Kin-Lic Chan and Martin Head-Gordon. "Highly correlated calculations with a polynomial cost algorithm: A study of the density matrix renormalization group". In: *The Journal of chemical physics* 116.11 (2002), pp. 4462–4476.

[18] Garnet Kin-Lic Chan, Mihály Kállay, and Jürgen Gauss. "State-of-the-art density matrix renormalization group and coupled cluster theory studies of the nitrogen binding curve". In: *J. Chem. Phys.* 121.13 (2004), pp. 6110–6116.

[19] Garnet Kin-Lic Chan et al. "Matrix product operators, matrix product states, and ab initio density matrix renormalization group algorithms". In: *The Journal of chemical physics* 145.1 (2016), p. 014102.

[20] Shubhayu Chatterjee, Nick Bultinck, and Michael P. Zaletel. "Symmetry breaking and skyrmionic transport in twisted bilayer graphene". In: *Phys. Rev. B* 101.16 (Apr. 2020).

[21] Youngjoon Choi et al. "Electronic correlations in twisted bilayer graphene near the magic angle". In: *Nature Physics* 15.11 (Aug. 2019), pp. 1174–1180. ISSN: 1745-2481. DOI: 10.1038/s41567-019-0606-5. URL: http://dx.doi.org/10.1038/s41567-019-0606-5.

[22] Maine Christos, Subir Sachdev, and Mathias S. Scheurer. "Superconductivity, correlated insulators, and Wess–Zumino–Witten terms in twisted bilayer graphene". In: *Proceedings of the National Academy of Sciences* 117.47 (Nov. 2020), pp. 29543–29554. ISSN: 1091-6490. DOI: 10.1073/pnas.2014691117. URL: http://dx.doi.org/10.1073/pnas.2014691117.

[23] Laura Classen, Carsten Honerkamp, and Michael M. Scherer. "Competing phases of interacting electrons on triangular lattices in moiré heterostructures". In: *Physical Review B* 99.19 (May 2019). ISSN: 2469-9969. DOI: 10.1103/physrevb.99.195120. URL: http://dx.doi.org/10.1103/PhysRevB.99.195120.

[24] Yuan Da Liao et al. "Correlation-Induced Insulating Topological Phases at Charge Neutrality in Twisted Bilayer Graphene". In: *Physical Review X* 11.1 (Jan. 2021). ISSN: 2160-3308. DOI: 10.1103/physrevx.11.011014. URL: http://dx.doi.org/10.1103/PhysRevX.11.011014.

[25] Ipsita Das et al. "Symmetry-broken Chern insulators and Rashba-like Landau-level crossings in magic-angle bilayer graphene". In: *Nat. Phys.* 17.6 (Mar. 2021), pp. 710–714.

[26] J. F. Dodaro et al. "Phases of a phenomenological model of twisted bilayer graphene". In: *Phys. Rev. B* 98 (7 Aug. 2018), p. 075154. DOI: 10.1103/PhysRevB.98.075154. URL: https://link.aps.org/doi/10.1103/PhysRevB.98.075154.

[27] Giampiero Esposito. *Dirac Operator and Eigenvalues in Riemannian Geometry*. 1995. arXiv: gr-qc/9507046 [gr-qc].

[28] Peng-Dong Fan, Karol Kowalski, and Piotr Piecuch. "Non-iterative corrections to extended coupled-cluster energies employing the generalized method of moments of coupled-cluster equations". In: *Mol. Phys.* 103.15-16 (2005), pp. 2191–2213.

[29] Chen Fang, Matthew J Gilbert, and B Andrei Bernevig. "Bulk topological invariants in noninteracting point group symmetric insulators". In: *Phys. Rev. B* 86.11 (2012), p. 115112.

[30] Fabian M. Faulstich et al. "Interacting models for twisted bilayer graphene: A quantum chemistry approach". In: *Physical Review B* 107.23 (June 2023). ISSN: 2469-9969. DOI: 10.1103/physrevb.107.235123. URL: http://dx.doi.org/10.1103/PhysRevB.107.235123.

[31] Antoine Georges and Gabriel Kotliar. "Hubbard model in infinite dimensions". In: *Phys. Rev. B* 45 (1992), pp. 6479–6483.

[32] J. González and T. Stauber. "Kohn-Luttinger Superconductivity in Twisted Bilayer Graphene". In: *Phys. Rev. Lett.* 122 (2 Jan. 2019), p. 026801. DOI: 10.1103/PhysRevLett.122.026801. URL: https://link.aps.org/doi/10.1103/PhysRevLett.122.026801.

[33] Francisco Guinea and Niels R. Walet. "Electrostatic effects, band distortions, and superconductivity in twisted graphene bilayers". In: *Proceedings of the National Academy of Sciences* 115.52 (Dec. 2018), pp. 13174–13179. ISSN: 1091-6490. DOI: 10.1073/pnas.1810947115. URL: http://dx.doi.org/10.1073/pnas.1810947115.

[34] Kasra Hejazi, Xiao Chen, and Leon Balents. "Hybrid Wannier Chern bands in magic angle twisted bilayer graphene and the quantized anomalous Hall effect". In: *Phys. Rev. Res.* 3 (1 Mar. 2021), p. 013242. DOI: 10.1103/PhysRevResearch.3.013242. URL: https://link.aps.org/doi/10.1103/PhysRevResearch.3.013242.

[35] Trygve Helgaker, Poul Jorgensen, and Jeppe Olsen. *Molecular electronic-structure theory*. John Wiley & Sons, 2014.

[36] So Hirata et al. "Coupled-cluster singles and doubles for extended systems". In: *J. Chem. Phys.* 120.6 (2004), pp. 2581–2592.

[37] Xiang Hu et al. "Geometric and Conventional Contribution to the Superfluid Weight in Twisted Bilayer Graphene". In: *Phys. Rev. Lett.* 123 (23 Dec. 2019), p. 237002. DOI: 10.1103/PhysRevLett.123.237002. URL: https://link.aps.org/doi/10.1103/PhysRevLett.123.237002.

[38] J.E. Humphreys. *Introduction to Lie Algebras and Representation Theory*. Graduate texts in mathematics. Springer, 1972. ISBN: 9780387900537. URL: https://books.google.com/books?id=TiUlAQAAIAAJ.

[39] Hiroki Isobe, Noah F. Q. Yuan, and Liang Fu. "Unconventional Superconductivity and Density Waves in Twisted Bilayer Graphene". In: *Phys. Rev. X* 8 (4 Dec. 2018), p. 041041. DOI: 10.1103/PhysRevX.8.041041. URL: https://link.aps.org/doi/10.1103/PhysRevX.8.041041.

[40] Karol Jankowski, Josef Paldus, and Piotr Piecuch. "Method of moments approach and coupled cluster theory". In: *Theor. Chim. Acta* 80.4 (1991), pp. 223–243.

[41] Yuhang Jiang et al. "Charge order and broken rotational symmetry in magic-angle twisted bilayer graphene". In: *Nature* 573.7772 (July 2019), pp. 91–95.

[42] A. Julku et al. "Superfluid weight and Berezinskii-Kosterlitz-Thouless transition temperature of twisted bilayer graphene". In: *Phys. Rev. B* 101 (6 Feb. 2020), p. 060505. DOI: 10.1103/PhysRevB.101.060505. URL: https://link.aps.org/doi/10.1103/PhysRevB.101.060505.

[43] Jian Kang and Oskar Vafek. "Non-Abelian Dirac node braiding and near-degeneracy of correlated phases at odd integer filling in magic-angle twisted bilayer graphene". In: *Phys. Rev. B* 102.3 (2020), p. 035161.

[44] Jian Kang and Oskar Vafek. "Strong coupling phases of partially filled twisted bilayer graphene narrow bands". In: *Phys. Rev. Lett.* 122.24 (2019), p. 246401.

[45] Jian Kang and Oskar Vafek. "Symmetry, Maximally Localized Wannier States, and a Low-Energy Model for Twisted Bilayer Graphene Narrow Bands". In: *Phys. Rev. X* 8 (3 Sept. 2018), p. 031088. DOI: 10.1103/PhysRevX.8.031088. URL: https://link.aps.org/doi/10.1103/PhysRevX.8.031088.

[46] Eslam Khalaf et al. "Charged skyrmions and topological origin of superconductivity in magic-angle graphene". In: *Science Advances* 7.19 (May 2021). ISSN: 2375-2548. DOI: 10.1126/sciadv.abf5299. URL: http://dx.doi.org/10.1126/sciadv.abf5299.

[47] G. Knizia and G. Chan. "Density matrix embedding: A simple alternative to dynamical mean-field theory". In: *Phys. Rev. Lett.* 109 (2012), p. 186404.

[48] E. J. König, Piers Coleman, and A. M. Tsvelik. "Spin magnetometry as a probe of stripe superconductivity in twisted bilayer graphene". In: *Physical Review B* 102.10 (Sept. 2020). ISSN: 2469-9969. DOI: 10.1103/physrevb.102.104514. URL: http://dx.doi.org/10.1103/PhysRevB.102.104514.

[49] Mikito Koshino et al. "Maximally localized wannier orbitals and the extended hubbard model for twisted bilayer graphene". In: *Phys.l Rev. X* 8.3 (2018), p. 031087.

[50] Karol Kowalski and Piotr Piecuch. "The method of moments of coupled-cluster equations and the renormalized CCSD[T], CCSD(T), CCSD(TQ), and CCSDT(Q) approaches". In: *J. Chem. Phys.* 113.1 (2000), pp. 18–35.

[51] Andre Laestadius and Fabian M. Faulstich. "The coupled-cluster formalism–a mathematical perspective". In: *Mol. Phys.* 117.17 (2019), pp. 2362–2373.

[52] H. BLAINE LAWSON and MARIE-LOUISE MICHELSOHN. *Spin Geometry (PMS-38)*. Princeton University Press, 1989. ISBN: 9780691085425. URL: http://www.jstor.org/stable/j.ctt1bpmb28 (visited on 11/26/2023).

[53] Patrick J Ledwith et al. "Fractional Chern insulator states in twisted bilayer graphene: An analytical approach". In: *Phys. Rev. Res.* 2.2 (2020), p. 023237.

[54] Jong Yeon Lee et al. "Theory of correlated insulating behaviour and spin-triplet superconductivity in twisted double bilayer graphene". In: *Nature Communications* 10.1 (Nov. 2019). ISSN: 2041-1723. DOI: 10.1038/s41467-019-12981-1. URL: http://dx.doi.org/10.1038/s41467-019-12981-1.

[55] Susi Lehtola, Frank Blockhuys, and Christian Van Alsenoy. "An overview of self-consistent field calculations within finite basis sets". In: *Molecules* 25.5 (2020), p. 1218.

[56] Cyprian Lewandowski, Debanjan Chowdhury, and Jonathan Ruhman. "Pairing in magic-angle twisted bilayer graphene: Role of phonon and plasmon umklapp". In: *Physical Review B* 103.23 (June 2021). ISSN: 2469-9969. DOI: 10.1103/physrevb.103.235401. URL: http://dx.doi.org/10.1103/PhysRevB.103.235401.

[57] Biao Lian, Zhijun Wang, and B. Andrei Bernevig. "Twisted Bilayer Graphene: A Phonon-Driven Superconductor". In: *Physical Review Letters* 122.25 (June 2019). ISSN: 1079-7114. DOI: 10.1103/physrevlett.122.257002. URL: http://dx.doi.org/10.1103/PhysRevLett.122.257002.

[58] Biao Lian et al. "Twisted bilayer graphene. IV. Exact insulator ground states and phase diagram". In: *Physical Review B* 103.20 (May 2021). ISSN: 2469-9969. DOI: 10.1103/physrevb.103.205414. URL: http://dx.doi.org/10.1103/PhysRevB.103.205414.

[59] Cheng-Cheng Liu et al. "Chiral Spin Density Wave and $d+id$ Superconductivity in the Magic-Angle-Twisted Bilayer Graphene". In: *Physical Review Letters* 121.21 (Nov. 2018). ISSN: 1079-7114. DOI: 10.1103/physrevlett.121.217001. URL: http://dx.doi.org/10.1103/PhysRevLett.121.217001.

[60] Jianpeng Liu and Xi Dai. "Theories for the correlated insulating states and quantum anomalous Hall effect phenomena in twisted bilayer graphene". In: *Physical Review B* 103.3 (Jan. 2021). ISSN: 2469-9969. DOI: 10.1103/physrevb.103.035427. URL: http://dx.doi.org/10.1103/PhysRevB.103.035427.

[61] Jianpeng Liu, Junwei Liu, and Xi Dai. "Pseudo Landau level representation of twisted bilayer graphene: Band topology and implications on the correlated insulating phase". In: *Physical Review B* 99.15 (Apr. 2019). ISSN: 2469-9969. DOI: 10.1103/physrevb.99.155415. URL: http://dx.doi.org/10.1103/PhysRevB.99.155415.

[62] Jianpeng Liu et al. "Quantum Valley Hall Effect, Orbital Magnetism, and Anomalous Hall Effect in Twisted Multilayer Graphene Systems". In: *Physical Review X* 9.3 (Aug. 2019). ISSN: 2160-3308. DOI: 10.1103/physrevx.9.031021. URL: http://dx.doi.org/10.1103/PhysRevX.9.031021.

[63] Shang Liu et al. "Nematic topological semimetal and insulator in magic-angle bilayer graphene at charge neutrality". In: *Phys. Rev. Res.* 3.1 (Jan. 2021).

[64] Marta W Loch et al. "Two new classes of non-iterative coupled-cluster methods derived from the method of moments of coupled-cluster equations". In: *Mol. Phys.* 104.13-14 (2006), pp. 2149–2172.

[65] Xiaobo Lu et al. "Multiple flat bands and topological Hofstadter butterfly in twisted bilayer graphene close to the second magic angle". In: *Proceedings of the National Academy of Sciences* 118.30 (July 2021). ISSN: 1091-6490. DOI: 10.1073/pnas.2100006118. URL: http://dx.doi.org/10.1073/pnas.2100006118.

[66] Xiaobo Lu et al. "Superconductors, orbital magnets and correlated states in magic-angle bilayer graphene". In: *Nature* 574.7780 (Oct. 2019), pp. 653–657.

[67] R. M. Martin, L. Reining, and D. M. Ceperley. *Interacting Electrons*. Cambridge Univ. Pr., 2016.

[68] James McClain et al. "Gaussian-Based Coupled-Cluster Theory for the Ground-State and Band Structure of Solids". In: *J. Chem. Theory Comput.* 13.3 (2017), pp. 1209–1218.

[69] H. J. Monkhorst and J. D. Pack. "Special points for Brillouin-zone integrations". In: *Phys. Rev. B* 13.12 (1976), p. 5188.

[70] Hendrik J Monkhorst. "Calculation of properties with the coupled-cluster method". In: *Int. J. Quantum Chem.* 12.S11 (1977), pp. 421–432.

[71] Nguyen N. T. Nam and Mikito Koshino. "Lattice relaxation and energy band modulation in twisted bilayer graphene". In: *Phys. Rev. B* 96.7 (Aug. 2017).

[72] Masayuki Ochi, Mikito Koshino, and Kazuhiko Kuroki. "Possible correlated insulating states in magic-angle twisted bilayer graphene under strongly competing interactions". In: *Physical Review B* 98.8 (Aug. 2018). ISSN: 2469-9969. DOI: 10.1103/physrevb.98.081102. URL: http://dx.doi.org/10.1103/PhysRevB.98.081102.

[73] Daniel Parker et al. "Field-tuned and zero-field fractional Chern insulators in magic angle graphene". In: *arXiv preprint arXiv:2112.13837* (2021).

[74] Daniel E. Parker et al. "Strain-Induced Quantum Phase Transitions in Magic-Angle Graphene". In: *Phys. Rev. Lett.* 127 (2 July 2021), p. 027601. DOI: 10.1103/PhysRevLett.127.027601. URL: https://link.aps.org/doi/10.1103/PhysRevLett.127.027601.

[75] P Piecuch et al. "Method of moments of coupled-cluster equations: a new formalism for designing accurate electronic structure methods for ground and excited states". In: *Theor. Chem. Acc.* 112.5 (2004), pp. 349–393.

[76] Piotr Piecuch. "Active-space coupled-cluster methods". In: *Mol. Phys.* 108.21-23 (2010), pp. 2987–3015.

[77] Piotr Piecuch et al. "Recent advances in electronic structure theory: Method of moments of coupled-cluster equations and renormalized coupled-cluster approaches". In: *Int. Rev. Phys. Chem.* 21.4 (2002), pp. 527–655.

[78] Jed H. Pixley and Eva Y. Andrei. "Ferromagnetism in magic-angle graphene". In: *Science* 365.6453 (2019), pp. 543–543. DOI: 10.1126/science.aay3409. eprint: https://www.science.org/doi/pdf/10.1126/science.aay3409. URL: https://www.science.org/doi/abs/10.1126/science.aay3409.

[79] Hoi Chun Po et al. "Origin of Mott Insulating Behavior and Superconductivity in Twisted Bilayer Graphene". In: *Phys. Rev. X* 8.3 (Sept. 2018).

[80] Pawel Potasz, Ming Xie, and A. H. MacDonald. "Exact Diagonalization for Magic-Angle Twisted Bilayer Graphene". In: *Phys. Rev. Lett.* 127.14 (2021), p. 147203.

[81] Krishnan Raghavachari et al. "A fifth-order perturbation comparison of electron correlation theories". In: *Chem. Phys. Lett.* 157.6 (1989), pp. 479–483.

[82] Yu Saito et al. "Hofstadter subband ferromagnetism and symmetry-broken Chern insulators in twisted bilayer graphene". In: *Nat. Phys.* 17.4 (Jan. 2021), pp. 478–481.

[83] Reinhold Schneider. "Analysis of the projected coupled cluster method in electronic structure calculation". In: *Numer. Math.* 113.3 (2009), pp. 433–471.

[84] Kangjun Seo, Valeri N. Kotov, and Bruno Uchoa. "Ferromagnetic Mott state in Twisted Graphene Bilayers at the Magic Angle". In: *Physical Review Letters* 122.24 (June 2019). ISSN: 1079-7114. DOI: 10.1103/physrevlett.122.246402. URL: http://dx.doi.org/10.1103/PhysRevLett.122.246402.

[85] Isaiah Shavitt and Rodney J Bartlett. *Many-body methods in chemistry and physics: MBPT and coupled-cluster theory*. Cambridge Univ. Pr., 2009.

[86] Tomohiro Soejima et al. "Efficient simulation of moiré materials using the density matrix renormalization group". In: *Phys. Rev. B* 102.20 (2020), pp. 1–31.

[87] Tomohiro Soejima et al. "Efficient simulation of moiré materials using the density matrix renormalization group". In: *Physical Review B* 102.20 (Nov. 2020). ISSN: 2469-9969. DOI: 10.1103/physrevb.102.205111. URL: http://dx.doi.org/10.1103/PhysRevB.102.205111.

[88] Zhi-da Song et al. "Twisted bilayer graphene. II. Stable symmetry anomaly". In: *Physical Review B* 103.20 (2021), p. 205412.

[89] Zhida Song et al. "All Magic Angles in Twisted Bilayer Graphene are Topological". In: *Phys. Rev. Lett.* 123.3 (July 2019).

[90] Q. Sun and G. K.-L. Chan. "Quantum embedding theories". In: *Acc. Chem. Res.* 49 (2016), pp. 2705–2712.

[91] Qiming Sun et al. "PySCF: the Python-based simulations of chemistry framework". In: *Wiley Interdiscip. Rev. Comput. Mol. Sci.* 8.1 (2018), e1340.

[92] Qiming Sun et al. "Recent developments in the PySCF program package". In: *J. Chem. Phys.* 153.2 (2020), p. 024109.

[93] A. Szabo and N.S. Ostlund. *Modern Quantum Chemistry: Introduction to Advanced Electronic Structure Theory*. McGraw-Hill, New York, 1989.

[94] Grigory Tarnopolsky, Alex Jura Kruchkov, and Ashvin Vishwanath. "Origin of Magic Angles in Twisted Bilayer Graphene". In: *Physical Review Letters* 122.10 (Mar. 2019). ISSN: 1079-7114. DOI: 10.1103/physrevlett.122.106405. URL: http://dx.doi.org/10.1103/PhysRevLett.122.106405.

[95] Grigory Tarnopolsky, Alex Jura Kruchkov, and Ashvin Vishwanath. "Origin of magic angles in twisted bilayer graphene". In: *Phys. Rev. Let.* 122.10 (2019), p. 106405.

[96] Alex Thomson et al. "Triangular antiferromagnetism on the honeycomb lattice of twisted bilayer graphene". In: *Physical Review B* 98.7 (Aug. 2018). ISSN: 2469-9969. DOI: 10.1103/physrevb.98.075109. URL: http://dx.doi.org/10.1103/PhysRevB.98.075109.

[97] Oskar Vafek and Jian Kang. "Lattice model for the Coulomb interacting chiral limit of magic-angle twisted bilayer graphene: Symmetries, obstructions, and excitations". In: *Phys. Rev. B* 104.7 (2021), p. 075143.

[98] Oskar Vafek and Jian Kang. "Renormalization Group Study of Hidden Symmetry in Twisted Bilayer Graphene with Coulomb Interactions". In: *Physical Review Letters* 125.25 (Dec. 2020). DOI: 10.1103/physrevlett.125.257602. URL: https://doi.org/10.1103%2Fphysrevlett.125.257602.

[99] Jörn W. F. Venderbos and Rafael M. Fernandes. "Correlations and electronic order in a two-orbital honeycomb lattice model for twisted bilayer graphene". In: *Physical Review B* 98.24 (Dec. 2018). ISSN: 2469-9969. DOI: 10.1103/physrevb.98.245103. URL: http://dx.doi.org/10.1103/PhysRevB.98.245103.

[100] Tianle Wang et al. "Kekulé spiral order in magic-angle graphene: a density matrix renormalization group study". In: (2022). DOI: 10.48550/ARXIV.2211.02693. URL: https://arxiv.org/abs/2211.02693.

[101] Alexander B Watson and Mitchell Luskin. "Existence of the first magic angle for the chiral model of bilayer graphene". In: *J. Math. Phys.* 62.9 (2021), p. 091502.

[102] S. R. White. "Density matrix formulation for quantum renormalization groups". In: *Phys. Rev. Lett.* 69.19 (1992), p. 2863.

[103] Steven R White and Richard L Martin. "Ab initio quantum chemistry using the density matrix renormalization group". In: *The Journal of chemical physics* 110.9 (1999), pp. 4127–4130.

[104] Fengcheng Wu, A. H. MacDonald, and Ivar Martin. "Theory of Phonon-Mediated Superconductivity in Twisted Bilayer Graphene". In: *Physical Review Letters* 121.25 (Dec. 2018). ISSN: 1079-7114. DOI: 10.1103/physrevlett.121.257001. URL: http://dx.doi.org/10.1103/PhysRevLett.121.257001.

[105] Fengcheng Wu and Sankar Das Sarma. "Collective Excitations of Quantum Anomalous Hall Ferromagnets in Twisted Bilayer Graphene". In: *Phys. Rev. Lett.* 124.4 (Jan. 2020).

[106] Xiao-Chuan Wu, Chao-Ming Jian, and Cenke Xu. "Coupled-wire description of the correlated physics in twisted bilayer graphene". In: *Physical Review B* 99.16 (Apr. 2019). ISSN: 2469-9969. DOI: 10.1103/physrevb.99.161405. URL: http://dx.doi.org/10.1103/PhysRevB.99.161405.

[107] Fang Xie et al. "Topology-Bounded Superfluid Weight in Twisted Bilayer Graphene". In: *Phys. Rev. Lett.* 124 (16 Apr. 2020), p. 167002. DOI: 10.1103/PhysRevLett.124.167002. URL: https://link.aps.org/doi/10.1103/PhysRevLett.124.167002.

[108] Fang Xie et al. "Twisted bilayer graphene. VI. An exact diagonalization study at nonzero integer filling". In: *Phys. Rev. B* 103 (20 May 2021), p. 205416. DOI: 10.1103/PhysRevB.103.205416. URL: https://link.aps.org/doi/10.1103/PhysRevB.103.205416.

[109] Ming Xie and Allan H MacDonald. "Nature of the correlated insulator states in twisted bilayer graphene". In: *Phys. Rev. Lett.* 124.9 (2020), p. 097601.

[110] Cenke Xu and Leon Balents. "Topological Superconductivity in Twisted Multilayer Graphene". In: *Physical Review Letters* 121.8 (Aug. 2018). ISSN: 1079-7114. DOI: 10.1103/physrevlett.121.087001. URL: http://dx.doi.org/10.1103/PhysRevLett.121.087001.

[111] Xiao Yan Xu, K. T. Law, and Patrick A. Lee. "Kekulé valence bond order in an extended Hubbard model on the honeycomb lattice with possible applications to twisted bilayer graphene". In: *Physical Review B* 98.12 (Sept. 2018). ISSN: 2469-9969. DOI: 10.1103/physrevb.98.121406. URL: http://dx.doi.org/10.1103/PhysRevB.98.121406.

[112] Matthew Yankowitz et al. "Tuning superconductivity in twisted bilayer graphene". In: *Science* 363.6431 (Mar. 2019), pp. 1059–1064.

[113] Yi-Zhuang You and Ashvin Vishwanath. "Superconductivity from valley fluctuations and approximate SO(4) symmetry in a weak coupling theory of twisted bilayer graphene". In: *npj Quantum Materials* 4.1 (Apr. 2019). ISSN: 2397-4648. DOI: 10.1038/s41535-019-0153-4. URL: http://dx.doi.org/10.1038/s41535-019-0153-4.

[114] Noah F. Q. Yuan and Liang Fu. "Model for the metal-insulator transition in graphene superlattices and beyond". In: *Phys. Rev. B* 98 (4 July 2018), p. 045103. DOI: 10.1103/PhysRevB.98.045103. URL: https://link.aps.org/doi/10.1103/PhysRevB.98.045103.

[115] Huanchen Zhai and Garnet Kin-Lic Chan. "Low communication high performance ab initio density matrix renormalization group algorithms". In: *The Journal of Chemical Physics* 154.22 (2021), p. 224116.

[116] Ya-Hui Zhang et al. "Nearly flat Chern bands in moiré superlattices". In: *Physical Review B* 99.7 (Feb. 2019). ISSN: 2469-9969. DOI: 10.1103/physrevb.99.075127. URL: http://dx.doi.org/10.1103/PhysRevB.99.075127.

[117] Yi Zhang et al. "Correlated insulating phases of twisted bilayer graphene at commensurate filling fractions: A Hartree-Fock study". In: *Phys. Rev. B* 102 (3 July 2020), p. 035136. DOI: 10.1103/PhysRevB.102.035136. URL: https://link.aps.org/doi/10.1103/PhysRevB.102.035136.

[118] Liujun Zou et al. "Band structure of twisted bilayer graphene: Emergent symmetries, commensurate approximants, and Wannier obstructions". In: *Physical Review B* 98.8 (Aug. 2018). ISSN: 2469-9969. DOI: 10.1103/physrevb.98.085435. URL: http://dx.doi.org/10.1103/PhysRevB.98.085435.